



TECHNISCHE
UNIVERSITÄT
DRESDEN

Dynamical Tunneling in Systems with a Mixed Phase Space

Dissertation
zur Erlangung des akademischen Grades
Doctor rerum naturalium

vorgelegt von

Steffen Löck

geboren am 22.03.1982 in Radebeul

Institut für Theoretische Physik
Fachrichtung Physik
Fakultät für Mathematik und Naturwissenschaften
Technische Universität Dresden

2009

Eingereicht am 16.12.2009

1. Gutachter: Prof. Dr. Roland Ketzmerick

2. Gutachter: Prof. Dr. Jan Wiersig

Verteidigt am 22.04.2010

Abstract

Tunneling is one of the most prominent features of quantum mechanics. While the tunneling process in one-dimensional integrable systems is well understood, its quantitative prediction for systems with a mixed phase space is a long-standing open challenge. In such systems regions of regular and chaotic dynamics coexist in phase space, which are classically separated but quantum mechanically coupled by the process of dynamical tunneling. We derive a prediction of dynamical tunneling rates which describe the decay of states localized inside the regular region towards the so-called chaotic sea. This approach uses a fictitious integrable system which mimics the dynamics inside the regular domain and extends it into the chaotic region. Excellent agreement with numerical data is found for kicked systems, billiards, and optical microcavities, if nonlinear resonances are negligible. Semiclassically, however, such nonlinear resonance chains dominate the tunneling process. Hence, we combine our approach with an improved resonance-assisted tunneling theory and derive a unified prediction which is valid from the quantum to the semiclassical regime. We obtain results which show a drastically improved accuracy of several orders of magnitude compared to previous studies.

Zusammenfassung

Der Tunnelprozess ist einer der bedeutendsten Effekte in der Quantenmechanik. Während das Tunneln in eindimensionalen integrablen Systemen gut verstanden ist, gestaltet sich dessen Beschreibung für Systeme mit gemischtem Phasenraum weitaus schwieriger. Solche Systeme besitzen Gebiete regulärer und chaotischer Bewegung, die klassisch getrennt sind, aber quantenmechanisch durch den Prozess des dynamischen Tunnelns gekoppelt werden. In dieser Arbeit wird eine theoretische Vorhersage für dynamische Tunnelraten abgeleitet, die den Zerfall von Zuständen, die im regulären Gebiet lokalisiert sind, in die sogenannte chaotische See beschreibt. Dazu wird ein fiktives integrables System konstruiert, das im regulären Bereich eine nahezu gleiche Dynamik aufweist und diese Dynamik in das chaotische Gebiet fortsetzt. Die Theorie zeigt eine ausgezeichnete Übereinstimmung mit numerischen Daten für gekickte Systeme, Billards und optische Mikrokavitäten, falls nichtlineare Resonanzketten vernachlässigbar sind. Semiklassisch jedoch bestimmen diese nichtlinearen Resonanzketten den Tunnelprozess. Daher kombinieren wir unseren Zugang mit einer verbesserten Theorie des Resonanz-unterstützten Tunnelns und erhalten eine Vorhersage, die vom Quanten- bis in den semiklassischen Bereich gültig ist. Ihre Resultate zeigen eine Genauigkeit, die verglichen mit früheren Theorien um mehrere Größenordnungen verbessert wurde.

Contents

1	Introduction	1
2	Barrier tunneling in one-dimensional systems	7
2.1	WKB method	7
2.2	Bohr-Sommerfeld quantization	12
2.3	Gamov theory	14
2.4	Application to double-well potential	15
2.5	Application to δ -potential	21
3	Model systems with a mixed phase space	25
3.1	Kicked systems	25
3.1.1	Classical maps	25
3.1.2	Examples	32
3.1.3	Classical perturbation theory	40
3.1.4	Quantization	53
3.1.5	Numerical methods for the calculation of tunneling rates	65
3.2	Billiard systems	71
3.2.1	Classical dynamics	72
3.2.2	Quantum billiards	75
3.2.3	Numerical methods for the calculation of tunneling rates	87
3.3	Optical microcavities	91
3.3.1	Ray dynamics	92
3.3.2	Wave mechanics	94
4	Dynamical tunneling in quantum maps	97
4.1	Direct regular-to-chaotic tunneling	98
4.1.1	Theoretical description	99
4.1.2	Fictitious integrable system and convergence	102
4.1.3	Semiclassical evaluation	105
4.1.4	Applications	110
4.2	Unification with resonance-assisted tunneling	121
4.2.1	Theory of resonance-assisted tunneling	122

4.2.2	Improvements of resonance-assisted tunneling	128
4.2.3	Multi-resonance effects	131
4.2.4	Applications	135
5	Dynamical tunneling in billiard systems	143
5.1	Direct regular-to-chaotic tunneling	143
5.2	Applications	145
5.2.1	Mushroom billiards	145
5.2.2	Annular billiards	157
5.2.3	Dynamical tunneling of bouncing-ball modes	162
5.2.4	Two-dimensional nanowires with a magnetic field	169
5.2.5	Cosine billiards	173
6	Quality factors of optical microcavities	179
6.1	The circular microcavity	179
6.2	Direct regular-to-chaotic tunneling in the annular microcavity	182
7	Summary and outlook	191
A	Dimensionless variables	195
B	Classical kicked systems	197
B.1	Smoothing of designed discontinuous mappings	197
B.2	An example of the Lie transformation	200
B.3	An example of the normal-form analysis	204
B.4	Calculation of the pendulum parameters $V_{r:s}$, $I_{r:s}$, $M_{r:s}$	207
C	Quantum maps	211
C.1	Semiclassical energies of kicked systems	211
C.2	Phase splittings and tunneling rates	213
C.3	Tunneling rates and coupling matrix elements	214
D	Billiard systems	215
D.1	Coupling matrix elements of non-orthogonal states	215
D.2	Derivation of A_{ch} for the mushroom billiard	216
D.3	Eigenmodes of a wire in a magnetic field	217
D.4	Semiclassical description of localization lengths in wires with one-sided disorder	219
	Bibliography	221

1 Introduction

The exponential decay rates of radioactive substances were found experimentally by Elster and Geitel [1] in 1899, three years after the discovery of natural radioactivity. One year later Rutherford introduced the concept of half-life times [2]. The radioactive decay is a purely quantum phenomenon. Due to the uncertainty principle for quantum particles the position and the momentum cannot be specified at the same time with arbitrary precision as in classical mechanics. Instead, it is described by a wave function which is given as a solution of the Schrödinger equation. The modulus squared of this wave function is a probability amplitude for the distribution of the particle. This probability can be positive even in regions where the classical motion is forbidden. For example this occurs for an energy barrier of finite height which classically cannot be passed if the energy of the particle is too low. Hence, a quantum mechanical particle may pass through such a potential barrier which is called *quantum tunneling*. This occurs for the α -decay which is described by the well-known Gamov formula [3–5]. Later, electron tunneling in solids was demonstrated by Esaki [6, 7] in 1957 who discovered the tunneling diode. In 1962 Josephson studied tunneling between two superconductors separated by a thin layer of insulating oxide which serves as a barrier. He predicted the existence of a supercurrent caused by the tunneling of electrons in pairs [8]. Today tunneling in individual atoms and molecules can be observed [9–12] and Bose-Einstein condensates are used to study the interplay of tunneling with effects caused by nonlinear interactions [13, 14].

The theoretical description of tunneling in all its varieties is still a challenging open problem. For one-dimensional time-independent systems, however, it is well understood. Therefore, these simple systems provide a good starting point for the more complicated analysis of higher dimensional problems. Classically, particles of low energy are trapped inbetween local maxima of a potential $V(q)$. One prominent example is the one-dimensional double-well potential which consists of two symmetry related wells. The classical motion is confined to either side of the wells. Quantum mechanically, however, a wave packet started in one of the wells performs Rabi oscillations between the two sites with a frequency which depends on the width and the height of the barrier and can be predicted using WKB theory [15]. The period τ of these oscillations is related to an energy splitting ΔE of quasi-degenerate eigenstates localized in the right and the left well, $\tau = \hbar/\Delta E$. This energy splitting occurs due to the tunneling process which couples the classically separated wells. It decreases exponentially, $\Delta E \sim e^{-S/\hbar}$, with increasing height and width of the barrier. This information is contained in the action $S = \int \sqrt{2m(V(q) - E)} dq$. For

small splittings ΔE the period τ goes to infinity and the tunneling process is suppressed. This happens when the imaginary part of the action S divided by Planck's constant h increases. To study this behavior quantitatively we introduce an effective Planck constant $h_{\text{eff}} = h/S_0$ which is the ratio of Planck's constant h and a typical action S_0 of the system. When approaching the classical regime, the action S_0 increases such that h_{eff} will go to zero. This is called the semiclassical limit. In this limit all tunneling processes have to vanish as they are forbidden in classical mechanics. For the energy splittings ΔE in the double well potential this behavior is predicted by its exponential decrease with $h_{\text{eff}} \rightarrow 0$.

Tunneling not only occurs for potential barriers but whenever a system consists of classically disconnected regions. Such regions exist for higher dimensional integrable systems due to additional integrals of motion [16,17]. Here, the tunneling process can be described by means of the WKB or the instanton approach [18,19]. Typical Hamiltonian systems, however, are not integrable. They have a mixed phase space where regions of regular motion, also called regular islands, and regions of chaotic motion, called the chaotic sea, coexist. While the classical motion is confined to these regions, quantum mechanically the dynamically generated barrier can be penetrated. According to the semiclassical eigenfunction hypothesis [20–22] the eigenstates of systems with a mixed phase space are semiclassically concentrated either in the regular islands or in the chaotic sea. For nonzero values of the effective Planck constant h_{eff} this classification still approximately holds such that the corresponding eigenstates are called regular or chaotic. However, each eigenstate has contributions in both regions of phase space, due to the coupling between these regions. The corresponding tunneling process has been called dynamical tunneling by Davis and Heller [23]. Finding a theoretical description of this tunneling process is a challenging problem for systems with a mixed phase space and the main subject of this thesis.

In order to study dynamical tunneling Tomsovic and Ullmo [24] considered a system whose phase space consists of two symmetry related regular islands surrounded by a chaotic sea. They observed that the energy splittings ΔE between two symmetry related regular states are drastically changed compared to the integrable potential systems discussed before, due to the appearing chaotic states. Under variation of external parameters or the effective Planck constant the energy of such a chaotic state will come close to those of the regular doublet. If this happens the chaotic state mediates the tunneling process between the two islands. The two-step process coupling the regular state from one island to the chaotic state and then to the other island dominates compared to the direct coupling of the two regular states. This leads to an enhancement of the energy splittings and was called *chaos-assisted tunneling* [24]. The spectrum of the regular and the chaotic states can be modeled by random matrix theory [25,26]. Hence, under variation of the effective Planck constant the distance between the energies of the regular doublet and the closest chaotic state will vary in a random way. This leads to strong fluctuations in the splittings ΔE [27–30] whose variance can be predicted by random matrix

theory. The smooth exponential decrease of ΔE in the semiclassical limit $h_{\text{eff}} \rightarrow 0$ found for the integrable case no longer occurs. This was theoretically verified for optical microcavities [31] and experimentally in microwave billiards [32, 33].

In Ref. [34] chaos-assisted tunneling has been studied in absence of reflection symmetry. Moreover, it was shown that in addition to enhanced splittings ΔE the complete suppression of tunneling can be observed if the chaotic energy influences the regular doublet such that it becomes degenerate [35, 36]. Furthermore, the random matrix ansatz has been generalized to the tunneling-induced decay of quasi-bound states in open systems, which enabled the investigation of the ionization of non-dispersive electronic wave packets in resonantly driven hydrogen atoms [37].

Throughout this thesis we will consider the tunneling process from a regular region to the chaotic sea which is characterized by tunneling rates γ . They describe the exponential decay $\sim \exp(-\gamma t)$ of a wave packet initially localized in the regular island to the chaotic region. This decay occurs at most until the Heisenberg time $\tau_H = h_{\text{eff}}/\Delta$, where Δ is the mean level spacing. The tunneling rates γ are directly related to the energy splittings between symmetry related regular states, $\Delta E \approx \gamma$, discussed before. Under variation of an external parameter they will also show the fluctuations of chaos-assisted tunneling. As we are not interested in the statistical properties of these fluctuations we consider an averaged tunneling rate, where the pronounced impact of avoided crossings between regular and chaotic states is negligible.

A reliable prediction of these averaged tunneling rates from the regular to the chaotic region is a longstanding open problem. As the tunneling process is significantly determined by the phase-

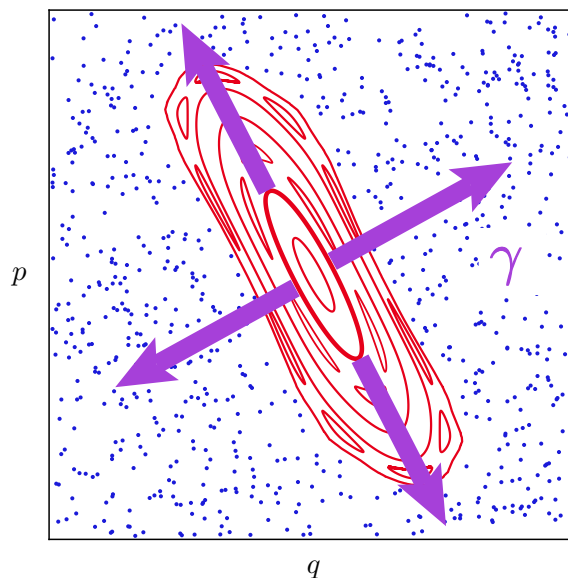


Figure 1.1: Dynamical tunneling in systems with a mixed phase space: The purple arrows indicate the tunneling process from a regular island (red lines) to the chaotic sea (blue dots) with a tunneling rate γ .

space structure of the system, semiclassical approaches which use this classical information have been considered [38–41]. In the quantum regime, $h_{\text{eff}} \lesssim A$, in which the effective Planck constant h_{eff} is smaller but of the same order as the area A of the regular island, fine-scale structures in phase space such as nonlinear resonances or the hierarchical transition region are expected not to affect quantum mechanics. Hence, the *direct regular-to-chaotic tunneling* process dominates, which couples the considered regular wave packet to the chaotic sea without intermediate processes. In Ref. [42] a qualitative argument for the tunneling rates to behave exponentially as $\gamma \propto \exp(-CA/h_{\text{eff}})$ was given, where A is the area of the regular island and C is a non-universal constant. The constant C has been calculated for various situations: For a Wannier-Stark potential one obtains $C = 2\pi$ [43] and $C > 2\pi$ for rough nanowires [44, 45]. Podolskiy and Narimanov [46] introduced an approach which claims a universal prediction of direct dynamical tunneling rates given by $C = 2 - \ln 4$ in the semiclassical limit. As shown in Ref. [47] a correct implementation of this approach actually yields $C = 3 - \ln 4$. However, even this corrected prediction fails for generically shaped regular islands as it uses a transformation to a harmonic oscillator which does not account for the variation of the rotation number from the center to the border of the regular island.

One aim of this thesis is to obtain an analytical prediction of the direct regular-to-chaotic tunneling process. For this we introduce a fictitious integrable system whose dynamics resembles the regular motion in the originally mixed system as closely as possible and extends it towards the chaotic sea, similar to the ideas presented in Refs. [28, 46]. This leads to a tunneling formula involving properties of this integrable system as well as its difference to the mixed system under consideration. It allows for the prediction of tunneling rates from any quantized torus within the regular island [48]. The successful application of this approach to quantum maps [48, 49], billiard systems [50], and optical microcavities [51] will be presented.

In the semiclassical limit, $h_{\text{eff}} \ll A$, the fine-scale structures of the classical phase space can be resolved by quantum mechanics. Especially nonlinear resonance chains have an essential influence on the tunneling process which cannot be described by direct tunneling. Due to these nonlinear resonances quasi-degeneracies between regular states occur [52], leading to couplings of these states which are located on different quantizing tori. This causes an enhancement of the tunneling rates for states located in the center of the regular island as they are coupled to higher excited regular states which have a larger tunneling probability. A quantitative understanding of these coupling processes was obtained within the theory of *resonance-assisted tunneling* [53–56]. It approximates the dynamics in the vicinity of a nonlinear resonance by a pendulum Hamiltonian which can explain the couplings between the regular states. They cause characteristic peak and plateau structures in the tunneling rates as observed for near integrable systems [53, 54], mixed quantum maps [55, 56], periodically driven systems [57, 58], quantum accelerator modes [43], and for multidimensional molecular systems [59, 60]. Quantitatively, however, deviations of several orders of magnitude appear, especially in the experimentally

relevant regime of large effective Planck's constant h_{eff} .

As a result, neither the direct tunneling process nor resonance-assisted tunneling alone provides an accurate prediction of tunneling rates in generic systems from the quantum to the semiclassical regime. A natural conclusion would be that a more sophisticated semiclassical approach has to be considered which e.g. uses the complex-paths formalism introduced in Refs. [38–41]. However, we show that by a combination of the direct tunneling process described by the approach using a fictitious integrable system and the resonance-assisted tunneling theory a prediction can be obtained which is valid from the quantum to the semiclassical regime. We derive a unified framework for the determination of dynamical tunneling rates and consider two improvements in the implementation of the resonance-assisted tunneling theory compared to previous studies [61]. This leads to an excellent prediction of tunneling rates compared to numerical data for one or multiple dominating resonances. It includes the regime where resonances start to become relevant which is of crucial importance for the experimental search of signatures of resonance-assisted tunneling.

This thesis is organized as follows: In Chapter 2 a short review of WKB theory is presented and applied to static one-dimensional potentials with a double-well shape, in order to understand one-dimensional tunneling in the semiclassical limit. Concepts introduced in this chapter will turn out to be useful for the description of dynamical tunneling in systems with a mixed phase space. For this purpose example systems with a suitable phase space are introduced in Chapter 3. Especially one-dimensional kicked systems can be tailored to special needs. Their classical dynamics can be visualized in phase space by a stroboscopic area preserving mapping which can be easily quantized. With particular choices for the potential energy $V(q)$ and the kinetic energy $T(p)$ we are able to design models in which one elliptic regular island without nonlinear resonance chains exists inside a homogeneous chaotic sea. The shape of this island can be deformed to obtain a more generic situation. This allows for studying the direct tunneling process without distracting effects caused by nonlinear resonances, partial barriers, or hierarchical regions. Furthermore, it allows to design systems which show one or multiple resonances in order to study the implications of resonance-assisted tunneling. We also discuss the design and the quantization of such mappings and numerical procedures suited to determine tunneling rates. Systems which are commonly used in experiments in quantum chaos are two-dimensional billiards and optical microcavities. We introduce their classical and quantum properties and show how tunneling rates can be determined numerically. In Chapter 4 dynamical tunneling is considered for quantum maps. First our approach using a fictitious integrable system is derived for the direct tunneling process and applied to various example systems. Then its unification with resonance-assisted tunneling is presented which shows excellent agreement to numerical data. In Chapter 5 the direct tunneling prediction is derived for billiard systems and applied to the mushroom, the annular, and the cosine billiard. Comparison with numerical data as well as experimental data for the mushroom billiard is presented. For billiards with two par-

allel walls, the tunneling of bouncing-ball modes which are localized on the marginally stable bouncing-ball orbits is investigated. The tunneling rates show a power-law behavior in contrast to the exponential decrease found for the mushroom and the annular billiard. The influence of dynamical tunneling on the quality factors for whispering-gallery modes in the annular microcavity is considered in Chapter 6. Finally, a summary of the results of this thesis and an overview of open questions is given in Chapter 7.

2 Barrier tunneling in one-dimensional systems

Before we study tunneling processes in systems with a mixed phase space we consider one-dimensional time-independent systems in which energy barriers may limit the classical motion of a particle. These barriers can be penetrated quantum mechanically due to tunneling. According to Bohr's correspondence principle we expect a transition from quantum to classical mechanics in the semiclassical limit. In the transition region signatures of classical trajectories can be found in quantum spectra and eigenfunctions. As we are particularly interested in a description of the tunneling process in the semiclassical limit the question arises if there exist certain methods which allow to solve the Schrödinger equation in this limit. One possibility is given by the WKB theory which is introduced in Section 2.1 according to the presentation in the textbook of Landau and Lifschitz [15]. It is applied to the derivation of the Bohr-Sommerfeld quantization and the Gamov theory. In Section 2.4 we present the double-well potential as an application and in Section 2.5 we discuss a δ -scatterer.

2.1 WKB method

In the following we consider a spinless particle of mass m which moves under the action of a potential $V(q)$. We use dimensionless variables as introduced in Appendix A. In 1926 Wentzel, Kramers, and Brillouin developed an approach for the approximate determination of eigenfunctions in one-dimensional time-independent systems which are separable. If the de-Broglie wave length λ of a particle is much smaller than the characteristic length of the considered system, it has almost classical properties. One example is given by a constant potential $V(q) := V_0$ for which the eigenfunctions of the Hamilton operator

$$\hat{H}(\hat{q}, \hat{p}) = \frac{\hat{p}^2}{2} + V(\hat{q}) \tag{2.1}$$

are simultaneously eigenfunctions of the momentum operator with the eigenenergies $E = p^2/2$. In position representation they are given by plane waves $\langle q|p\rangle = e^{ipq/\hbar_{\text{eff}}}/\sqrt{2\pi\hbar_{\text{eff}}}$. Hence, in the case of weakly changing potentials we may use the following approach for the determination of

the eigenfunctions $\psi(q)$ in position representation

$$\psi(q) = A \exp\left(\frac{i}{\hbar_{\text{eff}}} S(q)\right) \quad (2.2)$$

in which A denotes the amplitude and $S(q)$ the phase factor which depends on the position q . This approach can now be inserted into the time-independent Schrödinger equation in position representation

$$\left(-\frac{\hbar_{\text{eff}}^2}{2} \frac{d^2}{dq^2} + V(q) - E\right) \psi(q) = 0 \quad (2.3)$$

resulting in a differential equation for $S(q)$

$$\frac{1}{2} \left(\frac{dS(q)}{dq}\right)^2 + \frac{\hbar_{\text{eff}}}{2i} \frac{d^2 S(q)}{dq^2} + V(q) - E = 0. \quad (2.4)$$

Semiclassically the effective Planck constant \hbar_{eff} goes to zero. Hence, for a semiclassical prediction it is reasonable to expand the function $S(q)$ into a power series in \hbar_{eff}

$$S(q) = S_0(q) + \frac{\hbar_{\text{eff}}}{i} S_1(q) + \left(\frac{\hbar_{\text{eff}}}{i}\right)^2 S_2(q) + \dots \quad (2.5)$$

Approximate eigenfunctions are obtained by iteratively using the expansion of Eq. (2.5) in Eq. (2.4). In zeroth order we obtain

$$S_0(q) = \pm \int \sqrt{2(E - V(q))} dq = \pm \int p(q) dq. \quad (2.6)$$

The integrand is given by the classical momentum $p(q)$ of the particle at energy E . Neglecting all terms which are quadratic in \hbar_{eff} the first order of $S(q)$ is given by

$$S_1(q) = \ln \left(\frac{c}{\sqrt{|p(q)|}} \right) \quad (2.7)$$

with a prefactor c . Higher orders of $S(q)$ in \hbar_{eff} can be obtained in a similar way, yet they are more complicated and provide no further semiclassical insights. Hence, up to first order in \hbar_{eff} the WKB wave functions are determined as

$$\psi(q) = \frac{C_1}{\sqrt{|p(q)|}} \exp\left(\frac{i}{\hbar_{\text{eff}}} \int p(q) dq\right) + \frac{C_2}{\sqrt{|p(q)|}} \exp\left(-\frac{i}{\hbar_{\text{eff}}} \int p(q) dq\right) \quad (2.8)$$

inside the classically allowed region, in which $E > V(q)$. The prefactor $1/\sqrt{|p(q)|}$ can be understood in the following way: The spatial probability density $\psi^* \psi$ is proportional to $1/|p(q)|$

which is equal to the probability density of a classical particle with energy E confined in a potential $V(q)$. Inside the classically forbidden region, $E < V(q)$, the momentum is purely imaginary such that the exponents in Eq. (2.8) become real. We find

$$\psi(q) = \frac{D_1}{\sqrt{|p(q)|}} \exp\left(-\frac{1}{\hbar_{\text{eff}}} \int |p(q)| dq\right) + \frac{D_2}{\sqrt{|p(q)|}} \exp\left(\frac{1}{\hbar_{\text{eff}}} \int |p(q)| dq\right). \quad (2.9)$$

The wave functions described by Eqs. (2.8) and (2.9) are exact solutions of the Schrödinger equation for free particles and give a reliable approximation for weakly changing potentials. For its applicability the second term on the left-handed side of Eq. (2.4) has to be small compared to the first term, i.e.,

$$\hbar_{\text{eff}} \left| \frac{S_0''(q)}{S_0'(q)^2} \right| = \hbar_{\text{eff}} \left| \frac{d}{dq} \frac{1}{S_0'(q)} \right| = \hbar_{\text{eff}} \left| \frac{d}{dq} \frac{1}{p(q)} \right| = \frac{1}{2\pi} \left| \frac{d\lambda}{dq} \right| \ll 1 \quad (2.10)$$

in which $'$ denotes the derivative with respect to q . The de-Broglie wave length is not allowed to change considerably on the scale of its own length. This is equal to the requirement that the potential has only small changes on the length scale of λ

$$\left| \frac{dV}{dq} \right| \sim \frac{V_0}{\lambda} \ll 1. \quad (2.11)$$

For small momenta but especially at the classical turning points for which $p(q) = 0$ the WKB solution should not be used, as it diverges for $|p(q)| \rightarrow 0$. The de-Broglie wave length tends to infinity. Hence, it is not small compared to the variation of the potential $V(q)$. Using uniform approximations [62] this problem can be avoided. One approach for the semiclassical evaluation of the Schrödinger equation is given by using a slightly modified potential $U(q) \approx V(q)$, which is chosen in such a way that divergences do not appear [63, 64]. However, in general it is not possible to find such a potential $U(q)$ for all positions q . Hence, the modification of the potential is restricted to the vicinity of the classical turning points, e.g. by expanding the potential up to first order around a turning point [65, 66]. In this region the Schrödinger equation is identical to the Airy equation, whose solutions are the Airy functions $\text{Ai}(q)$ and $\text{Bi}(q)$. Finally, the WKB wave functions in the different regions have to be matched such that they are continuously differentiable. This fails if two turning points are too close together. Alternatively, the integration paths may be continued into the complex plane to avoid the divergences at the classical turning points. Here, however, the Stokes phenomenon has to be accounted for which leads to exponentially diverging solutions [15].

We will now consider the situation of classically bounded motion at energy E_0 in between two classical turning points a and b with $a < b$. In the regions $q < a$ and $q > b$ classical motion is forbidden. This situation is depicted in Fig. 2.1. The bounded solutions of the Schrödinger

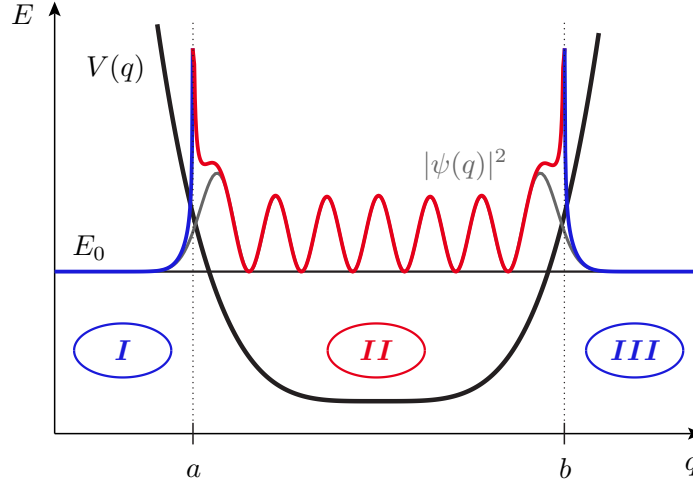


Figure 2.1: The WKB solution inside a confining potential $V(q)$ (black line) at energy E_0 is shown in the classically allowed region II (red line) and in the classically forbidden regions I and III (blue lines). At the turning points $q = a$ and $q = b$ for which $V(q) = E_0$ holds divergences occur due to the zero denominator appearing in Eq. (2.14). For comparison the exact eigenfunction of the system at E_0 is presented as a gray line. While in the vicinity of the turning points deviations to the WKB solutions are visible they vanish further away from these points.

equation have to be square-integrable. They have to fulfill

$$\int_{-\infty}^{\infty} |\psi(q)|^2 dq < \infty. \quad (2.12)$$

Hence, in the classically forbidden region the wave function results from the first exponentially decaying term in Eq. (2.9) only, as the second term would violate Eq. (2.12). To determine the unknown constants C_1 , C_2 , D_1 , and D_2 the wave functions defined on the different regions I , II , and III have to be matched. For this purpose we study the wave functions in vicinity of the classical turning points. To avoid the divergences at these turning points, the potential $V(q)$ can be linearized around $q = a$ and $q = b$. In the vicinity of a the expansion reads

$$E - V(q) \approx F_0(q - a), \quad F_0 = - \left. \frac{dV}{dq} \right|_{q=a} < 0. \quad (2.13)$$

The motion takes place under the action of a constant force for which the solution of the Schrödinger equation is known. This allows to match the wave functions defined in the classically allowed and forbidden region at the turning points. Using these procedures two of the constants C_1 , C_2 , D_1 , and D_2 are determined. We find $C := C_1$, $C' := C_2$, $D_1 = C/2$, and

$D_2 = C'/2$. Finally, for the WKB wave function at energy E_0 it is found in first order in \hbar_{eff}

$$\psi(q) = \begin{cases} \frac{C}{2\sqrt{|p(q)|}} \exp\left(-\frac{1}{\hbar_{\text{eff}}} \int_q^a |p(q')| dq'\right) , & q < a \\ \frac{C}{\sqrt{|p(q)|}} \sin\left(\frac{1}{\hbar_{\text{eff}}} \int_a^q p(q') dq' + \frac{\pi}{4}\right) , & a \leq q \leq b \\ \frac{C'}{2\sqrt{|p(q)|}} \exp\left(-\frac{1}{\hbar_{\text{eff}}} \int_b^q |p(q')| dq'\right) , & q > b. \end{cases} \quad (2.14)$$

It remains to determine the two unknown constants C and C' which are fixed due to the normalization of Eq. (2.14). As almost all of the weight of $\psi(q)$ is concentrated in the classically allowed region, it is sufficient to integrate over $|\psi|^2$ in the interval (a, b) . In the semiclassical limit \hbar_{eff} will go to zero such that the sine function in Eq. (2.14) becomes a rapidly oscillating quantity. Hence, its square can be approximated by its mean value $1/2$. Using the frequency of the classical motion $\omega = 2\pi/T$ the constant C is determined with

$$1 = \int_{-\infty}^{\infty} |\psi(q)|^2 dq \approx \int_a^b \frac{C^2}{|p(q)|} \sin^2\left(\frac{1}{\hbar_{\text{eff}}} \int_a^q p(q') dq' + \frac{\pi}{4}\right) dq \quad (2.15)$$

$$\approx \frac{C^2}{2} \int_a^b \frac{dq}{|p(q)|} = \frac{C^2}{2} \int_{t(a)}^{t(b)} dt = \frac{C^2 T(E)}{4} = \frac{C^2 \pi}{2\omega(E)} \quad (2.16)$$

such that

$$C = \pm \sqrt{\frac{2\omega}{\pi}} \quad (2.17)$$

in which the positive sign is relevant for C and $C' = C$ or $C' = -C$. The frequency $\omega(E)$ is a function of the energy.

Fig. 2.2 shows a comparison of the WKB solutions and the analytical eigenfunctions of the harmonic oscillator, $V(q) = \omega^2 q^2/2$, for $\omega = 1$. While the divergences in the vicinity of the turning points are visible, the affected region shrinks for higher excited regular states, which here corresponds to the semiclassical limit.

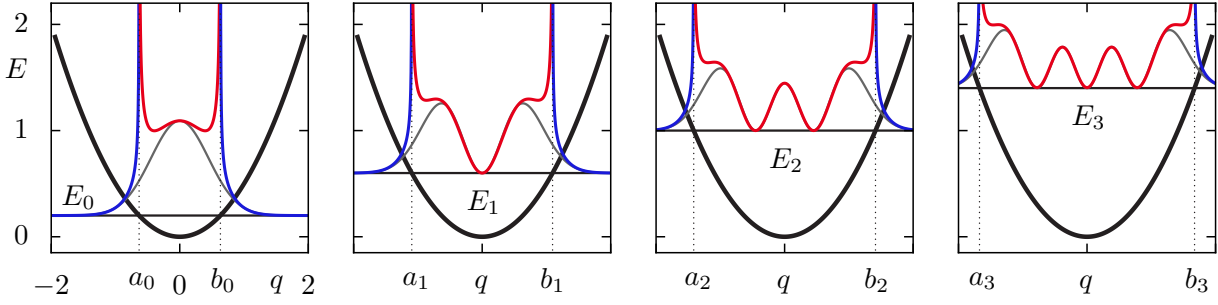


Figure 2.2: The WKB solutions for the first four eigenenergies E_i , $i \leq 3$, in the harmonic-oscillator potential are shown in the classically allowed region (red line) and in the classically forbidden regions (blue lines) for $\hbar_{\text{eff}} = 0.4$. At the turning points $q = a_i$ and $q = b_i$ divergences occur due to the zero denominator appearing in Eq. (2.14). For comparison the exact eigenfunctions of the system at energy E_i are presented as a gray line.

2.2 Bohr-Sommerfeld quantization

Using the Bohr-Sommerfeld quantization [15], to each bounded state a quantizing action is assigned which corresponds to an area in phase space. Its derivation results from the WKB solutions inside the classically allowed region. Using the abbreviations

$$A := \frac{1}{\hbar_{\text{eff}}} \int_a^q p(q') dq' + \frac{\pi}{4} \quad \text{and} \quad B := \frac{1}{\hbar_{\text{eff}}} \int_q^b p(q') dq' + \frac{\pi}{4} \quad (2.18)$$

we find with Eq. (2.14)

$$\frac{C}{\sqrt{|p(q)|}} \sin(A) = \frac{C'}{\sqrt{|p(q)|}} \sin(B). \quad (2.19)$$

The constants C and C' are allowed to differ only in their sign. Hence, for the arguments A and B we obtain

$$A + B = (m + 1)\pi, \quad m \in \mathbb{N} \quad (2.20)$$

due to

$$\sin(A) = \sin((m + 1)\pi - B) \quad (2.21)$$

$$= \sin(B) \cos((m + 1)\pi) = (-1)^{m+1} \sin(B) \quad (2.22)$$

$$\Rightarrow C' = (-1)^m C. \quad (2.23)$$

The situation $A = B$ is possible for $p = 0$ only which is not relevant. Furthermore, only non-negative quantum numbers m are considered. By insertion of Eq. (2.18) into Eq. (2.20) we

find

$$A + B = \frac{1}{\hbar_{\text{eff}}} \int_a^b p(q') dq' + \frac{\pi}{2} = (m + 1)\pi. \quad (2.24)$$

We obtain the Bohr-Sommerfeld quantization by replacing $2 \int_a^b = \oint_{\mathcal{C}_m}$ as

$$\oint_{\mathcal{C}_m} p(q) dq = 2\pi\hbar_{\text{eff}} \left(m + \frac{1}{2} \right) = h_{\text{eff}} \left(m + \frac{1}{2} \right) \quad (2.25)$$

in which the integral $\oint_{\mathcal{C}_m} p(q) dq$ determines the area enclosed inside of the phase-space trajectory \mathcal{C}_m of the classical particle. If we divide this area by h_{eff} we find approximately m partitions. At the same time m denotes the number of bounded states which have an energy smaller than the energy of the considered particle. Hence we can assign a phase-space cell of size h_{eff} to each state $|\psi\rangle$. For a visualization see Fig. 2.3. Trajectories which enclose an area of $h_{\text{eff}}(m + 1/2)$ in phase space are called quantizing tori and m is their quantum number.

The open question remains, which energy can be assigned to such a quantizing torus. As presented in Appendix C.1 we find

$$E(b) = \int_{q^*}^b \frac{dA(b')}{db'} \frac{1}{T(b')} db'. \quad (2.26)$$

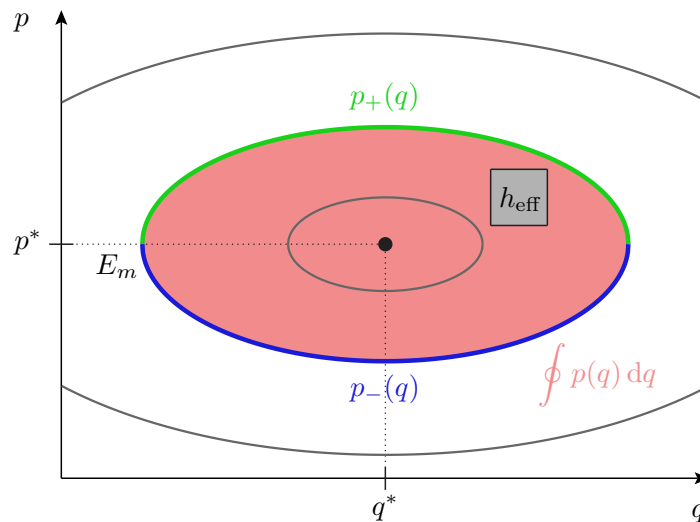


Figure 2.3: The phase space (q, p) of a one-dimensional time-independent system with a confining potential is shown. The Bohr-Sommerfeld quantization states that each trajectory which encloses an area of $h_{\text{eff}}(m + 1/2)$ (rose area) supports an eigenstate of the system with energy E_m . This area is obtained by integration along the momentum branches $p_+(q)$ (green line) and $p_-(q)$ (blue line). The effective Planck constant describes an area in this phase space which is marked by a small gray rectangle.

This expression is valid for trajectories with two turning points a and b . It predicts the energy as a function of the enclosed area A and the classical time-period of the motion T . It is also applicable to time-dependent one-dimensional systems as presented in Section 3.1.

2.3 Gamov theory

In the following we consider the scattering process of a particle at energy E_0 due to an energy barrier [67]. The classically forbidden region is limited by the turning points a and b , while for $q < a$ and $q > b$ classical motion is allowed. This situation is depicted in Fig. 2.4. The WKB solution within the region $q < a$ has the form

$$\psi_I(q) = \frac{C}{\sqrt{|p(q)|}} \sin \left(\frac{1}{\hbar_{\text{eff}}} \int_q^a p(q') dq' + \frac{\pi}{4} \right). \quad (2.27)$$

It can be decomposed into a wave which is incoming from the left and a wave which is reflected at the energy barrier

$$\psi_I(q) = \frac{C}{2i\sqrt{|p(q)|}} (e^{iA} - e^{-iA}), \quad A = \frac{1}{\hbar_{\text{eff}}} \int_q^a p(q') dq' + \frac{\pi}{4}. \quad (2.28)$$

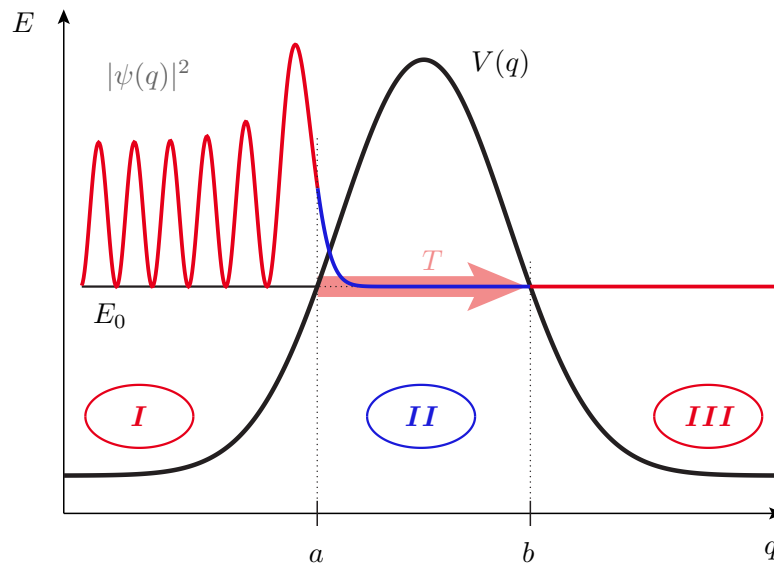


Figure 2.4: Illustration of transmission through a potential barrier. An incoming wave $\psi(q)$ of energy E_0 (red line) hits the barrier and decays exponentially to its inside (blue line) in region *II*. An exponentially small amount of probability is transferred to region *III* which depends on the width of the barrier (in between the turning points a and b) and its height.

Both contributions have the same amplitude, which is valid only for broad and high potential barriers such that the reflection probability is $R \approx 1$ and the transmission is $T \ll 1$. If we neglect the exponentially increasing term, the WKB wave function in the classically forbidden region is given by

$$\psi_{II}(q) = \frac{C}{2\sqrt{|p(q)|}} \exp\left(-\frac{1}{\hbar_{\text{eff}}} \int_a^q |p(q')| dq'\right) \quad (2.29)$$

and the transmitted wave is outgoing to the right

$$\psi_{III}(q) = \frac{C'}{2\sqrt{|p(q)|}} \exp\left(\frac{i}{\hbar_{\text{eff}}} \int_b^q p(q') dq'\right). \quad (2.30)$$

The WKB solutions have to be matched continuously at the turning points. Due to the condition $\psi_{II}(b) = \psi_{III}(b)$ we find

$$C' = C \exp\left(-\frac{1}{\hbar_{\text{eff}}} \int_a^b |p(q')| dq'\right). \quad (2.31)$$

The transmission probability T is determined using the probability currents

$$j = \text{Re}\left(\psi^*(q) \frac{\hbar_{\text{eff}}}{i} \frac{d}{dq} \psi(q)\right) \quad (2.32)$$

of the incoming and the transmitted wave, $T = |j_t|/|j_i|$, such that we obtain

$$T = \frac{\omega}{2\pi} \exp\left(-\frac{2}{\hbar_{\text{eff}}} \int_a^b |p(q)| dq\right). \quad (2.33)$$

Equation (2.33) allows to determine the transmission probability T through one-dimensional potential barriers of sufficient width and height. It is determined by the imaginary action which is obtained by integration of $p(q)$ in the classically forbidden region. Hence, it will decrease exponentially with increasing height and width of the barrier as well as in the semiclassical limit $\hbar_{\text{eff}} \rightarrow 0$.

2.4 Application to double-well potential

We consider the one-dimensional double-well potential which is used, e.g. in its symmetric version to describe the inversion oscillations of the NH_3 molecule. Furthermore, it has certain similarities to higher dimensional systems which will be employed to study dynamical tunneling

in Chapter 4. Hence, it is chosen as an example system to study the one-dimensional barrier-tunneling process [68]. The potential energy is given by

$$V(q) = q^4 - q^2 + \kappa q \quad (2.34)$$

in which the parameter κ can be chosen as an arbitrary real number. For $\kappa = 0$ the system has a reflection symmetry with respect to $q = 0$, while the double well is asymmetric for $\kappa \neq 0$. Particles which have an energy $E < 0$ are classically confined to the left or the right well. For such particles we can neglect the quantum mechanical coupling between the two wells in first order and separately apply the Bohr-Sommerfeld quantization to each of the wells. It allows to find the quantizing tori \mathcal{C}_L in the left and \mathcal{C}_R in the right well, which can be assigned with an energy $E_L(\kappa)$ and $E_R(\kappa)$ due to Eq. (2.26). The corresponding states $|\psi_L\rangle$ and $|\psi_R\rangle$ which are localized in the left or the right well are constructed by means of WKB theory. As the quantum numbers m_L and m_R are irrelevant in the following derivations they will not be explicitly mentioned.

Under variation of the parameter κ crossings between the semiclassical energies $E_R(\kappa)$ and $E_L(\kappa)$ appear at certain values of κ . As an example we find $E_L = E_R$ for $m_L = m_R$ if $\kappa = 0$. Hence, in the symmetric case, $\kappa = 0$, the WKB solutions with the same quantum number in the left and the right well are degenerate. In the asymmetric situation this is not possible and there only exist crossings with $m_L \neq m_R$.

The exact eigenfunctions of the double-well system are not limited exclusively to one of the two wells due to the tunneling effect. In the vicinity of a crossing of $E_L(\kappa)$ and $E_R(\kappa)$ the corresponding eigenenergies of the real system $E_+(\kappa)$ and $E_-(\kappa)$ exhibit an avoided crossing [69]. The minimal distance of the two energies is denoted by $\Delta E(\kappa) := E_-(\kappa) - E_+(\kappa)$. Fig. 2.5 visualizes this behavior. Our aim is to determine the energy splitting $\Delta E(\kappa)$ semiclassically. Hence, we choose $\kappa = \kappa_{\text{cr}}$ such that at least one avoided crossing appears, which we will consider in the following. We define

$$\hat{H} := \hat{H}(\kappa = \kappa_{\text{cr}}), \quad (2.35)$$

$$E_+ := E_+(\kappa = \kappa_{\text{cr}}), \quad (2.36)$$

$$E_- := E_-(\kappa = \kappa_{\text{cr}}), \quad (2.37)$$

$$E_0 := E_L = E_R := E_L(\kappa = \kappa_{\text{cr}}) = E_R(\kappa = \kappa_{\text{cr}}). \quad (2.38)$$

We want to approximately solve the eigenequation

$$\hat{H}|\psi_{\pm}\rangle = E_{\pm}|\psi_{\pm}\rangle. \quad (2.39)$$

The WKB wave functions in the left and the right well, $\psi_L(q)$ and $\psi_R(q)$, are constructed such that they decay exponentially into the other well. According to Tomsovic and Ullmo [24] this

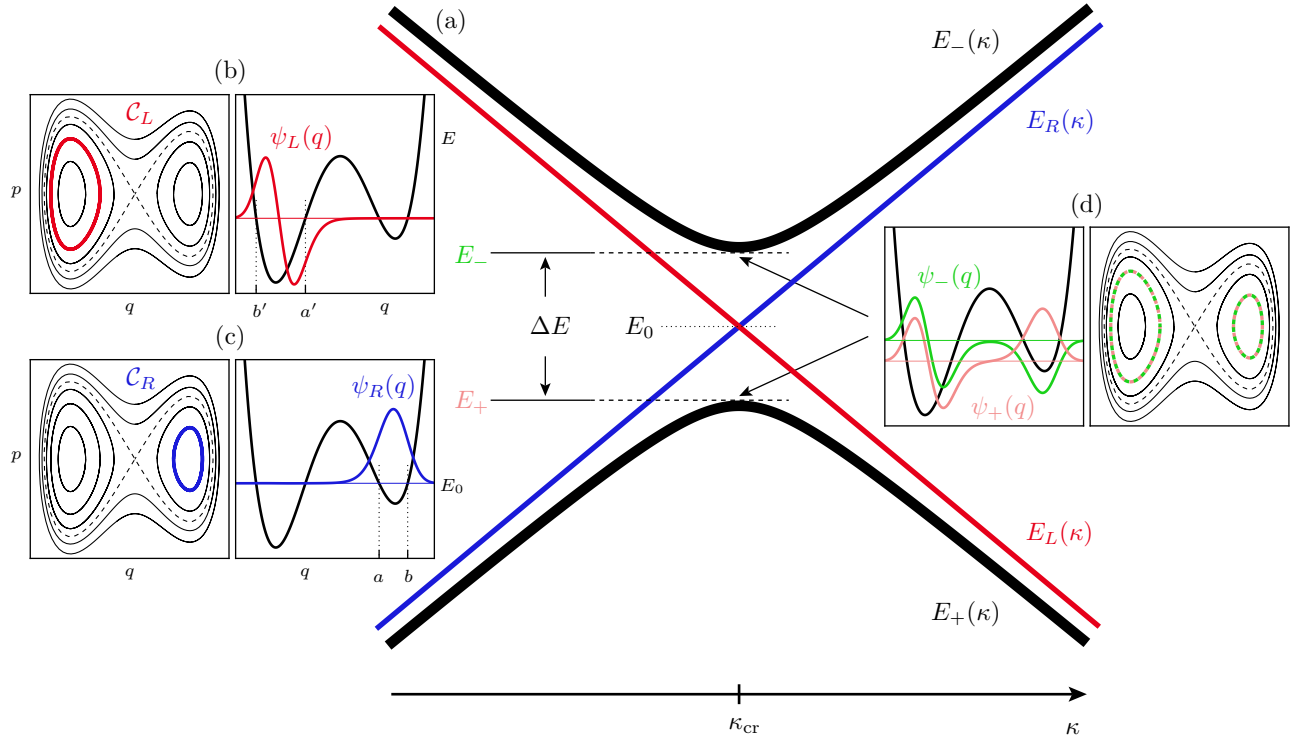


Figure 2.5: Two eigenenergies E_+ and E_- of the double-well potential perform an avoided crossing at κ_{cr} marked by the thick black line in (a). The corresponding WKB energies E_R (blue line) and E_L (red line) cross at κ_{cr} at energy E_0 . The energy splitting ΔE of E_+ and E_- at κ_{cr} is shown. The insets (b) and (c) show the WKB wave functions ψ_L and ψ_R at energy E_0 in the left and the right well and their quantizing curves \mathcal{C}_L and \mathcal{C}_R in phase space. The eigenfunctions of the real system ψ_+ and ψ_- are presented in (d) which are given as even and odd linear combination of ψ_L and ψ_R at different energies E_+ and E_- . The classically allowed regions are limited by the turning points a' , b' in the left and a , b in the right well.

can be achieved by the multiplication of the WKB solutions with arbitrary smooth functions, $\varphi_L(q)$ and $\varphi_R(q)$, which account for the exponential decay. This procedure is identical to the introduction of smooth potentials $V_L(q)$ and $V_R(q)$ which are equal to $V(q)$ in the left or the right well and fulfill the conditions $V_L(q) > E_0$ and $V_R(q) > E_0$ in the other well, respectively. Hence, the states $|\psi_L\rangle$ and $|\psi_R\rangle$ are eigenstates of the systems \hat{H}_L and \hat{H}_R which include just one region of bounded motion

$$\hat{H}_L := \frac{\hat{p}^2}{2} + V_L(\hat{q}), \quad (2.40)$$

$$\hat{H}_R := \frac{\hat{p}^2}{2} + V_R(\hat{q}). \quad (2.41)$$

They fulfill the eigenequations

$$\hat{H}_L|\psi_L\rangle = E_0|\psi_L\rangle, \quad (2.42)$$

$$\hat{H}_R|\psi_R\rangle = E_0|\psi_R\rangle \quad (2.43)$$

in which $|\psi_L\rangle$ and $|\psi_R\rangle$ are degenerate at E_0 . In the semiclassical limit it is not relevant how the potentials $V_L(q)$ and $V_R(q)$ are continued into the respective other well. The eigenstates $|\psi_\pm\rangle$ of the system are given as linear combinations of the WKB solutions $|\psi_L\rangle$ and $|\psi_R\rangle$ in lowest order

$$|\psi_\pm\rangle \approx \frac{1}{\sqrt{2}}(|\psi_L\rangle \pm |\psi_R\rangle) \quad (2.44)$$

in which we assumed $\langle\psi_L|\psi_R\rangle \ll \Delta E$ which is valid in the semiclassical limit. This assumption can be explicitly verified for a double well which consists of two joined harmonic oscillators [68]. Hence, the semiclassical eigenfunctions $|\psi_L\rangle$ and $|\psi_R\rangle$ are assumed to be orthogonal in the following.

To determine the energy splitting ΔE we consider the following expression

$$E_\pm = \langle\psi_\pm|\hat{H}|\psi_\pm\rangle \quad (2.45)$$

$$\approx \frac{1}{2}\langle\psi_L \pm \psi_R|\hat{H}|\psi_L \pm \psi_R\rangle \quad (2.46)$$

$$= \frac{1}{2}\left(\langle\psi_L|\hat{H}|\psi_L\rangle + \langle\psi_R|\hat{H}|\psi_R\rangle \pm \langle\psi_L|\hat{H}|\psi_R\rangle \pm \langle\psi_R|\hat{H}|\psi_L\rangle\right), \quad (2.47)$$

$$\Rightarrow E_\pm = \frac{1}{2}\left(2E_0 + \langle\psi_L|\hat{H} - \hat{H}_L|\psi_L\rangle + \langle\psi_R|\hat{H} - \hat{H}_R|\psi_R\rangle \pm 2\langle\psi_R|\hat{H} - \hat{H}_L|\psi_L\rangle\right). \quad (2.48)$$

One obtains

$$\Delta E = E_- - E_+ = -2\langle\psi_R|\hat{H} - \hat{H}_L|\psi_L\rangle \quad (2.49)$$

$$\approx -2\langle\psi_R|\hat{H}|\psi_L\rangle. \quad (2.50)$$

Furthermore, we consider the matrix elements

$$\langle\psi_{L/R}|\hat{H}|\psi_{L/R}\rangle = \frac{1}{2}\langle\psi_+ \pm \psi_-|\hat{H}|\psi_+ \pm \psi_-\rangle \quad (2.51)$$

$$= \frac{1}{2}\left(\langle\psi_+|\hat{H}|\psi_+\rangle + \langle\psi_-|\hat{H}|\psi_-\rangle \pm 2\langle\psi_+|\hat{H}|\psi_-\rangle\right) \quad (2.52)$$

$$= \frac{1}{2}(E_- + E_+) \quad (2.53)$$

$$\approx E_0. \quad (2.54)$$

The Hamilton operator projected onto the two states $|\psi_\pm\rangle$ which are involved in the avoided crossing is given by a 2×2 matrix

$$\hat{H}_{(2 \times 2)} = \begin{pmatrix} E_0 & -\frac{\Delta E}{2} \\ -\frac{\Delta E}{2} & E_0 \end{pmatrix}. \quad (2.55)$$

Hence, the avoided crossing is described by a two-level system. This assumes that the avoided crossing is isolated and any other states are far away in energy. Equation (2.55) has a similar form as presented in Ref. [24] but the off-diagonal elements show a different sign. This causes the symmetric eigenstate $|\psi_+\rangle$ to have a lower energy than the antisymmetric state, $E_+ < E_-$. For the eigenvalues and eigenvectors of $\hat{H}_{(2\times 2)}$ we find

$$|\psi_{\pm}\rangle = \frac{1}{\sqrt{2}} (|\psi_L\rangle \pm |\psi_R\rangle) \quad \text{with} \quad E_{\pm} = E_0 \mp \frac{\Delta E}{2}. \quad (2.56)$$

which is identical to Eq. (2.44). For the further analytical derivation we go to position representation and consider the difference

$$\psi_-(q)\hat{H}\psi_+(q) - \psi_+(q)\hat{H}\psi_-(q) = (E_+ - E_-)\psi_+(q)\psi_-(q). \quad (2.57)$$

As the eigenfunctions $\psi_{\pm}(q)$ are not exactly known we integrate Eq. (2.57) in the interval $[q_0, \infty)$ in which q_0 is an arbitrary position under the barrier, inbetween a' and a , see Fig. 2.5,

$$(E_+ - E_-) \int_{q_0}^{\infty} \psi_+(q')\psi_-(q') dq' = \int_{q_0}^{\infty} dq' \left(\psi_-(q')\hat{H}\psi_+(q') - \psi_+(q')\hat{H}\psi_-(q') \right). \quad (2.58)$$

Using

$$\int_{q_0}^{\infty} \psi_+(q')\psi_-(q') dq' \approx -\frac{1}{2} \quad \text{and} \quad E_+ - E_- = -\Delta E \quad (2.59)$$

we find

$$\Delta E = -\hbar_{\text{eff}}^2 \int_{q_0}^{\infty} dq' \left(\psi_-(q') \frac{d^2\psi_+(q')}{dq'^2} - \psi_+(q') \frac{d^2\psi_-(q')}{dq'^2} \right) \quad (2.60)$$

$$= \hbar_{\text{eff}}^2 \left(\psi_-(q') \frac{d\psi_+(q')}{dq'} \Big|_{q'=q_0} - \psi_+(q') \frac{d\psi_-(q')}{dq'} \Big|_{q'=q_0} \right). \quad (2.61)$$

After inserting Eq. (2.44) into Eq. (2.61) we obtain the final result for the energy splitting in the double-well potential

$$\Delta E = \hbar_{\text{eff}}^2 \left(\psi_L(q') \frac{d\psi_R(q')}{dq'} - \psi_R(q') \frac{d\psi_L(q')}{dq'} \right) \Big|_{q'=q_0} \quad (2.62)$$

which depends on the WKB solutions $\psi_L(q)$ and $\psi_R(q)$ and their derivatives.

This result can be obtained with an alternative approach. For this purpose we introduce a hermitian operator $\hat{\Theta}$ with the property: $\hat{\Theta}|\psi_L\rangle \approx 0$ and $\hat{\Theta}|\psi_R\rangle \approx |\psi_R\rangle$ [70]. Using the two-level

system, Eq. (2.55), we find

$$\langle \psi_R | [\hat{H}, \hat{\Theta}] | \psi_L \rangle = \frac{\Delta E}{2} \left(\langle \psi_R | \hat{\Theta} | \psi_R \rangle - \langle \psi_L | \hat{\Theta} | \psi_L \rangle \right) \approx \frac{\Delta E}{2}. \quad (2.63)$$

The energy splitting is given by the matrix element in Eq. (2.63) which involves the localized states $|\psi_L\rangle$ and $|\psi_R\rangle$. The operator $\hat{\Theta}$ can be defined as a projector onto the right well which can be modeled by a Heavyside step function $\Theta(q' - q_0)$. In position representation it follows

$$[\hat{H}, \hat{\Theta}] = \left[\frac{\hat{p}^2}{2}, \hat{\Theta} \right] = \frac{\hbar_{\text{eff}} \hat{p}}{2i} \left[\frac{d}{dq'}, \Theta(q' - q_0) \right] + \frac{\hbar_{\text{eff}}}{2i} \left[\frac{d}{dq'}, \Theta(q' - q_0) \right] \hat{p} \quad (2.64)$$

$$= \frac{\hbar_{\text{eff}}}{2i} (\hat{p} \delta(q' - q_0) + \delta(q' - q_0) \hat{p}) \quad (2.65)$$

which together with Eq. (2.63) leads to

$$\Delta E = 2 \langle \psi_R | [\hat{H}, \hat{\Theta}] | \psi_L \rangle = -\hbar_{\text{eff}}^2 \int_{-\infty}^{\infty} dq' \psi_R(q') \left(\frac{d\delta(q' - q_0)}{dq'} + \delta(q' - q_0) \frac{d}{dq'} \right) \psi_L(q') \quad (2.66)$$

$$= \hbar_{\text{eff}}^2 \left(\psi_L(q') \frac{d\psi_R(q')}{dq'} - \psi_R(q') \frac{d\psi_L(q')}{dq'} \right) \Big|_{q'=q_0}. \quad (2.67)$$

It is identical to Eq. (2.62). Now we may use the explicit expression for the WKB solution given by Eq. (2.14) in the classically forbidden region. The tunnel splitting is obtained as

$$\Delta E = \frac{\hbar_{\text{eff}} \omega}{\pi} \exp \left(-\frac{1}{\hbar_{\text{eff}}} \int_{a'}^a |p(q')| dq' \right) \quad (2.68)$$

in which $\omega := \sqrt{\omega_R \omega_L}$ and $\omega_{R,L}$ denote the oscillation frequencies in the two wells. The larger the energy E_0 , the smaller the integral in Eq. (2.68). Hence, the energy splitting increases with increasing energy and decreases exponentially in the semiclassical limit $\hbar_{\text{eff}} \rightarrow 0$. Note that this expression for the energy splitting and the Gamov result of Eq. (2.33) vary by a factor of two in the argument of the exponential. For situations with a large right well both are related by Fermi's golden rule

$$\gamma_{m_L \rightarrow m_R} = \frac{2\pi}{\hbar_{\text{eff}}} \left| \frac{\Delta E_{m_L \rightarrow m_R}}{2} \right|^2 \rho_R(E_{m_R}) \quad (2.69)$$

in which $\gamma_{m_L \rightarrow m_R}$ describes the tunneling rate from a state localized in the left well of quantum number m_L to the state m_R in the right well, $\rho_R(E_{m_R})$ is the density of states in the right well, and $\Delta E_{m_L \rightarrow m_R}$ denotes the energy splitting. Equation (2.69) describes an exponential decay of the initial wave function with $\gamma_{m_R \rightarrow m_L}$ at most up to the Heisenberg time $t_H = \hbar_{\text{eff}} \rho_R(E_{m_R})$.

2.5 Application to δ -potential

We study a one-dimensional system which consists of an infinitely high barrier at $q \leq -1$ and a δ -peak of strength U_0 at $q = 0$. We may close the system by an additional infinitely high potential barrier at $q \geq b$ or consider the situation in which $V(q) = 0$ for $q > 0$, see the inset in Fig. 2.6. We use $\hbar = 2m = 1$. This system shows similarities to time-dependent or higher dimensional systems which we will study in the next chapters and allows for an analytical analysis as well as simple numerical simulations. It is particularly suited to compare different numerical methods for the determination of tunneling rates. We consider (i) the time evolution of a wave packet localized in the left well, (ii) the determination of avoided crossings under the variation of b , and (iii) the determination of the poles of the scattering matrix for the open system.

Let us start with the closed case. For $-1 < q < b$ the Hamiltonian is given by

$$\hat{H} = \hat{p}^2 + U_0\delta(\hat{q}). \quad (2.70)$$

Its eigenfunctions have to be zero for $q \leq -1$ and $q \geq b$. In the region I for $-1 < q < 0$ and the region II for $0 < q < b$ we use as an ansatz for the wave function

$$\psi_I(q) = A \sin[k(q+1)], \quad (2.71)$$

$$\psi_{II}(q) = B \sin[k(q-b)]. \quad (2.72)$$

By integrating over an infinitesimal region including $q = 0$ we find for the continuity conditions at $q = 0$: $\psi_I(0) = \psi_{II}(0)$ and $\psi'_{II}(0) - \psi'_I(0) = U_0\psi_I(0)$. Using $A = a \sin(kb)$ we obtain $B = -a \sin(k)$ and the eigenenergies $E_n = k_n^2$ are given implicitly by

$$0 = U_0 \sin(k_n b) \sin(k_n) + k_n \sin(k_n b) \cos(k_n) + k_n \sin(k_n) \cos(k_n b). \quad (2.73)$$

This equation has to be solved numerically. By integrating over the squared wave function from $x = -1$ to $x = b$ we find the normalization constant as

$$a = \frac{1}{\sqrt{\frac{1}{2k} \sin^2(kb)(-\cos(k) \sin(k) + k) + \frac{1}{2k} \sin^2(k)(-\cos(kb) \sin(kb) + kb)}}. \quad (2.74)$$

After solving the implicit Eq. (2.73) to obtain the eigenvalues $E_n = k_n^2$ the eigenfunctions are analytically known.

For the open system we make the ansatz

$$\psi_I(q) = A \sin[k(q+1)], \quad (2.75)$$

$$\psi_{II}(q) = e^{-ikq} + r e^{ikq}. \quad (2.76)$$

At $q = 0$ the same conditions hold as for the closed system discussed before. This leads to the reflection coefficient

$$r = \frac{U_0 + ik + k \cot(k)}{ik - U_0 - k \cot(k)}. \quad (2.77)$$

Now we may compare tunneling rates obtained by three different approaches: (i) We start a wave packet in the left well and determine the overlap at time t with the initial wave packet at $t = 0$. For not too short times and sufficiently large b we expect

$$|\langle \psi(0) | \psi(t) \rangle|^2 \approx e^{-\gamma t} \quad (2.78)$$

and obtain γ by an exponential fit. (ii) In the closed system eigenenergies corresponding to states localized dominantly in the left well will stay almost unchanged under the variation of b . The eigenenergies associated with states which are localized in the right well, however will change. Therefore, under the variation of b we find avoided crossings between a state localized on the left and states localized on the right. We numerically determine the energy splittings ΔE and use Fermi's golden rule to obtain the tunneling rates

$$\gamma = \frac{\pi}{2} \langle |\Delta E^2| \rangle \rho(E) \quad (2.79)$$

in which

$$\rho(E) = \frac{1}{2\pi \sqrt{E} + \frac{\pi^2}{b^2}} \quad (2.80)$$

denotes the density of states in the right well. (iii) We determine the poles of the scattering matrix in the open case. For this purpose we insert complex k -values into the expression of the reflection coefficient, Eq. (2.77), and numerically determine its roots. The energies of the resonances are now complex: $E = E_0 + i\gamma/2$.

Comparing the three numerical methods under variation of U_0 we find agreement especially for small tunneling rates, see Fig. 2.6. Furthermore we find that these tunneling rates decay algebraically with U_0 for sufficiently small γ . For a theoretical prediction of the tunneling rates we consider a system which is open to the left and to the right with a δ -scatterer at $x = 0$. Here, the transmission probability is given by

$$T = \left| \frac{1}{1 + i\frac{U_0}{2k}} \right|^2 = \frac{1}{1 + \frac{U_0^2}{4k^2}}. \quad (2.81)$$

To predict the tunneling rate we use

$$\gamma \approx Tk = \frac{k}{1 + \frac{U_0^2}{4k^2}} \quad (2.82)$$

which is in good agreement to the numerical data, see Fig. 2.6. In contrast to the exponential decay which is found for solid barriers, see Eq. (2.33), the considered δ -barrier accounts for algebraically decaying tunneling rates.

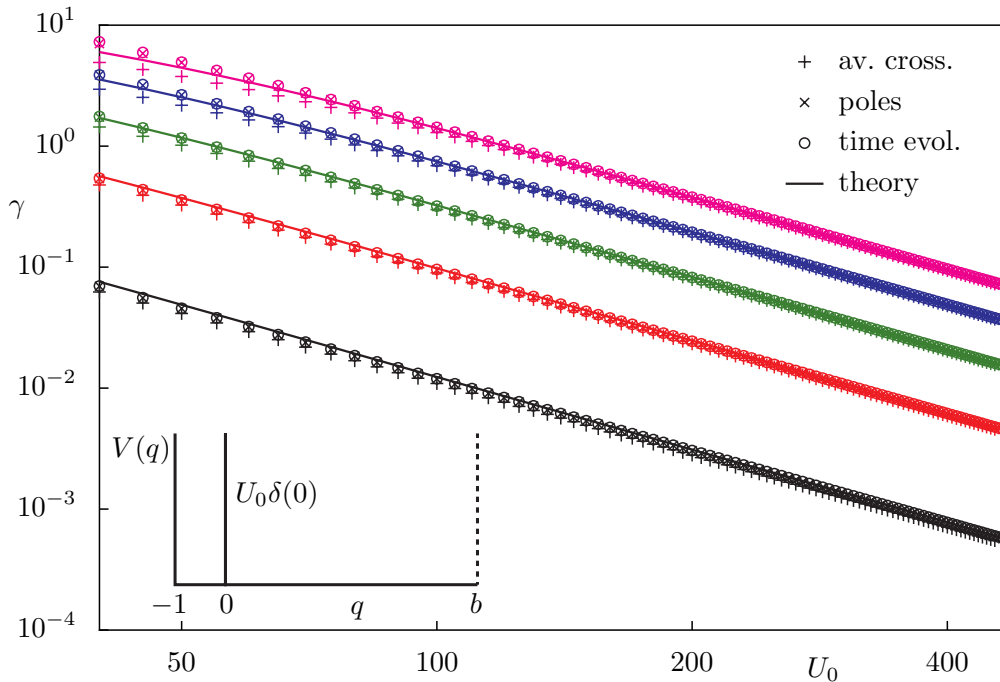


Figure 2.6: Tunneling rates γ under variation of the strength U_0 of the δ -barrier on a double-logarithmic scale for the four resonance states of lowest energy in the left well. We compare numerical data obtained by the evaluation of avoided crossings (plus symbols), poles (crosses), and time evolution (circles) to the prediction of Eq. (2.82) (lines). The lower inset shows the considered potential energy with a hard wall at $q = -1$, the δ -peak at $q = 0$, and the confining barrier at $q = b$ which does not exist for the open system.

3 Model systems with a mixed phase space

In the last chapter we have studied the process of barrier tunneling in one-dimensional time-independent systems which are integrable. The motion takes place on invariant tori. Now we want to investigate more complex systems which are called mixed systems as they show invariant tori as well as chaotic dynamics. Here the process of dynamical tunneling which is the topic of this thesis occurs. Thus, we want to introduce systems which are well suited to study this process. We restrict ourselves to systems with at most two degrees of freedom as already here all essential features of the mixed dynamics can be observed and numerical calculations are still feasible. Specifically, we consider kicked systems, billiards, and optical microcavities, which will be shortly introduced in this chapter.

3.1 Kicked systems

Kicked systems are particularly suited to study classical and quantum effects appearing in a mixed phase space as they can be easily treated analytically and numerically. In contrast to time-independent systems where at least two degrees of freedom are necessary to break integrability, one-dimensional kicked systems can show chaotic motion as the energy is not conserved due to their time dependence.

3.1.1 Classical maps

We study time-periodic one-dimensional kicked systems described by the Hamilton function

$$H(q, p, t) = T(p) + \tau V(q) \sum_{n \in \mathbb{Z}} \delta(t - n\tau) \quad (3.1)$$

where $T(p)$ is the kinetic energy and $V(q)$ is the potential. Some examples for the choice of these functions are given below. The potential $V(q)$ is applied just once per kick period τ at $t_n = n\tau$. In the mean time the dynamics evolves freely according to $T(p)$. Throughout this thesis we will use $\tau = 1$. To investigate these kicked systems it is appropriate to consider

Hamilton's equations of motion

$$\dot{q} = \frac{\partial H(q, p, t)}{\partial p} = \frac{\partial T(p)}{\partial p} =: T'(p), \quad (3.2)$$

$$\dot{p} = -\frac{\partial H(q, p, t)}{\partial q} = -\frac{\partial V(q)}{\partial q} \sum_{n \in \mathbb{Z}} \delta(n - t) =: -V'(q) \sum_{n \in \mathbb{Z}} \delta(n - t). \quad (3.3)$$

We find that in between the kicks the momentum p stays constant and is changed instantaneously at the kicking times $t_n = n$. As the dynamics in between the kicks is integrable it is sufficient to look at the dynamics of the system just once per kick period at $t_n = n + \epsilon$, where $0 < \epsilon < 1$. The continuous dynamical system described by Hamilton's equations of motion is reduced to a mapping $\bar{\mathcal{F}}_\epsilon$, which describes how the points (q_n, p_n) have evolved after one additional period of time

$$(q_{n+1}, p_{n+1}) = \bar{\mathcal{F}}_\epsilon(q_n, p_n). \quad (3.4)$$

Such a map is called a stroboscopic map, see Fig. 3.1. For kicked systems the map $\bar{\mathcal{F}}_\epsilon$ can be explicitly calculated by integrating Eqs. (3.2) and (3.3) over one period of the driving [71]

$$\begin{aligned} q_{n+1} - q_n &= \int_{n+\epsilon}^{n+1+\epsilon} \dot{q}(t) dt = \int_{n+\epsilon}^{n+1+\epsilon} T'(p) dt = \int_{n+\epsilon}^{n+1} T'(p) dt + \int_{n+1}^{n+1+\epsilon} T'(p) dt \\ &= (1 - \epsilon)T'(p_n) + \epsilon T'(p_{n+1}), \end{aligned} \quad (3.5)$$

$$\begin{aligned} p_{n+1} - p_n &= \int_{n+\epsilon}^{n+1+\epsilon} \dot{p}(t) dt = - \int_{n+\epsilon}^{n+1+\epsilon} V'(q) \sum_{m \in \mathbb{Z}} \delta(m - t) dt = -V'(q(n+1)) \\ &= -V'(q_n + (1 - \epsilon)T'(p_n)). \end{aligned} \quad (3.6)$$

The phase-space coordinates (q_{n+1}, p_{n+1}) result from the coordinates at the previous time (q_n, p_n) through the mapping $\bar{\mathcal{F}}_\epsilon$

$$\bar{\mathcal{F}}_\epsilon : \begin{cases} q_{n+1} = q_n + (1 - \epsilon)T'(p_n) + \epsilon T'(p_{n+1}), \\ p_{n+1} = p_n - V'(q_n + (1 - \epsilon)T'(p_n)). \end{cases} \quad (3.7)$$

In the literature three specific values for ϵ are commonly used. First, one can consider the limes $\epsilon \rightarrow 0^+$ which means that we evaluate the dynamics infinitesimally short after each kick at $t_n = n$. The mapping $\bar{\mathcal{F}}_0 =: \bar{\mathcal{F}}$ then has a simpler form

$$\bar{\mathcal{F}} : \begin{cases} q_{n+1} = q_n + T'(p_n), \\ p_{n+1} = p_n - V'(q_{n+1}) \end{cases} \quad (3.8)$$

which we will use throughout the thesis. Other common values for ϵ are $\epsilon \rightarrow 1^-$ which evaluates

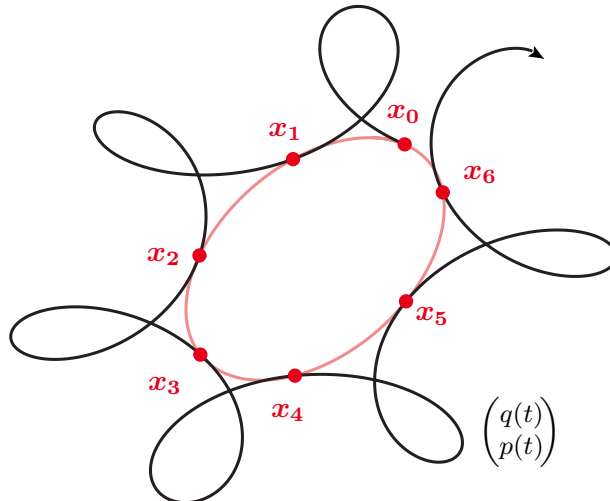


Figure 3.1: Illustration of the stroboscopic mapping: The continuous trajectory in phase space $(q(t), p(t))$ (black line) is evaluated for times $t_n = n$ resulting in the phase-space points $\mathbf{x}_n = (q_n, p_n)$ (red dots) which for the shown example form an invariant torus (rose line).

the dynamics before each kick and $\epsilon = 1/2$, the so-called half-free map, which explicitly shows existing symmetries.

Before we take a closer look on the dynamics generated by such kicked maps we want to specify the space on which they act. In Eq. (3.8) the phase-space variables (q, p) are allowed to take any real value. The maps we study in the following, however, are defined on a limited area of phase space only, whose topology is a 2-torus \mathbb{T}^2 . It is given as a product manifold $\mathbb{T}^2 := S^1 \times S^1$ of two unit circles $S^1 := \{z \in \mathbb{C} \mid |z| = 1\} = \{e^{2\pi i \varphi} \mid \varphi \in \mathbb{R}\}$. All points $(q, p) \in \mathbb{R}^2$ whose coordinates differ by elements in \mathbb{Z} are identified

$$(q, p) = (q', p') \Leftrightarrow q - q' \in \mathbb{Z}, p - p' \in \mathbb{Z}. \quad (3.9)$$

A natural representation of \mathbb{T}^2 is given by the unit square

$$\mathbb{T}^2 = [0, 1) \times [0, 1) = \{(q, p) \in \mathbb{R}^2 \mid (q, p) = (q, p) \bmod 1\} \quad (3.10)$$

where opposing sides are identified. We use the abbreviation $(q, p) \bmod 1$ for $q \bmod 1$ and $p \bmod 1$. An extension of the unit square to a rectangle of size (M_q, M_p) , where $M_q \in \mathbb{N}$ and $M_p \in \mathbb{N}$ will be used in this thesis. The representation of the torus is then found as

$$[0, M_q) \times [0, M_p) = \{(q, p) \in \mathbb{R}^2 \mid (q, p) = (q, p) \bmod (M_q, M_p)\}. \quad (3.11)$$

Here, phase-space points which differ by integer multiples of M_q in position and M_p in momen-

tum are identified. The map \mathcal{F} on the torus is finally obtained as

$$\mathcal{F}(q, p) = \bar{\mathcal{F}}(q, p) \bmod (M_q, M_p) \quad (3.12)$$

where $\bar{\mathcal{F}} : \mathbb{R}^2 \rightarrow \mathbb{R}^2$. The natural invariant measure μ is the Lebesgue measure $d\mu = dp dq$. Further discussions can be found in Refs. [72–74].

Let us now consider the famous Chirikov standard map [75] as an example for a kicked system with a mixed phase space. Its Hamilton function is given by

$$H(q, p, t) = \frac{p^2}{2} + \frac{K}{4\pi^2} \cos(2\pi q) \sum_{n \in \mathbb{Z}} \delta(t - n). \quad (3.13)$$

In the kinetic energy we used $m = 1$ and the potential is periodic in position space with period one. The associated mapping evaluated just after the kick \mathcal{F} is found using Eq. (3.8)

$$q_{n+1} = [q_n + p_n] \bmod 1, \quad (3.14)$$

$$p_{n+1} = \left[p_n + \frac{K}{2\pi} \sin(2\pi q_{n+1}) \right] \bmod 1. \quad (3.15)$$

It depends on one free parameter K which is called kicking strength.

If we choose $K = 0$ the momentum is a constant of motion. It does not change under the iteration of the map. Thus, the dynamics takes place on invariant tori $p = \text{const.}$ and the system is integrable. If K is changed to a small value larger than zero the integrability of the system

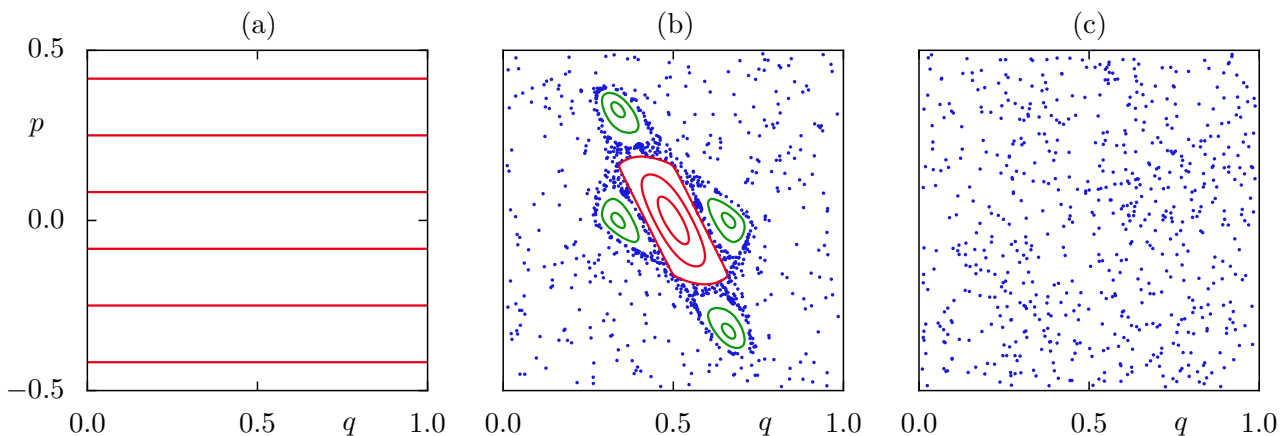


Figure 3.2: Phase space of the standard map for (a) $K = 0$, (b) $K = 2.4$, and (c) $K = 8$. In (a) the potential energy $V(q)$ is zero such that the momentum p is a conserved quantity and the system is integrable. The phase space is filled by invariant tori (red lines). The second figure (b) shows a mixed phase space with regular motion (red lines), nonlinear resonance chains (green lines), and a chaotic sea (blue dots). In this chaotic sea partial barriers exist, which is reflected by the different densities of chaotic points. For large values of K as in (c) the phase space is macroscopically chaotic.

is destroyed. However, as explained by the KAM theorem [76], many invariant tori persist under this perturbation. In between these tori, where the external frequency of the driving is a rational multiple of the internal frequency of the unperturbed motion, sequences of stable and unstable fixed points emerge which is described by the Poincaré-Birkhoff theorem [77]. The stable fixed points of such a sequence form so-called nonlinear resonance chains (green lines in Fig. 3.2) while in the vicinity of the unstable fixed points typically chaotic dynamics is found. If we further increase the perturbation parameter K more and more regular tori break up and the chaotic dynamics occupies more and more of the phase space. At $K \approx 3$ we have the situation of one large regular region, which we call regular island due to its elliptic shape, surrounded by a region of chaotic dynamics, which we in analogy call chaotic sea. Especially in the transition region from regular to chaotic dynamics an interesting phenomenon appears: Around each regular island of a nonlinear resonance chain the same scenario as described above takes place. Again some tori persist while others are destroyed and form nonlinear resonance chains and regions of chaotic dynamics. This behavior can be seen down to arbitrary small scales in phase space. It is called self similarity. Furthermore, additional structures can be found in the chaotic sea. Here, so-called partial barriers limit the classical flux between different regions of chaotic motion caused by the stable and unstable manifolds of unstable periodic orbits or caused by the remnants of regular tori, called cantori [78]. By further increasing K the regular islands vanish and the motion seems to be completely chaotic. However, the chaoticity of the standard map for large values of K is not proven. Note that in this thesis we characterize orbits as “chaotic” if they fill a two-dimensional region in phase space and show a sensitive dependence on initial conditions. The corresponding chaotic region in phase space might still contain tiny regular regions which, however, are not relevant for the considered problems. The described zoology of phenomena occurring in systems with a mixed phase space is depicted in Fig. 3.2 for specifically chosen values of K .

Linearized map and stability

A lot of insight on the dynamics of a map with a mixed phase space can be obtained by considering its linearized dynamics, especially around fixed points or periodic orbits. The linearized map (also called the monodromy matrix \mathcal{M}) is derived for kicked systems using Eq. (3.8) as

$$\mathcal{M} = \begin{pmatrix} \frac{\partial q_{n+1}}{\partial q_n} & \frac{\partial q_{n+1}}{\partial p_n} \\ \frac{\partial p_{n+1}}{\partial q_n} & \frac{\partial p_{n+1}}{\partial p_n} \end{pmatrix} = \begin{pmatrix} 1 & T''(p_n) \\ -V''(q_n + T'(p_n)) & 1 - V''(q_n + T'(p_n))T''(p_n) \end{pmatrix}. \quad (3.16)$$

We find that the determinant $\det(\mathcal{M})$ equals one for arbitrary q_n and p_n such that these systems are area-preserving. The area of a region of phase-space remains constant under the iteration of the map. This reflects that we have no dissipation in these systems.

A point (q^*, p^*) is called a fixed point of the map \mathcal{F} if it remains unchanged after the application of \mathcal{F} : $(q^*, p^*) = \mathcal{F}(q^*, p^*)$. A periodic orbit of period r is a fixed point of the map \mathcal{F}^r which denotes the r -times application of \mathcal{F} . The trace of the linearized mapping \mathcal{M} at a fixed point (q^*, p^*) reveals its stability properties

$$\text{Tr}(\mathcal{M}) = 2 - V''(q^* + T'(p^*))T''(p^*) \quad (3.17)$$

with the residuum

$$R := \frac{2 - \text{Tr}(\mathcal{M})}{4}. \quad (3.18)$$

If the modulus of the trace of the monodromy matrix is smaller than two, $|\text{Tr}(\mathcal{M})| < 2$, the fixed point is stable. The dynamics in the vicinity of this fixed point occurs on ellipses in phase space as the application of \mathcal{M} on phase-space coordinates (q, p) describes just a rotation and squeezing of these points. Therefore, these stable fixed points are also called elliptic fixed points. The dynamics in the vicinity of an elliptic fixed point is shown in Fig. 3.3. The elliptic motion in phase space is determined by the lengths of the two half-axis a and b , by the tilting angle θ of the ellipse compared to the line $p = p^*$, and by the rotation number w_r of the orbit. The rotation number w_r is given by the ratio of the external driving period to the internal oscillation period. If it is rational with $w_r = s/r$, $s, r \in \mathbb{N}$, the orbit is a periodic orbit of period r . All the characteristic parameters of the ellipse can be calculated from the linearized map in

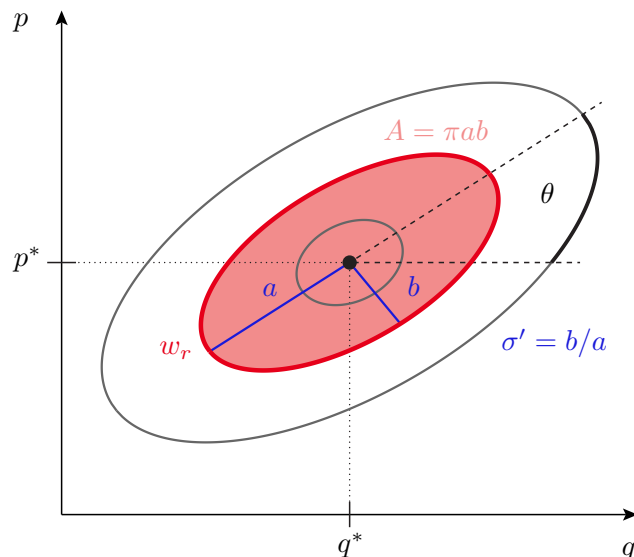


Figure 3.3: Illustration of the phase-space dynamics in the vicinity of an elliptic fixed point (q^*, p^*) . The orbits are ellipses (red line) with the half-axis a and b , whose ratio $\sigma' = b/a$ is constant and defined by the linearized mapping. With respect to the line $p = p^*$ these ellipses are tilted by the angle θ and have a constant rotation number w_r .

the stable fixed point. We find for the tilting angle

$$\theta = \frac{1}{2} \arctan \left(\frac{\mathcal{M}_{22} - \mathcal{M}_{11}}{\mathcal{M}_{12} - \mathcal{M}_{21}} \right) \quad (3.19)$$

and for the squeezing $\sigma' = b/a$

$$\sigma' = \sqrt{\frac{|\mathcal{M}_{12} - \mathcal{M}_{21}| - c}{|\mathcal{M}_{12} - \mathcal{M}_{21}| + c}} \quad \text{with} \quad c = \sqrt{(\mathcal{M}_{12} + \mathcal{M}_{21})^2 + (\mathcal{M}_{22} - \mathcal{M}_{11})^2}. \quad (3.20)$$

The residuum of an elliptic fixed point is given by $R = \sin^2(\pi w_r)$ [79]. This relation and Eq. (3.18) can be used to find a connection between the trace of the linearized map and the rotation number

$$w_r = \frac{1}{\pi} \arcsin \left(\sqrt{\frac{2 - \text{Tr}(\mathcal{M})}{4}} \right) = \frac{1}{2\pi} \arccos \left(\frac{\text{Tr}(\mathcal{M})}{2} \right). \quad (3.21)$$

We find that the dynamics in the vicinity of an elliptic fixed point is completely determined by the linearized map at that fixed point. If $\text{Tr}(\mathcal{M}) > 2$ or $\text{Tr}(\mathcal{M}) < -2$ the fixed point is unstable and called hyperbolic or inverse hyperbolic, respectively. The dynamics in its vicinity is typically chaotic. For $|\text{Tr}(\mathcal{M})| = 2$ the fixed point is called parabolic. By determining the stability properties of fixed points of a map one can obtain a first impression on how the structure of the phase space can be described. This will be useful when designing model systems with a particularly simple phase-space structure, see Section 3.1.2.

Transport properties

The mixed phase space of kicked systems generically consists of regions of regular motion surrounded by a chaotic sea. The transport properties of this chaotic region, such as its average drift velocity [80], are important classically, e.g. to reveal if the chaotic dynamics is diffusive. They are also relevant quantum mechanically and determine the appearance of dynamical localization [81, 82].

The velocity v is defined as

$$v := \frac{\partial H(q, p, t)}{\partial p} = T'(p). \quad (3.22)$$

If we label the regular islands with $i = 1, 2, \dots$ their transport velocity is given by v_i . For the chaotic region with the phase-space volume V_{ch} we have

$$v_{\text{ch}} = \frac{1}{V_{\text{ch}}} \int_{\Gamma_{\text{ch}}} dq dp dt T'(p) \quad \text{with} \quad V_{\text{ch}} = \int_{\Gamma_{\text{ch}}} dq dp dt. \quad (3.23)$$

For each regular region i of volume V_i we can calculate the parameters $\kappa_i := V_i v_i$ and obtain

$$\langle T \rangle_u - \langle T \rangle_l = V_{\text{ch}} v_{\text{ch}} + \sum_i \kappa_i \quad (3.24)$$

where $\langle T \rangle_u$ and $\langle T \rangle_l$ denote the averaged kinetic energy along the upper or the lower KAM torus which separates regular from chaotic dynamics. For the systems studied in this thesis there exist no such upper or lower KAM tori such that the phase-space boundaries have to be considered as their analog [80]. In our case, where the kicking period is unity, the phase-space volumina V_i are equal to areas in the stroboscopic phase-space section A_i and the transport velocity of the chaotic sea is given by

$$v_{\text{ch}} = \frac{\langle T \rangle_u - \langle T \rangle_l - \sum_i A_i v_i}{A - \sum_i A_i} \quad (3.25)$$

with the area A of phase space between the two limiting tori and the transport velocities of the regular islands v_i . For the case of just one non-transporting regular island, $v_1 = 0$, of area A_1 embedded in the chaotic sea and $A = 1$ the average chaotic velocity is obtained as

$$v_{\text{ch}} = \frac{\langle T \rangle_u - \langle T \rangle_l}{1 - A_1}. \quad (3.26)$$

Hence, we find transport within the chaotic sea only if the difference of the kinetic energies along the limiting KAM tori or along the borders of phase space does not vanish. This has to be considered when designing maps which should not show quantum mechanical localization in the chaotic region. It is caused by classically diffusive and drift-free motion which occurs if $v_{\text{ch}} = 0$.

3.1.2 Examples

In this section we want to discuss certain example systems and their classical dynamics. The choice of these example systems is motivated by their usefulness in studying the dynamical tunneling process. On the one hand maps like the standard map, which has been introduced in the last section, are commonly used for various investigations including the study of dynamical tunneling. One final test of our theory for dynamical tunneling is given by its application to such a generic system. On the other hand, as discussed in the last section, these systems show the full variety of effects which exist in a mixed phase space such as nonlinear resonances, a broad hierarchical transition region from regular to chaotic dynamics, and partial barriers in the chaotic phase-space region. Hence, it is reasonable to start with simpler systems which do not show all of these structures. By designing maps such that these features can be switched on and off one-by-one it is possible to study their influence on the dynamical tunneling process separately and confirm the assigned theoretical descriptions. This allows to identify certain

patterns appearing in numerical data with classical structures existing in the mixed phase space.

According to these thoughts we will now introduce mappings starting from the most simplest phase-space structure. Then we will introduce additional parameters which cause perturbations to these mappings and more complicated features arise, as described above. We will be able to tune our system such that none, one, or more than one relevant resonance chains appear, and we can vary the size of the hierarchical region. It is also possible to construct single partial barriers in the chaotic part of phase space.

Designed map \mathcal{F}_1 with one regular island

Our first example \mathcal{F}_1 shall be the most simple kicked system with a mixed phase space which consists of one elliptic resonance-free regular island surrounded by a structureless chaotic sea, similar to the system introduced in Ref. [83]. For this purpose we use our knowledge about the linearized dynamics in the vicinity of a fixed point, described in Section 3.1.1. If this fixed point is stable the linearized dynamics generates elliptic orbits in its vicinity whose rotation number w_r can be determined by Eq. (3.21). For an unstable fixed point the dynamics is chaotic. By choosing the kinetic and the potential energy as a quadratic function in q and p , respectively, this linearized dynamics is extended to the whole phase space and the mapping is either integrable or fully chaotic. To design a map with an elliptic regular island and a chaotic sea at the same time we consider a compact phase space with $q \in [-1/2 + k_{\min}, -1/2 + k_{\max})$ and $p \in [-1/2, 1/2)$ where $k_{\max} - k_{\min} = M_q \in \mathbb{N}$. Opposite sides are identified to describe the mapping on a torus. This phase space consists of M_q unit cells of volume 1 in q -direction and one unit cell in p -direction. For each unit cell, labelled by $k = k_{\min}, \dots, k_{\max} \in \mathbb{Z}$, we piecewisely define the potential $v(q)$ as a quadratic function in q such that in the central cell, $k = 0$, a stable fixed point exists whose counterpart in the other cells is unstable. Hence, in the cell $k = 0$ we find a regular island while in the other cells we find chaotic dynamics. One choice for such a kicked system is given by the kinetic energy

$$t(p) = -p^2 - \frac{1}{2}p, \quad p \in [-\frac{1}{2}, \frac{1}{2}) \quad (3.27)$$

and the potential energy

$$v(q) = \begin{cases} -\frac{r_1}{2}q^2 & , \quad q \in [-\frac{1}{2}, \frac{1}{2}) \\ \frac{r_2}{2}(q - k)^2 & , \quad q \in [-\frac{1}{2} + k, \frac{1}{2} + k), \quad k \neq 0 \end{cases} \quad (3.28)$$

where r_1 and r_2 are real parameters which define the structure of the phase space. Note that the kinetic energy $t(p)$ is not periodic, $\Delta t := t(-\frac{1}{2}) - t(\frac{1}{2}) = \frac{1}{2}$. This is necessary to enable a global transport in the chaotic region according to Eq. (3.26) as the considered phase space contains just one non-transporting regular island. Without this transport the classically chaotic

dynamics would be diffusive which leads to dynamical localization in quantum mechanics.

To study the classical dynamics of this system \mathcal{F}_1 we consider the associated map, Eq. (3.8), evaluated just after each kick. It requires the derivatives of the kinetic and potential energy

$$t'(p) = -2p - \frac{1}{2}, \quad p \in [-\frac{1}{2}, \frac{1}{2}), \quad (3.29)$$

$$v'(q) = \begin{cases} -r_1 q & , \quad q \in [-\frac{1}{2}, \frac{1}{2}) \\ r_2(q - k) & , \quad q \in [-\frac{1}{2} + k, \frac{1}{2} + k), \quad k \neq 0. \end{cases} \quad (3.30)$$

These functions show discontinuities at $p = \pm 1/2$ and $q = -1/2 + k$ which cause unwanted effects such as eigenfunctions localized on these discontinuities in quantum mechanics. Hence, we smooth the functions $t'(p)$ and $v'(q)$ by a convolution with a Gaussian of width ε

$$G_\varepsilon(x) = \frac{1}{\sqrt{2\pi\varepsilon^2}} e^{-\frac{x^2}{2\varepsilon^2}} \quad (3.31)$$

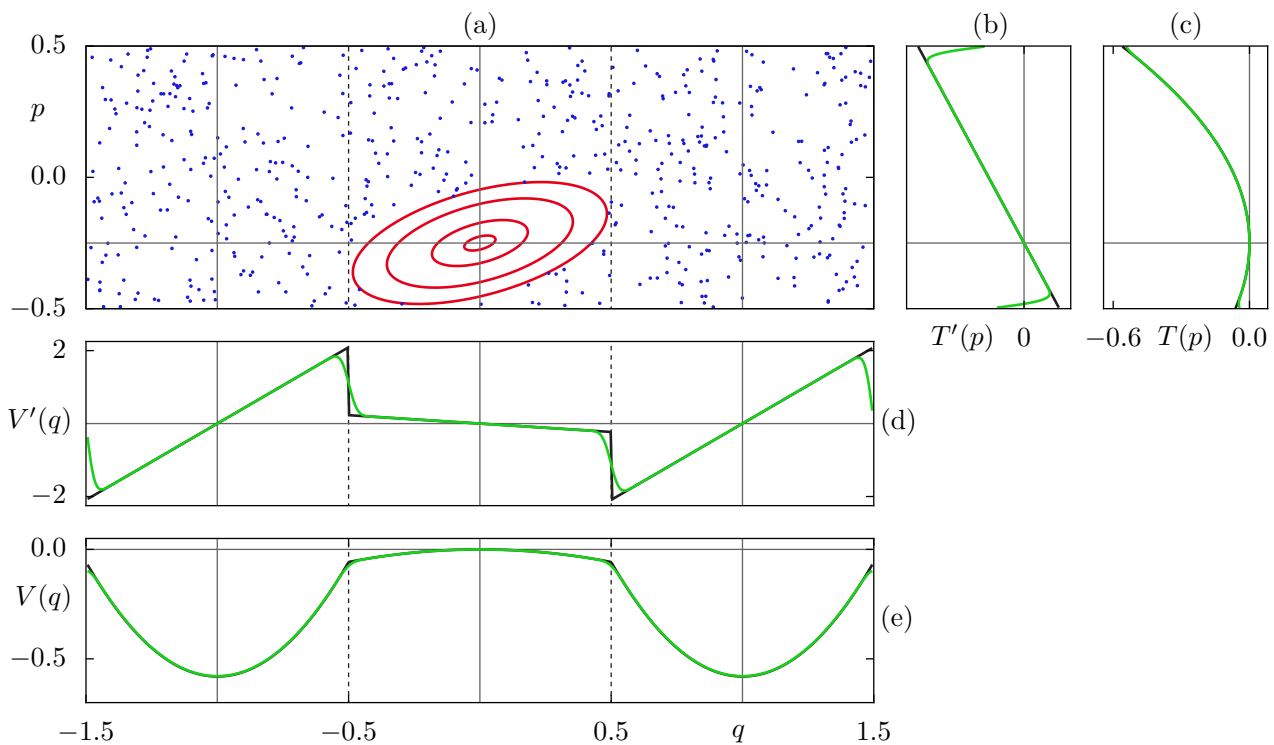


Figure 3.4: In (a) the phase space of the mapping \mathcal{F}_1 is presented for the parameters $r_1 = 0.46$, $r_2 = 4.185$, $R = 0$, $Z = 0$, $\varepsilon = 0.005$, and $M_q = 3$. The regular island is marked in red while the chaotic sea is drawn in blue. The insets (b)-(e) show the kinetic energy $T(p)$, the potential energy $V(q)$, and their derivatives $T'(p)$ and $V'(q)$. These functions are presented discontinuously (black lines) and in the smoothed version (green lines). The gray lines mark the positions for which $V'(q)$ or $T'(p)$ are zero. At the crossings of these gray lines in (a) the mapping has a fixed point which is stable in the central and unstable in the other cells. The black dashed lines separate the different unit cells.

and obtain the continuous functions

$$T'(p) = \int_{-\frac{1}{2}}^{\frac{1}{2}} G_\varepsilon(p-x)t'(x) dx, \quad V'(q) = \int_{-\frac{1}{2}+k_{\min}}^{-\frac{1}{2}+k_{\max}} G_\varepsilon(q-x)v'(x) dx. \quad (3.32)$$

The smoothed kinetic energy $T(p)$ and the potential energy $V(q)$ is obtained by integration as presented in Appendix B.1. If the parameter ε is small the convolution with the Gaussian does only change the piecewise defined functions $t'(p)$ and $v'(q)$ in the vicinity of their discontinuities such that the classical dynamics of the system remains almost unchanged. Fig. 3.4 shows the phase space of this mapping for $r_1 = 0.46$, $r_2 = 4.185$ (used throughout the thesis), and $\varepsilon = 0.005$ as well as the functions discussed above. We find one elliptic regular island in the central cell $k = 0$ surrounded by chaotic motion in the central and the other cells.

To understand this structure of the phase space we consider the fixed points of the piecewise defined mapping \mathcal{F}_1 . They are found to be stable or unstable according to the trace the monodromy matrix

$$\mathcal{M} = \begin{pmatrix} 1 & -2 \\ \pm r_{1/2} & 1 \mp 2r_{1/2} \end{pmatrix} \quad (3.33)$$

where the upper sign belongs to $k = 0$ and the lower sign to $k \neq 0$. This matrix is constant for each unit cell and its trace is found to be

$$\text{Tr}(\mathcal{M}) = 2 \mp 2r_{1/2}. \quad (3.34)$$

With the choices $0 < r_1 < 2$ and $r_2 > 0$ each fixed point in the central cell has to be stable as $|\text{Tr}(\mathcal{M})| < 2$ and each fixed point in the other cells has to be unstable. Of particular interest is the fixed point in the central cell. It is located at $(q^*, p^*) = (0, -1/4)$ and forms the center of the elliptic island. The prediction of Eq. (3.21) for the winding number w_r is valid for the whole regular island due to the linear choice of the functions $v'(q)$ and $t'(p)$. Hence, its shape is elliptic. Its area is limited by the borders to the other unit cells or the border of phase space. With the parameter M_q the number of additional unit cells of completely chaotic dynamics can be adjusted. This freedom will turn out to be useful in following numerical calculations.

After the convolution with a Gaussian the analysis of the linearized dynamics of \mathcal{F}_1 remains unchanged for fixed points far away from the border of the unit cells as e.g. for the fixed point at $(q^*, p^*) = (0, -1/4)$ forming the regular island. However, in the vicinity of these borders the functions $T'(p)$ and $V'(q)$ are no longer linear functions. Hence, the dynamics of the regular island at its border is changed and shows hierarchical structures, see Fig. 3.5(b)-(d). For small values of the smoothing parameter ε the affected region will also be very small such that it cannot be revealed quantum mechanically, unless the effective Planck constant h_{eff} is chosen small enough. This is not the case for the parameters used for this system throughout the thesis.

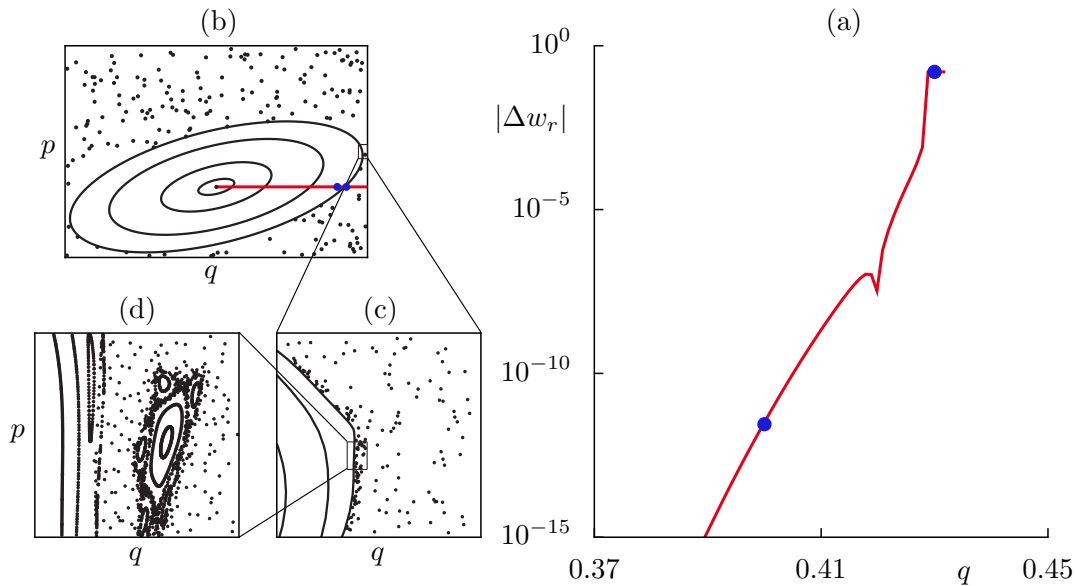


Figure 3.5: Comparison of numerically determined rotation numbers $w_r(q^* + q, p^*)$ to the prediction of the linearized dynamics $w_r(q^*, p^*)$, Eq. (3.21). For the parameters presented in Fig. 3.4 we show (a) the difference of these two quantities $\Delta w_r := w_r(q^* + q, p^*) - w_r(q^*, p^*)$ on a logarithmic scale in the vicinity of the border of the regular island (red line). The appearing dip around $q = 0.42$ occurs due to a change in sign. In (b) we show the phase space of the system. The blue dots in (a) and (b) are placed at the same q -values to show that only a small region around the boundary of the regular island is considered. The magnifications (c) and (d) reveal that due to the smoothing of the map a tiny hierarchical transition region from regular to chaotic motion exists.

The deviations from the original dynamics caused by the Gaussian smoothing can be studied with the frequency map analysis [84, 85] which computes the rotation number w_r of a regular orbit. Using initial conditions from the center of the regular island to its border the results of the frequency map analysis are compared to the constant rotation number of the piecewise defined map. The result is given in Fig. 3.5(a) for $r_1 = 0.46$, $r_2 = 4.185$, and $\varepsilon = 0.005$. It shows that the deviations are negligible except for a small region at the border of the regular island.

In conclusion, by using piecewise defined quadratic functions for the kinetic and the potential energy with different prefactors r_1 and r_2 we designed a kicked system with one elliptic regular island in the central cell while the dynamics in the other cells is completely chaotic and shows no additional substructures. Hence, it is a convenient system to investigate the process of dynamical tunneling as the regular region and the chaotic sea appear in the most simple form.

Extension of the mapping \mathcal{F}_1

We want to extend the designed system \mathcal{F}_1 discussed above such that the regular island shows a non-constant rotation number. This allows to study its influence on the tunneling process and

we are able to force the appearance or disappearance of nonlinear resonances. As before, we aim for a homogeneous chaotic sea and a small hierarchical region. These objectives can be achieved by adding higher order terms to the potential energy of the system \mathcal{F}_1 in the central unit cell

$$v(q) = \begin{cases} -\frac{r_1}{2}q^2 + \frac{R}{3}q^3 + \frac{Z}{4}q^4 & , \quad q \in [-\frac{1}{2}, \frac{1}{2}) \\ \frac{r_2}{2}(q-k)^2 & , \quad q \in [-\frac{1}{2} + k, \frac{1}{2} + k), \quad k \neq 0 \end{cases} \quad (3.35)$$

where the parameters $R, Z \in \mathbb{R}$ control the strength of the cubic and the quartic term. The kinetic energy remains unchanged. For the derivative of $v(q)$ we obtain

$$v'(q) = \begin{cases} -r_1q + Rq^2 + Zq^3 & , \quad q \in [-\frac{1}{2}, \frac{1}{2}) \\ r_2(q-k) & , \quad q \in [-\frac{1}{2} + k, \frac{1}{2} + k), \quad k \neq 0. \end{cases} \quad (3.36)$$

The continuous functions $V'(q)$ and $V(q)$ are again obtained by the convolution of $v'(q)$ with a Gaussian and integration afterwards. In Fig. 3.6 we present the phase space of this extended mapping and show the kinetic and potential energy and their derivatives for $r_1 = 0.266$, $r_2 = 4.185$, $R = 0.4$, $Z = 0$, and $\varepsilon = 0.005$. While compared to Fig. 3.4 the elliptic shape of the island is lost, the position of its central fixed point and the chaotic dynamics in the other cells

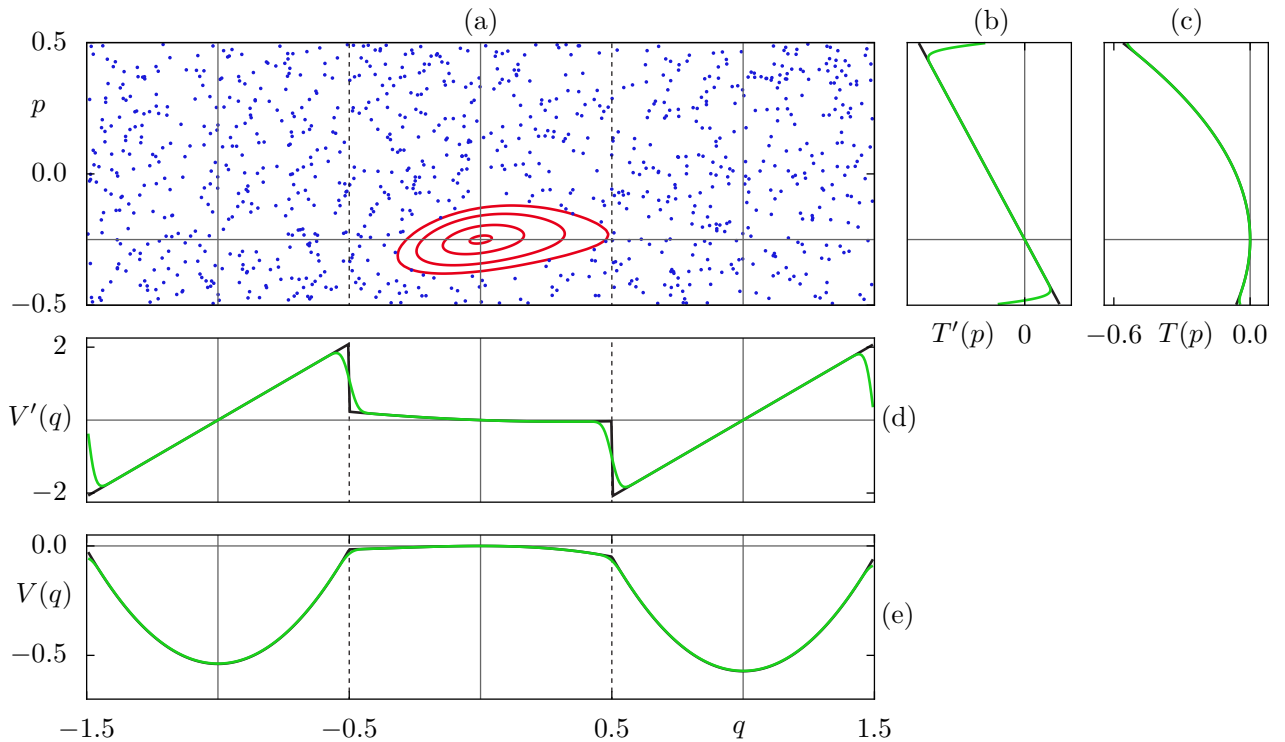


Figure 3.6: Same as Fig. 3.4 for the mapping \mathcal{F}_1 with parameters $r_1 = 0.266$, $r_2 = 4.185$, $R = 0.4$, $Z = 0$, $\varepsilon = 0.005$, and $M_q = 3$. Due to the non-zero cubic term in the potential $V(q)$ the shape of the island is deformed compared to the previously discussed elliptic case.

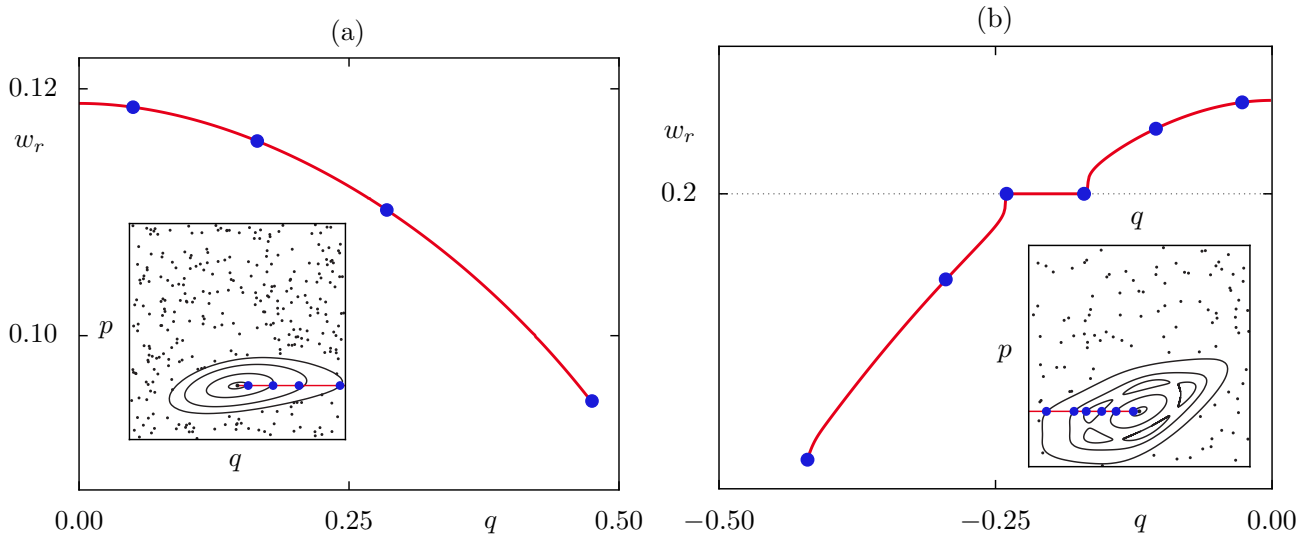


Figure 3.7: Numerically determined rotation number along the line $(q, p) = (q, p^*)$ for (a) the parameters presented in Fig. 3.6 and (b) for $r_1 = -0.71$, $R = 0.62$, and $Z = 0$ (red lines). While in (a) nonlinear resonances are very small and not recognized in the winding number on the shown scale (b) shows a large 5:1 resonance (see insets in (a) and (b)). For orbits started inside this resonance the rotation number is equal to $1/5$. For comparison the blue dots which are placed at the same q -values in the main plots and the insets are shown.

remains unchanged.

With the two parameters R and Z we can adjust the shape of the regular island and define the range in which the rotation number varies from the center to the border of the regular island. This allows to find situations where just one dominant resonance chain exists inside the regular island, as presented in Fig. 3.7(b). This system will show resonance-assisted tunneling without the additional effects from partial barriers or a large hierarchical region and allows its undisturbed investigation. In addition, regular islands with more than one large resonance chain or with only tiny resonances can be found. The rotation number w_r is shown in Fig. 3.7 for two examples. Note that the parameter R breaks existing symmetries of the mapping and that for too large values of R and Z the regular island is destroyed before reaching the borders of the unit cell and thus has a larger hierarchical region.

Designed map \mathcal{F}_2 with many regular islands

In Refs. [48, 61, 83, 86, 87] a kicked system similar to the one presented in the last section is used which we call \mathcal{F}_2 . It shows the same phase-space structure as the mapping \mathcal{F}_1 . However, it has one regular island in each unit cell localized around its central fixed point of the M_q -fold map at $(q^*, p^*) = (k, 1/4)$. While each regular island has the same shape as those which appear in the system \mathcal{F}_1 , here the regular islands are transporting. Each point localized in the regular region of the k th cell will be mapped into the $(k + 1)$ st cell with periodic boundary conditions.

Hence, the average velocity of orbits within the regular island is unity and using Eq. (3.25) we have transport inside the chaotic region also for a kinetic energy $T(p)$ which is periodic in p . Besides, the same parameters r_1 , R , and Z appear as in \mathcal{F}_1 which manipulate the regular islands in the same way as described before.

The piecewise defined derivatives $t'(p)$ and $v'(q)$ of the kinetic and potential energy are given by

$$t'(p) = \frac{1}{2} + \text{sign}(p)(1 - 2p), \quad p \in [-\frac{1}{2}, \frac{1}{2}), \quad (3.37)$$

$$v'(q) = -k - r_1(q - k) + R(q - k)^2 + Z(q - k)^3, \quad q \in [-\frac{1}{2} + k, \frac{1}{2} + k) \quad (3.38)$$

and $k = k_{\min}, \dots, k_{\min} + M_q \in \mathbb{Z}$, while $t(p)$ and $v(q)$ read

$$t(p) = \frac{p}{2} + \text{sign}(p)(p - p^2), \quad p \in [-\frac{1}{2}, \frac{1}{2}), \quad (3.39)$$

$$v(q) = -kq - \frac{r_1}{2}(q - k)^2 + \frac{R}{3}(q - k)^3 + \frac{Z}{4}(q - k)^4, \quad q \in [-\frac{1}{2} + k, \frac{1}{2} + k). \quad (3.40)$$

In order to avoid the appearing discontinuities we smooth the functions $v'(q)$ and $t'(p)$ with a Gaussian G_ε as presented in the last section. The phase space of this system is shown for $M_q = 3$, $r_1 = 0.65$, $R = Z = 0$, and $\varepsilon = 0.015$ in Fig. 3.8. It also presents the kinetic energy, the potential, and their derivatives piecewise defined and smoothed as introduced above.

Standard map

We also consider the standard map, Eqs. (3.14) and (3.15), which has been introduced and discussed in Section 3.1.1. It shows all phenomena which appear in a two-dimensional mixed phase space and will be used as an example system to show that our theory for dynamical tunneling is applicable to such generic systems as well.

Map \mathcal{F}_3 with a regular stripe

Another interesting kicked system was introduced by Shudo et. al in Ref. [41]. It does not show a regular island as the maps considered before but a regular stripe in phase space. Adapted to the considered phase-space unit cell the derivatives $T'(p)$ and $V'(q)$ of the kinetic and potential energy are given by

$$\begin{aligned} V'(q) &= -\frac{1}{2\pi}(8\pi aq + d_1 - d_2 \\ &\quad + \frac{1}{2}[8\pi aq - \omega + d_1] \tanh[b(8\pi q - q_d)] \\ &\quad + \frac{1}{2}[-8\pi aq + \omega + d_2] \tanh[b(8\pi q + q_d)]), \end{aligned} \quad (3.41)$$

$$T'(p) = -\frac{K}{8\pi} \sin(2\pi p) \quad (3.42)$$

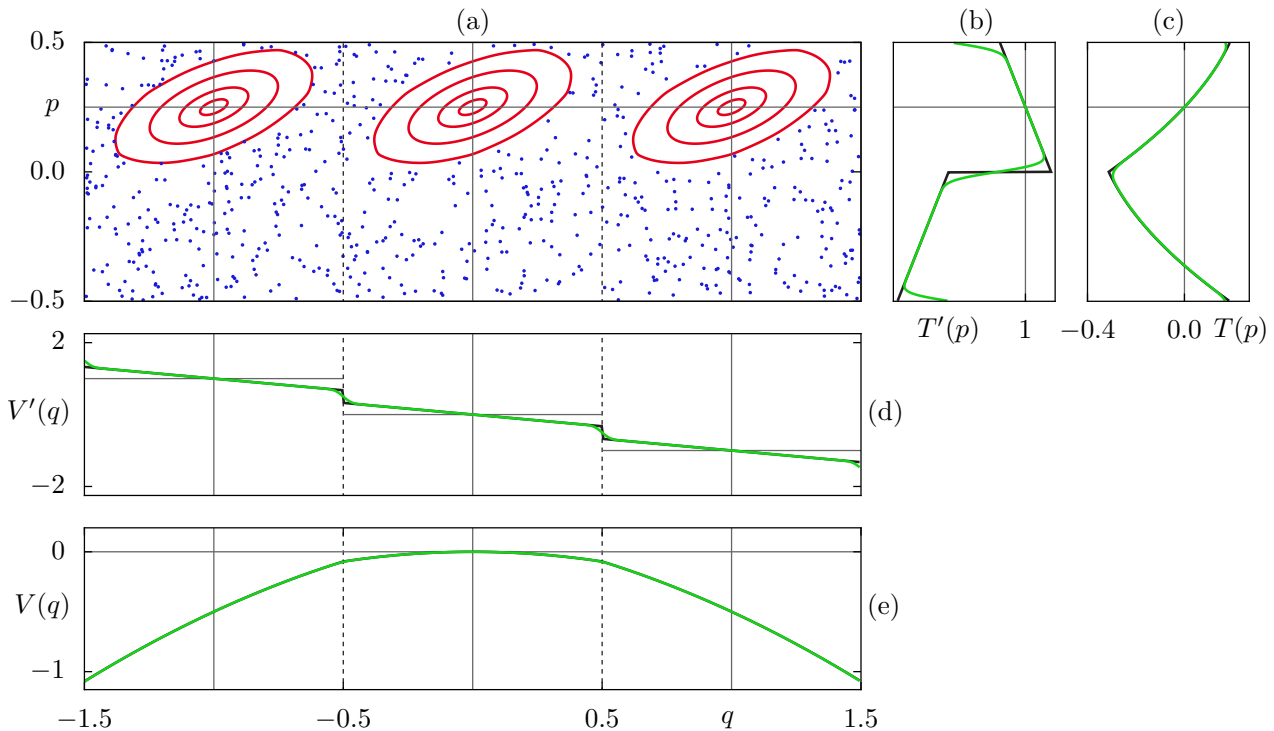


Figure 3.8: Same as Fig. 3.4 for the mapping \mathcal{F}_2 with the parameters $r_1 = 0.65$, $R = 0$, $Z = 0$, $\varepsilon = 0.015$, and $M_q = 3$. In contrast to the systems \mathcal{F}_1 we find a regular island in each cell which has its center at $(q^*, p^*) = (k, 1/4)$.

with the parameters $a, b, d_1, d_2, \omega, q_d$, and K . The kinetic energy $T(p)$ is periodic

$$T(p) = -\frac{K}{16\pi^2} \cos(2\pi p) \quad (3.43)$$

and equivalent to the potential of the kicked rotor while $V(q)$ has to be found by numerical integration. The map \mathcal{F}_3 given by Eqs. (3.41) and (3.42) is similar to the system \mathcal{F}_1 discussed above as it also cuts the integrable region by changing the function $V'(q)$ at $q = \pm q_d/(8\pi)$. The smoothing is realized by the tanh-function and the smoothing parameter is b . For large $b \gg 1$ inside the region $q < |q_d/(8\pi)|$ the potential energy depends linearly on q such that the winding number w_r is constant, while for $q > |q_d/(8\pi)|$ we recover the behavior of the standard map which is macroscopically chaotic for large K . Fig. 3.9 shows a phase-space portrait of this system and the functions discussed above.

3.1.3 Classical perturbation theory

Further insight on our kicked systems can be obtained using classical perturbation theory. It allows to construct a Hamilton function H_{reg} which is integrable and whose dynamics resembles the dynamics of a map with a mixed phase space in the regular region around an elliptic fixed point. Such systems H_{reg} will be important when studying the dynamical tunneling process in

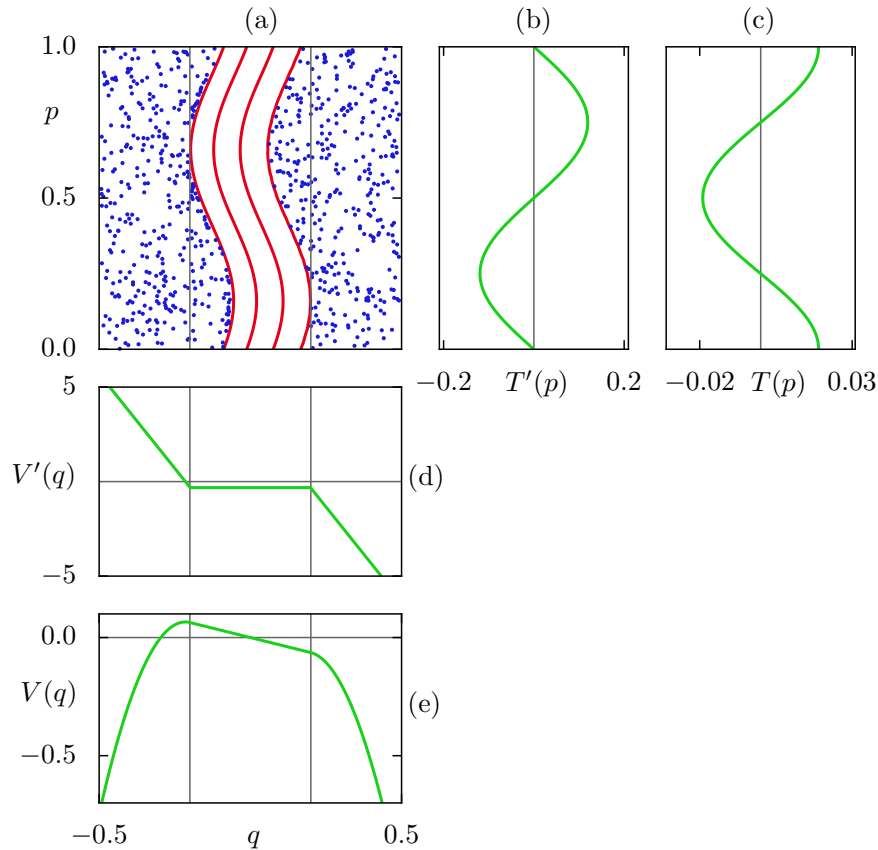


Figure 3.9: Same as Fig. 3.4 for the mapping \mathcal{F}_3 with the parameters $a = 5$, $b = 20$, $d_1 = -24$, $d_2 = -26$, $q_d = 5$, $\omega = 1$, and $K = 3$. In contrast to the systems \mathcal{F}_1 and \mathcal{F}_2 discussed before we find a regular stripe (marked in red) surrounded by chaotic motion (blue dots). In (b)-(e) the gray lines mark where the considered functions are zero and the stripe for which $V'(q)$ is constant. In this region the regular domain is located.

Chapter 4. Hence, we will present suited approaches for the determination of such systems and discuss their limitations.

We start with a time-dependent non-integrable system H which is decomposed into an integrable part H_0 and a perturbation ϵH_1 whose strength can be varied by the parameter ϵ

$$H(\mathbf{I}, \boldsymbol{\theta}, t) = H_0(\mathbf{I}) + \epsilon H_1(\mathbf{I}, \boldsymbol{\theta}, t) \quad (3.44)$$

in action-angle variables $(\mathbf{I}, \boldsymbol{\theta})$ which are marked in bold as the considered system can have more than one degree of freedom. As H_0 is integrable it solely depends on the actions \mathbf{I} . Our aim is to approximate H by such an integrable system which is determined as a power-series expansion in the perturbation parameter ϵ . In the case of one-dimensional systems this will be achieved by a time-independent system.

The commonly used classical perturbation theory of Poincaré and Von Zeipel [88] is based on a change of coordinates to new action-angle variables $(\bar{\mathbf{I}}, \bar{\boldsymbol{\theta}})$ induced by a generating function

S which depends on the old as well as on the new variables. The transformation to the new coordinates reads

$$\bar{\boldsymbol{\theta}}(\boldsymbol{\theta}, \bar{\mathbf{I}}, t) = \frac{\partial S(\boldsymbol{\theta}, \bar{\mathbf{I}}, t)}{\partial \bar{\mathbf{I}}}, \quad \mathbf{I}(\boldsymbol{\theta}, \bar{\mathbf{I}}, t) = -\frac{\partial S(\boldsymbol{\theta}, \bar{\mathbf{I}}, t)}{\partial \boldsymbol{\theta}} \quad (3.45)$$

where the transformation to the new Hamilton function \bar{H} is given by

$$\bar{H}(\bar{\mathbf{I}}, \bar{\boldsymbol{\theta}}, t) = H(\mathbf{I}, \boldsymbol{\theta}, t) + \frac{\partial S(\bar{\mathbf{I}}, \boldsymbol{\theta}, t)}{\partial t}. \quad (3.46)$$

If the new Hamilton function can be expressed as a power series in ϵ the computation of the perturbation expansion is possible in arbitrary order. However, even the term with ϵ^2 can be a complicated expression which conceals its physical content. If higher perturbational orders are needed other methods should be used as e.g. the Lie transformation [88]. Its advantage is that no functions which simultaneously depend on the old and the new phase-space coordinates appear and that the theory is canonically invariant.

Lie transformation

Our aim is to construct the simpler system \bar{H} which in the case of one-dimensional systems is integrable and resembles the classically regular motion of H . Therefore, we first sketch the derivation of the Lie transformation for autonomous systems of dimension d [88]. The vector $\boldsymbol{x} = (\boldsymbol{q}, \boldsymbol{p})$ describes the generalized position and momentum coordinates and represents one point in phase space. We consider a generating function $w(\bar{\boldsymbol{x}}, \epsilon)$ which satisfies the equation

$$\frac{d\bar{\boldsymbol{x}}}{d\epsilon} = [\bar{\boldsymbol{x}}, w] \quad \text{with} \quad [a, b] = \sum_{i=1}^d \left(\frac{\partial a}{\partial q_i} \frac{\partial b}{\partial p_i} - \frac{\partial a}{\partial p_i} \frac{\partial b}{\partial q_i} \right) \quad (3.47)$$

where we introduced the Poisson bracket as $[\cdot, \cdot]$. Equation (3.47) generates a canonical transformation for every ϵ : $\bar{\boldsymbol{x}} = \bar{\boldsymbol{x}}(\boldsymbol{x}, \epsilon)$ where $\bar{\boldsymbol{x}}$ are the new phase-space variables fulfilling $[\bar{q}_i, \bar{q}_j] = [\bar{p}_i, \bar{p}_j] = 0$ and $[\bar{q}_i, \bar{p}_j] = \delta_{ij}$. Further we introduce an operator T which transforms every function g which depends on the new phase-space variables $\bar{\boldsymbol{x}}$ to a function f depending on the original coordinates \boldsymbol{x} : $f = Tg$. In particular, if g is identity we obtain

$$\bar{\boldsymbol{x}} = T\boldsymbol{x}. \quad (3.48)$$

To find the transformation T we introduce the Lie operator $L := [w, \cdot]$ with

$$\frac{dT}{d\epsilon} = -TL \quad (3.49)$$

using Eqs. (3.47) and (3.48). For all canonical transformations the new Hamilton function \bar{H} in the new coordinates $\bar{\mathbf{x}}$ has to be identical to the old Hamilton function H in the old coordinates \mathbf{x} which can be written using the operator T , $\bar{H} = T^{-1}H$. For time-dependent systems the quantities w , L , and T will be time-dependent as well and following Ref. [88] the transformation from the old to the new Hamiltonian function reads

$$\bar{H} = T^{-1}H + T^{-1} \int_0^\epsilon d\epsilon' T(\epsilon') \frac{\partial w(\epsilon')}{\partial t}. \quad (3.50)$$

To determine the perturbational expansion the quantities w , L , T , T^{-1} , H , and \bar{H} are written as a power series in ϵ

$$w = \sum_{n=0}^{\infty} \epsilon^n w_{n+1} \quad (3.51) \quad T = \sum_{n=0}^{\infty} \epsilon^n T_n \quad (3.53) \quad H = \sum_{n=0}^{\infty} \epsilon^n H_n \quad (3.55)$$

$$L = \sum_{n=0}^{\infty} \epsilon^n L_{n+1} \quad (3.52) \quad T^{-1} = \sum_{n=0}^{\infty} \epsilon^n T_n^{-1} \quad (3.54) \quad \bar{H} = \sum_{n=0}^{\infty} \epsilon^n \bar{H}_n. \quad (3.56)$$

Inserting Eqs. (3.52) and (3.53) in Eq. (3.49) we find

$$T_n = -\frac{1}{n} \sum_{m=0}^{n-1} T_m L_{n-m} \quad (3.57)$$

where $L_n := [w_n, \cdot]$. By differentiating TT^{-1} a similar expression can be found for T^{-1}

$$T_n^{-1} = \frac{1}{n} \sum_{m=0}^{n-1} L_{n-m} T_m^{-1}. \quad (3.58)$$

Now we apply T to Eq. (3.50), differentiate with respect to ϵ , and use the power series expansions to get the final result for the perturbation theory of n th order

$$\frac{\partial w_n}{\partial t} = n\bar{H}_n - \sum_{m=0}^{n-1} L_{n-m} \bar{H}_m - \sum_{m=1}^n m T_{n-m}^{-1} H_m. \quad (3.59)$$

By explicitly writing down the first term of the first sum and the last term of the second sum this result can be transposed to a simpler form. Using $D_0 := \frac{\partial}{\partial t} + [\cdot, H_0]$ we find

$$D_0 w_n = n(\bar{H}_n - H_n) - \sum_{m=1}^{n-1} (L_{n-m} \bar{H}_m + m T_{n-m}^{-1} H_m). \quad (3.60)$$

Using Eq. (3.60) and the initial values $w_0 = L_0 = 0$ and $T_0 = \mathbf{1}$ all coefficients w_n , T_n , T_n^{-1} , L_n , and \bar{H}_n of this so-called Deprit perturbation expansion can be iteratively calculated. This

determines the new Hamilton function in the new phase-space variables $\bar{H}(\bar{\mathbf{x}})$. A detailed example of this procedure is performed in the Appendix B.2 for the kicked system \mathcal{F}_1 defined in Section 3.1.2.

Using the Lie transformation for one-dimensional kicked systems a new time-independent Hamilton function $\bar{H}(\bar{p}, \bar{q})$ is found which is integrable, interpolates the regular dynamics of the original time-dependent system, and extends it into the chaotic region. For these kicked systems one can even show that the new phase space variables $\bar{\mathbf{x}}$ are identical to the old ones \mathbf{x} such that $T = \mathbb{1}$. The obtained integrable Hamiltonian will be denoted as $H_{\text{reg}}(q, p)$ in the following. It will be most relevant when studying dynamical tunneling processes. Especially the deviations between the regular dynamics generated by H_{reg} and the regular dynamics in the mixed system H will be important. A major source for deviations is given by nonlinear resonance chains which exist in the mixed system but cannot be reproduced by the Lie transformation. The larger these resonances are the larger the deviations will be. A second cause for discrepancies in the regular dynamics is found if the perturbation ϵ is too large. The perturbation expansion will then diverge after only a few orders and a good resemblance of the regular dynamics of the given mixed system is not possible. For the maps \mathcal{F}_1 introduced in Section 3.1.2, Fig. 3.10 shows the results of the Lie transformation compared to the original dynamics in the case of only small existing nonlinear resonance chains (a) and a large 5:1 resonance (b). In the latter case larger deviations are visible. As the Deprit perturbation expansion, Eq. (3.60), is generally not convergent it is necessary to determine which order of this expansion is sufficient for a good approximation of the original regular dynamics. Fig. 3.11 shows the difference of the dynamics generated by H_{reg} to the dynamics of the mixed system H introduced in Section 3.1.2 under variation of the maximal used order N of the perturbation expansion. We find that for $N > 8$ this difference does not decrease anymore, such that a choice of $N = 8$ for this system is sufficient. Similar considerations are possible for any other example system.

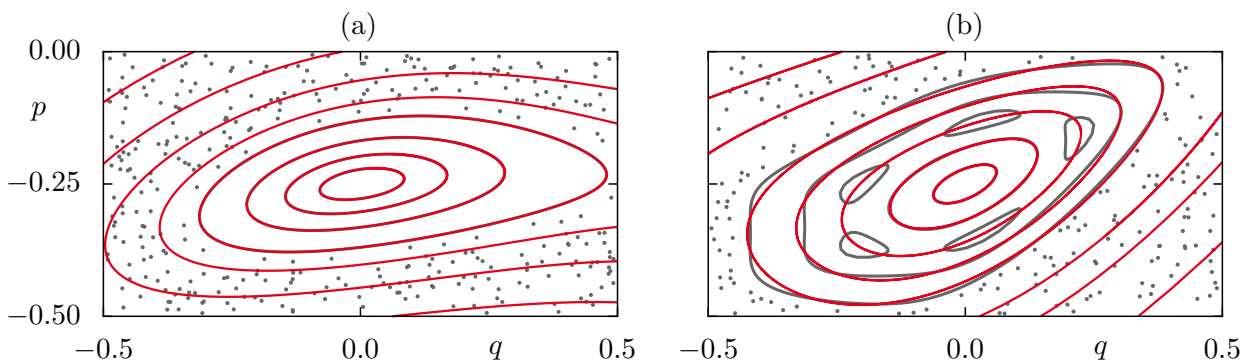


Figure 3.10: Comparison of the mixed phase space of the system \mathcal{F}_1 (gray lines and dots) and the dynamics of the one-dimensional time-independent Hamilton function obtained by the Lie transformation (red lines). We choose the parameters (a) $r_1 = 0.266$, $R = 0.4$, $Z = 0$, $\epsilon = 0.005$ and (b) $r_1 = -0.71$, $R = 0.62$, $Z = 0$, $\epsilon = 0.005$.

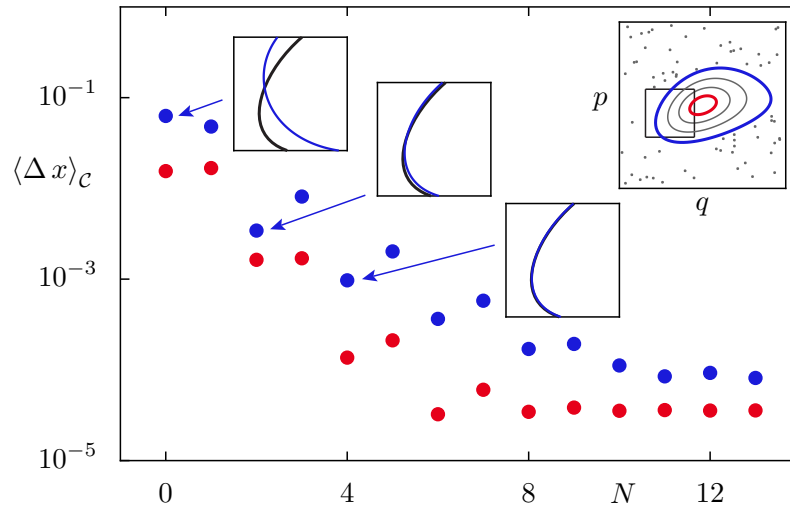


Figure 3.11: Deviations between the dynamics of the mixed system \mathcal{F}_1 and the integrable approximation H_{reg} obtained by the Lie transformation are visualized for two different regular orbits (red and blue dots) in dependence of the order N of the Lie transformation. We show the averaged difference $\langle \Delta x \rangle_C$ of the orbit obtained by the mapping \mathcal{F}_1 to that of H_{reg} . It decreases up to $N \approx 8$ and stays almost constant afterwards. The upper right inset shows the phase space of the system and the two chosen orbits while the small insets illustrate the deviations between the two systems for the orders $N = 0, 2$, and 4 .

Classical normal-form analysis

The aim of the normal-form analysis is the same as discussed previously for the Lie transformation. We want to approximate our system with a mixed phase space by a simpler system which for example has an interpolating flow, more symmetries, or more constants of motion. We discuss two-dimensional symplectic mappings \mathcal{F} which have a regular region around a stable fixed point at $(q^*, p^*) = (0, 0)$ in phase space and want to find a nonlinear transformation of coordinates Φ such that the new mappings \mathcal{U} in these new coordinates have a simpler form. For the mappings \mathcal{U} , which are in normal form, an integrable one-dimensional Hamiltonian function can be found which interpolates the dynamics of \mathcal{U} for non-integer times. We will discuss the non-resonant and the resonant normal-form analysis.

In contrast to the Lie transformation, which performs a global approximation of the dynamics of the mapping \mathcal{F} , the normal-form analysis is based on a perturbation expansion around the central stable fixed point. As discussed in Section 3.1.1 the dynamics in the vicinity of such a fixed point can be entirely described by the linearized mapping \mathcal{M} of \mathcal{F} . The dynamics takes place on elliptic tori. Using the Courant-Snyder transformation T

$$T = \begin{pmatrix} \sqrt{\beta} & 0 \\ -\frac{\alpha}{\sqrt{\beta}} & \frac{1}{\sqrt{\beta}} \end{pmatrix} \Rightarrow T^{-1} = \begin{pmatrix} \frac{1}{\sqrt{\beta}} & 0 \\ \frac{\alpha}{\sqrt{\beta}} & \sqrt{\beta} \end{pmatrix} \quad (3.61)$$

the linearized dynamics generated by \mathcal{M} can be described as a pure rotation R [89]

$$T^{-1}\mathcal{M}T = R \quad \text{with} \quad R = \begin{pmatrix} \cos(\omega) & \sin(\omega) \\ -\sin(\omega) & \cos(\omega) \end{pmatrix}. \quad (3.62)$$

By equating the coefficients the parameters α , β , and ω can be determined

$$\alpha = \pm \sqrt{-\frac{\mathcal{M}_{21}}{\sin(\omega)}\beta - 1}, \quad \beta = \frac{\mathcal{M}_{12}}{\sin(\omega)}, \quad \omega = \arccos\left(\frac{\mathcal{M}_{11} + \mathcal{M}_{22}}{2}\right) \quad (3.63)$$

where $\omega = 2\pi w_r$ is the winding number of the mapping \mathcal{F} in the vicinity of the stable fixed point, see Eq. (3.21). After the Courant-Snyder transformation the linearized dynamics is given by a pure rotation in new coordinates $(q, p) := T(q, p)$

$$\begin{pmatrix} q' \\ p' \end{pmatrix} = R \begin{pmatrix} q \\ p \end{pmatrix}. \quad (3.64)$$

To simplify the following calculations we introduce complex phase-space variables z and z^* in which the rotation R is given by the multiplication with a complex phase factor. The new coordinates read

$$z = q - ip, \quad (3.65)$$

$$z^* = q + ip. \quad (3.66)$$

For the inverse transformation we obtain

$$q = \frac{1}{2}(z + z^*), \quad (3.67)$$

$$p = \frac{i}{2}(z - z^*) \quad (3.68)$$

and Eq. (3.64) simplifies to $z' = e^{i\omega}z$. The Jacobi determinant of this transformation is $\det(\partial(z, z^*)/\partial(q, p)) = 2i$ which can be included in the Hamilton function: $H(z, z^*) = 2iH(q, p)$.

The described transformations will now be applied to a nonlinear mapping \mathcal{F} . This separates the linearized dynamics and we find

$$z' = \mathcal{F}(z, z^*) = e^{i\omega}z + \sum_{n \geq 2} [\mathcal{F}]_n(z, z^*) \quad (3.69)$$

where $[\mathcal{F}]_n$ denotes all monomials of order n in z and z^* which contribute to \mathcal{F} . As \mathcal{F} is symplectic the determinant of the Jacobi matrix \mathcal{F}_J has to be unity

$$\det(\mathcal{F}_J) := \frac{\partial \mathcal{F}}{\partial z} \frac{\partial \mathcal{F}^*}{\partial z^*} - \frac{\partial \mathcal{F}}{\partial z^*} \frac{\partial \mathcal{F}^*}{\partial z} = 1. \quad (3.70)$$

The relation between the given mapping \mathcal{F} and its normal form \mathcal{U} is depicted in the following diagram [90]

$$\begin{array}{ccc} (z, z^*) & \xrightarrow{\mathcal{F}} & (z', z'^*) \\ \Phi \uparrow & & \uparrow \Phi \\ (\xi, \xi^*) & \xrightarrow{\mathcal{U}} & (\xi', \xi'^*) \end{array}$$

where Φ transforms the new complex phase-space coordinates (ξ, ξ^*) to the old ones (z, z^*) . This scheme can be formally compared with the transformation of a matrix into diagonal form. However, \mathcal{F} , \mathcal{U} , and Φ are no matrices but nonlinear mappings which satisfy the following functional equation

$$\Phi^{-1} \circ \mathcal{F} \circ \Phi(\xi, \xi^*) = \mathcal{U}(\xi, \xi^*). \quad (3.71)$$

The transformation Φ can be written as a power series in ξ and ξ^*

$$z = \Phi(\xi, \xi^*) = \xi + \sum_{n \geq 2} [\Phi]_n(\xi, \xi^*) \quad \text{with} \quad [\Phi]_n = \sum_{k=0}^n \phi_{k, n-k} \xi^k \xi^{*n-k}. \quad (3.72)$$

As the linear part of the mapping \mathcal{F} is already in normal form it remains unchanged under the transformation Φ . The new mapping \mathcal{U} can be also written as a power series in ξ and ξ^*

$$\xi' = \mathcal{U}(\xi, \xi^*) = e^{i\omega} \xi + \sum_{n \geq 2} [\mathcal{U}]_n(\xi, \xi^*) \quad \text{with} \quad [\mathcal{U}]_n = \sum_{k=\bullet} u_{k, n-k} \xi^k \xi^{*n-k} \quad (3.73)$$

where \bullet denotes that only specific terms will contribute to the normal form. They can be found by symmetry considerations.

The one-dimensional torus is described by the real interval $[0, 2\pi)$ where the borders of this interval are identified. We consider the symmetry group \mathcal{G}_ω which is generated by $e^{i\omega}$. Its elements are the transformations $\xi \rightarrow e^{in\omega} \xi$ with $\xi \in \mathbb{C}$. The group \mathcal{G}_ω is equivalent to the group of translations on a one-dimensional torus. If $\omega/(2\pi)$ is irrational subsequent applications of $e^{i\omega}$ are dense on the torus and \mathcal{G}_ω is the rotational group $U(1)$. If $\omega/(2\pi) = s/r$ where s and r are integer numbers without a common factor it only consists of r elements. The group \mathcal{G}_ω then is a discrete subgroup of $U(1)$ with rotations of angle $2\pi j/r$, $j = 1, \dots, r$.

The mapping \mathcal{U} is in normal form if it commutes with the group \mathcal{G}_ω which is equivalent to to commuting with the generator of \mathcal{G}_ω

$$\mathcal{U}(e^{i\omega} \xi, e^{-i\omega} \xi^*) = e^{i\omega} \mathcal{U}(\xi, \xi^*). \quad (3.74)$$

\mathcal{U} is obtained by an expansion into a Taylor series where all monomials are in normal form.

For a monomial $\xi^n \xi^{*m}$ the condition

$$e^{i\omega(n-m)} \xi^n \xi^{*m} = e^{i\omega} \xi^n \xi^{*m} \quad (3.75)$$

has to be satisfied. It can be written as $\boldsymbol{\omega} \cdot \mathbf{k} = 0$ where $\boldsymbol{\omega} := (\omega, 2\pi)$ and $\mathbf{k} := (n - m - 1, -j)$ with $j \in \mathbb{N}$. The normal form \mathcal{U} of \mathcal{F} is obtained by iteratively using the Taylor series of Eqs. (3.69), (3.72), and (3.73) with the functional Eq. (3.71). An explicit example for this procedure is given in Appendix B.3.

Non-resonant normal form

If $\omega/(2\pi)$ is irrational the equation $\boldsymbol{\omega} \cdot \mathbf{k} = 0$ is only satisfied for $\mathbf{k} = (0, 0)$. Hence, only monomials with $n = m + 1$ contribute to the normal form which allows us to write the mapping \mathcal{U} as

$$\mathcal{U} = u(\xi \xi^*) \xi. \quad (3.76)$$

By further including the symplectic character of \mathcal{U} it can be shown [90] that it simplifies to

$$\mathcal{U} = e^{i\Omega(\xi \xi^*)} \xi \quad (3.77)$$

with the real function $\Omega(\xi \xi^*)$. Hence, the non-resonant normal form is an amplitude-dependent rotation with a nonlinear frequency $\Omega(\xi \xi^*)$.

By evaluating the Hamiltonian flux a time-independent Hamilton function can be determined which interpolates the dynamics of \mathcal{U} and depends only on the monomials $(\xi \xi^*)^n$

$$H_{\text{reg}}(\xi \xi^*) = i\omega \xi \xi^* + i \sum_{n=1}^{(N-1)/2} \frac{\Omega_{2n}}{n+1} (\xi \xi^*)^{n+1} \quad (3.78)$$

where N specifies the maximal order of the expansion in ξ .

Resonant normal form

If $\omega/(2\pi) = s/r$ is rational the equation $\boldsymbol{\omega} \cdot \mathbf{k} = 0$ is satisfied for $n = m + 1 + rl$ with $j = ls$, $l \in \mathbb{Z}$. Hence, more monomials contribute to the normal form than in the non-resonant case. For the mapping \mathcal{U} we find

$$U(\xi, \xi^*) = \sum_{n=0}^{\infty} (\xi \xi^*)^n \left[\sum_{l=0}^{\infty} u_{n,l}^{(+)} \xi^{rl+1} + \sum_{l=1}^{\infty} u_{n,l}^{(-)} \xi^{*rl-1} \right] \quad (3.79)$$

where $u_{n,l}^{(+)}$ and $u_{n,l}^{(-)}$ are the expansion coefficients of \mathcal{U} .

For the time-independent Hamilton function which interpolates the dynamics of \mathcal{U} we obtain up to order $N = r$

$$H_{\text{reg}}(\xi, \xi^*) = i\omega\xi\xi^* + i \sum_{n=1}^{(r-1)/2} \frac{\Omega_{2n}}{n+1} (\xi\xi^*)^{n+1} + \frac{e^{-i\omega}u_{0,r-1}}{r}\xi^{*r} - \frac{e^{i\omega}u_{0,r-1}^*}{r}\xi^r. \quad (3.80)$$

It is identical to the non-resonant Hamilton function up to order $r - 1$. Beyond, further corrections are necessary to describe the influence of the resonant behavior.

In addition the quasi-resonant normal form is considered where $\omega/(2\pi)$ is irrational but close to a rational number $\omega/(2\pi) - s/r = \epsilon \ll 1$ of low order r . The analysis can then be performed as in the resonant case such that the quasi-resonant behavior is accounted for.

As for the Lie transformation above, we now want to compare the dynamics of the time-independent integrable Hamilton function H_{reg} , obtained by the normal-form analysis, with the regular dynamics of the original system H with a mixed phase space. Fig. 3.12 shows such a

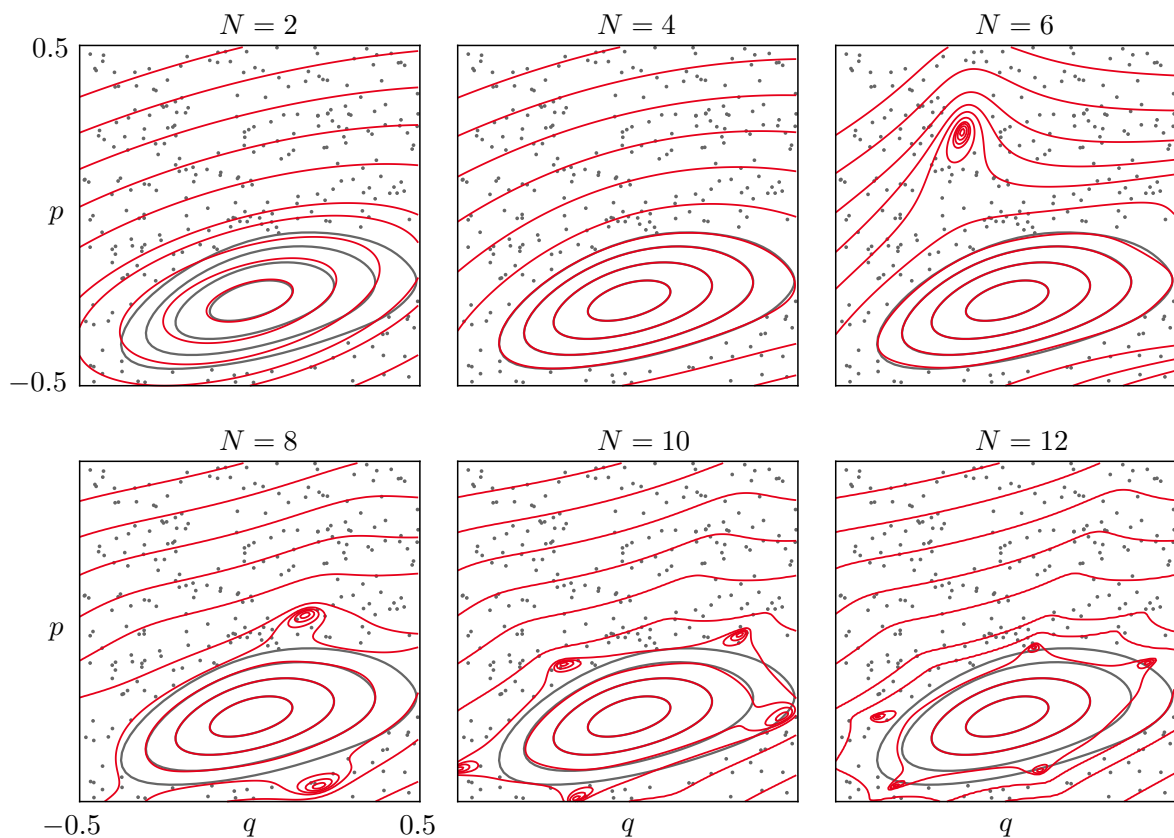


Figure 3.12: Comparison of the mixed phase space of the system \mathcal{F}_1 (gray lines and dots) and the dynamics of the one-dimensional time-independent Hamilton function obtained by the normal-form analysis (red lines) under variation of its maximal order N . We choose for the parameters $r_1 = 0.481$, $R = 0.5$, $Z = 0$, $\varepsilon = 0.005$. Up to order $N = 4$ we find convergence while for larger N resonance structures appear in the integrable approximation and move towards the center of the island.

comparison for the systems \mathcal{F}_1 with increasing order N of the normal-form analysis in the non-resonant case. We find that already at $N = 4$ a good approximation of the original dynamics is found within the regular island. However, for larger orders N resonance structures appear which are not present in the original mapping \mathcal{F} which leads to deviations between the original dynamics of H and that of H_{reg} . By comparing the dynamics of the regular systems H_{reg} obtained using the Lie transformation or the normal-form analysis we find that the result of the Lie transformation at $N \leq 8$ reproduces the original dynamics of H with a higher accuracy than the normal form analysis at any order N . If applicable it should be preferred. However, the procedure of the normal-form analysis gives insight into the structure of the considered mapping and determines a Hamilton function H_{reg} of particularly simple form as it depends on the terms $\xi\xi^*$ only. This provides advantages for its quantization. Using the quantum normal-form analysis [91, 92] might improve the accuracy of the results and should be an alternative to be considered in the future.

Method based on the frequency map analysis

Up to this point we have studied the Lie transformation which determines an accurate regular approximation H_{reg} of the original system H with a mixed phase space if its nonlinearity is small enough. Additionally, we have considered the normal-form analysis which diverges rather quickly with increasing order. For systems with a strong nonlinearity and many occurring nonlinear resonances these two approaches may fail. Hence, we propose a new method which is based on the frequency map analysis [84, 85].

The frequency map analysis is suited to study the regular dynamics of a kicked system. As mentioned in Section 3.1.2 it can be used to determine the rotation number w_r of a quasi-periodic orbit. In addition it allows a reconstruction of the given orbit and its interpolation to non-integer times. It uses the given points of a regular orbit (q_t, p_t) with $t \in \mathbb{N}$ and expands them into a Fourier series

$$z_t := q_t + ip_t = \sum_{k=-N/2}^{N/2-1} A_k e^{i\phi_k} e^{2\pi i k w_r t}. \quad (3.81)$$

The real parameters A_k , ϕ_k , and the rotation number w_r can be determined using the iterates (q_t, p_t) . If all coefficients are determined up to the maximal order N , Eq. (3.81) interpolates the given orbit for all $t \in \mathbb{R}$. A remarkable feature of the frequency map analysis is its fast convergence. Even 1000 iterations are sufficient to determine the rotation number of this orbit with double precision. In case of close-by nonlinear resonances, however, its results are not trustworthy.

We now consider a mapping \mathcal{F} with a regular island which has a stable fixed point in its center at (q^*, p^*) . We define a straight line $u \mapsto [q(u), p(u)]$ from the center of the regular island

to its border with the chaotic sea, such that the enclosed area A of the orbits started on this line increases with increasing u and compute the expansion coefficients $A_k(u)$, $\phi_k(u)$, and the rotation number $w_r(u)$. These functions are continuous if we are not too close to a resonance. They can be numerically interpolated and expressed as a power series in u . One possible choice of the straight line is given by $u \mapsto [q^* + u, p^*]$. Fig. 3.13 shows the rotation number $w_r(u)$ and its extrapolation beyond the border of the regular island.

The area enclosed by a quasi-periodic orbit with initial condition $[q(u), p(u)]$ is given by

$$A(u) = \pi \sum_{k=-\infty}^{\infty} k A_k(u)^2. \quad (3.82)$$

From this enclosed area and the rotation number $w_r(u)$ we can determine an energy associated with this orbit as derived in Appendix C.1

$$E(u) = \int_0^u \frac{dA(u')}{du'} w_r(u') du'. \quad (3.83)$$

With this equation we assign an energy E to each point (q, p) inside the regular island of the phase space. To obtain the regular system $H_{\text{reg}}(q, p)$ for the whole phase space this function $E(q, p)$ has to be extrapolated into the chaotic sea of H . This is done by expanding the numerically determined triples $(q_t(u), p_t(u), E(u))$ in a two-dimensional Fourier series. The Fourier coefficients c_{mn} of this series are the solution of the corresponding least-squares minimization with the given numerical data. As the final result we obtain a one-dimensional time-independent Hamilton function $H_{\text{reg}}(q, p)$ which interpolates the regular dynamics of H and extends it into the chaotic sea

$$H_{\text{reg}}(q, p) = \sum_{m, n=-N/2}^{N/2-1} c_{mn} \exp \left(2\pi i \left[m \frac{q}{l_q} + n \frac{p}{l_p} \right] \right) \quad (3.84)$$

where l_q and l_p determine the periodicities in q and p -direction, respectively. The order of the expansion is given by N .

Again we want to study the agreement of the dynamics induced by the regular system H_{reg} and the mixed system H in its regular region. While for small orders N of the expansion large deviations occur, they decrease with increasing order N . However, for large N the continuation into the chaotic sea becomes questionable. We find strongly oscillating behavior due to the higher harmonics in the Fourier series. If we assume that a smooth continuation of the regular dynamics to the chaotic sea is aspired, we have to find a compromise between good agreement inside the regular region and the smooth continuation to the chaotic sea. Fig. 3.14 shows the comparison of the dynamics of H and H_{reg} for two different orders N . Furthermore, the

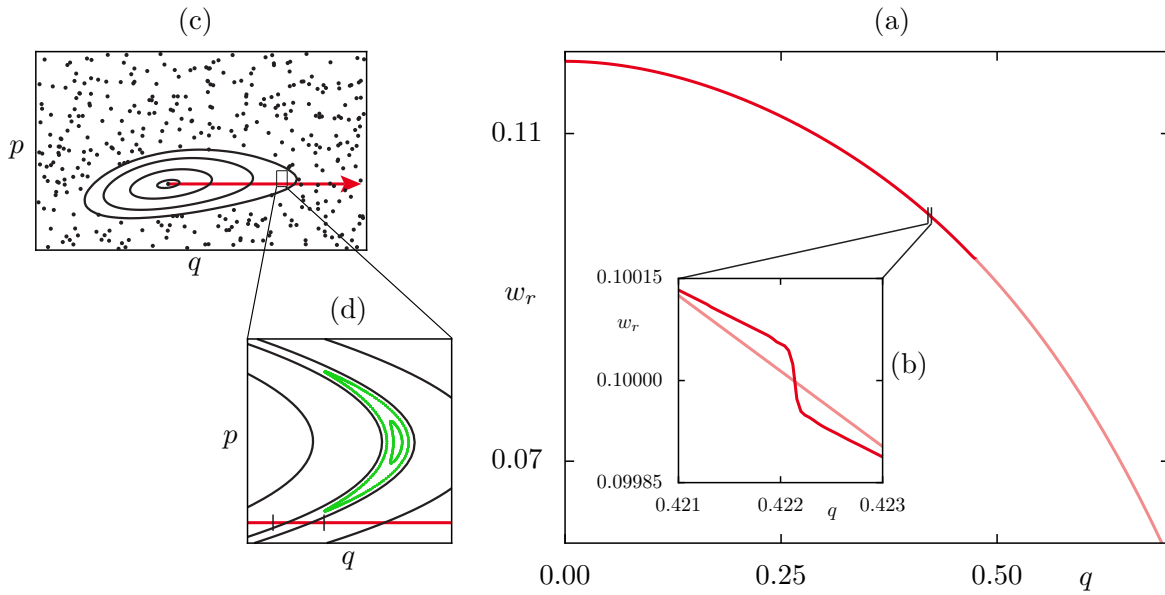


Figure 3.13: As in Fig. 3.7 the rotation number w_r is shown for orbits started on the line (q, p^*) for the system \mathcal{F}_1 with parameters $r_1 = 0.266$, $R = 0.4$, $Z = 0$, and $\varepsilon = 0.005$ (red line). Here we extrapolate w_r into the chaotic region (rose line) and interpolate the exceptional behavior of w_r at rational frequencies, see (b). In (c) the mixed phase space is shown with the red line of initial conditions. In (d) we magnify a region in which a 10:1 resonance (green lines) with $w_r = 1/10$ appears. The rotation numbers in this region are shown in (b).

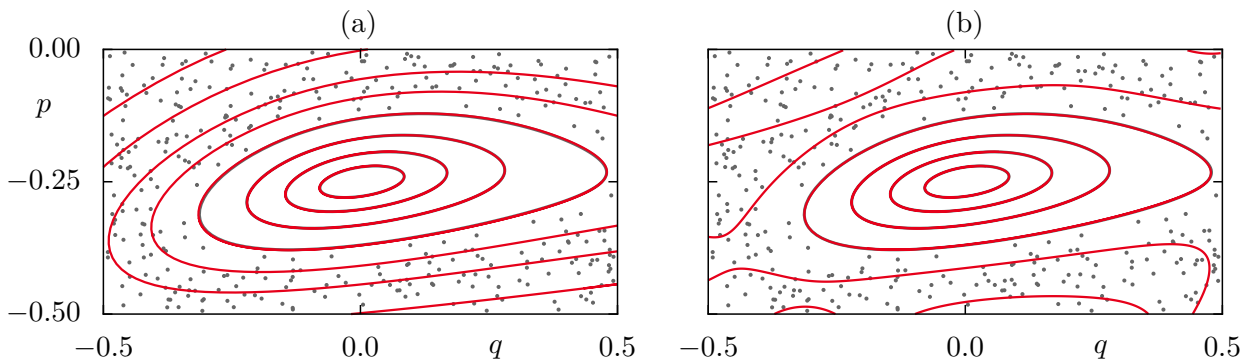


Figure 3.14: Comparison of the mixed phase space of the system \mathcal{F}_1 (gray lines and dots) and the dynamics of the one-dimensional time-independent Hamilton function obtained by the frequency-map analysis (red lines) under variation of its maximal order N . We choose the parameters $r_1 = 0.266$, $R = 0.4$, $Z = 0$, $\varepsilon = 0.005$. For $N = 5$ (a) we find agreement in the regular island and a smooth continuation of the dynamics of H_{reg} to the chaotic sea while for $N = 9$ (b) this continuation shows unphysical oscillations.

parameters l_q and l_p have to be chosen appropriately. We find that for this example $N = 5$ is a good choice while the continuation of H_{reg} into the chaotic sea is changed for $N = 9$.

Compared to the Lie transformation or the normal-form analysis this method involves more parameters such as N , l_q , l_p which have to be chosen to some extent by trial and error until a good regular approximation is found. Nevertheless, this method can be used for any kicked system independent of its nonlinearity or appearing resonance chains which makes it more flexible than the Lie transformation or the normal-form analysis.

3.1.4 Quantization

After discussing the classical properties of kicked maps we consider the corresponding quantum systems in order to study quantum effects such as dynamical tunneling which is the focus of this thesis. A quantum state $|\psi\rangle$ is given by a normalized vector in a Hilbert space \mathcal{H} . Non-relativistically its time-evolution is described by the time-dependent Schrödinger equation

$$i\hbar_{\text{eff}}\frac{\partial}{\partial t}|\psi(t)\rangle = \hat{H}|\psi(t)\rangle \quad (3.85)$$

where \hat{H} is the Hamilton operator which for the case of our kicked systems is time periodic, $\hat{H}(t+1) = \hat{H}(t)$. The unitary time-evolution operator $\hat{U}(t, t_0)$ maps the state $|\psi(t_0)\rangle$ at time t_0 to the state $|\psi(t)\rangle$ which has evolved from $|\psi(t_0)\rangle$ using Eq. (3.85) at time t

$$|\psi(t)\rangle = \hat{U}(t, t_0)|\psi(t_0)\rangle \quad \text{with} \quad \hat{U}(t, t_0) := \hat{O} \exp\left(-\frac{i}{\hbar_{\text{eff}}} \int_{t_0}^t \hat{H}(t') dt'\right) \quad (3.86)$$

where \hat{O} is the time-ordering operator. For kicked systems with the Hamiltonian

$$\hat{H}(\hat{q}, \hat{p}, t) = T(\hat{p}) + V(\hat{q}) \sum_{n \in \mathbb{Z}} \delta(t - n) \quad (3.87)$$

the following semi-group property of the time-evolution operator is useful to derive $\hat{U}(t, t_0)$

$$\hat{U}(t, t_0) = \hat{U}(t, t_1) \hat{U}(t_1, t_0), \quad \forall t_1 \in \mathbb{R}. \quad (3.88)$$

We are especially interested in the time evolution of a state after one period of the external driving in analogy to the classical stroboscopic mapping [93]. If this mapping is obtained by evaluating the kicked system just after each kick, as in Eq. (3.8), in each time period first the free evolution takes place and subsequently the kick appears. The time-evolution operator

$\hat{U}(1, 0)$ with $t = 1$ and $t_0 = 0$ can be decomposed into two parts

$$\hat{U} := \hat{U}(1, 0) = \lim_{\delta \rightarrow 0} \hat{U}(1 + \delta, 1 - \delta) \hat{U}(1 - \delta, \delta) \quad (3.89)$$

$$= \lim_{\delta \rightarrow 0} \hat{O} \exp \left(-\frac{i}{\hbar_{\text{eff}}} \int_{1-\delta}^{1+\delta} \hat{H}(\hat{q}, \hat{p}, t) dt \right) \hat{O} \exp \left(-\frac{i}{\hbar_{\text{eff}}} \int_{\delta}^{1-\delta} \hat{H}(\hat{q}, \hat{p}, t) dt \right) \quad (3.90)$$

$$= \lim_{\delta \rightarrow 0} \exp \left(-\frac{i}{\hbar_{\text{eff}}} [V(\hat{q}) + 2\delta T(\hat{p})] \right) \exp \left(-\frac{i}{\hbar_{\text{eff}}} T(\hat{p}) [1 - 2\delta] \right) \quad (3.91)$$

$$= \exp \left(-\frac{i}{\hbar_{\text{eff}}} V(\hat{q}) \right) \exp \left(-\frac{i}{\hbar_{\text{eff}}} T(\hat{p}) \right) \quad (3.92)$$

$$= \hat{U}_V \hat{U}_T. \quad (3.93)$$

It is decomposed into two unitary operators: The free evolution is given by \hat{U}_T and the action of the kick by \hat{U}_V . It is most remarkable that each of the operators \hat{q} and \hat{p} appears in one of these two contributions only, which makes the quantization particularly easy. Note that the split-operator method is exact here.

Periodicity conditions

We want to consider the effect of a kinetic energy $T(p)$ and potential energy $V(q)$, which are chosen such that $e^{-iT(p)/\hbar_{\text{eff}}}$ and $e^{-iV(q)/\hbar_{\text{eff}}}$ are periodic functions, onto the quantum system following Ref. [94]. It will allow to describe the quantum dynamics on the torus where also the classical map is defined. The translation operator in phase space is given by

$$\hat{T}(q, p) = e^{\frac{i}{\hbar_{\text{eff}}} (p\hat{q} - q\hat{p})}. \quad (3.94)$$

It shifts the phase space coordinates by q in position and by p in momentum direction. Using the operator identities

$$e^{\hat{A}} e^{\hat{B}} = e^{\hat{A} + \hat{B}} e^{\frac{1}{2}[\hat{A}, \hat{B}]}, \quad (3.95)$$

$$e^{\hat{A}} e^{\hat{B}} = e^{\hat{B}} e^{\hat{A}} e^{[\hat{A}, \hat{B}]}, \quad (3.96)$$

which are valid if $[\hat{A}, [\hat{A}, \hat{B}]] = 0$ and $[\hat{B}, [\hat{A}, \hat{B}]] = 0$ are fulfilled, Eq. (3.94) can be rewritten as

$$\hat{T}(q, p) = e^{-\frac{i}{2\hbar_{\text{eff}}} qp} e^{\frac{i}{\hbar_{\text{eff}}} p\hat{q}} e^{-\frac{i}{\hbar_{\text{eff}}} q\hat{p}} \quad (3.97)$$

$$= e^{-\frac{i}{2\hbar_{\text{eff}}} qp} \hat{T}(0, p) \hat{T}(q, 0) \quad (3.98)$$

$$= e^{\frac{i}{2\hbar_{\text{eff}}} qp} e^{-\frac{i}{\hbar_{\text{eff}}} q\hat{p}} e^{\frac{i}{\hbar_{\text{eff}}} p\hat{q}} \quad (3.99)$$

$$= e^{\frac{i}{2\hbar_{\text{eff}}} qp} \hat{T}(q, 0) \hat{T}(0, p). \quad (3.100)$$

The expression $\hat{T}(\delta, 0)|q\rangle$ can be evaluated using $\hat{q}|q\rangle = q|q\rangle$ and $[\hat{q}, f(\hat{p})] = i\hbar_{\text{eff}}f'(\hat{p})$

$$\begin{aligned}
\hat{q}\hat{T}(\delta, 0)|q\rangle &= \hat{q}e^{-\frac{i}{\hbar_{\text{eff}}}\delta\hat{p}}|q\rangle \\
&= e^{-\frac{i}{\hbar_{\text{eff}}}\delta\hat{p}}\hat{q}|q\rangle + i\hbar_{\text{eff}}\left(-\frac{i}{\hbar_{\text{eff}}}\right)\delta e^{-\frac{i}{\hbar_{\text{eff}}}\delta\hat{p}}|q\rangle \\
&= \hat{T}(\delta, 0)\hat{q}|q\rangle + \delta\hat{T}(\delta, 0)|q\rangle \\
&= (q + \delta)\hat{T}(\delta, 0)|q\rangle
\end{aligned} \tag{3.101}$$

where $\hat{T}(\delta, 0)|q\rangle$ is an eigenvector of \hat{q} with eigenvalue $q + \delta$ such that

$$\hat{T}(\delta, 0)|q\rangle = |q + \delta\rangle. \tag{3.102}$$

Using Eq. (3.94) we find

$$\langle q|\hat{T}(\delta, 0) = \langle q - \delta|. \tag{3.103}$$

With the relations $[\hat{p}, g(\hat{q})] = -i\hbar_{\text{eff}}g'(\hat{q})$ and $\hat{p}|p\rangle = p|p\rangle$ also the translation of β in momentum direction can be evaluated

$$\begin{aligned}
\hat{p}\hat{T}(0, \beta)|p\rangle &= \hat{p}e^{\frac{i}{\hbar_{\text{eff}}}\beta\hat{q}}|p\rangle \\
&= e^{\frac{i}{\hbar_{\text{eff}}}\beta\hat{q}}\hat{p}|p\rangle - i\hbar_{\text{eff}}\frac{i}{\hbar_{\text{eff}}}\beta e^{\frac{i}{\hbar_{\text{eff}}}\beta\hat{q}}|p\rangle \\
&= \hat{T}(0, \beta)\hat{p}|p\rangle + \beta\hat{T}(0, \beta)|p\rangle \\
&= (p + \beta)\hat{T}(0, \beta)|p\rangle
\end{aligned} \tag{3.104}$$

where $\hat{T}(0, \beta)|p\rangle$ is an eigenvector of \hat{p} with eigenvalue $p + \beta$ such that

$$\hat{T}(0, \beta)|p\rangle = |p + \beta\rangle. \tag{3.105}$$

Using Eq. (3.94) we find

$$\langle p|\hat{T}(0, \beta) = \langle p - \beta|. \tag{3.106}$$

The mappings presented in Section 3.1.2 are periodic in position and momentum direction with the periodicities M_q and M_p . Hence, in analogy to the Bloch theorem [95] we find for all wave functions $|\psi\rangle$

$$\langle q + M_q|\psi\rangle = e^{2\pi i\theta_q}\langle q|\psi\rangle, \tag{3.107}$$

$$\langle p + M_p|\psi\rangle = e^{-2\pi i\theta_p}\langle p|\psi\rangle \tag{3.108}$$

with the Bloch phases θ_q and θ_p . The choice of the sign in the exponents of Eqs. (3.107) and

(3.108) will be discussed below. If we use $\delta = M_q$ in Eq. (3.102) we find

$$|q + M_q\rangle = \hat{T}(M_q, 0) |q\rangle \quad (3.109)$$

and therefore

$$\langle q + M_q| = \langle q| \hat{T}^\dagger(M_q, 0). \quad (3.110)$$

It follows

$$\begin{aligned} \langle q + M_q| \psi\rangle &= \langle q| \hat{T}^\dagger(M_q, 0) |\psi\rangle \\ &\stackrel{(3.107)}{=} e^{2\pi i \theta_q} \langle q| \psi\rangle. \end{aligned} \quad (3.111)$$

Equation (3.111) is valid for arbitrary $\langle q|$. Thus we find

$$\hat{T}^\dagger(M_q, 0) |\psi\rangle = e^{2\pi i \theta_q} |\psi\rangle, \quad (3.112)$$

$$\hat{T}(M_q, 0) |\psi\rangle = e^{-2\pi i \theta_q} |\psi\rangle. \quad (3.113)$$

In analogy it is obtained

$$|p + M_p\rangle = \hat{T}(0, M_p) |p\rangle \quad (3.114)$$

by using $\beta = M_p$ in Eq. (3.105). We find

$$\langle p + M_p| = \langle p| \hat{T}^\dagger(0, M_p), \quad (3.115)$$

and

$$\begin{aligned} \langle p + M_p| \psi\rangle &= \langle p| \hat{T}^\dagger(0, M_p) |\psi\rangle \\ &\stackrel{(3.108)}{=} e^{-2\pi i \theta_p} \langle p| \psi\rangle. \end{aligned} \quad (3.116)$$

Equation (3.116) is valid for arbitrary $\langle p|$ and we obtain

$$\hat{T}^\dagger(0, M_p) |\psi\rangle = e^{-2\pi i \theta_p} |\psi\rangle, \quad (3.117)$$

$$\hat{T}(0, M_p) |\psi\rangle = e^{2\pi i \theta_p} |\psi\rangle. \quad (3.118)$$

We will now separately consider the consequences of the quasi-periodicity in position and momentum direction.

Quasi periodicity in position and momentum

We have

$$\begin{aligned}
e^{-2\pi i\theta_q} e^{2\pi i\theta_p} |\psi\rangle &\stackrel{(3.118)}{=} e^{-2\pi i\theta_q} \hat{T}(0, M_p) |\psi\rangle \\
&= \hat{T}(0, M_p) e^{-2\pi i\theta_q} |\psi\rangle \\
&\stackrel{(3.113)}{=} \hat{T}(0, M_p) \hat{T}(M_q, 0) |\psi\rangle \\
&\stackrel{(3.98),(3.100)}{=} e^{\frac{i}{\hbar_{\text{eff}}} M_q M_p} \hat{T}(M_q, 0) \hat{T}(0, M_p) |\psi\rangle \\
&\stackrel{(3.118)}{=} e^{\frac{2\pi i}{\hbar_{\text{eff}}} M_q M_p} \hat{T}(M_q, 0) e^{2\pi i\theta_p} |\psi\rangle \\
&= e^{2\pi i \frac{M_q M_p}{\hbar_{\text{eff}}}} e^{2\pi i\theta_p} \hat{T}(M_q, 0) |\psi\rangle \\
&\stackrel{(3.113)}{=} e^{2\pi i \frac{M_q M_p}{\hbar_{\text{eff}}}} e^{2\pi i\theta_p} e^{-i2\pi\theta_q} |\psi\rangle. \tag{3.119}
\end{aligned}$$

By equating the first and the last term in Eq. (3.119) with $\hbar_{\text{eff}} > 0$ it results

$$\frac{M_q M_p}{\hbar_{\text{eff}}} = N \quad \text{with } N \in \mathbb{N}, \tag{3.120}$$

and thus

$$\hbar_{\text{eff}} = \frac{M_q M_p}{2\pi N}. \tag{3.121}$$

The quasi-periodicity in position and momentum leads to an effective Planck constant \hbar_{eff} which is allowed to take only discrete values.

Quasi periodicity in position

Using Eq. (3.112) we find

$$\begin{aligned}
\langle p | \hat{T}^\dagger(M_q, 0) | \psi \rangle &= \langle \hat{T}(M_q, 0) p | \psi \rangle \\
&= \langle e^{-\frac{i}{\hbar_{\text{eff}}} M_q \hat{p}} p | \psi \rangle \\
&= e^{\frac{i}{\hbar_{\text{eff}}} M_q p} \langle p | \psi \rangle \\
&\stackrel{(3.112)}{=} e^{2\pi i\theta_q} \langle p | \psi \rangle \tag{3.122}
\end{aligned}$$

which leads to

$$e^{\frac{i}{\hbar_{\text{eff}}} M_q p} = e^{2\pi i\theta_q} e^{2\pi i m} \quad \text{with } m \in \mathbb{Z}. \tag{3.123}$$

The possible values of \hbar_{eff} given by Eq. (3.121) cause the discreteness of the momentum: $p \rightarrow p_m$

$$p_m = \frac{M_p}{N}(m + \theta_q) \quad \text{with } m = 0, \dots, N - 1. \quad (3.124)$$

Hence, the quasi-periodicity in position causes the discreteness of the momentum.

Quasi periodicity in momentum

Using (3.117) we find

$$\begin{aligned} \langle q | \hat{T}^\dagger(0, M_p) | \psi \rangle &= \langle \hat{T}(0, M_p) q | \psi \rangle \\ &= \langle e^{\frac{i}{\hbar_{\text{eff}}} M_p \hat{q}} q | \psi \rangle \\ &= e^{-\frac{i}{\hbar_{\text{eff}}} M_p q} \langle q | \psi \rangle \\ &\stackrel{(3.117)}{=} e^{-2\pi i \theta_p} \langle q | \psi \rangle \end{aligned} \quad (3.125)$$

which leads to

$$e^{\frac{i}{\hbar_{\text{eff}}} M_p q} = e^{2\pi i \theta_p} e^{2\pi i n} \quad \text{with } n \in \mathbb{Z}. \quad (3.126)$$

The possible values of \hbar_{eff} given by Eq. (3.121) cause the discreteness of the position: $q \rightarrow q_n$

$$q_n = \frac{M_q}{N}(n + \theta_p) \quad \text{with } n = 0, \dots, N - 1. \quad (3.127)$$

Hence, the quasi-periodicity in momentum causes the discreteness of the position variable. The signs of the exponents in Eqs. (3.107) and (3.108) are chosen such that in Eqs. (3.124) and (3.127) the phases θ_q and θ_p appear additive.

Time-evolution operator in position representation

We want to evaluate the time-evolution operator in position representation such that its eigenfunctions and eigenvalues can be calculated [96]. As previously shown the Hilbert space \mathcal{H} has a finite dimension N due to the quasi-periodicity of the kinetic and potential energy. Let $\{|q_k\rangle\}$ and $\{|p_n\rangle\}$, $k, n = 0, \dots, N - 1$, be the discrete and complete eigenvectors of the position and momentum operator, respectively. They are related by the Fourier transformation \mathcal{F}_t

$$\langle q_k | p_l \rangle = \sum_{j=0}^{N-1} (\mathcal{F}_t^{-1})_{j,l} \langle q_k | q_j \rangle = \frac{1}{\sqrt{N}} e^{\frac{2\pi i}{N}(k+\theta_p)(l+\theta_q)}. \quad (3.128)$$

Using this relation and Eqs. (3.127) and (3.124) the time evolution operator \hat{U} can be explicitly evaluated in position representation

$$U_{k,n} := \langle q_k | \hat{U} | q_n \rangle = \langle q_k | \hat{U}_V \hat{U}_T | q_n \rangle \quad (3.129)$$

$$= \sum_{i=0}^{N-1} \sum_{l=0}^{N-1} \langle q_k | \hat{U}_V | q_i \rangle \langle q_i | \hat{U}_T | p_l \rangle \langle p_l | q_n \rangle \quad (3.130)$$

$$= \frac{1}{N} e^{-\frac{i}{\hbar_{\text{eff}}} V(q_k)} \sum_{l=0}^{N-1} e^{\frac{2\pi i}{N} (k-n)(l+\theta_q)} e^{-\frac{i}{\hbar_{\text{eff}}} T(p_l)}. \quad (3.131)$$

If the considered kicked system is defined on a torus $[q_{\min}, q_{\min} + M_q) \times [p_{\min}, p_{\min} + M_p)$ where q_{\min} and p_{\min} are not equal to zero, Eq. (3.129) has to be modified. The modified position and momentum lattices read

$$q_k = \frac{M_q}{N} (k + n_q^{(0)} + \theta_p), \quad k = 0, \dots, N-1, \quad (3.132)$$

$$p_l = \frac{M_p}{N} (l + n_p^{(0)} + \theta_q), \quad l = 0, \dots, N-1 \quad (3.133)$$

where $n_q^{(0)} = \lceil Nq_{\min}/M_q - \theta_p \rceil$, $n_p^{(0)} = \lceil Np_{\min}/M_p - \theta_q \rceil$, and $\lceil x \rceil$ denotes the smallest integer number larger or equal x . Hence, the parameters $n_q^{(0)}$ and $n_p^{(0)}$ shift the position and momentum lattices by multiples of the lattice spacing according to q_{\min} and p_{\min} . They are introduced such that k and l take values from 0 to $N-1$. For the time evolution operator in position representation we finally obtain

$$U_{k,n} = \frac{1}{N} e^{-\frac{i}{\hbar_{\text{eff}}} V(q_k)} \sum_{l=0}^{N-1} e^{\frac{2\pi i}{N} (k-n)(l+n_p^{(0)}+\theta_q)} e^{-\frac{i}{\hbar_{\text{eff}}} T(p_l)} \quad \text{with} \quad (3.134)$$

$$\langle q_k | p_l \rangle = \frac{1}{\sqrt{N}} e^{\frac{2\pi i}{N} (k+n_q^{(0)}+\theta_p)(l+n_p^{(0)}+\theta_q)}. \quad (3.135)$$

Due to the quasi-periodicity in position and momentum direction $U_{k,n}$ has to satisfy $U_{k,n} = U_{k+N,n+N}$. Note that $V(q)$ and $T(p)$ do not have to be periodic. It is sufficient that the exponentiated functions $\exp(-iV(q)/\hbar_{\text{eff}})$ and $\exp(-iT(p)/\hbar_{\text{eff}})$ show these periodicities with the periods M_q and M_p as required in the derivations performed in the last section. These conditions may lead to restrictions in choosing the phases θ_q , θ_p , or the effective Planck constant \hbar_{eff} as presented below.

Restrictions for the example systems

Example system \mathcal{F}_1

The kinetic energy $T(p)$ of the system \mathcal{F}_1 is not periodic with the period $M_p = 1$. We find $\Delta T = T(p_l) - T(p_{l+N}) = 1/2$ with $T'(p) = T'(p+1)$. Hence, the quasi-periodicity condition

for $T(p)$ is only satisfied if

$$e^{-\frac{i}{\hbar_{\text{eff}}}T(p_l)} = e^{-\frac{i}{\hbar_{\text{eff}}}T(p_{l+N})} = e^{-\frac{i}{\hbar_{\text{eff}}}T(p_l)} e^{\frac{i}{\hbar_{\text{eff}}}\Delta T} \quad (3.136)$$

and therefore

$$\frac{\Delta T}{\hbar_{\text{eff}}} = 2\pi j, \quad j \in \mathbb{Z}. \quad (3.137)$$

This requirement leads to a restriction of the allowed values of \hbar_{eff} and thus the dimension N of Hilbert space

$$\frac{\Delta T N}{M_q} = \frac{N}{2M_q} \in \mathbb{N}. \quad (3.138)$$

The ratio N/M_q has to be an even number which for $M_q = 1$ requires an even dimension N of the Hilbert space.

Example system \mathcal{F}_2

The kinetic energy $V(q)$ of the system \mathcal{F}_2 is not periodic with the period M_q . We have to fulfill

$$e^{-\frac{i}{\hbar_{\text{eff}}}V(q_k)} = e^{-\frac{i}{\hbar_{\text{eff}}}V(q_{k+N})}, \quad \text{with} \quad q_k = \frac{M_q}{N}(k + n_q^{(0)} + \theta_p). \quad (3.139)$$

From Eq. (3.40) we find for the potential energy

$$V(q) = -\frac{k^2}{2} - k\tilde{q} + \mathcal{V}(\tilde{q}) \quad \text{with} \quad q = k + \tilde{q}. \quad (3.140)$$

It consists of a contribution depending on the unit cell k described by the first two terms in Eq. (3.140) and the k -independent term $\mathcal{V}(\tilde{q})$. Hence, we find

$$V(q_{k+N}) - V(q_k) = V(q_k + M_q) - V(q_k) = -\frac{M_q^2}{2} - q_k M_q. \quad (3.141)$$

Using this expression in Eq. (3.134) we obtain

$$e^{i\pi N M_q} e^{2\pi i M_q \theta_p} = 1 \quad (3.142)$$

which restricts the possible phases θ_p in dependence of N and M_q

$$\theta_p = \begin{cases} \frac{l}{M_q} & \text{for } N \text{ even and } N \text{ odd, } M_q \text{ even} \\ \frac{2l+1}{2M_q} & \text{for } N \text{ odd and } M_q \text{ odd} \end{cases} \quad (3.143)$$

with $l = 0, \dots, M_q - 1$. These restrictions for the phase θ_p can also be derived with an approach based on the classical dynamics of the map, see Ref. [97].

Eigenvalues, eigenvectors, and quasimodes

The eigenvalues and eigenvectors of \hat{U} are determined by the eigenequation

$$\hat{U}|\psi_n\rangle = e^{-\frac{i}{\hbar_{\text{eff}}}\varepsilon_n}|\psi_n\rangle = e^{i\varphi_n}|\psi_n\rangle \quad (3.144)$$

where $|\psi_n\rangle$ are the eigenvectors, ε_n denote the quasi-energies, and φ_n the eigenphases which we will also refer to as quasi-energies. As \hat{U} is unitary the eigenvalues $z_n = e^{i\varphi_n}$ lie on the unit circle, $|z_n| = 1$. According to the semiclassical eigenfunction hypothesis [20–22] we expect that semiclassically the eigenvectors $|\psi_n\rangle$ are localized in those phase-space regions which a typical classical orbit explores in the long-time limit. Hence, for our example systems they will be located either in the regular island or in the chaotic sea. However, as these two regions of different dynamics are quantum mechanically coupled the eigenvectors $|\psi_n\rangle$ will always have a contribution in the other region of phase space which is typically small. Those eigenstates of \hat{U} which have a dominant contribution in the regular island are called regular states $|\psi_m\rangle$ labelled by the quantum number $m = 0, \dots, m_{\text{max}}$. The others are called chaotic. The regular states are mainly localized on a classical torus inside the regular island which according to the Bohr-Sommerfeld quantization (see Section 2.2) includes an area

$$A_m = h_{\text{eff}} \left(m + \frac{1}{2} \right). \quad (3.145)$$

If A denotes the area of the regular island in phase space there will exist $m_{\text{max}} = \lfloor A/h_{\text{eff}} - 1/2 \rfloor$ regular states with quantum number $m = 0, \dots, m_{\text{max}}$. Their quasi-energy can be semiclassically predicted [98] if the regular region is not transporting

$$\varphi_m = 2\pi w_{r, \mathcal{C}_m} \left(m + \frac{1}{2} \right) - 2\pi N (\langle T \rangle_{\mathcal{C}_m} - \langle V \rangle_{\mathcal{C}_m}), \quad (3.146)$$

where w_{r, \mathcal{C}_m} is the rotation number of the m th quantized torus \mathcal{C}_m and $\langle T \rangle_{\mathcal{C}_m}$, $\langle V \rangle_{\mathcal{C}_m}$ denote the average of the kinetic and potential energy on this torus. Note that situations may occur such that less than m_{max} regular states exist. This phenomena is called flooding of regular states and has been discussed in Refs. [86, 87] in detail. However, for the examples considered in this thesis it is not relevant.

The regular eigenstates $|\psi_m\rangle$ of \hat{U} can be approximated by semiclassical regular states $|\psi_{\text{reg}}^m\rangle$ which only have an exponentially decreasing contribution in the chaotic sea. They are also called quasimodes. The error δ of each quasimode is determined by $\|\hat{U}|\psi_{\text{reg}}^m\rangle - z_m|\psi_{\text{reg}}^m\rangle\| = \delta$ with $\langle \psi_{\text{reg}}^m | \psi_{\text{reg}}^m \rangle = 1$ [99]. For $|\psi_{\text{reg}}^m\rangle = |\psi_m\rangle$ this error is zero. The construction of such quasimodes is a difficult task for general kicked systems. One possibility is to find an integrable system H_{reg} which interpolates the regular dynamics of the island. Semiclassical eigenstates of this system can be determined and used as quasimodes. This procedure is discussed in Section 3.1.3. For

mappings with an harmonic oscillator-like regular island such as the system \mathcal{F}_1 and \mathcal{F}_2 with $R = Z = 0$, however, the eigenfunctions of the harmonic oscillator can be used. By rotating and squeezing they can be adjusted to the regular island [94]. Finally we find

$$\psi_{\text{reg}}^m(q) = \frac{1}{\sqrt{2^m m!}} \left(\frac{\text{Re}(\sigma)}{\pi \hbar_{\text{eff}}} \right)^{\frac{1}{4}} H_m \left(\sqrt{\frac{\text{Re}(\sigma)}{\hbar_{\text{eff}}}} q \right) e^{-\frac{\sigma}{\hbar_{\text{eff}}} \frac{q^2}{2}} \quad (3.147)$$

with the the Hermite polynomials H_m and the complex squeezing parameter σ . This result is obtained using the tilting angle θ of the elliptic island with respect to the momentum axis and the ratio σ' of its half axes, determined from the linearized dynamics with Eqs. (3.19) and (3.20), see also Fig. 3.3. The squeezing σ is given by

$$\text{Re}(\sigma) = \frac{1}{\frac{1}{\sigma'} \cos^2(\theta) + \sigma' \sin^2(\theta)}, \quad (3.148)$$

$$\text{Im}(\sigma) = \text{Re}(\sigma) \left(\frac{1}{\sigma'} - \sigma' \right) \sin(\theta) \cos(\theta). \quad (3.149)$$

Husimi representation

We want to visualize quantum states $|\psi\rangle$ in phase space in order to compare the result to classical phase-space structures. Therefore, we introduce the Husimi representation $h(q, p)$ which is given by the projection of the state $|\psi\rangle$ onto a coherent state $|\chi_{q,p}\rangle$ which shows the same periodicity as the considered phase space. Its center is localized in the point $(q, p) \in [q_{\min}, q_{\min} + M_q) \times [p_{\min}, p_{\min} + M_p)$

$$h(q, p) = |\langle \chi_{q,p} | \psi \rangle|^2 \quad (3.150)$$

$$= \left| \sum_{k=0}^{N-1} \langle \chi_{q,p} | q_k \rangle \langle q_k | \psi \rangle \right|^2 \quad (3.151)$$

$$= \left| \sum_{k=0}^{N-1} (2N)^{\frac{1}{4}} e^{-\pi N(q^2 - ipq)} e^{\pi N(-q_k^2 + 2(q-ip)q_k)} \cdot \vartheta_3 \left(i\pi N \left(q_k - \frac{i\theta_q}{N} - q + ip \right) \middle| iN \right) \psi(q_k) \right|^2 \quad (3.152)$$

where $\vartheta_3(Z|\alpha)$ denotes the Jacobi theta function, defined as

$$\vartheta_3(Z|\alpha) := \sum_{n \in \mathbb{Z}} e^{i\pi \alpha n^2 + 2inZ} \quad \text{with} \quad Z, \alpha \in \mathbb{C}, \text{Im}(\alpha) > 0. \quad (3.153)$$

In Fig. 3.15 the Husimi representation of three characteristic eigenstates of the standard map is presented for $K = 2.4$ and $\hbar_{\text{eff}} = 1/100$.

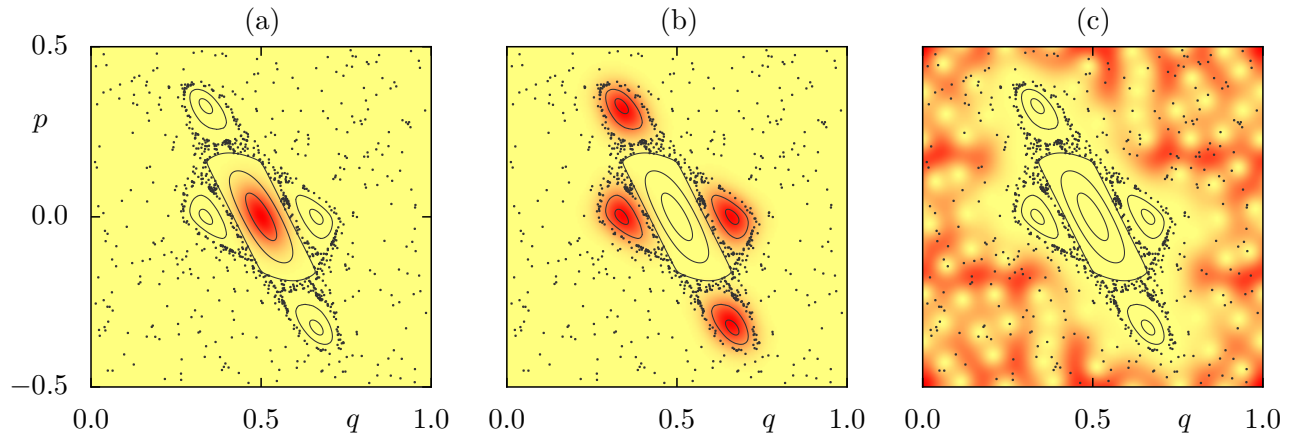


Figure 3.15: Husimi representation of eigenstates of the quantized standard map for $K = 2.4$ and $h_{\text{eff}} = 1/100$. We show (a) a regular state mainly localized inside the central island, (b) a state living inside a 4:1 resonance chain, and (c) a chaotic state. Red color represents high values of the Husimi function while its low values are marked in yellow. For comparison the classical phase space is shown in gray.

Quantization of classical Hamilton functions

In Chapter 4 we have to determine the eigenfunctions $|\psi_{\text{reg}}\rangle$ of the quantum system which corresponds to some integrable Hamilton function $H_{\text{reg}}(q, p)$ in order to predict dynamical tunneling rates. Hence, we present two numerical methods which allow the quantization of such classical Hamilton functions $H(q, p)$.

Discretization in position space

Let the Hamilton function be given as a power series of order N in q and p . After its symmetrization and quantization

$$H(q, p) = \sum_{n=0}^N \sum_{k=0}^n h_{k, n-k} q^k p^{n-k} \Rightarrow \hat{H}(\hat{q}, \hat{p}) = \frac{1}{2} \sum_{n=0}^N \sum_{k=0}^n h_{k, n-k} (\hat{q}^k \hat{p}^{n-k} + \hat{p}^{n-k} \hat{q}^k) \quad (3.154)$$

we introduce a discrete position lattice

$$q_i = q_{\min} + i \frac{q_{\max} - q_{\min}}{M}, \quad i = 0, \dots, M-1 \quad (3.155)$$

with the minimal value q_{\min} and the spacing $\Delta q = (q_{\max} - q_{\min})/M$. We choose q_{\min} and q_{\max} such that at these positions $H(q, p)$ is much larger than the energies we are interested in. In position representation the momentum operator is replaced by the derivative $\hat{p} = -i\hbar_{\text{eff}} \frac{d}{dq}$. The time-independent Schrödinger equation reads

$$\hat{H} \left(q, -i\hbar_{\text{eff}} \frac{d}{dq} \right) \psi(q) = E\psi(q). \quad (3.156)$$

On the given position lattice we approximate the derivative with respect to q by difference quotients. For the first derivative we obtain

$$\begin{aligned} \left. \frac{d}{dq} \psi(q) \right|_{q_i} &\approx \frac{\psi(q_i + \Delta q) - \psi(q_i - \Delta q)}{2\Delta q} + O(\Delta q^2) \\ &\approx \frac{\psi_{i+1} - \psi_{i-1}}{2\Delta q}, \quad \Delta q = \frac{q_{\max} - q_{\min}}{M}. \end{aligned} \quad (3.157)$$

After expressing all appearing derivatives by difference quotients the Hamiltonian can be written as a banded matrix in position representation. This matrix has dimension M with n occupied diagonals where n depends on the maximal appearing order of the momentum operator

$$\begin{pmatrix} \ddots & \ddots & & & & & 0 \\ \ddots & \ddots & \ddots & & & & \\ \ddots & \ddots & \ddots & \ddots & & & \\ & \ddots & \ddots & \ddots & \ddots & & \\ & & \ddots & \ddots & \ddots & \ddots & \\ 0 & & & \ddots & \ddots & \ddots & \ddots \end{pmatrix} \begin{pmatrix} \psi_0 \\ \vdots \\ \psi_{M-1} \end{pmatrix} = E \begin{pmatrix} \psi_0 \\ \vdots \\ \psi_{M-1} \end{pmatrix}. \quad (3.158)$$

By diagonalizing this matrix the approximate eigenvalues and eigenfunctions of the system are obtained. Their error decreases $\sim M^{-2}$. Note that this procedure becomes more elaborate if higher orders of \hat{p} appear in the Hamilton function.

Direct quantization

If the classical Hamilton function is periodic in p , $H(q, p) = H(q, p + l_p)$, this is also the case for the corresponding quantum Hamiltonian. The periodicity in momentum direction implies a quantization of the position coordinate. We restrict the discrete position lattice q_i to the region of interest $[q_{\min}, q_{\max})$ with the spacing $\Delta q = h_{\text{eff}}/l_p$. The Hamiltonian in position representation is given as a finite dimensional Matrix with elements

$$H_{ij} = \langle q_i | \hat{H}(\hat{q}, \hat{p}) | q_j \rangle, \quad i = 0, \dots, M-1. \quad (3.159)$$

In order to evaluate this expression we symmetrically insert the identity operator in the momentum basis

$$H_{ij} = \frac{1}{2} \int_{p_{\min}}^{p_{\min}+l_p} (\langle q_i | \hat{H}(\hat{q}, \hat{p}) | p \rangle \langle p | q_j \rangle + \langle q_i | p \rangle \langle p | \hat{H}(\hat{q}, \hat{p}) | q_j \rangle) dp \quad (3.160)$$

$$\approx \frac{1}{2l_p} \int_{p_{\min}}^{p_{\min}+l_p} [H(q_i, p) + H(q_j, p)] e^{\frac{i}{h_{\text{eff}}}(q_i - q_j)p} dp. \quad (3.161)$$

By diagonalizing the matrix H_{ij} we obtain approximate eigenvalues and eigenfunctions of the

system \hat{H} using classical information only. As a test we applied this procedure to the rotated and squeezed harmonic oscillator, discussed above, whose eigenfunctions are analytically given by Eq. (3.147). The numerically determined low-energy eigenstates of Eq. (3.161) showed no deviations to the analytical result. However, as only classical data is used and the position lattice is restricted to $[q_{\min}, q_{\max})$ an error of order \hbar_{eff}^2 is expected for more generic systems [91].

3.1.5 Numerical methods for the calculation of tunneling rates

In this section we present numerical methods for quantum maps which determine tunneling rates describing the decay of a quasimode from the regular region to the chaotic sea. The numerical data obtained using these methods will be compared to the analytical prediction derived in the next chapter in order to verify this analytical result.

Opening the system

The energy spectrum of a time-independent unbounded system is continuous. States which exist for long times are called quasi-stationary [15]. The spectrum of such states is quasi-discrete and consists of a number of energy levels of width $\Gamma_n := \hbar_{\text{eff}}/\tau_n$, where τ_n characterizes the life-time of the state. For $q \rightarrow \pm\infty$ the quasi-stationary states are described by an outgoing spheric wave. Hence, the solution of the Schrödinger equation yields complex eigenvalues

$$E_n = E_{0,n} - i\Gamma_n, \quad E_{0,n}, \Gamma_n \in \mathbb{R}. \quad (3.162)$$

For the time evolution of a quasi-stationary state we obtain

$$|\psi_n(t)\rangle \approx e^{-\frac{i}{\hbar_{\text{eff}}}E_{0,n}t - \frac{\Gamma_n}{\hbar_{\text{eff}}}t} |\psi_n(0)\rangle. \quad (3.163)$$

The modulus squared of the wave function decays exponentially with $e^{-\frac{2\Gamma_n}{\hbar_{\text{eff}}}t} = e^{-\gamma_n t}$, where $\gamma_n := 2\Gamma_n/\hbar_{\text{eff}}$ denotes the decay- or tunneling rate of the state.

These concepts for open continuous systems can be transferred to our quantum maps. We consider kicked systems whose phase space consists of one regular region surrounded by the chaotic sea. This specific structure of phase space allows for determining tunneling rates numerically by applying absorbing boundary conditions in the chaotic part of phase space. This will affect the regular states as much as they are coupled to the chaotic region while the chaotic states are affected more drastically. The quasi-stationary regular states will decay with a tunneling rate γ which describes the coupling of this regular state towards the chaotic region if we assume that the subsequent coupling from the chaotic region to the opening is a fast process.

We construct an open quantum map by

$$\hat{U}^s = \hat{P}\hat{U}\hat{P}, \quad (3.164)$$

where \hat{P} is a projection operator. It has to be chosen such that it projects onto regions in phase space which include the regular island and absorption occurs in the chaotic sea only. An example is given by a sum of projectors on position eigenstates, $\hat{P} = \sum_{q_0}^{q_1} |q\rangle\langle q|$, where the regular island is located in the interval $[q_0, q_1]$. While the eigenvalues of \hat{U} are located on the unit circle the eigenvalues of \hat{U}^s will move to the inside of this unit circle as \hat{U}^s is not unitary, see Fig. 3.16. The eigenequation of \hat{U}^s reads

$$\hat{U}^s |\psi_n^s\rangle = z_n |\psi_n^s\rangle \quad (3.165)$$

with the eigenvalues

$$z_n = e^{i(\varphi_n + i\frac{\Gamma_n}{\hbar_{\text{eff}}})}. \quad (3.166)$$

If the chaotic region is transporting it is justified to assume that the probability of escaping the regular island is equal to the probability of leaving through the openings located in the chaotic sea. In generic systems, however, more complicated phase-space structures such as partial barriers appear in the chaotic region of phase space. The additional transition through these structures further limits the quantum transport such that the calculated decay through the opening occurs slower than the decay from the regular island to its border with the chaotic sea. This influence on the tunneling process can be suppressed by moving the absorbing boundaries closer to the regular island.

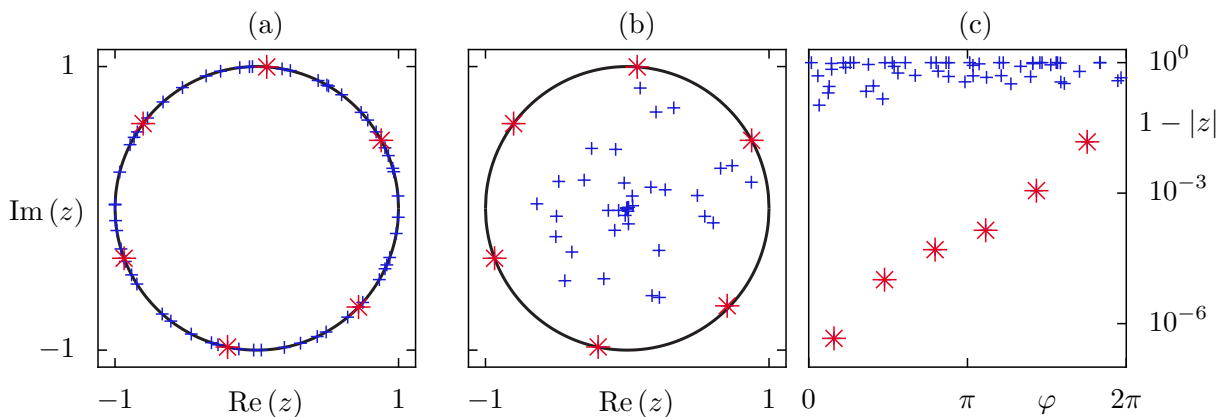


Figure 3.16: For the closed quantum map \hat{U} all eigenvalues z lie on the unit circle. This is shown in (a) in which the red symbols denote the eigenvalues corresponding to regular states and the blue symbols represent chaotic eigenvalues. The eigenvalues of the open system \hat{U}^s are presented in (b). They move to the inside of the unit circle. While the chaotic ones move close to zero the regular eigenvalues stay in the vicinity of the unit circle. This behavior is visualized in (c) where $1 - |z|$ is shown on a logarithmic scale over the polar angle φ .

We consider the time evolution of $|\psi_m^s\rangle$ with \hat{U}^s and obtain

$$\|\hat{U}^s|\psi_m^s\rangle\|^2 = e^{-\frac{2\Gamma_m}{\hbar_{\text{eff}}}} = e^{-\gamma_m}. \quad (3.167)$$

It decays with a rate $\gamma_m = 2\Gamma_m/\hbar_{\text{eff}}$ which is determined by the eigenvalues of \hat{U}^s . We find

$$|z_m| = e^{-\frac{\Gamma_m}{\hbar_{\text{eff}}}} = e^{-\frac{\gamma_m}{2}}. \quad (3.168)$$

Hence, the tunneling rate γ_m is given by twice the distance of the corresponding eigenvalue z_m from the unit circle (see Fig. 3.16)

$$\gamma_m = -2 \log |z_m| \approx 2(1 - |z_m|) \quad (3.169)$$

for $\gamma_m \ll 1$. To numerically determine the tunneling rates we have to find an appropriate projection operator \hat{P} , diagonalize the resulting non-unitary operator \hat{U}^s , and identify the eigenvalues z_m of \hat{U}^s which correspond to the quasi-bound regular states. Their distance from the unit circle determines the tunneling rates γ_m via Eq. (3.169). This implies that the eigenvalues of \hat{U}^s can be ordered according to their distance from the unit circle, which allows a separation of long and short-lived states corresponding to regular and chaotic states, respectively.

For kicked systems with quasi-periodic potential $V(q)$ and kinetic energy $T(p)$ the time-evolution operator is given as a finite dimensional matrix [96], see Eq. (3.134). Ignoring the quasi-periodicity in position direction we obtain

$$U_{k,n} = \frac{1}{M_p} e^{-\frac{i}{\hbar_{\text{eff}}}V(q_k)} \int_{p_{\min}}^{p_{\min}+M_p} dp e^{\frac{i}{\hbar_{\text{eff}}}(q_k-q_n)p} e^{-\frac{i}{\hbar_{\text{eff}}}T(p)} \quad (3.170)$$

with the position lattice

$$q_n = \frac{2\pi\hbar_{\text{eff}}}{M_p}(n + \theta_p), \quad n \in \mathbb{Z}, \quad (3.171)$$

and the Bloch phase θ_p . The matrix $U_{k,n}$ is infinite dimensional and unitary. Now we restrict the position lattice to a finite number of lattice points, e.g. in an interval $[q_0, q_1]$. The corresponding truncated matrix, denoted by \hat{U}^s , is not unitary. It does not include information about periodic boundary conditions in position direction. Any probability which would be mapped to $q > q_1$ or $q < q_0$ with the unitary map \hat{U} is absorbed. The absorbing regions are visualized in Fig. 3.17 for a specific example.

This procedure which uses the eigenvalues of the non-unitary operator \hat{U}^s for the determination of dynamical tunneling rates is a fast and reliable method. It is commonly used for quantum maps throughout this thesis. Note that for systems such as the mappings \mathcal{F}_2 in which the regular island is transporting a section of the infinite dimensional matrix $U_{k,n}$ has to be

used which includes this transport. For the system \mathcal{F}_2 with a velocity $v_{\text{reg}} = 1$ it is given by $U_{k+N/M_q, n}$ in which k and n take values such that the position lattice is restricted to one unit cell. This is visualized in Fig. 3.18.

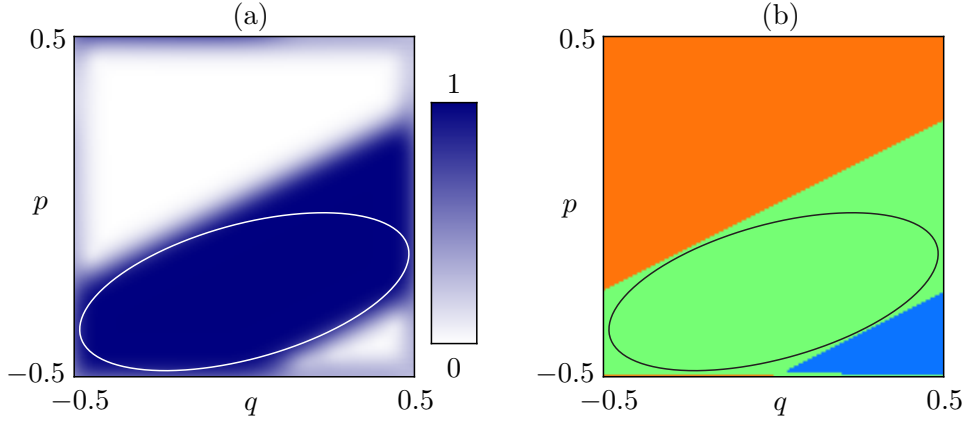


Figure 3.17: The effect of one application of \hat{U}^s to coherent states $|\chi_{q,p}\rangle$ centered in $q, p \in [-1/2, 1/2]$ is presented in (a). In the blue region the norm of $\hat{U}^s|\chi_{q,p}\rangle$ is close to one. States localized in this region will decay slowly. In the white region this norm is close to zero and states localized here will rapidly decay. This behavior is closely related to the classical dynamics of the system \mathcal{F}_1 (b). After one iteration points in the green region will stay inside the shown unit cell while points initially located in the blue or orange region will leave this cell to the right or to the left, respectively. As \hat{U}^s does not respect the periodic boundary conditions in q -direction all points in the orange and blue domain will escape which is exactly the white leaky region in (a).

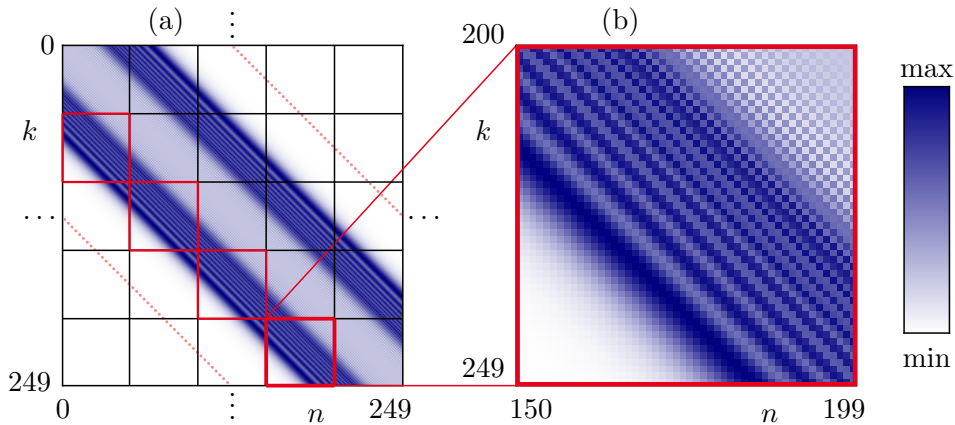


Figure 3.18: Modulus squared of the matrix \hat{U} in position representation for the mapping \mathcal{F}_2 . We show a section of $M_q = 5$ unit cells and $N = 250$. To determine tunneling rates of regular states localized in the transporting regular island we have to restrict this matrix to one unit cell and consider its elements $\hat{U}_{k+N/M_q, n}$ with $k, n = lN/M_q, \dots, (l+1)N/M_q$, $l \in 0, \dots, M_q - 1$, and $N/M_q \in \mathbb{N}$. These regions are marked in red in (a) and one of them is enlarged in (b).

Evaluation of avoided crossings

A commonly used method for the determination of tunneling rates is given by means of the evaluation of avoided crossings. Exemplarily, we consider a quantum map \hat{U} and determine the quasi-energies φ of all eigenstates under variation of a system-specific parameter, e.g. the Bloch phases θ_q or θ_p . Now we follow the quasi-energy φ_m of one chosen regular state, predicted by Eq. (3.146), and determine the widths of the avoided crossings between this regular and several chaotic states under variation of the parameter. Note that the semiclassical expression for the quasi-energy of a state localized in the regular region given by Eq. (3.146) has been generalized to transporting islands in Ref. [94]. It allows a numerically efficient determination of the quasi-energy splittings $\Delta\varphi_{m,\text{ch}} = \varphi_m - \varphi_{\text{ch}}$. The connection between these splittings $\Delta\varphi_{m,\text{ch}} = 2\langle\psi_{\text{ch}}|\hat{U}|\psi_{\text{reg}}^m\rangle$ and the tunneling rate is given in Appendix C.3

$$\gamma_m = \sum_{\text{ch}} \langle\psi_{\text{ch}}|\hat{U}|\psi_{\text{reg}}^m\rangle \quad (3.172)$$

$$\approx \frac{N_{\text{ch}}}{4} \langle|\Delta\varphi_{m,\text{ch}}|^2\rangle_{\text{ch}} \quad (3.173)$$

where N_{ch} denotes the number of chaotic eigenstates of \hat{U} . In Eq. (3.173) we average over all determined avoided crossings to minimize the appearing fluctuations of the widths of the single splittings (see Fig. 3.19).

The applicability of this method is limited by the following restrictions: For small dimensions

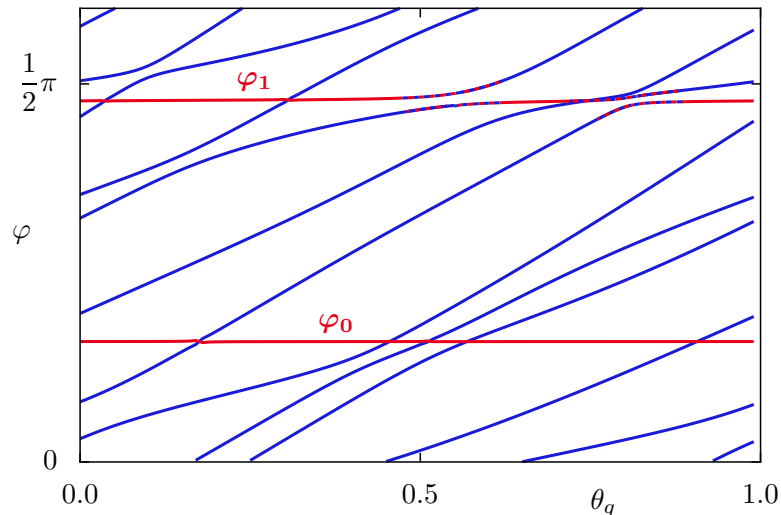


Figure 3.19: Part of the quasi-energy spectrum of the quantized mapping \mathcal{F}_1 for the parameters $r_1 = 0.46$, $R = 0$, $Z = 0$, $\varepsilon = 0.005$, $M_q = 3$, and $1/h_{\text{eff}} = 10$ under variation of θ_q . Quasi-energies which correspond to chaotic eigenstates of \hat{U} are marked in blue while the quasi-energies of the regular states are colored in red. We find that the quasi-energies of the ground state φ_0 and the first excited state φ_1 remain almost unchanged under this variation and perform avoided crossings with chaotic states (red-blue dashed lines).

N of the Hilbert space only a few chaotic eigenstates exist. Hence, the average taken in Eq. (3.173) includes just a few different splittings $\Delta\varphi_{m,\text{ch}}$. Consequently, the predicted tunneling rates have a large statistical error. For large N the quasi-energies are more densely distributed in $\varphi \in [0, 2\pi)$. Therefore, resolving the single avoided crossings is more difficult and avoided crossings which involve more than two states appear.

Time evolution of wave packets

A simple method to obtain a numerical prediction of the tunneling rates is given by the time-evolution of a purely regular state $|\psi_{\text{reg}}^m\rangle$ with a non-unitary operator $\hat{U}^s = \hat{P}\hat{U}\hat{P}$. Here \hat{P} projects onto regions in phase space which include the regular island. We consider

$$P_m(t) = \sum_{n=0}^{m_{\text{max}}} |\langle \psi_{\text{reg}}^n | (\hat{U}^s)^t | \psi_{\text{reg}}^m \rangle|^2 \quad (3.174)$$

for $t \in \mathbb{N}$ which describes the probability of the time-evolved regular state within the regular island at time t . At each time step probability of $|\psi_{\text{reg}}^m\rangle$ is lost in the chaotic region due to the openness of the quantum map \hat{U}^s . Consequently, $P_m(t)$ decays exponentially $P_m(t) \approx e^{-\gamma_m t}$ and the tunneling rates γ_m can be determined by a fit of the numerical data. If $|\psi_{\text{reg}}^m\rangle$ contains admixtures from lower excited regular states (with smaller tunneling rate) their decay dominates for times $t \gg 1/\gamma_m$. If it contains admixtures from higher excited regular states (with larger tunneling rate) their decay will be seen for small times (see Fig. 3.20). The presented method works best for regular states $|\psi_{\text{reg}}^m\rangle$ which resemble the corresponding eigenstates of the mixed system \hat{U} with high accuracy. It is particularly useful for Hilbert spaces of large dimension N where diagonalizing the matrix \hat{U}^s would take a long time.

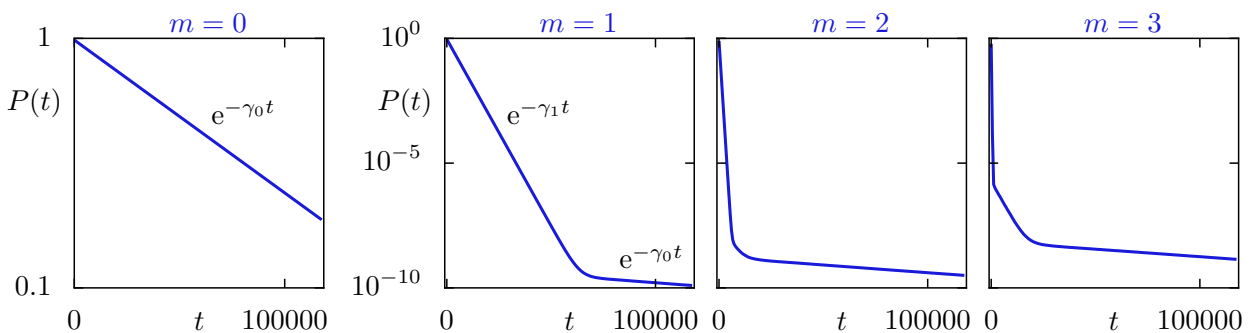


Figure 3.20: Time evolution of a purely regular state: We present $P(t)$ as a function of t obtained by Eq. (3.174) on a semi-logarithmic scale. The slope of the blue line in the left plot determines the tunneling rate of the regular ground state $m = 0$ to the chaotic sea. For the higher excited states $m = 1, 2, 3$ we find the same behavior for small times t , while for larger times the decay of lower excited states with a different slope is found.

Comparison of the methods

We compare tunneling rates obtained for the system \mathcal{F}_1 under variation of the effective Planck constant h_{eff} using the three methods discussed above. The results are shown in Fig. 3.21 for states with quantum number $m \leq 3$. While the method of opening the system and the time evolution produce similar results, the data obtained using avoided crossings shows deviations which are, however, smaller than a factor of two. They arise due to the limitations of this approach.

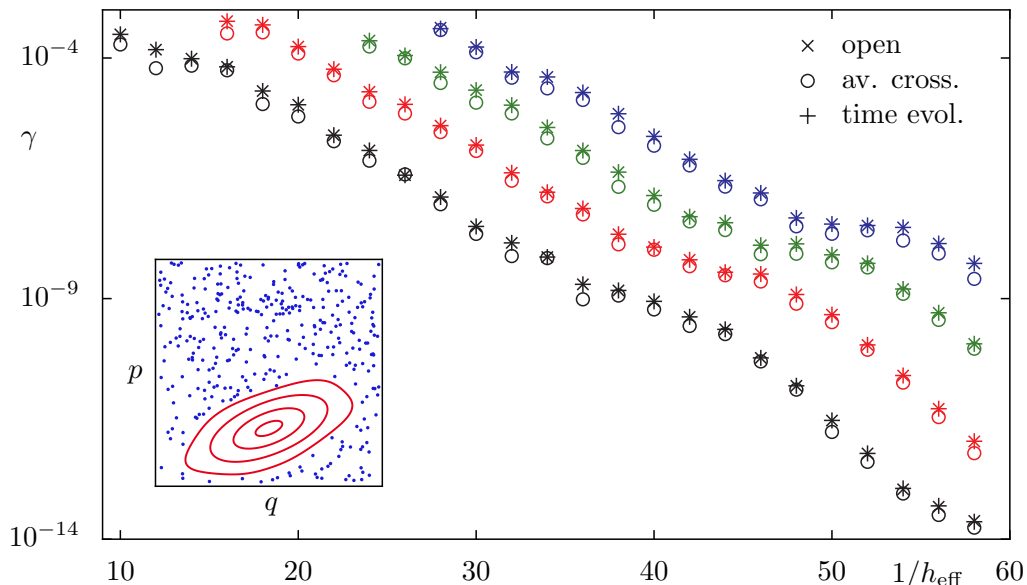


Figure 3.21: Comparison of numerical tunneling rates under variation of $1/h_{\text{eff}}$ on a semi-logarithmic scale obtained by opening the system (crosses), the evaluation of avoided crossings (circles), and time evolution (plus symbols). We use the mapping \mathcal{F}_1 with $r_1 = 0.65$, $R = 0$, $Z = 0$, $\varepsilon = 0.025$ and consider the regular states $m = 0$ (black), $m = 1$ (red), $m = 2$ (green), and $m = 3$ (blue). The inset shows the phase space of the system.

3.2 Billiard systems

An important class of systems considered in quantum chaos are billiards which are given by the free motion of a point particle inside a two-dimensional domain and elastic reflections at its boundary. The classical dynamics is defined by the shape of this boundary. Similar to the kicked systems described before it can be completely regular, chaotic, or mixed which is the case we are interested in. While the theoretical description of such billiard systems is more challenging compared to the mappings introduced in Section 3.1 they, however, are of major importance. Billiard systems can be observed experimentally, e.g. using microwaves [100, 101] or as mesoscopic quantum dots [102, 103].

In this section we present classical and quantum properties of billiards with a focus on numerical methods which allow to determine its eigenvalues, eigenstates, and dynamical tunneling rates. The aim is to introduce the information necessary to understand the dynamical tunneling process in these systems and not to cover all details for which the reader should consult Refs. [104–109] and references therein.

3.2.1 Classical dynamics

Billiards are dynamical systems given by a point particle of mass m which moves with constant velocity inside a compact domain $\Omega \in \mathbb{R}^2$. It is elastically reflected at its boundary $\partial\Omega$ such that the angle of incidence and the angle of reflection are identical. The boundary consists of a finite number of smooth components characterized by their curvature κ which does not have to be constant. For $\kappa < 0$ the resulting dynamics is defocusing, for $\kappa > 0$ focusing, and for $\kappa = 0$ it is neutral. The singular points at which the different parts of the boundary meet are called corners, see Fig. 3.22.

The Hamiltonian of the billiard system is given (with $2m = 1$) by

$$H(\mathbf{q}, \mathbf{p}) = \begin{cases} \mathbf{p}^2, & \mathbf{q} \in \Omega \\ \infty, & \mathbf{q} \notin \Omega \end{cases} \quad (3.175)$$

in which \mathbf{q} and \mathbf{p} denote the two-dimensional position and momentum coordinates, respectively. It describes the motion of a particle in a potential $V(\mathbf{q})$ which is zero for $\mathbf{q} \in \Omega$ and infinity

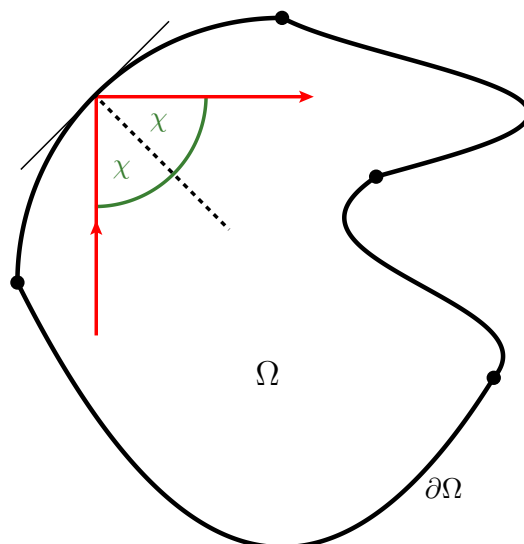


Figure 3.22: Sketch of a billiard system: In the interior Ω a particle moves freely and is elastically reflected at the billiard boundary $\partial\Omega$ (red line). The angle of incidence χ is equal to the angle of reflection. The different smooth parts of the boundary are connected at corners marked by black dots.

outside. The phase space is given by

$$\{(\mathbf{q}, \mathbf{p}) \in \Omega \times \mathbb{R}^2\} \subset \mathbb{R}^4 \quad (3.176)$$

which is four-dimensional. As billiard systems are time-independent the energy E is conserved and the motion takes place on three-dimensional hyperplanes in \mathbb{R}^4

$$\Sigma_E := \{(\mathbf{q}, \mathbf{p}) \in \Omega \times \mathbb{R}^2 \mid \mathbf{p}^2 = E\}. \quad (3.177)$$

Due to the Hamilton function which is quadratic in \mathbf{p} the scaling property

$$\Sigma_E = \sqrt{E}\Sigma_1 := \{(\mathbf{q}, \sqrt{E}\mathbf{p}) \mid (\mathbf{q}, \mathbf{p}) \in \Sigma_1\} \quad (3.178)$$

holds. Thus it is possible to restrict the momenta to $|\mathbf{p}| = 1$ and identify the quasi-energy surface as follows

$$\Sigma_1 = \{(\mathbf{q}, \mathbf{p}) \in \Omega \times \mathbb{R}^2 \mid |\mathbf{p}| = 1\} \simeq \Omega \times S_1 \quad (3.179)$$

in which S_1 is the unit circle.

To completely describe the motion of the particle it is sufficient to consider the positions of its incidents with the boundary $\partial\Omega$ and the direction of momentum after each reflection. Inside the billiard it moves on straight lines which are determined by this information. Hence, the billiard boundary provides a natural two-dimensional section of the phase space which can be used to visualize the classical dynamics. This Poincaré section is defined as

$$\mathcal{P} := \{\mathbf{x} = (\mathbf{q}, \mathbf{p}) \in \Sigma_1 \mid \mathbf{q} \in \partial\Omega, \mathbf{p} \in T_{\mathbf{q}}^*(\partial\Omega) \text{ with } \langle \mathbf{p}, \mathbf{N}(\mathbf{q}) \rangle \geq 0\} \quad (3.180)$$

in which $\mathbf{N}(\mathbf{q})$ denotes the inward pointing normal vector in the point $\mathbf{q} \in \partial\Omega$, $T_{\mathbf{q}}^*(\partial\Omega)$ is the tangent space in \mathbf{q} , and $\langle \cdot, \cdot \rangle$ denotes the usual scalar product. The Poincaré section defines a mapping $P : \mathcal{P} \rightarrow \mathcal{P}$ for the billiard dynamics which describes how the position and momentum of each reflection at the boundary follows from the preceding one. A parameterization of \mathcal{P} can be obtained using the arclength s along $\partial\Omega$ and the tangential projection p of the momentum \mathbf{p} after reflection

$$\mathcal{P} := \{(s, p) \mid s \in [0, L], p \in [-1, 1]\} \quad (3.181)$$

in which L is the length of the billiard boundary. The reduced phase space of the Poincaré mapping is similar to the stroboscopic phase space of kicked systems introduced in Section 3.1.2 as it allows for a two-dimensional visualization of the dynamics.

Depending on the shape of the boundary $\partial\Omega$ the classical dynamics of the corresponding

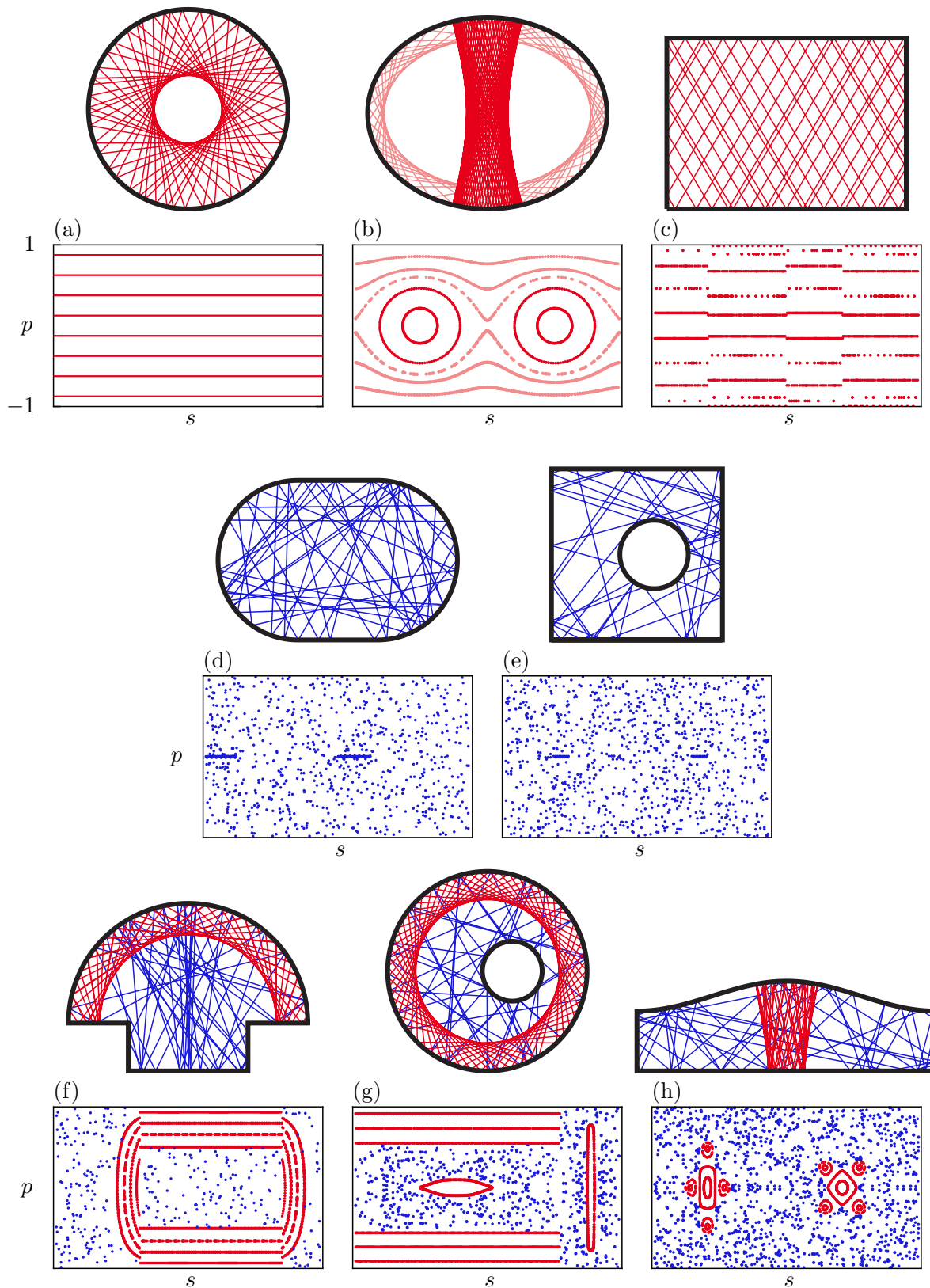


Figure 3.23: Sketch of billiard systems used throughout this thesis: We present the configuration space with typical trajectories and a Poincaré section for the integrable (a) circular, (b) elliptical, and (c) rectangular billiard, the chaotic (d) stadium and (e) Sinai billiard, and the mixed (f) mushroom, (g) annular, and (h) cosine billiard. Regular trajectories are marked in red while chaotic ones are depicted in blue.

billiard can be regular, chaotic, or mixed. As the circular billiard has a radial symmetry the angular momentum is conserved in addition to the energy. Due to these two constants of motion it is integrable. The same situation occurs for the rectangular and the elliptical billiard [110, 111]. Figure 3.23(a)-(c) shows typical classical trajectories for these billiards and the corresponding Poincaré sections. Each trajectory is confined to a two-dimensional torus which appears as a one-dimensional line in the Poincaré section.

In contrast to these integrable systems, shapes exist such that the dynamics is completely ergodic which means that for long times almost all trajectories fill the whole energy plane with uniform measure [72] such that they fill a two-dimensional region in the Poincaré section. Famous examples are given by the Bunimovich stadium [112, 113], the cardioid [114], or the Sinai billiard [106, 115], see Fig. 3.23(d)-(e). A lot of effort has been taken to prove universal features of these systems [106, 112, 113, 116–120].

However, generic Hamiltonian systems have a phase space in which regular and chaotic dynamics coexist. This behavior can also be modeled by billiards. We mention the cosine [121], the annular [29, 30, 122], and the mushroom billiard [123, 124]. Fig. 3.23(f)-(h) shows the geometries of these billiards with typical trajectories which in the Poincaré section form regular tori surrounded by the chaotic sea. A particularly interesting example is the mushroom billiard. It is constructed such that the regular and chaotic parts of phase space are sharply separated. Inside the regular region no resonance structures appear and besides the bouncing-ball orbits the chaotic sea has no additional structures. Hence, the mushroom billiard is similar to the mappings \mathcal{F}_1 with $R = Z = 0$ which show a resonance-free regular island. In contrast, typically the phase space of the annular and the cosine billiard exhibits nonlinear resonance chains, a relevant hierarchical region, and partial barriers in phase space, as discussed in Section 3.1.1 for the standard map.

3.2.2 Quantum billiards

Quantum mechanically billiards are described by the time-independent Schrödinger equation (in units $\hbar = 2m = 1$)

$$-\Delta\psi_n(\mathbf{q}) = E_n\psi_n(\mathbf{q}), \quad \mathbf{q} \in \Omega \quad (3.182)$$

with the Dirichlet boundary condition $\psi_n(\mathbf{q}) = 0$, $\mathbf{q} \in \partial\Omega$. In Eq. (3.182) Δ denotes the Laplace operator in two dimensions

$$\Delta = \frac{\partial^2}{\partial x^2} + \frac{\partial^2}{\partial y^2}. \quad (3.183)$$

Equation (3.182) is identical to the eigenvalue problem of the two-dimensional Helmholtz equation which for example also describes the eigenvalues of a vibrating membrane or of a microwave

cavity. This equivalence allowed for the simulation of quantum billiards by experiments using microwave cavities [100, 101, 125–127]. One application is presented for the mushroom billiard in Section 5.2.1.

The state of a particle is described by a wave function $\psi(\mathbf{q}) \in L^2(\Omega)$ in position representation in which $L^2(\Omega)$ is the Hilbert space of square integrable functions on Ω . Due to the compactness of Ω the eigenvalues $\{E_n\}$ are discrete and can be ordered as $0 \leq E_1 \leq E_2 \leq E_3 \leq \dots$. The eigenfunctions can be chosen real and form an orthonormal basis on $L^2(\Omega)$

$$\langle \psi_n | \psi_k \rangle := \int_{\Omega} \psi_n(\mathbf{q}) \psi_k(\mathbf{q}) \, d^2q = \delta_{kn}. \quad (3.184)$$

In contrast to the kicked maps discussed in Section 3.1.4 we find infinitely many eigenvalues and eigenfunctions. Any wave function $\psi(\mathbf{q}) \in L^2(\Omega)$ can be decomposed into the eigenfunctions $\psi_n(\mathbf{q})$

$$\psi(\mathbf{q}) = \sum_{n=1}^{\infty} c_n \psi_n(\mathbf{q}) \quad (3.185)$$

in which c_n are the expansion coefficients

$$c_n = \langle \psi_n | \psi \rangle = \int_{\Omega} \psi_n(\mathbf{q}) \psi(\mathbf{q}) \, d^2q. \quad (3.186)$$

The time-evolution of the wave packet is obtained by

$$\psi(\mathbf{q}, t) = \sum_{n=1}^{\infty} c_n e^{-iE_n t} \psi_n(\mathbf{q}). \quad (3.187)$$

Hence, the full quantum information of the billiard is included in the eigenvalues E_n and the eigenfunctions ψ_n . Note that for billiard systems we choose $\hbar = 1$ such that the semiclassical limit, formerly given by the effective Planck constant $h_{\text{eff}} \rightarrow 0$, is now reached if the energies tend to infinity, $E_n \rightarrow \infty$.

Spectral staircase function and density of states

A lot of insight on quantum systems can be obtained by analyzing their spectrum. One relevant property is the spectral staircase function $N(E)$. It counts the number of eigenstates with an energy E_n smaller than a given energy E

$$N(E) := \#\{n \mid E_n < E\} \quad (3.188)$$

and can be decomposed into a smooth and a fluctuating part $N(E) = \bar{N}(E) + N_{\text{fluct}}(E)$. For large E the smooth part is given by the generalized Weyl law [128]

$$\bar{N}(E) = \frac{A}{4\pi}E - \frac{L}{4\pi}\sqrt{E} + C + \dots \quad (3.189)$$

Here, A denotes the area of the billiard and L is the length of its boundary. The constant C is determined by the curvature and by properties of the corners of the billiard [104]

$$C = \sum_i b(\Gamma_i) + \sum_j c(\alpha_j) \quad (3.190)$$

in which Γ_i are the smooth pieces of the boundary and α_j denote the interior angles of the corners. The curvature terms $b(\Gamma_i)$ read

$$b(\Gamma_i) = \frac{1}{12\pi} \int \kappa_i(s) ds \quad (3.191)$$

where $\kappa_i(s)$ is the curvature of Γ_i in dependence of the arclength s . The corner contribution is given by

$$c(\alpha) = \frac{\pi^2 - \alpha^2}{24\pi\alpha} = \frac{1}{24} \left(\frac{\pi}{\alpha} - \frac{\alpha}{\pi} \right), \quad 0 < \alpha \leq 2\pi. \quad (3.192)$$

The derivative of the spectral staircase function is the density of states $d(E)$. For its smooth part $\bar{d}(E)$ we find

$$\bar{d}(E) = \frac{d\bar{N}(E)}{dE} = \frac{A}{4\pi} - \frac{L}{8\pi} \frac{1}{\sqrt{E}} + \dots \quad (3.193)$$

For large E the density of states is independent of the energy E .

Eigenfunctions and random wave models

According to the semiclassical eigenfunction hypothesis [20–22] we expect that the eigenfunctions $\psi_n(\mathbf{q})$ of high energy will be localized in those phase-space regions which a typical classical orbit explores in the long-time limit. Hence, for regular billiards they will localize on quantizing tori while for chaotic billiards they are spread over the whole energy surface. Mixed systems will show both of the two possibilities, i.e. states mainly localized on quantizing tori which we call regular and states spread out over the chaotic sea which we call chaotic. However, due to dynamical tunneling in between the classically separated regions they will have at least a small contribution in the other region of phase space. Examples of such eigenstates are presented in Fig. 3.26 on page 86.

For regular billiards quasimodes can be constructed by means of WKB techniques [99, 129,

130]. They approximate eigenfunctions of the billiard which appear isolated in the spectrum. For quasi-degenerate eigenfunctions a linear combination of the quasimodes has to be used. If applied to regular states in billiards with a mixed phase space, the WKB techniques do not allow for calculating the quasimodes in the classically chaotic region which will, however, turn out to be important in Chapter 5. Hence, these methods are not considered in this thesis.

Eigenfunctions of chaotic systems show universal features. For example Berry conjectured [21] that their amplitude distribution is Gaussian, which has been found in many numerical studies [131–133]. Hence, he introduced a model which describes such chaotic eigenfunctions by a random superposition of plane waves. For the two-dimensional case on the region Ω it is given by

$$\psi(\mathbf{q}) = \sqrt{\frac{2}{\text{vol}(\Omega)N}} \sum_{s=1}^N c_s \cos(\mathbf{k}_s \mathbf{q} + \varphi_s) \quad (3.194)$$

in which the c_s are assumed to be independent Gaussian random variables with mean zero and variance one. The wave numbers \mathbf{k}_s fulfill $|\mathbf{k}_s| = \sqrt{E}$ and are uniformly distributed on the circle of radius \sqrt{E} . The phases φ_s show a uniform distribution in $[0, 2\pi)$ and the prefactor accounts for the normalization of the wave function such that

$$\int_{\Omega} \psi^2(\mathbf{q}) \, d\mathbf{q} = 1. \quad (3.195)$$

The amplitude distribution $P(\psi)$ of a real state $\psi(\mathbf{q})$ is defined as follows

$$\frac{\text{vol}(\{\mathbf{q} \in \Omega \mid \psi(\mathbf{q}) \in [a, b] \subset \mathbb{R}\})}{\text{vol}(\Omega)} =: \int_a^b P(\psi) \, d\psi. \quad (3.196)$$

For random waves as introduced in Eq. (3.194) the central limit theorem states that for $N \rightarrow \infty$ the amplitude distribution is a Gaussian [21]

$$P(\psi) = \frac{1}{\sqrt{2\pi\sigma^2}} \exp\left(-\frac{\psi^2}{2\sigma^2}\right) \quad (3.197)$$

in which the variance σ^2 is given by the inverse area of the billiard

$$\sigma^2 = \frac{1}{\text{vol}(\Omega)}. \quad (3.198)$$

Hence, in the sense of a Gaussian amplitude distribution the plane wave model, Eq. (3.194), gives indeed a valid approximation of real chaotic eigenstates. The validity has been shown for other statistical properties as well.

The random wave model presented in Eq. (3.194) fulfills no boundary conditions. It can be

adapted to respect a Dirichlet boundary condition at $x = 0$ [134], where $\mathbf{q} = (x, y)$. Hence, the prediction for $\psi(\mathbf{q})$ has to be equal to zero on this line. This can be achieved with the following model

$$\psi(\mathbf{q}) = \frac{2}{\sqrt{\text{vol}(\Omega)N}} \sum_{s=1}^N c_s \sin(k \cos(\vartheta_s)x) \cos(k \sin(\vartheta_s)y + \varphi_s) \quad (3.199)$$

in which the angles ϑ_s are uniformly distributed on $[0, 2\pi)$ and $k = |\mathbf{k}|$ is the wave number. Equation (3.199) has the following relevant statistical property

$$\langle |\psi(\mathbf{q})|^2 \rangle = \frac{1}{\text{vol}(\Omega)} (1 - J_0(2kx)) \quad (3.200)$$

in which $\langle \cdot \rangle$ denotes an ensemble average and J_0 is the zeroth Bessel function of the first kind. It fulfills $J_0(0) = 1$ such that the wave functions vanish at $x = 0$ and start to oscillate for larger values of x . For $x \gg 1$ we find $J_0(2kx) \approx 0$ and the behavior of the plane wave model, Eq. (3.194), is recovered.

In Ref. [135] it was shown that the solutions of the Schrödger equation in the vicinity of a corner at $\mathbf{q} = (0, 0)$ of angle θ and energy $E = k^2$ are given by

$$\psi_s(\mathbf{q}) = J_{\frac{\pi}{\theta}s}(kr) \sin\left(\frac{\pi\varphi}{\theta}s\right) \quad (3.201)$$

in which we use polar coordinates $\mathbf{q} = (r, \varphi)$ and $s = 1, 2, \dots$. Using these basis functions a random wave model can be found which respects Dirichlet boundary conditions of such a corner of angle θ

$$\psi(\mathbf{q}) = \sqrt{\frac{C}{\text{vol}(\Omega)}} \sum_{s=1}^{\infty} c_s \psi_s(\mathbf{q}). \quad (3.202)$$

Again, the c_s are assumed to be independent Gaussian random variables with mean zero and variance one and the normalization constant C depends on θ and has to be determined numerically. No other random parameters appear. This makes the ensemble average $\langle |\psi(\mathbf{q})|^2 \rangle$ particularly simple. We obtain

$$\langle |\psi(\mathbf{q})|^2 \rangle = \frac{C}{\text{vol}(\Omega)} \sum_{s=1}^{\infty} \psi_s^2(\mathbf{q}). \quad (3.203)$$

Note that this random wave model can also be applied to Dirichlet boundary conditions at a straight line with $\theta = \pi$ as discussed previously in Eq. (3.199). Fig. (3.24) shows a result of the three random wave models.

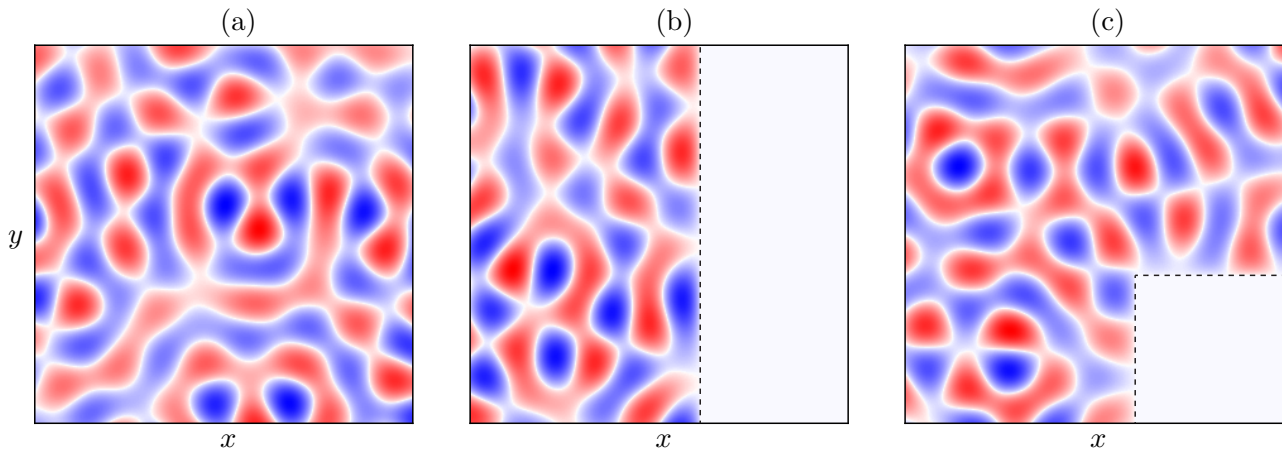


Figure 3.24: Amplitude of wave functions generated by different random wave models: In (a) no boundary conditions are imposed, see Eq. (3.194), in (b) a Dirichlet boundary condition holds at $x = 0$ (dashed line), see Eq. (3.199), and in (c) Dirichlet boundary conditions are fulfilled at a corner of angle $3\pi/2$ (dashed line), see Eq. (3.202). Positive amplitudes are marked in red while negative amplitudes are shown in blue.

Eigenfunctions in phase space

In order to compare the properties of eigenstates to classical phase-space structures we consider their representation on the Poincaré section given by the Poincaré-Husimi function [136]. Therefore, we have to calculate the normal derivative of $\psi_n(\mathbf{q})$ along the boundary

$$\frac{\partial}{\partial N}\psi_n(\mathbf{q}) := \mathbf{N}\nabla\psi_n(\mathbf{q}), \quad (3.204)$$

where $\mathbf{N} = (N_x, N_y)$ denotes the unit normal vector on the boundary. In Cartesian coordinates is given by

$$\frac{\partial}{\partial N}\psi_n(x, y) := N_x \frac{\partial}{\partial x}\psi_n(x, y) + N_y \frac{\partial}{\partial y}\psi_n(x, y) \quad (3.205)$$

while we obtain for polar coordinates

$$\frac{\partial}{\partial N}\psi_n(\mathbf{q}) = (N_x \cos \varphi + N_y \sin \varphi) \frac{\partial}{\partial r}\psi_n(r, \varphi) + (-N_x \sin \varphi + N_y \cos \varphi) \frac{1}{r} \frac{\partial}{\partial \varphi}\psi_n(r, \varphi). \quad (3.206)$$

After the parameterization of the boundary with the arclength s , $\mathbf{q}(s) = (x(s), y(s)) = (r(s), \varphi(s))$, one finally obtains the normal derivative of $\psi_n(\mathbf{q})$ depending only on one variable s , $\partial\psi_n/\partial N(s)$.

This derivative can now be used to calculate the representation of the eigenstate on the Poincaré section. Thus, we introduce the Husimi representation

$$h(s, p) = \left| \int_0^L \frac{\partial}{\partial N}\psi_n(s') e^{ipk_n s'} \phi_0(s' - s) ds' \right|^2 \quad (3.207)$$

in which

$$\phi_0(s) = \left(\frac{1}{\pi\sigma^2} \right)^{\frac{1}{4}} e^{-\frac{s^2}{4\sigma^2}}, \quad (3.208)$$

σ is the squeezing parameter ($\sigma \approx 0.076$ [136]), k_n is the wave number corresponding to $\psi_n(\mathbf{q})$, $p \in [-1, 1]$, and $s \in [0, L]$. For an example, see Fig. 3.26.

Analytical quantization of integrable billiards

To determine the eigenvalues and eigenstates of a billiard we have to solve the Schrödinger equation (3.182) on Ω with Dirichlet boundary conditions on the boundary $\partial\Omega$. Analytically, this is only possible for integrable systems such as the rectangular, the circular, and the elliptic billiard.

For a rectangular billiard of side lengths a and b the eigenfunctions are

$$\psi_{mn}(\mathbf{q}) = \frac{2}{\sqrt{ab}} \sin\left(\frac{m\pi x}{a}\right) \sin\left(\frac{n\pi y}{b}\right) \quad (3.209)$$

and for the eigenvalues we find

$$E_{mn} = \pi^2 \left[\left(\frac{m}{a}\right)^2 + \left(\frac{n}{b}\right)^2 \right]. \quad (3.210)$$

They are characterized by the two quantum numbers $m = 1, 2, \dots$ and $n = 1, 2, \dots$ which determine the number of oscillations of the wave function in x and y -direction, respectively.

For the circular billiard of radius R the eigenfunctions in polar coordinates are

$$\psi_{mn}(\mathbf{q}) = N_{mn} J_m\left(\frac{j_{mn}r}{R}\right) [A \cos(m\varphi) + B \sin(m\varphi)] \quad (3.211)$$

in which J_m is the m th Bessel function of the first kind, j_{mn} is the n th root of this Bessel function, and $N_{mn} = \sqrt{2/\pi}/(J_{m-1}(j_{mn})R)$ accounts for its normalization. The constants A and B are zero or ± 1 where \pm accounts for the sign of the angular momentum. Here, $m = 0, 1, \dots$ denotes the angular quantum number while $n = 1, 2, \dots$ is the radial quantum number. The eigenenergies are given by

$$E_{mn} = \frac{j_{mn}^2}{R^2}. \quad (3.212)$$

For the ellipse the Schrödinger equation is separable using elliptic coordinates $\mathbf{q} = (\xi, \eta)$ such

that $\psi(\xi, \eta) = R(\xi)\phi(\eta)$ which leads to two Mathieu equations

$$\frac{d^2\phi}{d\eta^2} + (d - 2q \cos(2\eta))\phi = 0, \quad (3.213)$$

$$\frac{d^2R}{d\xi^2} - (d - 2q \cosh(2\xi))R = 0, \quad (3.214)$$

where d is the separation constant, $q = f^2 E/4$, r_a and r_b are the lengths of the two half axis, and $f = \sqrt{r_a^2 - r_b^2}$. The angular Mathieu equation is solved by the even and odd angular Mathieu functions

$$\phi_m(\eta) = \begin{cases} ce_m(\eta, q), & m = 0, 1, 2, \dots, \\ se_m(\eta, q), & m = 1, 2, 3, \dots \end{cases} \quad (3.215)$$

while the radial solutions are given by the even and odd oscillatory Mathieu functions of the first and second kind for $q > 0$ [137]

$$R_m(\xi, q) = \begin{cases} Mc_m^{(1)}(\xi, q) \text{ or } Ms_m^{(1)}(\xi, q), \\ Mc_m^{(2)}(\xi, q) \text{ or } Ms_m^{(2)}(\xi, q). \end{cases} \quad (3.216)$$

The eigenenergies are found considering the Dirichlet boundary conditions. It demands that the radial component $R_m(\xi, q)$ vanishes at the elliptic boundary. For $q = q_{mn}$ the n th zero of the radial function $R_m(\xi, q_{mn})$ is located at the elliptic boundary and the eigenenergy is given by $E_{mn} = k_{mn}^2 = 4q_{mn}/f^2$. The eigenstates are finally obtained as

$$\psi_{mn}(\xi, \eta) = N_{mn} R_m(\xi, q_{mn}) \phi_m(\eta, q_{mn}) \quad (3.217)$$

with the normalization constant N_{mn} .

Numerical quantization of billiards

Billiards with more complicated boundaries than discussed before have to be treated numerically. Especially systems with a mixed phase space cannot be quantized analytically. There exist several methods for the numerical computation of eigenvalues and eigenfunctions in two-dimensional billiard systems. The boundary integral method is used most commonly throughout the literature [138–140]. While it works for arbitrary shapes of the boundary $\partial\Omega$ and does not depend on specific basis functions its accuracy is not sufficient to determine the small level splittings which are required for the prediction of dynamical tunneling rates. Hence, we choose the improved method of particular solutions [141]. It is especially useful for the determination of small energy splittings due to its high accuracy and speed. However, it cannot be applied to arbitrarily shaped billiard boundaries and has to be adapted for each specific billiard. Nevertheless, it is the choice for the computation of low energy eigenvalues throughout the thesis. If high energy eigenvalues are required the scaling method [142] is well suited. Alternatively, the

plane wave decomposition [132, 143] or scattering methods [144–146] have been considered.

We want to discuss the improved method of particular solutions in more detail. The main idea is given by the decomposition of the eigenfunctions of the billiard ψ_n into a set of basis functions ϕ_j which fulfill the Schrödinger equation (3.182) on Ω but do not account for the Dirichlet boundary conditions on $\partial\Omega$

$$\psi_n = \sum_{j=1}^N c_j \phi_j. \quad (3.218)$$

Under variation of the energy E we want to find the expansion coefficients c_j such that the linear combination ψ_n also fulfills the boundary conditions on $\partial\Omega$ as the quantization condition. The expansion of Eq. (3.218) is truncated at $j = N$ such that the problem can be treated numerically and we use polar coordinates in real space $\mathbf{q} = (r, \varphi)$.

The original method of particular solutions [147] consists of taking N points (r_i, φ_i) , $i = 1, \dots, N$, which are randomly located on the boundary $\partial\Omega$ and solving a set of linear equations $A(E)c = 0$ with the matrix A given by

$$A_{ij}(E) = \phi_j(r_i, \varphi_i, E). \quad (3.219)$$

As the amplitude of each eigenfunction on the billiard boundary has to be equal to zero, an eigenvalue is found if the determinant $\det(A(E)) = 0$ is zero. This approach can be generalized by using $N_p > N$ points on the boundary such that the matrix A becomes an $N_p \times N$ matrix. Then, an eigenvalue is found if the lowest singular value of this matrix is equal to zero.

However, the described method is delicate as spurious solutions may occur which are zero on the boundary and in the interior of the billiard simultaneously. These solutions lead to predicted energies which are not eigenenergies of the system. To solve this problem the improved method of particular solutions [141, 148] additionally considers N_p randomly chosen points inside the billiard. Hence, the matrix A is a composition of one block A_B in which the basis functions are evaluated at the boundary and another block A_I where they are evaluated in the interior of the billiard

$$A(E) = \begin{bmatrix} A_B(E) \\ A_I(E) \end{bmatrix}. \quad (3.220)$$

It is a $2N_p \times N$ matrix. To find the eigenvalues of the system we orthogonalize this matrix A using a QR-decomposition where Q is orthogonal and R is an upper triangular matrix

$$A(E) = \begin{bmatrix} Q_B(E) \\ Q_I(E) \end{bmatrix} R(E) = Q(E)R(E). \quad (3.221)$$

We denote the range of $A(E)$ by $\mathcal{A}(E)$ which describes the space of basis functions evaluated at the boundary $\partial\Omega$ and the interior Ω of the billiard. For $u \in \mathcal{A}(E)$ there exists a $v \in \mathbb{R}^N$

such that

$$u = Q(E)v, \quad \|v\| = 1, \quad v \in \mathbb{R}^N. \quad (3.222)$$

For the identification of a certain energy E as an eigenenergy of the billiard we consider the vector $\tilde{v} \in \mathbb{R}^N$ for which $\tilde{u} \in \mathcal{A}(E)$ is minimal on the boundary

$$\sigma(E) = \|Q_B(E)\tilde{v}\| = \min_{v \in \mathbb{R}^N, \|v\|=1} \|Q_B(E)v\|. \quad (3.223)$$

Numerically, \tilde{v} and $\sigma(E)$ are determined by the singular value decomposition of $Q_B(E)$ in which \tilde{v} is the right singular vector of $Q_B(E)$ with the corresponding smallest singular value $\sigma(E)$. Now let us consider the norm of $\tilde{u} = Q(E)\tilde{v}$

$$1 = \|\tilde{v}\|^2 = \|Q(E)\tilde{v}\|^2 = \|Q_B(E)\tilde{v}\|^2 + \|Q_I(E)\tilde{v}\|^2 = \sigma(E)^2 + \|Q_I(E)\tilde{v}\|^2 = \|\tilde{u}\|^2. \quad (3.224)$$

Spurious solutions as mentioned before can no longer occur as the vector \tilde{u} has approximately norm one inside the billiard, if $\sigma(E) \approx 0$. The eigenvalues E_n of the system are determined by calculating $\sigma(E)$ under variation of E and by finding its minima $\sigma(E_n) \approx 0$, see Fig. 3.25. The distance of $\sigma(E_n)$ from zero is a direct measure of the error of the determined eigenenergy E_n . The coefficients c for the decomposition of the eigenfunction ψ_n are given as

$$c = R(E)^{-1}\tilde{v}. \quad (3.225)$$

Using these coefficients c the eigenfunction ψ_n is found, see Fig. 3.26 for an example. Note that degeneracies in the spectrum can be located by the evaluation of the second smallest singular value. If a quasi-degeneracy occurs this second smallest singular value will show a minimum in between the two energy levels, which allows to determine the corresponding two eigenvalues. One of them is located at an energy smaller than the minimum of the second singular value and the other is found at a larger energy, see Fig. 3.25.

An alternative formulation is given by the tension function $t[u]$

$$t[u] = \frac{\|u\|_{\partial\Omega}}{\|u\|_{\Omega}}, \quad t_{\min}(E) = \min_{u \in \mathcal{A}(E)} t[u]. \quad (3.226)$$

If $t_{\min}(E)$ is zero an eigenvalue E_n is found. Its error is estimated by $d \cdot t_{\min}(E_n)$ in which d is a constant [149]. For increasing energies the number of necessary basis functions N increases which slows down the calculation (effort $\sim N^3$). A good choice in the semiclassical limit is given by $N = 9k/4$ [149].

The results of the described method of particular solutions substantially depend on the choice of the basis functions ϕ_j . Particularly suited for the billiards studied in this thesis are the so-

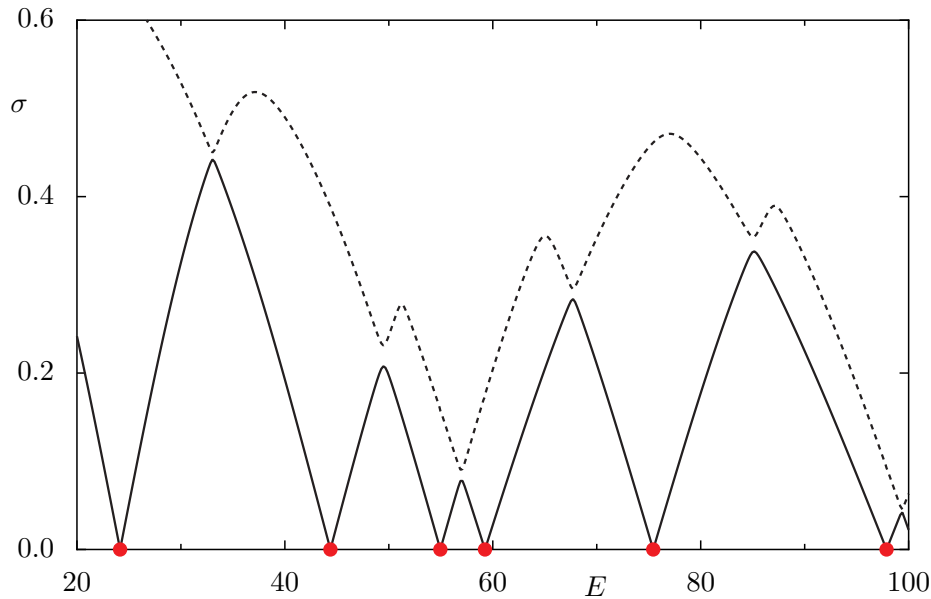


Figure 3.25: The smallest singular value σ (solid line) and the second smallest singular value (dashed line) is shown under variation of the energy E for an example billiard. Positions at which the smallest singular value has a minimum are marked by red dots. They correspond to eigenenergies of the system.

called Bessel-Fourier functions

$$\phi_j(r, \varphi, E) = J_{\alpha_j}(\sqrt{E}r) \sin(j\alpha\varphi). \quad (3.227)$$

They are zero on a corner of angle π/α located at the origin. Hence, an appearing Dirichlet boundary condition of such a corner is already accounted for by the choice of these basis functions. Examples are given by $\alpha = 2/3$ for the mushroom billiard or $\alpha = 2$ for each billiard with a corner of angle $\pi/2$ such as the desymmetrized stadium billiard. Furthermore, these basis functions give the possibility to avoid singular behavior resulting from corners of angle $\theta \neq \pi/n$, $n \in \mathbb{N}$, which would otherwise result in a slow convergence of the method.

The basis functions, Eq. (3.227), are highly ill-conditioned leading to a large null space of A . For large $\sigma(E)$ this singular value shows fluctuations under variation of E which makes the determination of the minima of $\sigma(E)$ more difficult. One method to avoid these fluctuations is given by the regularization procedure. For this regularization we consider the QR-decomposition of the matrix A . Calculating the singular values of $R(E)$ leads to the representation

$$R(E) = U(E)S(E)V(E), \quad (3.228)$$

in which $S(E)$ contains the singular values of $R(E)$ on its diagonal. We define a threshold $\epsilon \approx 10^{-13}$, sort the singular values $\sigma_1 \geq \sigma_2 \geq \dots > \sigma_{N(\epsilon)} > \epsilon$, and consider only those singular values which are larger than ϵ . We define the matrix \tilde{U} containing all left singular vectors of U

with corresponding singular values $\sigma_i > \epsilon$ and instead of Eq. (3.223) we solve

$$\sigma(E) = \|Q_B(E)\tilde{U}\tilde{v}\| = \min_{v \in \mathbb{R}^{N(\epsilon)}, \|v\|=1} \|Q_B(E)\tilde{U}v\| \quad (3.229)$$

to find the eigenvalues of the system. With this procedure the large null space of the ill-conditioned basis can be avoided and $\sigma(E)$ does not fluctuate under small variations of E . However, by this regularization the eigenvalues E_n are slightly shifted [149]. Hence, we use the regularization on a coarse energy grid to approximately find the minima of $\sigma(E)$ and the non-regularized procedure for the accurate determination of the eigenenergies E_n .

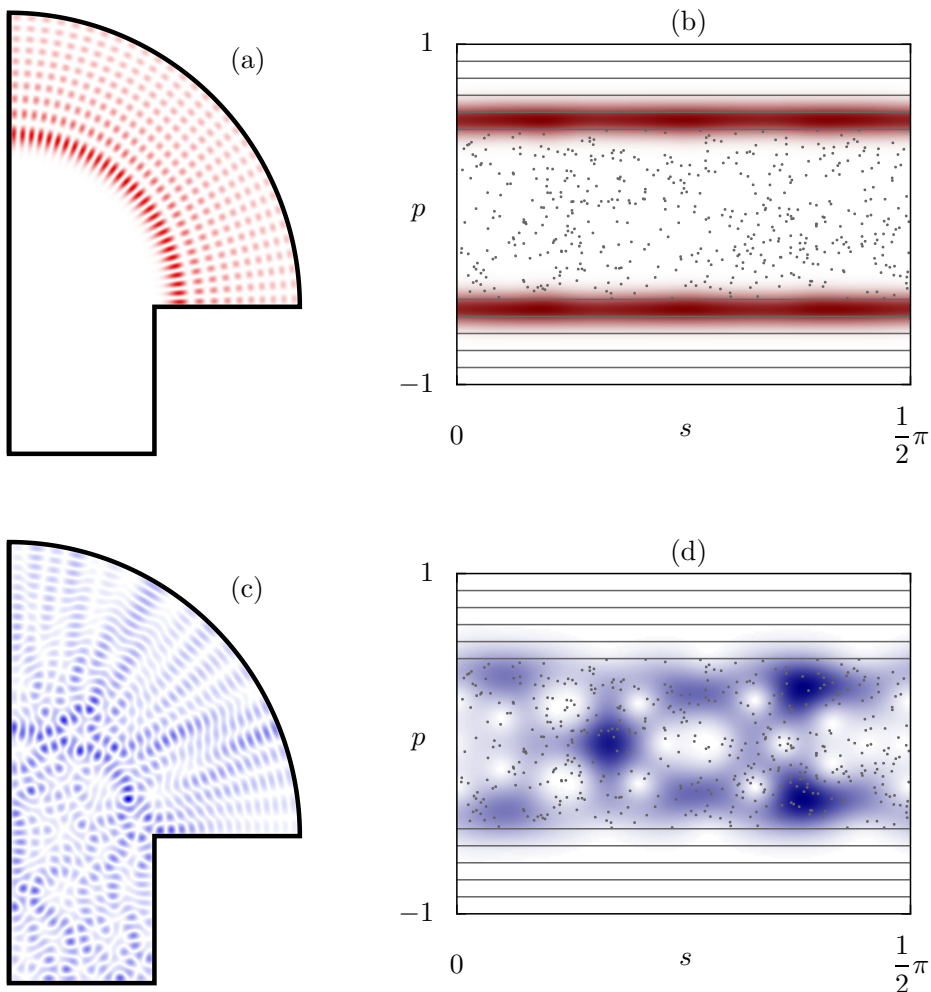


Figure 3.26: Modulus squared of a regular eigenfunction (a) and a chaotic eigenfunction (c) of the desymmetrized mushroom billiard at energy $E \approx 11596.3$ (a) and $E \approx 11836.9$ (c). The corresponding Poincaré Husimi function is mainly localized either in the regular region of phase space (b) or in the chaotic sea (d). Here, we show only the part of the Poincaré section which corresponds to the circular part of the boundary and use $l = 0.5$ as the length of the stem, $a = 0.5$ as its width, and $R = 1$ for the radius of the cap.

3.2.3 Numerical methods for the calculation of tunneling rates

In Chapter 5 we want to study the dynamical tunneling process in billiard systems with a mixed phase space. In order to verify our theoretical prediction it will be compared to numerical data. Hence, in this section we introduce two approaches for the numerical determination of tunneling rates. While the first method evaluates the widths of avoided crossings the second approach uses scattering theory. The results of the two methods are found to be in good agreement for the considered billiards.

Evaluation of avoided crossings

Similar as presented for quantum maps in Section 3.1.5 we find the tunneling rate of a regular state by averaging over widths of avoided crossings between this regular and several chaotic states. Numerically, we determine the spectrum in the vicinity of the considered regular energy under variation of the boundary of the billiard. If we vary those parts of the boundary which are located in the classically chaotic region of phase space only, the regular eigenenergies are almost unaffected and remain constant while the eigenenergies of the chaotic states vary drastically. Hence, avoided crossings of widths $\Delta E_i = E_{\text{reg}} - E_{\text{ch},i}$ appear, see Fig. 3.27. The tunneling rate is given by Fermi's golden rule

$$\gamma = 2\pi \frac{\langle |\Delta E_i|^2 \rangle_i}{4} \rho_{\text{ch}} \approx \frac{A_{\text{ch}}}{8} \langle |\Delta E_i|^2 \rangle_i \quad (3.230)$$

where we average over all numerically determined widths ΔE_i and ρ_{ch} is the density of chaotic states which we approximate by its leading Weyl term, $\rho_{\text{ch}} \approx A_{\text{ch}}/(4\pi)$. The area A_{ch} is the

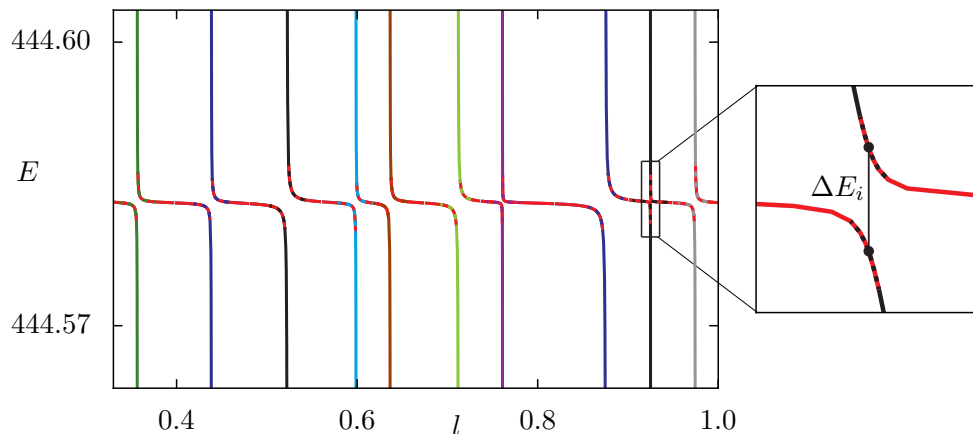


Figure 3.27: The eigenvalues of mushroom billiards with stem width $a = 0.5$ and radius $R = 1$ are presented under variation of the height of the stem l . While the energy of the regular state remains almost unaffected (red line) the chaotic eigenenergies vary drastically (colored lines). This leads to avoided crossings between the regular and the chaotic eigenvalues with splittings ΔE_i (dashed lines). In the inset one of the avoided crossings is magnified.

area of the billiard times the fraction of the chaotic phase-space volume.

Note that this method is applied to determine dynamical tunneling rates for most of the billiards discussed in Chapter 5. Compared to quantum maps the computing time to obtain an equal number of tunneling rates may increase by a factor of more than 1000. It can be a challenging task to deform a part of the billiard boundary such that the regular dynamics is unchanged and the numerical methods for the determination of eigenvalues are still applicable.

Scattering approach

In analogy to the approach of opening the system for quantum maps (see Section 3.1.5) we consider a method presented in Ref. [150] which can be applied to determine tunneling rates in billiards. It consists of attaching a lead to a part of the billiard and allows to calculate the decay of a quasi-stationary state through this lead. If the lead is placed into a region of the billiard in which the classical dynamics is completely chaotic, the regular states will appear as such quasi-stationary states and their decay can be determined. Note that this approach assumes that after tunneling from the regular island to the chaotic sea, the transport to the lead is a fast process. This assumption is violated for example if partial barriers are relevant in the chaotic part of phase space which limit the quantum transport.

Let $H = \mathbf{p}^2 + V(\mathbf{q})$ be the Hamiltonian of the given system which can also have a soft-wall potential. The time-independent Schrödinger equation reads

$$(\hat{H} - E_n)\psi_n(\mathbf{q}) = 0 \quad (3.231)$$

or by means of the Green's function

$$(\hat{\mathbf{p}}^2 + V(\mathbf{q}) - E) G(\mathbf{q}, \mathbf{q}', E) = \delta(\mathbf{q} - \mathbf{q}'). \quad (3.232)$$

In spectral representation the Green's function reads

$$G(\mathbf{q}, \mathbf{q}', E) = \sum_{n=1}^{\infty} \frac{\psi_n^*(\mathbf{q})\psi_n(\mathbf{q}')}{E - E_n}. \quad (3.233)$$

Now we cut the position space Ω of the billiard by a one-dimensional line $\partial\Omega_c$ into two regions Ω^+ and Ω^- . The vector $\mathbf{q} = (\xi, \eta)$ is decomposed into a part ξ which determines the position on $\partial\Omega_c$ and a part η perpendicular to it. For potentials $V(\mathbf{q})$ which are continuous on the boundary $\eta = 0$ we introduce $H^\pm = \mathbf{p}^2 + V_\pm(\mathbf{q})$ in which $V_\pm(\mathbf{q}) = \Theta(\pm\eta)V(\mathbf{q}) + \Theta(\mp\eta)V_{\text{lead}}(\xi, \eta)$. For the sign $+$, which we use for our billiard systems, Ω^- becomes an infinitely long lead and for the $-$ sign Ω^+ is the lead described by the potential $V_{\text{lead}}(\xi, \eta)$ (see Fig. 3.28 for an illustration).

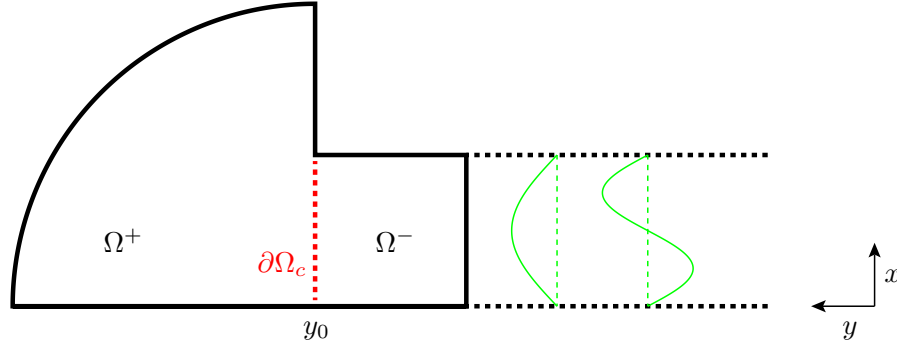


Figure 3.28: Illustration of the transition from the closed and desymmetrized mushroom billiard (black solid lines) to a scattering system. The billiard is cut at $\partial\Omega_c$ (red dashed line) into two regions Ω^+ and Ω^- such that Ω^- becomes an infinitely long lead (black dashed lines). The first two transverse modes in this lead are shown in green.

The transverse modes in the lead are determined by

$$(\hat{p}_\xi^2 + V_{\text{lead}}(\xi, 0) - E_l) \phi_l(\xi) = 0 \quad (3.234)$$

which for infinitely high potential walls in a distance a results in

$$\phi_l(\xi) = \sqrt{\frac{2}{a}} \sin\left(\frac{\pi\xi}{a} l\right). \quad (3.235)$$

Their energies are $E_l = \pi^2 l^2 / a^2$. The full lead modes read

$$\phi_l^\pm(\xi, \eta) = \frac{1}{\sqrt{k_l}} \phi_l(\xi) e^{\pm i k_l \eta}, \quad (3.236)$$

where $k_l = \sqrt{E - E_l}$ for open and $k_l = i\sqrt{E_l - E}$ for evanescent modes. In the vicinity of $\partial\Omega_c$ the eigenstates of the systems $H^\pm \psi^\pm = E^\pm \psi^\pm$ are given as superpositions of the lead modes

$$\psi^\pm(\mathbf{q}) = \sum_l c_l^\pm \psi_l^\pm(\mathbf{q}), \quad (3.237)$$

$$\psi_l^\pm(\mathbf{q}) = \sum_k \delta_{kl} \phi_k^\pm + S_{kl}^\pm \phi_k^\mp. \quad (3.238)$$

They have the form of scattering wave functions with a single incoming wave in channel l and a linear combination of outgoing waves determined by the scattering matrix S . The sum is not restricted to open modes such that the usual unitary S -matrix is a subblock in S . Now we represent the Green's function in the vicinity of $\partial\Omega_c$ in terms of the scattering functions $\psi^\pm(\mathbf{q})$

$$G(\mathbf{q}, \mathbf{q}') = \frac{1}{2i} \sum_{k,l} g_{kl} \psi_k^+(\mathbf{q}_>) \psi_l^-(\mathbf{q}_<), \quad (3.239)$$

$$G(\mathbf{q}, \mathbf{q}') = \frac{1}{2i} \sum_{l, l'} \frac{\phi_l(\xi) \phi_{l'}(\xi')}{\sqrt{k_l} \sqrt{k_{l'}}} \left[\delta_{ll'} e^{ik_l |\eta - \eta'|} + \sum_{\sigma, \sigma' = \pm} g_{ll'}^{\sigma\sigma'} e^{i\sigma k_l \eta + i\sigma' k_{l'} \eta'} \right] \quad (3.240)$$

in which the symbols $>$ ($<$) are introduced to select the argument with the larger (smaller) coordinate η . For $\eta \leq \eta'$ we write in matrix form $g^{++} = gS^-$, $g^{--} = S^+g$, $\mathbb{1} + g^{+-} = g$, and $g^{-+} = S^+gS^-$. Using $g^{+-} = g^{-+}$ we find $g = (\mathbb{1} - S)^{-1}$ in which $S = S^+S^-$.

Evaluating the Green's function we finally obtain

$$iK = -(g^{++} + g^{--}) = \frac{\mathbb{1} - S^-}{\mathbb{1} + S^+}, \quad (3.241)$$

in which

$$K_{ll'} = \frac{1}{\sqrt{k_l k_{l'}}} \frac{\partial^2}{\partial \eta \partial \eta'} g_{ll'}(0, 0). \quad (3.242)$$

Now we represent K by

$$K = \pi W^\dagger \frac{1}{E - H} W, \quad (3.243)$$

in which

$$W_{ml} = \frac{1}{\sqrt{\pi k_l}} \left. \frac{d\psi_{ml}(\eta)}{d\eta} \right|_{\eta=0} \quad (3.244)$$

includes the first derivative of

$$\psi_{ml}(\eta) = \int_{\partial\Omega_c} d\xi \phi_l^*(\xi) \psi_m(\xi, \eta) \quad (3.245)$$

with respect to η and describes the coupling of $\psi_m(\mathbf{q})$ to the l th scattering channel. Summarized, the final result reads [150]

$$W_{ml} = \frac{1}{\sqrt{\pi k_l}} \int_{\partial\Omega_c} d\xi \phi_l^*(\xi) \left. \frac{\partial \psi_m(\xi, \eta)}{\partial \eta} \right|_{\eta=0}. \quad (3.246)$$

To determine the tunneling rate of the m th regular state we sum over the modulus squared of the couplings to all open channels

$$\gamma_m \approx \sum_l |W_{ml}|^2. \quad (3.247)$$

For billiards with a hard wall boundary the potential is not continuous along each cut $\partial\Omega_c$. This difficulty can be solved if we start with a smooth potential and introduce a parameter

δ such that for $\delta \rightarrow 0$ the hard-wall billiard is recovered. Using this formal limiting process Eq. (3.247) can be applied numerically.

We present the mushroom billiard as an illustration: For the cut we choose $\partial\Omega_c$ along the x -axis in the stem at $y = y_0 < 0$. We numerically calculate a regular eigenfunction of the billiard ψ_m and its derivative with respect to y . With Eq. (3.246) we determine the couplings W_{ml} to the l th lead mode. The tunneling rate is then given by the sum over all couplings in Eq. (3.247). For the mushroom billiard the result is independent of the actual choice of y_0 . This does not hold for arbitrary billiards as partial barriers might exist in the chaotic part of phase space which lower the determined tunneling rates.

Problematic is the usage of real eigenfunctions in Eq. (3.246). Their weight in the chaotic part of phase space depends on the energy distance to the next chaotic state. In the most extreme case, at an avoided crossing, half of the weight is located in the chaotic region and the predicted tunneling rates are useless. Hence, we only consider parameter values for which the next chaotic state is located at least the mean level spacing away from the regular energy. These situations are obtained under variation of the length of the stem. This procedure is applicable also to other systems and has been successfully implemented for the cosine and the annular billiard. The most important advantage of this method compared to the evaluation of avoided crossings discussed previously is the significant gain in computing time. It allows a reliable and fast computation of resonance properties using only information of the closed billiard systems.

3.3 Optical microcavities

Optical microcavities confine photons inside a dielectric medium due to total internal reflection at its boundary. They are most relevant for various applications such as ultralow-threshold lasers [151, 152], single-photon emitters [153, 154], or correlated photon-pair emitters [155]. We consider two-dimensional cavities and describe the classical dynamics within the ray picture. Depending on the shape of the cavity this ray dynamics can be regular, chaotic, or mixed. Rays which do not fulfill the condition of total internal reflection escape to the outside. Hence, optical microcavities are open systems in which the openness is related to the possibility of refractive escape. We want to study the dependence of this escape on the classical phase-space structure considering dynamical tunneling in Chapter 6.

In this section the classical ray picture for microcavities will be shortly introduced and we discuss their quantum (wave) behavior which is described by the two-dimensional Schrödinger equation for transverse magnetic polarization. For more detailed information the reader should consult Refs. [156, 157] and references therein.

3.3.1 Ray dynamics

We consider optical microcavities which consist of a two-dimensional compact domain $\Omega \in \mathbb{R}^2$ filled with a dielectric medium of refractive index $n_\Omega > 1$. It is surrounded by a medium of refractive index n_0 which is usually air with $n_0 = 1$. For $n_\Omega > n_0$ light can be confined inside the domain Ω due to total internal reflection at the optically thinner medium if its angle of incidence χ is larger than the critical angle χ_c ,

$$\chi > \chi_c := \arcsin\left(\frac{n_0}{n_\Omega}\right). \quad (3.248)$$

If Eq. (3.248) is fulfilled the ray is elastically reflected at the boundary of the cavity $\partial\Omega$ such that the angle of incidence and the angle of reflection are identical. The boundary consists of a finite number of smooth components which are characterized by their curvature κ . For $\kappa < 0$ the resulting dynamics is defocusing, for $\kappa > 0$ focusing, and for $\kappa = 0$ it is neutral. The singular points at which the different parts of the boundary meet are called corners, see Fig. 3.29. As long as the light ray fulfills the condition of total internal reflection it can be described identical to a classical particle moving in a hard-wall billiard, introduced in Section 3.2.1. Its energy is conserved and its motion is limited to a three-dimensional energy plane. The Poincaré section can be used to visualize its dynamics in phase space. If the angle of incidence is smaller than the critical angle of total internal reflection the light ray escapes to the outside, without considering ray-splitting effects. This critical angle is given by the lines $p_c = \pm n_0/n_\Omega$ in the

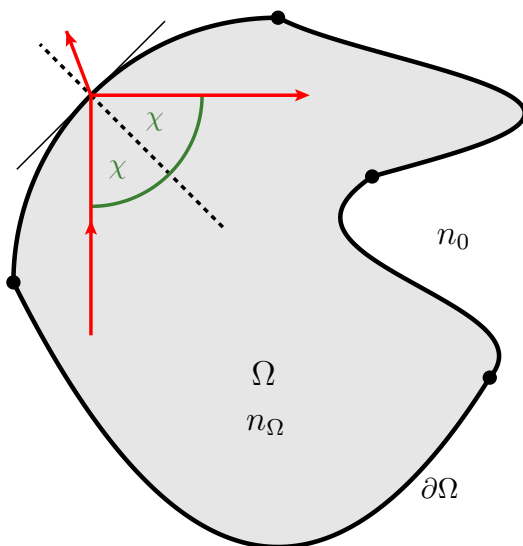


Figure 3.29: Sketch of an optical microcavity: It consists of the interior Ω (gray region) with refractive index n_Ω and the exterior with refractive index n_0 . For $n_\Omega > n_0$ light can be trapped inside the cavity by total internal reflection or leave the cavity due to refraction (red lines). For $\chi > \chi_c$ the ray is assumed to be elastically reflected at the boundary $\partial\Omega$. The different smooth parts of the boundary are connected at corners marked by black dots.

Poincaré section ($p = \sin \chi$). Hence we may use the simplified picture of a cavity with hard wall boundary conditions, which we find for $n_\Omega \rightarrow \infty$, and consider the region $|p| < p_c$ as absorbing.

While the discussed ray-dynamics can explain many quantum mechanical features using semiclassical approaches [158–162] it fails for certain situations and has to be corrected e.g. by considering the Goos-Hänchen shift [163–165] and Fresnel filtering [164, 166, 167]. These effects are related to the fact that the dimension of the cavities are of the order of the wavelength of the confined light such that the wave nature of light is relevant. They change the dynamics such that it becomes non-Hamiltonian [168, 169]. For our purposes, however, the ray picture is sufficient.

Depending on the shape of the boundary $\partial\Omega$ rays which fulfill the condition of total internal reflection can show regular, chaotic, or mixed dynamics, see the discussion in Section 3.2.1 for hard-wall billiard systems and Fig. 3.30 which presents the classical Poincaré section of an annular microcavity. Rays which show chaotic dynamics usually spread exponentially fast in phase space and quickly violate the condition of total internal reflection. Of particular interest are those chaotic trajectories which under forward or backward time evolution remain infinitely long inside the cavity. They form the so-called chaotic repeller which has a fractal dimension. Quantum mechanically, it is relevant for the exponent of the fractal Weyl law [170] and can be used to obtain directional emission as well as high quality factors at the same time [171].

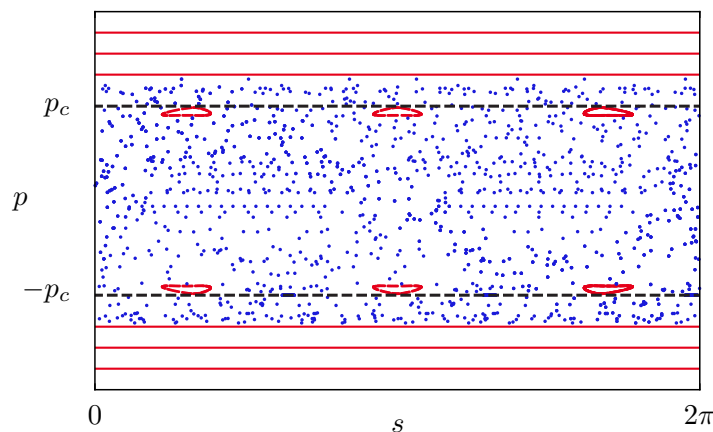


Figure 3.30: Poincaré section of an annular cavity with $n_\Omega = 2$ and $n_0 = 1$ for which we applied hard-wall boundary conditions at the exterior boundary (same as Fig. 6.2(b)). We find whispering-gallery motion and small regular islands (red) as well as chaotic motion (blue). The critical angle of total internal reflection at $p = \pm p_c$ is marked by black dashed lines. All points inside the strip $|p| < p_c$ will escape to the outside of the cavity.

3.3.2 Wave mechanics

In order to describe the wave mechanics of an optical microcavity we consider the two Maxwell equations [172, 173]

$$\nabla \times \mathbf{E} = -\frac{1}{c} \frac{\partial \mathbf{H}}{\partial t} = ik\mathbf{H}, \quad (3.249)$$

$$\nabla \times \mathbf{H} = \frac{1}{c} \frac{\partial \mathbf{D}}{\partial t} = -ikn_{\Omega}^2 \mathbf{E} \quad (3.250)$$

in which \mathbf{E} is the electric and \mathbf{H} the magnetic field vector, c denotes the speed of light in vacuum, and we assume that all fields have the time dependency $e^{-i\omega t}$ with a frequency ω . The wave number k is given by $k = \omega/c$. Combining these equations we find the following wave equations

$$\nabla \times (\nabla \times \mathbf{E}) = (n_{\Omega}k)^2 \mathbf{E}, \quad (3.251)$$

$$\nabla \times (\nabla \times \mathbf{H}) = (n_{\Omega}k)^2 \mathbf{H}. \quad (3.252)$$

Charge density can appear only at the surface of the dielectric components such that we have $\nabla \cdot \mathbf{E} = 0$ in each domain of constant refraction index. If \mathbf{E} is parallel to the z -axis this holds even at the interfaces which is the case we focus on. For Eq. (3.251) we obtain

$$-\nabla^2 \mathbf{E} = n_{\Omega}^2 k^2 \mathbf{E}. \quad (3.253)$$

It can be rewritten in a form similar to the Schrödinger equation

$$-\nabla^2 \mathbf{E} + k^2(1 - n_{\Omega}^2) \mathbf{E} = k^2 \mathbf{E} \quad (3.254)$$

in which a potential term $k^2(1 - n_{\Omega}^2)$ appears which in contrast to the time-independent Schrödinger equation depends on the wave number k .

So far we have not considered any boundary conditions between the dielectric medium and vacuum (or air). These boundary conditions depend on the polarization of \mathbf{E} . We choose the polarization such that $\mathbf{E} = \mathcal{E} \mathbf{e}_z$ is parallel to the z -axis with a perpendicular propagation direction. This situation is called transverse magnetic (TM) polarization as the magnetic field \mathbf{H} is transverse to the z -axis. \mathbf{H} has to be continuous for a dielectric insulator without current flows. For the azimuthal component of the magnetic field in polar coordinates (r, φ) one finds

$$H_{\varphi} = -\frac{i}{k} [\nabla \times \mathcal{E} \mathbf{e}_z]_{\varphi} = \frac{i}{k} \frac{\partial \mathcal{E}}{\partial r}. \quad (3.255)$$

The tangential components of \mathbf{E} are continuous at the interface which for TM polarization applies to \mathcal{E} itself. Hence, \mathcal{E} and $\partial \mathcal{E} / \partial r$ have to be continuous at the interface. One finds that

TM polarization leads to the same boundary conditions as are found in quantum mechanics. In transverse electric (TE) polarization the same holds for the magnetic field $\mathbf{H} = \mathcal{H}\mathbf{e}_z$.

We introduce a wave function $\psi(\mathbf{q})$ defined on the two-dimensional (x, y) -plane according to $\mathcal{E}(\mathbf{q}, t) = \text{Re}[\psi(\mathbf{q}) \exp(-i\omega t)]$ such that ψ represents the time-independent z -component of the electric field vector. For TM polarization Eq. (3.253) reads

$$-\nabla^2\psi = n_\Omega^2 k^2 \psi. \quad (3.256)$$

The boundary conditions are dependent on the experimental situation. In scattering experiments the wave function is composed of an incoming plane wave of wave vector \mathbf{k} and an outgoing scattered wave. Its asymptotic form is

$$\psi \sim \psi_{\text{in}} + \psi_{\text{out}} = e^{i\mathbf{k}\mathbf{q}} + f(\varphi, \mathbf{k}) \frac{e^{ikr}}{\sqrt{r}} \quad (3.257)$$

in which $f(\varphi, \mathbf{k})$ is the angle-dependent differential amplitude for elastic scattering. In lasers the radiation is generated within the cavity such that we have no incoming wave

$$\psi \sim \psi_{\text{out}} = f(\varphi, \mathbf{k}) \frac{e^{ikr}}{\sqrt{r}}. \quad (3.258)$$

For real valued refractive index n_Ω this situation leads to states that are exponentially decaying in time. The life-time τ of these resonant states which are also called resonances is given by the imaginary part of the wave number, $\tau = -1/(2c\text{Im}(k))$, with $\text{Im}(k) < 0$ and we choose $c = 1$. The life-time τ is related to the quality factor Q by $Q = \text{Re}(\omega)\tau$. The resonances are connected to peak structures in scattering spectra [174] and were introduced in Refs. [3, 175]. In contrast to Eq. (3.189) for hard-wall billiards their counting function obeys a fractal Weyl law [170].

The wave equation (3.256) with outgoing boundary conditions (3.258) can be solved analytically only for special geometries such as the circular cavity, introduced in Section 6.1, or the symmetric annular cavity [176]. In general, numerical methods have to be applied. While wave-function matching methods are applicable for slightly deformed circular cavities [156] we choose a boundary element method [177] which allows a determination of the resonances for more general systems. Related to the boundary integral method for hard-wall billiards it replaces the two-dimensional Eq. (3.256) by one-dimensional boundary-integral equations which are evaluated on the discretized boundary $\partial\Omega$. For dielectric cavities the wave function and its normal derivative are continuous on $\partial\Omega$. The boundary element method has been extended to this situation in Refs. [177, 178]. Throughout this thesis this method will be used to determine resonance states of dielectric microcavities and their decay rates γ [179]. The interested reader is referred to Ref. [177] for more details on the numerical implementation of the boundary element method. An example is presented in Fig. 3.31.

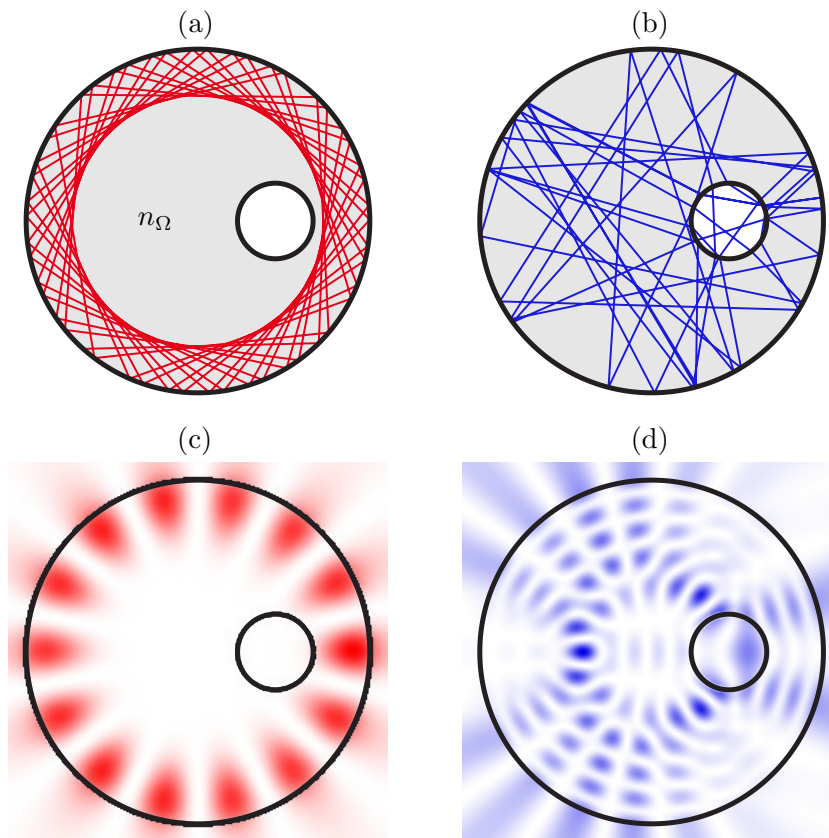


Figure 3.31: Ray and wave mechanics in the annular cavity: In (a) a regular whispering-gallery trajectory is shown while (c) presents a corresponding solution of the wave equation obtained by the boundary integral method [179]. The chaotic trajectory in (b) shows reflection at the inner disk while the outer boundary is considered as a hard wall. A similar looking chaotic mode is determined numerically and presented in (d) without using hard wall boundary conditions.

4 Dynamical tunneling in quantum maps

In Chapter 2 we studied the tunneling process in one-dimensional time-independent systems and obtained smoothly decaying tunneling rates γ when approaching the semiclassical limit. This behavior can change drastically if higher dimensional or time-dependent systems are considered. We study systems with a mixed phase space, in which regular and chaotic motion coexist. While the classical motion is regular or chaotic at all times and separated by a so-called dynamical barrier, this barrier can be penetrated quantum mechanically due to dynamical tunneling [23]. This has also been observed experimentally using cold atoms in periodically modulated optical lattices [11, 12].

The influence of chaotic dynamics on the tunneling process between separated regular regions has been studied by Tomsovic and Ullmo [24, 34]. Typically one observes enhanced tunneling rates compared to the exponential behavior found for integrable systems. This enhancement occurs if chaotic states are energetically close to the considered regular states and is called chaos-assisted tunneling [24]. While the statistical properties of this tunneling process are well understood, a quantitative prediction of the mean tunneling rate is still missing. The aim of this chapter is to derive such a quantitative prediction of dynamical tunneling rates, describing the decay of a regular state towards the chaotic sea.

In the quantum regime, $h_{\text{eff}} \lesssim A$, in which the effective Planck constant is smaller but comparable to the size of the regular island A , small features in the classical phase space, such as nonlinear resonances inside the regular region, are expected to be irrelevant for quantum mechanics. In this regime dynamical tunneling leads to a coupling of a regular state to the chaotic sea without intermediate processes. Thus, we call this process direct regular-to-chaotic tunneling. It has been investigated in Ref. [46]; however, the prediction is not generally applicable (see Section 4.1.4). Other studies in this regime consider situations where dynamical tunneling can be described by one-dimensional tunneling under a barrier [43–45]; however, in our opinion the general scenario is more complicated. In the next Section 4.1 we present a new approach to direct dynamical tunneling from a regular island to the chaotic sea. The central idea is the use of a fictitious integrable system resembling the regular island. This leads to a tunneling formula involving properties of this integrable system as well as its difference to the mixed system under consideration. It allows for predicting tunneling rates from any quantized

torus within the regular island. We find excellent agreement with numerical data for quantum maps if tunneling is not affected by additional phase-space structures in the chaotic sea, such as partial barriers. The applicability to more general systems is demonstrated for the standard map, see Section 4.1.4.

In the semiclassical regime, $h_{\text{eff}} \ll A$, nonlinear resonances can be resolved by quantum mechanics and dominate the tunneling process. In 2001 Brodier, Schlagheck, and Ullmo derived the theory of resonance-assisted tunneling [53, 54] which describes the effect of such nonlinear resonances on the tunneling process. It explains the characteristic peaks and plateaus which appear in the tunneling rates due to quasi-degeneracies between regular states of different quantum number. However, quantitative deviations of several orders of magnitude arise when comparing the theoretical prediction to numerical data. Especially in the initial regime where resonances start to become relevant, which is of crucial importance to find the first experimental signatures of resonance-assisted tunneling, it cannot be applied. To overcome these problems we combine the approach for the direct tunneling mechanism using a fictitious integrable system with resonance-assisted tunneling and obtain a unified theory which is valid from the quantum to the semiclassical regime, see Section 4.2. Using two improvements to the original theory of resonance-assisted tunneling we obtain quantitative agreement with numerical data for a quantum map with one or multiple dominating resonances. Even for the standard map deep in the semiclassical regime as well as in the experimentally relevant regime excellent agreement is found.

4.1 Direct regular-to-chaotic tunneling

In the quantum regime, $h_{\text{eff}} \lesssim A$, in which the effective Planck constant h_{eff} is smaller but comparable to the size of the regular island A , the direct regular-to-chaotic tunneling process dominates. Here, nonlinear resonances and the hierarchical transition region are not resolved quantum mechanically and have no influence on the tunneling process.

In Section 4.1.1 we derive a theoretical prediction for the direct tunneling process. Its results depend on the choice of the fictitious integrable systems and we discuss its determination and convergence properties in Section 4.1.2. We present a semiclassical evaluation of our approach in Section 4.1.3. This leads to a formula predicting tunneling rates for systems with a harmonic oscillator-like regular island which requires only classical information.

In order to compare our theoretical predictions to numerical data we choose example maps which show only very small nonlinear resonance chains and a tiny hierarchical region, as discussed in Section 3.1.2. Hence, these structures will have no influence on the tunneling process for a large range of Planck's constant h_{eff} and we can compare our prediction to numerical data far into the semiclassical regime. We will discuss the relation of our approach to previous studies and consider generic systems such as the standard map in Section 4.1.4.

4.1.1 Theoretical description

We consider quantum maps with a mixed phase space described by a unitary time evolution operator \hat{U} [98]. Classically, the phase space is divided into parts of regular and chaotic dynamics, where we focus on situations of just one existing regular island in the chaotic sea. While classically no transition between the two phase-space regions is possible, they are quantum mechanically coupled due to the process of dynamical tunneling. This coupling has consequences for the eigenstates of the mixed system. While they are mainly regular or chaotic, i.e. concentrated on a torus inside the regular region or spread out over the chaotic sea, they do have at least a small component in the other region of phase space. This is most clearly seen for hybrid states (see Fig. 4.1(d)) which have the same weight in each of the components as they are involved in an avoided quasi-energy crossing. For a wave packet started on a quantized torus in the regular island coupled to an infinite chaotic sea the decay $e^{-\gamma t}$ is described by a tunneling rate γ . For systems with a finite phase space this exponential decay occurs at most up to the Heisenberg time $\tau_H = h_{\text{eff}}/\Delta_{\text{ch}}$, where Δ_{ch} is the mean level spacing of the chaotic states.

The main idea for the derivation of our theory which determines direct regular-to-chaotic tunneling rates γ is the decomposition of the mixed system \hat{U} into two main parts which describe the purely regular and purely chaotic dynamics as well as a part which includes the couplings of both phase-space regions, see Fig. 4.1. A similar approach has been presented in Section 2.4 where we decomposed the Hamiltonian of the one-dimensional double-well potential into two parts describing the dynamics in each well separately. For systems with a mixed phase space this separation is a complicated task as the couplings cannot be easily extracted from the mixed quantum map \hat{U} . In order to find the decomposition we introduce a fictitious integrable system \hat{U}_{reg} (a related idea was presented in Refs. [28, 46]). It has to be chosen such that its dynamics over one time unit resembles the classical motion corresponding to \hat{U} within the regular island as closely as possible and continues this regular dynamics into the chaotic region of \hat{U} , see Fig. 4.1(b). The eigenstates $|\psi_{\text{reg}}^m\rangle$ of \hat{U}_{reg} are purely regular in the sense that they are localized on the m th quantized torus of the regular region and continue to decay into the chaotic sea (Fig. 4.1(e)). This is the decisive property of $|\psi_{\text{reg}}^m\rangle$, which in contrast to the predominantly regular eigenstates of \hat{U} have no chaotic admixture. The explicit construction of \hat{U}_{reg} and further properties are discussed in the next section.

With the eigenstates $|\psi_{\text{reg}}^m\rangle$ of \hat{U}_{reg} , $\hat{U}_{\text{reg}}|\psi_{\text{reg}}^m\rangle = e^{i\varphi_{\text{reg}}^m}|\psi_{\text{reg}}^m\rangle$, we define a projection operator

$$\hat{P}_{\text{reg}} \approx \sum_{m=0}^{m_{\text{max}}} |\psi_{\text{reg}}^m\rangle\langle\psi_{\text{reg}}^m|, \quad (4.1)$$

which semiclassically projects onto the regular island only. The number of appearing regular states is limited by $m_{\text{max}} = \lfloor A/h_{\text{eff}} - 1/2 \rfloor$ in which A is the area of the regular island and h_{eff}

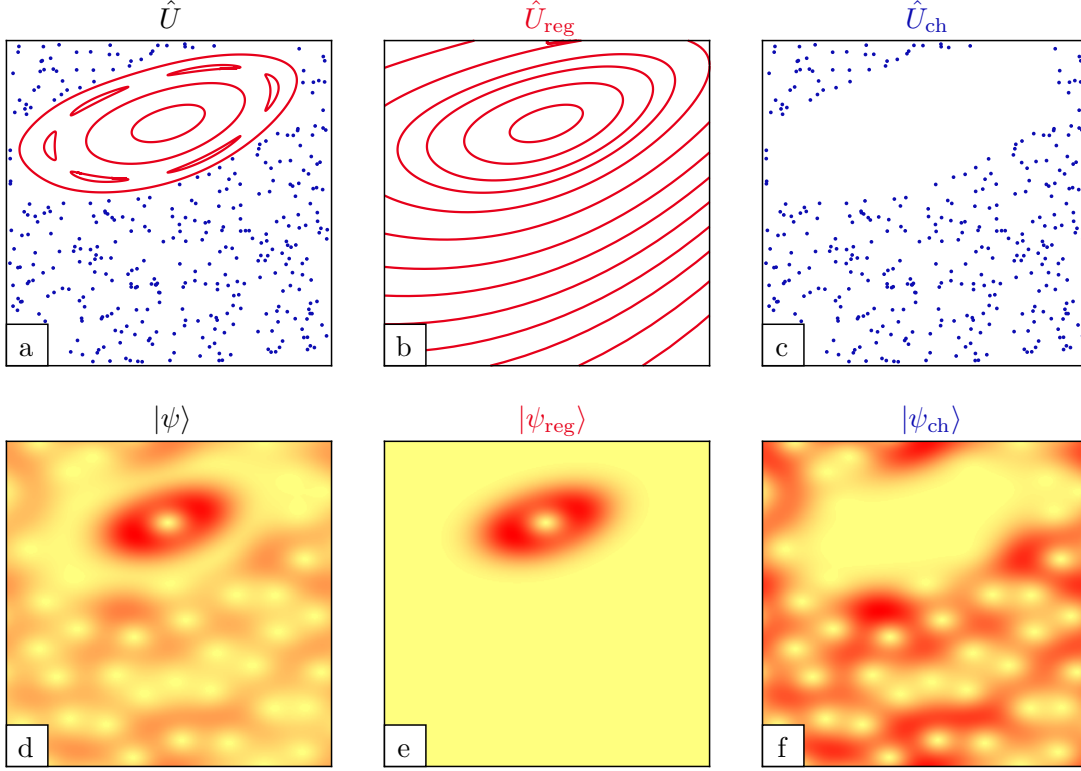


Figure 4.1: (a)-(c) The classical phase space corresponding to some quantum maps \hat{U} , \hat{U}_{reg} , and $\hat{U}_{\text{ch}} = \hat{P}_{\text{ch}}\hat{U}\hat{P}_{\text{ch}}$. (d)-(f) Husimi representation of eigenstates of such maps. Eigenstates of \hat{U} have a regular and a chaotic component, as illustrated in the strongest form of a hybrid state (d). The eigenstates $|\psi_{\text{reg}}^m\rangle$ ($|\psi_{\text{ch}}\rangle$) of \hat{U}_{reg} (\hat{U}_{ch}) are purely regular (chaotic).

is the effective Planck constant. The orthogonal projector $\hat{P}_{\text{ch}} = \hat{\mathbb{1}} - \hat{P}_{\text{reg}}$ then projects onto the chaotic phase-space component. For quantum maps \hat{U} we obtain

$$\hat{U} = (\hat{P}_{\text{reg}} + \hat{P}_{\text{ch}})\hat{U}(\hat{P}_{\text{reg}} + \hat{P}_{\text{ch}}) = \hat{P}_{\text{reg}}\hat{U}\hat{P}_{\text{reg}} + \hat{P}_{\text{ch}}\hat{U}\hat{P}_{\text{ch}} + \hat{P}_{\text{reg}}\hat{U}\hat{P}_{\text{ch}} + \hat{P}_{\text{ch}}\hat{U}\hat{P}_{\text{reg}}. \quad (4.2)$$

The time evolution operator \hat{U} is decomposed into a regular part $\hat{P}_{\text{reg}}\hat{U}\hat{P}_{\text{reg}}$, a chaotic part $\hat{P}_{\text{ch}}\hat{U}\hat{P}_{\text{ch}}$, and operators $\hat{P}_{\text{reg}}\hat{U}\hat{P}_{\text{ch}}$, $\hat{P}_{\text{ch}}\hat{U}\hat{P}_{\text{reg}}$, which couple the regular and the chaotic parts. They include the relevant information on dynamical tunneling. We now approximate Eq. (4.2) in order to diagonalize the regular part of \hat{U}

$$\hat{U} = \hat{P}_{\text{reg}}\hat{U}\hat{P}_{\text{reg}} + \hat{P}_{\text{reg}}(\hat{U} - \hat{U}_{\text{reg}})\hat{P}_{\text{reg}} + \hat{P}_{\text{ch}}\hat{U}\hat{P}_{\text{ch}} + \hat{P}_{\text{reg}}\hat{U}\hat{P}_{\text{ch}} + \hat{P}_{\text{ch}}\hat{U}\hat{P}_{\text{reg}} \quad (4.3)$$

$$\approx \hat{P}_{\text{reg}}\hat{U}\hat{P}_{\text{reg}} + \hat{P}_{\text{ch}}\hat{U}\hat{P}_{\text{ch}} + \hat{P}_{\text{reg}}\hat{U}\hat{P}_{\text{ch}} + \hat{P}_{\text{ch}}\hat{U}\hat{P}_{\text{reg}}. \quad (4.4)$$

The term $\hat{P}_{\text{reg}}(\hat{U} - \hat{U}_{\text{reg}})\hat{P}_{\text{reg}}$ accounts for couplings between regular states localized inside the same island, which are only relevant in the case of resonance-assisted tunneling. Here, they can be neglected. For the regular part of phase space we use the regular eigenstates $|\psi_{\text{reg}}^m\rangle$ of \hat{U}_{reg} as a basis, while for the chaotic component we may use an arbitrary basis $|\psi_{\text{ch}}\rangle$ which is

orthogonal to the states $|\psi_{\text{reg}}^m\rangle$ leading to

$$\hat{P}_{\text{ch}} = \sum_{\text{ch}} |\psi_{\text{ch}}\rangle\langle\psi_{\text{ch}}| \quad (4.5)$$

in which we sum over all $N_{\text{ch}} = N - m_{\text{max}} - 1$ purely chaotic states, see Fig. 4.1(f) for an example. In this basis the time evolution operator \hat{U} has the following matrix representation

$$\hat{U} \approx \left(\begin{array}{cc|cc} e^{i\varphi_{\text{reg}}^0} & 0 & v_{0,0} & v_{0,1} \\ 0 & e^{i\varphi_{\text{reg}}^1} & v_{1,0} & v_{1,1} \\ & & \ddots & \ddots \\ \hline v_{0,0}^* & v_{1,0}^* & w_{0,0} & w_{0,1} \\ v_{0,1}^* & v_{1,1}^* & w_{0,1}^* & w_{1,1} \\ & & \ddots & \ddots \end{array} \right). \quad (4.6)$$

It is diagonal in the regular part due to neglecting the regular-to-regular coupling term $\hat{P}_{\text{reg}}(\hat{U} - \hat{U}_{\text{reg}})\hat{P}_{\text{reg}}$. The coupling matrix elements $v_{j,m}$ in the off-diagonal blocks describe the coupling between the m th regular and j th chaotic state while the shape of the chaotic part depends on the chosen basis $|\psi_{\text{ch}}\rangle$, with $w_{i,j} := \langle\psi_{\text{ch}}^i|\hat{U}|\psi_{\text{ch}}^j\rangle$. Hence, the coupling matrix elements $v_{\text{ch},m}$ are

$$v_{\text{ch},m} = \langle\psi_{\text{ch}}|\hat{U}|\psi_{\text{reg}}^m\rangle \quad (4.7)$$

where $|\psi_{\text{reg}}^m\rangle$ and $|\psi_{\text{ch}}\rangle$ are orthogonal. The tunneling rate is obtained using

$$\gamma_m = \sum_{\text{ch}} |v_{\text{ch},m}|^2 \quad (4.8)$$

where we sum over coupling matrix elements $v_{\text{ch},m}$ between one particular regular state of quantum number m and different orthogonal chaotic states, see Appendix C.3 for its derivation. Using Eq. (4.7) in Eq. (4.8) we obtain

$$\gamma_m = \|\hat{P}_{\text{ch}}\hat{U}|\psi_{\text{reg}}^m\rangle\|^2 = \|(\hat{\mathbb{1}} - \hat{P}_{\text{reg}})\hat{U}|\psi_{\text{reg}}^m\rangle\|^2 \quad (4.9)$$

as our main result. It allows for the determination of tunneling rates from a regular state localized on the m th quantized torus to the chaotic sea. In Eq. (4.9) properties of the fictitious integrable system \hat{U}_{reg} and the chaotic projector $\hat{P}_{\text{ch}} = \hat{\mathbb{1}} - \hat{P}_{\text{reg}}$ enter. This projector allows to apply the result even if \hat{U} and \hat{U}_{reg} show slightly different dynamics within the regular region, as it projects out these differences. For the evaluation of Eq. (4.9) in Section 4.1.3 we use

$$\gamma_m = \|\hat{U}|\psi_{\text{reg}}^m\rangle - \hat{P}_{\text{reg}}\hat{U}\hat{P}_{\text{reg}}|\psi_{\text{reg}}^m\rangle\|^2 \quad (4.10)$$

$$= \|\hat{U}|\psi_{\text{reg}}^m\rangle - (\hat{P}_{\text{reg}}\hat{U}_{\text{reg}}\hat{P}_{\text{reg}} + \hat{P}_{\text{reg}}(\hat{U} - \hat{U}_{\text{reg}})\hat{P}_{\text{reg}})|\psi_{\text{reg}}^m\rangle\|^2. \quad (4.11)$$

With the approximation $\hat{P}_{\text{reg}}(\hat{U} - \hat{U}_{\text{reg}})\hat{P}_{\text{reg}} \approx 0$ discussed for Eq. (4.4) we obtain

$$\gamma_m \approx \|(\hat{U} - \hat{U}_{\text{reg}})|\psi_{\text{reg}}^m\rangle\|^2. \quad (4.12)$$

The projector onto the chaotic region has been replaced by the difference $\hat{U} - \hat{U}_{\text{reg}}$, $(\hat{U} - \hat{U}_{\text{reg}}) \approx (\hat{\mathbf{1}} - \hat{P}_{\text{reg}})\hat{U}$. In contrast to Eq. (4.9) this approximation only predicts tunneling rates accurately if \hat{U} and \hat{U}_{reg} show almost identical dynamics within the regular region of phase space.

In the following sections we will discuss the construction of the fictitious integrable system \hat{U}_{reg} and a semiclassical evaluation of the final result, Eq. (4.9). Finally, we will compare our prediction of direct dynamical tunneling rates to numerical data.

4.1.2 Fictitious integrable system and convergence

The most difficult step in the application of our main result, Eq. (4.9), to a given quantum map \hat{U} is the determination of the fictitious integrable system \hat{U}_{reg} . On the one hand its dynamics should resemble the classical motion of the considered mixed system within the regular island as closely as possible. As a result the contour lines of the corresponding integrable Hamiltonian H_{reg} (Fig. 4.1(b)) approximate the KAM-curves of the classically mixed system (Fig. 4.1(a)) in phase space. This resemblance is not possible with arbitrary precision as the integrable approximation cannot contain e.g. nonlinear resonance chains and small embedded chaotic regions. Moreover, it cannot account for the hierarchical regular-to-chaotic transition region. On the other hand the dynamics of \hat{U}_{reg} should extrapolate sufficiently smooth to the chaotic phase-space region of the mixed system. This is essential for the quantum eigenstates of \hat{U}_{reg} to have reasonable tunneling tails determining the wanted tunneling rate. Therefore, barrier tunneling processes inside the regular system should be avoided. While typically tunneling from the regular island occurs to regions within the chaotic sea close to the border of the regular island, there exist other cases, where it occurs to regions deeper inside the chaotic sea, as studied in Ref. [43]. Here \hat{U}_{reg} has to be constructed such that its eigenstates have the appropriate tunneling tails up to this region.

In the semiclassical limit a global approximation \hat{U}_{reg} of the regular dynamics within the mixed system including a reasonable behavior of its quantum eigenstates in the chaotic region is not possible due to the increasing number of important resonance chains and the complex nature of the hierarchical region. Similar problems appear for the analytic continuation of a regular torus into complex space due to the existence of natural boundaries [16, 38–40, 53–55, 70]. However, for the quantum tunneling problem at not too small \hbar_{eff} , where these small structures are not yet resolved, an integrable approximation with finite accuracy is sufficient.

For the determination of \hat{U}_{reg} we proceed in the following way: We employ methods of classical perturbation theory to obtain a one-dimensional time-independent Hamiltonian $H_{\text{reg}}(q, p)$ which is integrable by definition and resembles the classically regular motion corresponding to the

mixed system. Two examples for such an explicit construction will be discussed below. After the determination of H_{reg} (see also Ref. [180]) and its quantization we obtain the regular quantum map $\hat{U}_{\text{reg}} = e^{-i\hat{H}_{\text{reg}}/\hbar_{\text{eff}}}$ with corresponding eigenfunctions $|\psi_{\text{reg}}^m\rangle$. For the numerical evaluation of Eq. (4.12) it is convenient to replace $\hat{U}_{\text{reg}}|\psi_{\text{reg}}^m\rangle$ by $e^{-iE_m/\hbar_{\text{eff}}}|\psi_{\text{reg}}^m\rangle$ and we use $P_{\text{reg}} \approx \sum |\psi_{\text{reg}}^m\rangle\langle\psi_{\text{reg}}^m|$, where the sum extends over $m = 0, 1, \dots, m_{\text{max}}$.

Lie-transformation method

For the systems \mathcal{F}_1 and \mathcal{F}_2 the Lie-transformation method [88] introduced in Section 3.1.3 is used for the determination of a regular Hamilton function, leading to

$$H_{\text{reg}}(q, p) = \sum_{k=1}^N \sum_{l=0}^k h_{k,l} q^l p^{k-l}. \quad (4.13)$$

The coefficients $h_{k,l}$ are determined during the perturbation expansion, see Appendix B.2 for an example. The order of the expansion N can be increased up to 20 with reasonable numerical effort. Note that the Lie-transformation method provides a regular approximation H_{reg} which interpolates the dynamics inside the regular region and gives a smooth continuation into the chaotic sea. At some maximal order N the series will start to diverge due to the existing nonlinear resonances inside the regular island.

Method based on the frequency map analysis

For strongly perturbed systems such as the standard map at $K > 2.5$ the Lie-transformation method may not converge. Therefore we introduced a method based on the frequency map analysis [84] in Section 3.1.3, which is applicable to any periodically driven one-dimensional system. The integrable approximation is determined by

$$H_{\text{reg}}(q, p) = \sum_{k,l=-N/2}^{N/2-1} h_{k,l} e^{2\pi i k q/l_q} e^{2\pi i l p/l_p}. \quad (4.14)$$

It depends on the maximal order N of the expansion and the periods l_q and l_p in position and momentum direction. If we choose l_q and l_p equal to the periodicities of the considered map, the resulting integrable approximation, Eq. (4.14), will show the same periodicities. Note that this method only uses the classical information obtained from the dynamics inside the regular region of the mixed system. Its continuation into the chaotic sea has to be reasonably smooth, such that no tunneling processes inside the regular system occur. Thus, the order of the expansion in Eq. (4.14) should not be chosen too large as $H_{\text{reg}}(q, p)$ starts to oscillate in the former chaotic region for large N and the determined regular states $|\psi_{\text{reg}}^m\rangle$ cannot be used to determine tunneling rates with Eq. (4.9).

Convergence

An important question is whether the direct tunneling rates obtained using Eq. (4.9) depend on the actual choice of H_{reg} and how these results converge in dependence of the maximal order N of its perturbation series. There arise two main problems: First the classical expansion is asymptotically divergent, which means that from some order N on the series fails in reproducing the dynamics of the mixed system inside the regular region. Secondly, for the quantization of H_{reg} its behavior in the vicinity of the last surviving KAM torus must be smoothly continued into the chaotic sea. Large fluctuations of H_{reg} in this region lead to unwanted tunneling processes making the use of Eq. (4.9) impossible.

Ideally one would like to use the classical measures introduced in Section 3.1.3, which describe the deviations of the regular system H_{reg} from the originally mixed one, to predict the error of Eq. (4.9) for the tunneling rates. However, these classical measures can only account for the deviations in the regular region but not for the quality of the continuation of H_{reg} to the chaotic sea. It remains an open question how to obtain a direct connection between these classical measures and the tunneling rates.

The convergence of the integrable approximation can be studied by considering the tunneling rates determined with Eq. (4.9) under variation of the perturbation order N . For the example map \mathcal{F}_2 with the parameters $r_1 = 0.26$, $R = 0.4$, $\varepsilon = 0.005$ we find convergence up to the maximal considered order, see Fig. 4.2(a), while for the standard map at $K = 2.9$ the rates diverge rather quickly beyond $N = 4$, see Fig. 4.2(b). Hence, we choose the respective optimal order for the comparison of Eq. (4.9) and numerical data.

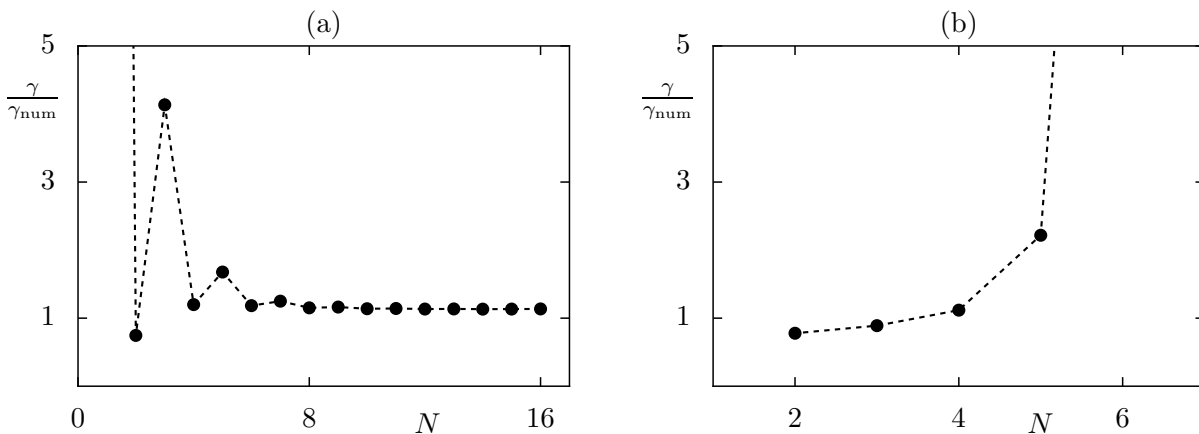


Figure 4.2: Tunneling rates determined with Eq. (4.9), normalized by the numerical value for $m = 0$, $h_{\text{eff}} = 1/32$ vs order N of H_{reg} . In (a) we choose the system \mathcal{F}_2 with $r_1 = 0.26$, $R = 0.4$, $Z = 0$ and use the Lie-transformation for the determination of H_{reg} while in (b) the standard map at $K = 2.9$ is considered for which we determine H_{reg} using the method based on the frequency map analysis. For (a) the optimal order $N = 10$ is found while for (b) it is $N = 4$ as the results diverge for larger N .

In general, different classical methods are applicable to determine a fictitious integrable system \hat{U}_{reg} which leads to an accurate prediction of tunneling rates with Eq. (4.9). Hence, the determination of \hat{U}_{reg} is not unique. The quality of an integrable system can be estimated according to the predicted tunneling rates. If different integrable approximations exist we choose the system which leads to the lowest tunneling rates γ as the true rates should represent a lower bound of our theory.

4.1.3 Semiclassical evaluation

An analytical evaluation of the final result for the prediction of direct dynamical tunneling rates, Eq. (4.9), is possible for certain situations. We define functions $\tilde{V}(q)$ and $\tilde{T}(p)$ by a low order Taylor expansion of $V(q)$ and $T(p)$, respectively, around the center of the regular island. The following derivation is promising if the resulting unitary operator $\hat{U}_{\tilde{V}}\hat{U}_{\tilde{T}} = e^{-i\tilde{V}(q)/\hbar_{\text{eff}}}e^{-i\tilde{T}(p)/\hbar_{\text{eff}}}$ has the following properties: The corresponding classical dynamics is not necessarily regular. It is close, however, to a regular quantum map \hat{U}_{reg} beyond the border of the island and can therefore be used in Eq. (4.9) instead of \hat{U}_{reg} . Within the island it has an almost identical classical dynamics as \hat{U} . Therefore $(\hat{U} - \hat{U}_{\tilde{V}}\hat{U}_{\tilde{T}})|\psi_{\text{reg}}^m\rangle$ has almost all of its weight in the chaotic region and Eq. (4.12) can be applied. With the definitions

$$\hat{\mathbb{1}} + \hat{\varepsilon}_V := e^{-\frac{i}{\hbar_{\text{eff}}}[V(\hat{q}) - \tilde{V}(\hat{q})]}, \quad (4.15)$$

$$\hat{\mathbb{1}} + \hat{\varepsilon}_T := e^{-\frac{i}{\hbar_{\text{eff}}}[T(\hat{p}) - \tilde{T}(\hat{p})]} \quad (4.16)$$

we evaluate the difference $\hat{U} - \hat{U}_{\text{reg}}$

$$\hat{U} - \hat{U}_{\text{reg}} \approx \hat{U}_V\hat{U}_T - \hat{U}_{\tilde{V}}\hat{U}_{\tilde{T}} \quad (4.17)$$

$$= \hat{U}_{\tilde{V}}\hat{U}_{\tilde{V}}^\dagger \left(\hat{U}_V\hat{U}_T - \hat{U}_{\tilde{V}}\hat{U}_{\tilde{T}} \right) \hat{U}_{\tilde{T}}^\dagger\hat{U}_{\tilde{T}} \quad (4.18)$$

$$= \hat{U}_{\tilde{V}} \left(\hat{U}_{\tilde{V}}^\dagger\hat{U}_V\hat{U}_T\hat{U}_{\tilde{T}}^\dagger - \hat{\mathbb{1}} \right) \hat{U}_{\tilde{T}} \quad (4.19)$$

$$= \hat{U}_{\tilde{V}}(\hat{\varepsilon}_V + \hat{\varepsilon}_T + \hat{\varepsilon}_V\hat{\varepsilon}_T)\hat{U}_{\tilde{T}} \quad (4.20)$$

and therefore Eq. (4.12) reads

$$\gamma_m = \|\hat{U}_{\tilde{V}}[\hat{\varepsilon}_V + \hat{\varepsilon}_T + \hat{\varepsilon}_V\hat{\varepsilon}_T]\hat{U}_{\tilde{T}}|\psi_{\text{reg}}^m\rangle\|^2. \quad (4.21)$$

The vector $(\hat{U} - \hat{U}_{\text{reg}})|\psi_{\text{reg}}^m\rangle$ is decomposed into three contributions $\hat{\kappa}_T|\psi_{\text{reg}}^m\rangle := \hat{U}_{\tilde{V}}\hat{\varepsilon}_T\hat{U}_{\tilde{T}}|\psi_{\text{reg}}^m\rangle$, $\hat{\kappa}_V|\psi_{\text{reg}}^m\rangle := \hat{U}_{\tilde{V}}\hat{\varepsilon}_V\hat{U}_{\tilde{T}}|\psi_{\text{reg}}^m\rangle$, and $\hat{\kappa}_{VT}|\psi_{\text{reg}}^m\rangle := \hat{U}_{\tilde{V}}\hat{\varepsilon}_V\hat{\varepsilon}_T\hat{U}_{\tilde{T}}|\psi_{\text{reg}}^m\rangle$ which are visualized in Fig. 4.3 for an example system. We find that typically the third contribution is negligible. Also the mixed terms including $\hat{\kappa}_T$ and $\hat{\kappa}_V$ which appear in Eq. (4.21) can be neglected. Now we have to evaluate Eq. (4.21) in which only the terms $\|\hat{\kappa}_V|\psi_{\text{reg}}^m\rangle\|^2$ and $\|\hat{\kappa}_T|\psi_{\text{reg}}^m\rangle\|^2$ remain. We obtain

$$\gamma_m \approx \|\hat{\kappa}_T|\psi_{\text{reg}}^m\rangle\|^2 + \|\hat{\kappa}_V|\psi_{\text{reg}}^m\rangle\|^2 \quad (4.22)$$

$$= \langle \psi_{\text{reg}}^m | \hat{U}_{\tilde{T}}^\dagger \hat{\varepsilon}_T^\dagger \hat{U}_{\tilde{V}}^\dagger \hat{U}_{\tilde{V}} \hat{\varepsilon}_T \hat{U}_{\tilde{T}} | \psi_{\text{reg}}^m \rangle + \langle \psi_{\text{reg}}^m | \hat{U}_{\tilde{T}}^\dagger \hat{\varepsilon}_V^\dagger \hat{U}_{\tilde{V}}^\dagger \hat{U}_{\tilde{V}} \hat{\varepsilon}_V \hat{U}_{\tilde{T}} | \psi_{\text{reg}}^m \rangle \quad (4.23)$$

$$= \langle \psi_{\text{reg}}^m | \hat{U}_{\tilde{T}}^\dagger \hat{\varepsilon}_T^\dagger \hat{\varepsilon}_T \hat{U}_{\tilde{T}} | \psi_{\text{reg}}^m \rangle + \langle \psi_{\text{reg}}^m | \hat{U}_{\tilde{T}}^\dagger \hat{\varepsilon}_V^\dagger \hat{\varepsilon}_V \hat{U}_{\tilde{T}} | \psi_{\text{reg}}^m \rangle \quad (4.24)$$

$$= \langle \psi_{\text{reg}}^m | \hat{U}_{\tilde{T}}^\dagger \hat{\varepsilon}_T^\dagger \hat{\varepsilon}_T \hat{U}_{\tilde{T}} | \psi_{\text{reg}}^m \rangle + \langle \psi_{\text{reg}}^m | \hat{U}_{\tilde{T}}^\dagger \hat{U}_{\tilde{V}}^\dagger \hat{U}_{\tilde{V}} \hat{\varepsilon}_V^\dagger \hat{\varepsilon}_V \hat{U}_{\tilde{V}} \hat{U}_{\tilde{T}} | \psi_{\text{reg}}^m \rangle \quad (4.25)$$

$$= \langle \psi_{\text{reg}}^m | \hat{U}_{\tilde{T}}^\dagger \hat{\varepsilon}_T^\dagger \hat{\varepsilon}_T \hat{U}_{\tilde{T}} | \psi_{\text{reg}}^m \rangle + \langle \psi_{\text{reg}}^m | \hat{U}_{\tilde{V}} \hat{\varepsilon}_V^\dagger \hat{\varepsilon}_V \hat{U}_{\tilde{V}} | \psi_{\text{reg}}^m \rangle \quad (4.26)$$

$$\begin{aligned} &= \sum_{k=0}^{N-1} \langle \psi_{\text{reg}}^m | e^{\frac{i}{\hbar_{\text{eff}}} \tilde{T}(\hat{p})} | p_k \rangle 2 \left[1 - \cos \left(\frac{T(p_k) - \tilde{T}(p_k)}{\hbar_{\text{eff}}} \right) \right] \\ &\quad \cdot \langle p_k | e^{-\frac{i}{\hbar_{\text{eff}}} \tilde{T}(\hat{p})} | \psi_{\text{reg}}^m \rangle \\ &\quad + \sum_{k=0}^{N-1} \langle \psi_{\text{reg}}^m | e^{-\frac{i}{\hbar_{\text{eff}}} \tilde{V}(\hat{q})} | q_k \rangle 2 \left[1 - \cos \left(\frac{V(q_k) - \tilde{V}(q_k)}{\hbar_{\text{eff}}} \right) \right] \\ &\quad \cdot \langle q_k | e^{\frac{i}{\hbar_{\text{eff}}} \tilde{V}(\hat{q})} | \psi_{\text{reg}}^m \rangle \end{aligned} \quad (4.27)$$

$$\begin{aligned} &= 2 \sum_{k=0}^{N-1} e^{\frac{i}{\hbar_{\text{eff}}} \tilde{T}(p_k)} \langle \psi_{\text{reg}}^m | p_k \rangle \left[1 - \cos \left(\frac{T(p_k) - \tilde{T}(p_k)}{\hbar_{\text{eff}}} \right) \right] e^{-\frac{i}{\hbar_{\text{eff}}} \tilde{T}(p_k)} \langle p_k | \psi_{\text{reg}}^m \rangle \\ &\quad + 2 \sum_{k=0}^{N-1} e^{-\frac{i}{\hbar_{\text{eff}}} \tilde{V}(q_k)} \langle \psi_{\text{reg}}^m | q_k \rangle \left[1 - \cos \left(\frac{V(q_k) - \tilde{V}(q_k)}{\hbar_{\text{eff}}} \right) \right] e^{\frac{i}{\hbar_{\text{eff}}} \tilde{V}(q_k)} \langle q_k | \psi_{\text{reg}}^m \rangle. \end{aligned} \quad (4.28)$$

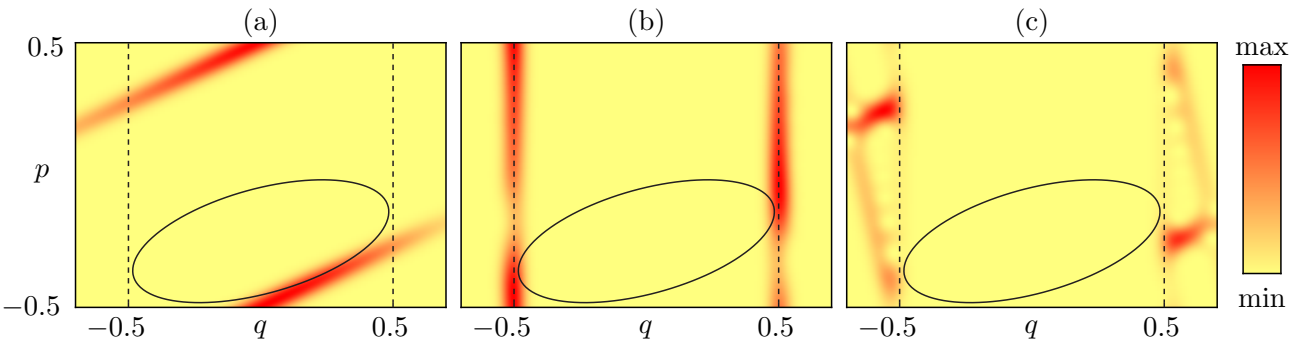


Figure 4.3: Husimi representation of the vectors (a) $\hat{\kappa}_T|\psi_{\text{reg}}^m\rangle$, (b) $\hat{\kappa}_V|\psi_{\text{reg}}^m\rangle$, and (c) $\hat{\kappa}_{VT}|\psi_{\text{reg}}^m\rangle$ for the system \mathcal{F}_1 with $r_1 = 0.46$, $R = 0$, $Z = 0$, and $\varepsilon = 0.005$ for $m = 0$.

From Eq. (4.28) we finally find

$$\begin{aligned} \gamma_m \approx & 2 \sum_{k=0}^{N-1} |\psi_{\text{reg}}^m(q_k)|^2 \left[1 - \cos \left(\frac{V(q_k) - \tilde{V}(q_k)}{\hbar_{\text{eff}}} \right) \right] \\ & + 2 \sum_{k=0}^{N-1} |\psi_{\text{reg}}^m(p_k)|^2 \left[1 - \cos \left(\frac{T(p_k) - \tilde{T}(p_k)}{\hbar_{\text{eff}}} \right) \right]. \end{aligned} \quad (4.29)$$

In the semiclassical limit the sums over discrete position and momentum values in Eq. (4.29) can be replaced by an integral

$$\begin{aligned} \gamma_m \approx & 2 \int_{q_{\text{min}}}^{q_{\text{min}}+M_q} dq |\psi_{\text{reg}}^m(q)|^2 \left[1 - \cos \left(\frac{V(q) - \tilde{V}(q)}{\hbar_{\text{eff}}} \right) \right] \\ & + 2 \int_{p_{\text{min}}}^{p_{\text{min}}+M_p} dp |\psi_{\text{reg}}^m(p)|^2 \left[1 - \cos \left(\frac{T(p) - \tilde{T}(p)}{\hbar_{\text{eff}}} \right) \right] \end{aligned} \quad (4.30)$$

where q_{min} and p_{min} denote the minimal position and momentum coordinate in phase space, respectively, and we have M_q unit cells in position and M_p cells in momentum direction. The contributions which appear in Eq. (4.30) are visualized in Fig. 4.4 and agreement with the direct evaluation of Eq. (4.9) is presented in Section 4.1.4.

If an analytical WKB-like expression for the regular states $|\psi_{\text{reg}}^m\rangle$ is known, Eq. (4.30) can

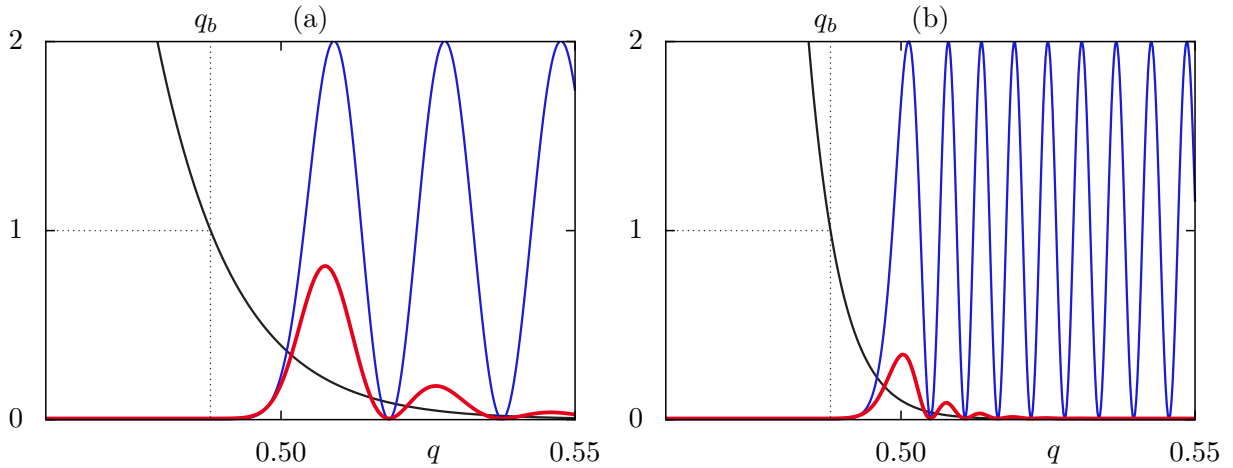


Figure 4.4: Illustration of the contributions appearing in the first term of Eq. (4.30). The exponentially decaying regular wave function $|\psi_{\text{reg}}^m(q)/\psi_{\text{reg}}^m(q_b)|^2$ is presented as a black line while $1 - \cos([V(q) - \tilde{V}(q)]/\hbar_{\text{eff}})$ is shown in blue. The product of these two functions is depicted in red. It is zero inside the regular island for $q < q_b$ and has its maximal contribution near the border of this island at $q \approx q_b$. In (a) we use $m = 0$, $\hbar_{\text{eff}} = 1/30$ and in (b) $m = 15$ and $\hbar_{\text{eff}} = 1/100$.

be evaluated further. This is the case for the mappings \mathcal{F}_1 and \mathcal{F}_2 yielding a tilted harmonic oscillator-like island embedded in a chaotic sea for $R = Z = 0$. In normal coordinates its regular system has the form $H_{\text{reg}}(p, q) = p^2/2 + \sigma^2 q^2/2$, where σ denotes the ratio of the two half axes of the ellipse, see Eq. (3.20). The eigenfunctions $\psi_{\text{reg}}^m(q)$ of H_{reg} are given in position representation by means of the WKB theory as

$$\psi_{\text{reg}}^m(q) = \frac{C}{2\sqrt{|p(q)|}} \exp\left(-\frac{1}{\hbar_{\text{eff}}} \int_{q_m}^q |p(q')| dq'\right) \quad (4.31)$$

with the classical turning points q_m and the normalization constant C . The momentum p at the border of the regular island q_b is denoted by $p_b := p(q_b)$. We write

$$\psi_{\text{reg}}^m(q) = \frac{C}{2\sqrt{|p(q)|}} \exp\left(-\frac{1}{\hbar_{\text{eff}}} \int_{q_m}^{q_b} |p(q')| dq'\right) \exp\left(-\frac{1}{\hbar_{\text{eff}}} \int_{q_b}^q |p(q')| dq'\right) \quad (4.32)$$

$$\approx \psi_{\text{reg}}^m(q_b) \exp\left(-\frac{1}{\hbar_{\text{eff}}} \int_{q_b}^q |p(q')| dq'\right) \quad (4.33)$$

$$\approx \psi_{\text{reg}}^m(q_b) \exp\left(-\frac{1}{\hbar_{\text{eff}}}(q - q_b)|p_b|\right). \quad (4.34)$$

The difference of the potential energies $\Delta V(q) = V(q) - \tilde{V}(q)$ should vanish in the regular region. Its most important contribution arises near the border of the regular island, as the regular wave function exponentially decays into the chaotic sea, see Fig. 4.4. Therefore $\Delta V(q)$ can be approximated using a Taylor expansion in linear order around q_b

$$\Delta V(q) \approx \tilde{c}(q - q_b). \quad (4.35)$$

Assuming $\Delta V = 0$ inside the regular island and using that $H_{\text{reg}}(p, q) = H_{\text{reg}}(p, -q)$ we insert Eqs. (4.34) and (4.35) into the first term in Eq. (4.30) and find

$$\gamma_m = 4\hbar_{\text{eff}} |\psi_{\text{reg}}^m(q_b)|^2 \int_0^{x_{\text{max}}} e^{-2x|p_b|} (1 - \cos(\tilde{c}x)) dx \quad (4.36)$$

$$= c_1 \hbar_{\text{eff}} |\psi_{\text{reg}}^m(q_b)|^2, \quad (4.37)$$

where $x = (q - q_b)/\hbar_{\text{eff}}$ and $x_{\text{max}} = (q_{\text{max}} - q_b)/\hbar_{\text{eff}}$. A similar result is obtained for the second term in Eq (4.30). In the semiclassical limit $x_{\text{max}} \rightarrow \infty$ and the integral $I = \pi c_1/2$ in Eq. (4.36) becomes an \hbar_{eff} -independent constant. The tunneling rate is given by the square of the modulus of the regular wave function at the border of the regular island. With Eq. (4.31) we obtain

$$\gamma_m = \frac{c_2 \hbar_{\text{eff}}}{|p(q_b)|} \exp\left(-\frac{2}{\hbar_{\text{eff}}} \int_{q_m}^{q_b} |p(q')| dq'\right), \quad (4.38)$$

in which we use $C = \sqrt{2\omega/\pi}$ for the normalization of the WKB-function and $c_2 = c_1\omega/2\pi$. For

the Hamiltonian of the harmonic oscillator the classical turning points $q_m = \sqrt{2E_m}/\sigma$ with the eigenenergies $E_m = \hbar_{\text{eff}}\sigma(m + 1/2)$ and the momentum $p(q) = \sqrt{2E_m - q^2\sigma^2}$ are known. Using these expressions in Eq. (4.38) we finally find

$$\gamma_m = c \frac{\hbar_{\text{eff}}}{\beta_m} \exp\left(-\frac{2A}{\hbar_{\text{eff}}}\left[\beta_m - \alpha_m \ln\left(\frac{1 + \beta_m}{\sqrt{\alpha_m}}\right)\right]\right) \quad (4.39)$$

as the semiclassical prediction for the tunneling rate of the m th regular state, where $\alpha_m = (m + 1/2)(A/\hbar_{\text{eff}})^{-1}$, $\beta_m = \sqrt{1 - \alpha_m}$, and A is the area of the regular island. The \hbar_{eff} -independent prefactor $c = c_2\sqrt{\pi}/(A\sigma) \approx 1$ is given by a rough semiclassical estimate below. The prediction, Eq. (4.39), gives excellent agreement with numerically determined data over 10 orders of magnitude in γ (see Fig. 4.8). Let us make the following remarks concerning Eq. (4.39): The only information about this non-generic island with constant rotation number is A/\hbar_{eff} as in Ref. [46]. In contrast to the resulting Eq. (4.9) derived in the last section it does not require further quantum information such as the quantum map \hat{U} . While the term in square brackets semiclassically approaches one, it is relevant for large \hbar_{eff} . In contrast to Eq. (4.30), where the chaotic properties are contained in the differences $V(q) - \tilde{V}(q)$ and $T(p) - \tilde{T}(p)$, they appear in the prefactor c via the linear approximation of these differences.

The prefactor c in Eq. (4.39) can be estimated by

$$c = \sqrt{\frac{\pi}{A\sigma}} \frac{\omega}{\pi^2} I, \quad (4.40)$$

where the integral I can be evaluated analytically in the semiclassical limit

$$I \approx \int_0^\infty e^{-2x|p_b|} (1 - \cos(\tilde{c}x)) dx \quad (4.41)$$

$$= \frac{1}{2|p(q_b)|} - \frac{2|p(q_b)|}{4|p(q_b)|^2 + \tilde{c}^2}. \quad (4.42)$$

This result can be compared to the numerical evaluation of Eq. (4.30) which does not include the above approximations and depends on \hbar_{eff} . We find good agreement between the two quantities.

In the semiclassical limit the prediction of Eq. (4.39) decreases exponentially. For $\hbar_{\text{eff}} \rightarrow 0$ the values α_m go to zero and β_m to one, such that $\gamma \sim e^{-2A/\hbar_{\text{eff}}}$ remains which reproduces the qualitative prediction obtained in Ref. [42]. We find that the non-universal constant in the exponent is 2 which is comparable to the prefactor derived in the corrected version of Ref. [46, 47] which is given by $3 - \ln 4 \approx 1.61$. However, our result shows more accurate agreement to numerical data and does not require an additional fitting parameter, as presented in Section 4.1.4.

4.1.4 Applications

We want to apply our theory for the direct regular-to-chaotic tunneling process, Eq. (4.9), to example systems and compare its predictions to numerical data. The different approximations of Eqs. (4.29), (4.30), and (4.37) in the semiclassical derivation performed in Section 4.1.3 will be verified as well as the final semiclassical result, Eq. (4.39).

System \mathcal{F}_1 with harmonic oscillator-like island

As a first example we consider the kicked systems \mathcal{F}_1 introduced in Section 3.1.2 with $R = Z = 0$. These systems have a mixed phase space with one harmonic oscillator-like regular island of constant rotation number surrounded by a structureless chaotic sea. Hence, the tunneling process from the regular island to the chaotic sea cannot be disturbed by nonlinear resonances or partial barriers in phase space and the direct tunneling process dominates far into the semiclassical limit. Thus, these systems are perfectly suited for a comparison of the numerically determined tunneling rates to our theoretical prediction. For the fictitious integrable system \hat{U}_{reg} we use the Hamiltonian of a harmonic oscillator which is squeezed and tilted according to the linearized dynamics in the vicinity of the fixed point located in the center of the regular island, see Section 3.1.4. Its eigenfunctions are analytically known, according to Eq. (3.147). This integrable system can even be written as a quantum map, which is given by extending the quadratic kinetic energy $T(p)$ and the potential $V(q)$ from the vicinity of the stable fixed point to the whole phase space. With this regular quantum map we are able to evaluate Eqs. (4.29), (4.30), and (4.37). Also the analysis of the final semiclassical result Eq. (4.39) is possible.

Figure 4.5 shows the prediction of Eq. (4.9) compared to numerical data obtained by applying absorbing boundary conditions at $q = \pm 1/2$. We find excellent agreement over more than 10 orders of magnitude in γ . In the regime of large tunneling rates γ deviations occur which can be attributed to the influence of the chaotic sea onto the regular states. For large γ these states are located on quantizing tori close to the border of the regular island and are affected by the regular-to-chaotic transition region which cannot be predicted by our theory. However, the deviation to numerical data is smaller than a factor of two.

Starting from Eq. (4.9) we derived Eq. (4.29) which can be applied if \hat{U}_{reg} is constructed as a kicked system which resembles the regular dynamics of the originally mixed quantum map and extends it considerably into the chaotic region of \hat{U} . In the semiclassical limit the sum in Eq. (4.29) can be replaced by an integral which leads to Eq. (4.30). Fig. 4.6 shows the comparison of numerically determined tunneling rates to the results of Eqs. (4.29) and (4.30). While Eq. (4.29) shows excellent agreement small deviations to Eq. (4.30) are visible. They occur as the considered values of h_{eff} are not located in the deep semiclassical regime. For the tunneling process in the considered system with the parameters $r_1 = 0.46$ and $\varepsilon = 0.005$ the first contribution in Eq. (4.29) is relevant. The second contribution can be neglected. This also

holds for the evaluation of Eq. (4.37) which shows agreement to numerical data, as presented in Fig. 4.7. As a last step we compare the results of the semiclassical prediction, Eq. (4.39), to numerical data in Fig. 4.8. Due to the numerous approximations performed in the derivation of this formula stronger deviations are visible in the regime of large tunneling rates while the agreement in the semiclassical regime is still excellent.

Podolskiy and Narimanov also derived a prediction for the direct regular-to-chaotic tunneling process. In the semiclassical limit they obtain for the ground state [46, 47, 56]

$$\gamma_0 = c \cdot h_{\text{eff}}^{\frac{5}{2}} e^{-\frac{A}{h_{\text{eff}}}(3-\ln 4)} \quad (4.43)$$

in which the free fit-parameter c appears. Figure 4.8 shows the comparison of this prediction (dotted line) to numerical data for the considered kicked system \mathcal{F}_1 . While Eq. (4.43) shows qualitative agreement, especially in the semiclassical limit deviations are visible. The predicted prefactor of 2 which appears in the exponent of Eq. (4.39) is found to be more accurate than the prefactor of $3 - \ln 4$ derived by Podolskiy and Narimanov.

Under variation of the parameter r_1 one finds situations in which the numerically determined tunneling rates show additional oscillations on top of the dominating exponential decay with $1/h_{\text{eff}}$. This appears more prominently when increasing the smoothing parameter ε . An example for this behavior is presented in Fig. 4.9. For the parameter $r_1 = 0.737$ the rotation number is determined by the linearized dynamics as $w_r \approx 0.207$ according to Eq. (3.21). It is close to the rational value of $1/5$. Due to the drastic modification of the kinetic energy $T(p)$ and the potential $V(q)$ at the border of the regular region, a large number of unstable periodic orbits exist in the chaotic domain close to the regular island including orbits of period five. They affect the regular states located on quantizing tori close to the border of the regular island. The oscillations in the tunneling rates can be qualitatively understood by considering the quasi-energy spectrum under variation of h_{eff} as presented in Fig. 4.9. It shows that the quasi-energy of the $(m + 5l)$ th regular state is located close to that of the m th state when it starts to exist. For larger values of $1/h_{\text{eff}}$ the difference between the two quasi-energies increases. Similar to resonance-assisted tunneling, which is discussed in the next section, we find couplings between the states $|\psi_{\text{reg}}^m\rangle$ and $|\psi_{\text{reg}}^{m+5l}\rangle$ due to unstable periodic orbits in the chaotic region of phase space. The strength of these couplings depends on the trace of the linearized mapping of the period-five orbit. It is small for large values of the parameter ε for which this orbit is located close to the border of the regular island and has a relevant influence on the tunneling rates. For small values of ε , however, its trace is large which weakens the couplings and the oscillations vanish. The theoretical prediction of these oscillations is still an open problem and might be found by extending the resonance-assisted tunneling theory to unstable periodic orbits.

To summarize, we have demonstrated that our prediction of dynamical tunneling rates shows excellent agreement to numerical data for systems with a harmonic oscillator-like regular island.

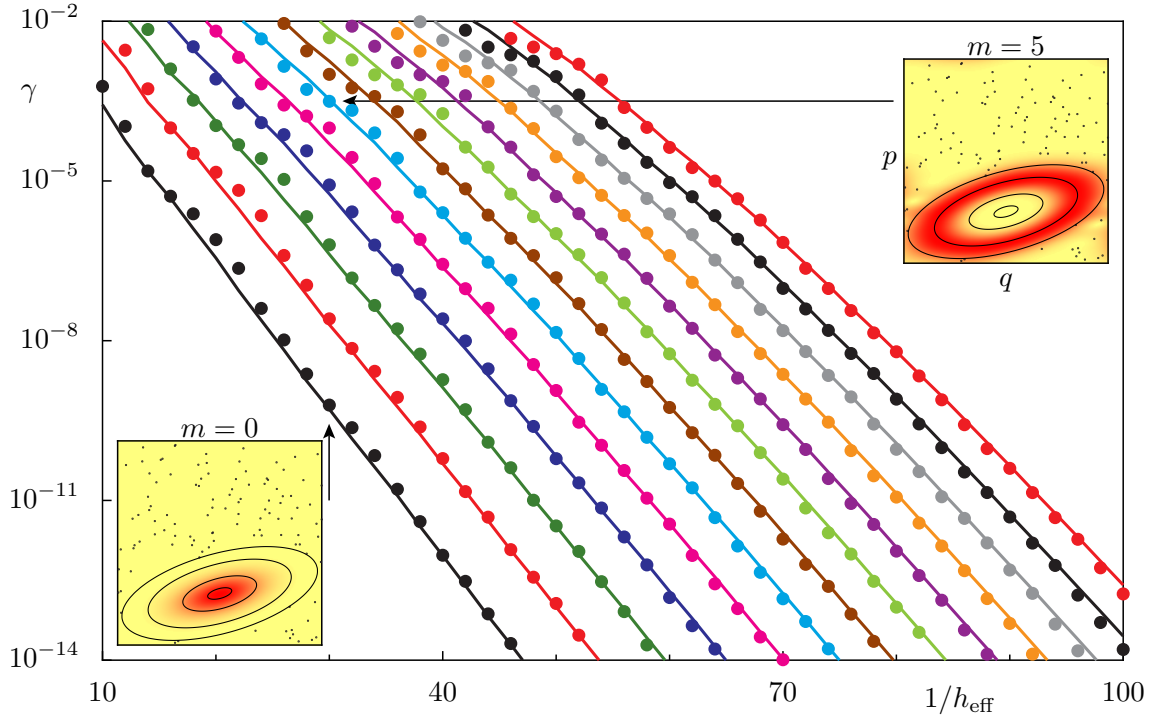


Figure 4.5: Dynamical tunneling rates from a harmonic oscillator-like regular island to the chaotic sea for the kicked system \mathcal{F}_1 with $r_1 = 0.46$, $R = 0$, $Z = 0$, and $\varepsilon = 0.005$: We compare numerical results (dots) and the prediction following from Eq. (4.9) (lines) vs $1/h_{\text{eff}}$ for the quantum numbers $m \leq 12$. The insets show Husimi representations of the regular states $m = 0$ and $m = 5$ at $1/h_{\text{eff}} = 30$ and the phase space of the system.

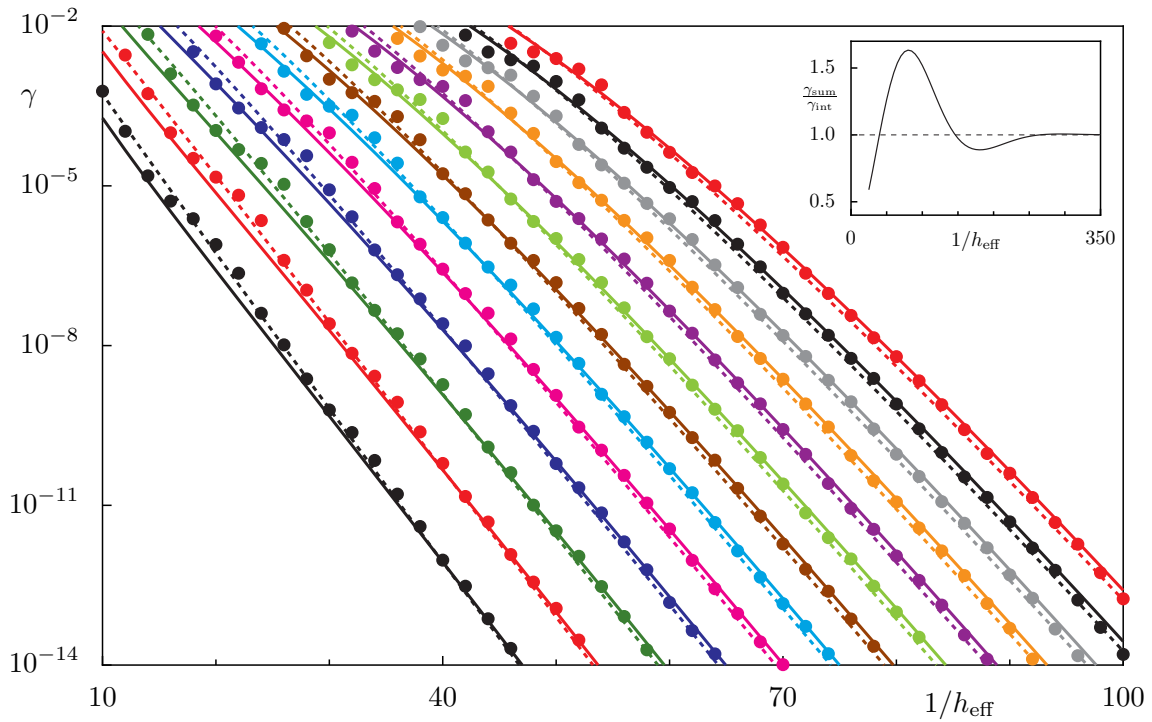


Figure 4.6: Dynamical tunneling rates for the system used in Fig. 4.5: We compare numerical results (dots) and the prediction following from Eqs. (4.29) (solid lines) and (4.30) (dashed lines) vs $1/h_{\text{eff}}$ for the quantum numbers $m \leq 12$. The inset shows the ratio of Eqs. (4.29) and (4.30) vs $1/h_{\text{eff}}$ which goes to unity in the semiclassical limit.

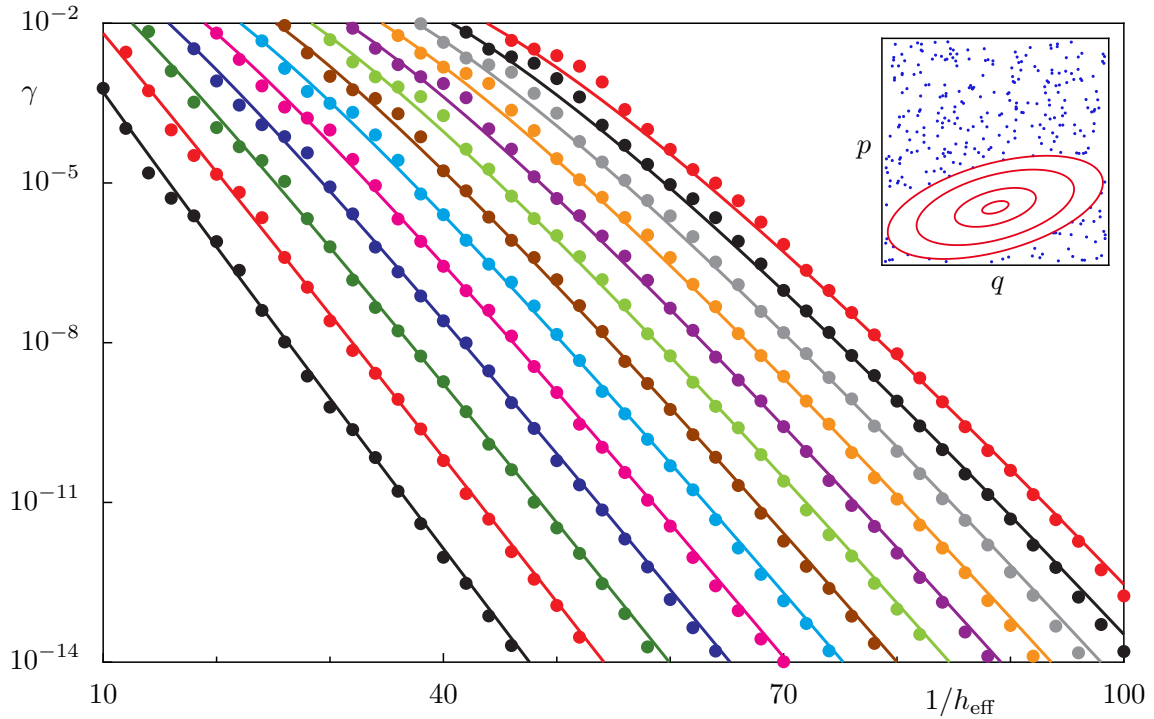


Figure 4.7: Dynamical tunneling rates for the system used in Fig. 4.5: We compare numerical results (dots) and the prediction following from Eq. (4.37) (lines) vs $1/h_{\text{eff}}$ for the quantum numbers $m \leq 12$. The inset shows the phase space of the system.

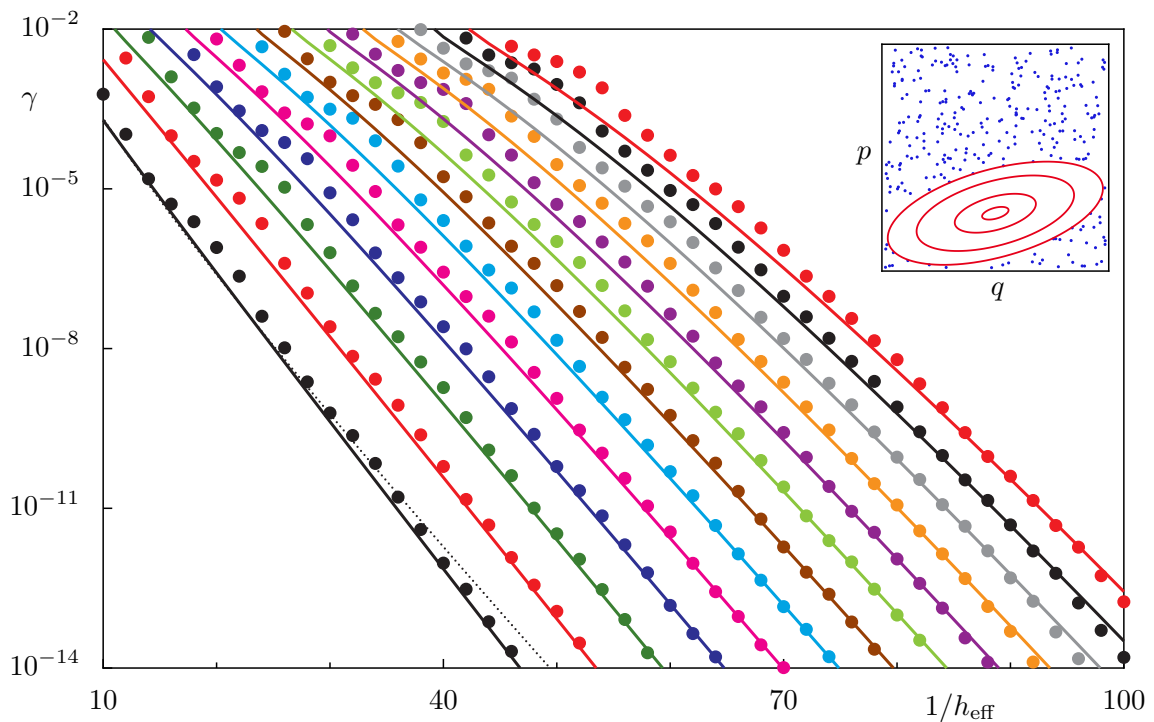


Figure 4.8: Dynamical tunneling rates for the system used in Fig. 4.5: We compare numerical results (dots) and the prediction following from Eq. (4.39) (lines) vs $1/h_{\text{eff}}$ for the quantum numbers $m \leq 12$. The prediction of Eq. (4.43) [46, 47] is presented for $m = 0$ with a fitted prefactor (dotted line). The inset shows the phase space of the system.

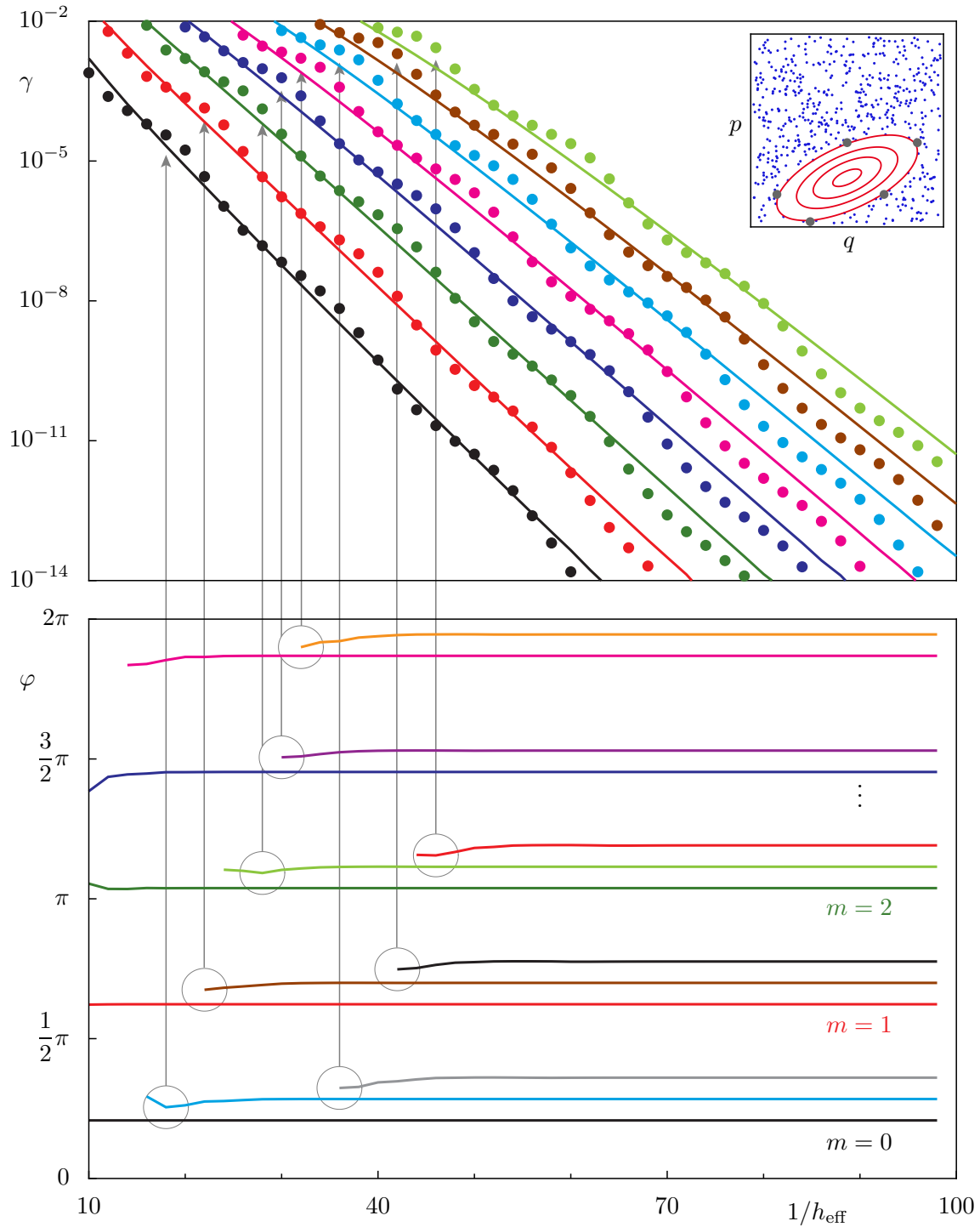


Figure 4.9: Dynamical tunneling rates from a harmonic oscillator-like regular island to the chaotic sea for the system \mathcal{F}_1 with $r_1 = 0.737$, $R = 0$, $Z = 0$, $\varepsilon = 0.01$ (top): We compare numerical results (dots) and the prediction following from Eq. (4.9) (lines) vs $1/h_{\text{eff}}$ for the quantum numbers $m \leq 7$. Appearing oscillations can be explained with the influence of an unstable fixed point of period five close to the border of the regular island which is shown in the upper inset (gray dots). It causes near degeneracies in the spectrum (bottom) which lead to enhanced tunneling rates (marked by gray arrows).

System \mathcal{F}_1 with deformed island

However, such a situation with a harmonic oscillator-like island is nongeneric. In typical systems the rotation number will change from the center of the regular region to its border which has a non-elliptic shape. Such a situation can be achieved using the kicked system \mathcal{F}_1 or \mathcal{F}_2 with the parameter $R \neq 0$. For most combinations of the parameters r_1 and R resonance structures appear inside the regular island. They limit the h_{eff} -regime in which the direct regular-to-chaotic tunneling process dominates. Hence, we choose a situation in which the appearing nonlinear resonances are small such that their influence on the tunneling process is expected only at large $1/h_{\text{eff}}$. Even for such systems with small resonance chains the application of our theory using a fictitious integrable system becomes more involved since we cannot use the simple harmonic oscillator as the integrable system \hat{U}_{reg} . Also its eigenstates $|\psi_{\text{reg}}^m\rangle$ are not analytically known. Hence, a full semiclassical analysis such as Eq. (4.39) is not available. Nevertheless Eqs. (4.9), (4.29), (4.30), and (4.37) can be applied.

We determine the fictitious integrable system by means of the Lie-transformation method described in Section 3.1.3. It is quantized according to Eq. (3.161) and its eigenfunctions can be determined numerically. If we compare the resulting regular eigenfunctions to the corresponding eigenstates of the mixed system \hat{U} we find deviations in the regular phase space region of the order of 10^{-5} . Note that these small deviations are irrelevant as the projector $\hat{\mathbb{1}} - \hat{P}_{\text{reg}}$ which appears in Eq. (4.9) cancels these contributions.

Similar to the case of the harmonic oscillator-like island a regular kicked system \hat{U}_{reg} can be found by extending the potential energy of the central unit cell to the whole phase space. It reads $\tilde{V}(q) = -r_1 q^2/2 + Rq^3/3$. As the regular states appear in Eqs. (4.29), (4.30), and (4.37) as a factor only, their deviations from the real eigenfunctions in the regular region are negligible and these equations can be evaluated. Fig. 4.10 shows a comparison of numerically determined tunneling rates (dots) to the prediction of Eq. (4.30) yielding excellent agreement for tunneling rates $\gamma \gtrsim 10^{-11}$. For smaller values of γ deviations occur due to resonance-assisted tunneling which is caused by a small 10:1 resonance chain. This resonance is presented in the lower inset of Fig. 4.10 and leads to increasing tunneling rates as described in Section 4.2. The prediction of Eq. (4.43) [46,47] (dotted line) shows large deviations to numerical data which confirms our expectation that Eq. (4.43) should work for harmonic oscillator-like islands only.

A WKB-like expression for the direct tunneling process can also be found for the distorted island at hand. The eigenfunctions of an arbitrary integrable Hamiltonian H_{reg} can be determined semiclassically by [181]

$$\psi_{\text{reg}}^m(q) = \sum_{\alpha} c_{\alpha} \psi_{\alpha}(q) \quad \text{in which} \quad \psi_{\alpha}(q) = \left(\frac{\partial H_{\text{reg}}}{\partial p} \right)_{\alpha}^{-\frac{1}{2}} \exp \left(\frac{i}{\hbar_{\text{eff}}} \int_{q_m}^q p_{\alpha}(q') dq' \right). \quad (4.44)$$

In this equation q_m denote the classical turning points, $p_{\alpha}(q)$ the branches of the momentum at

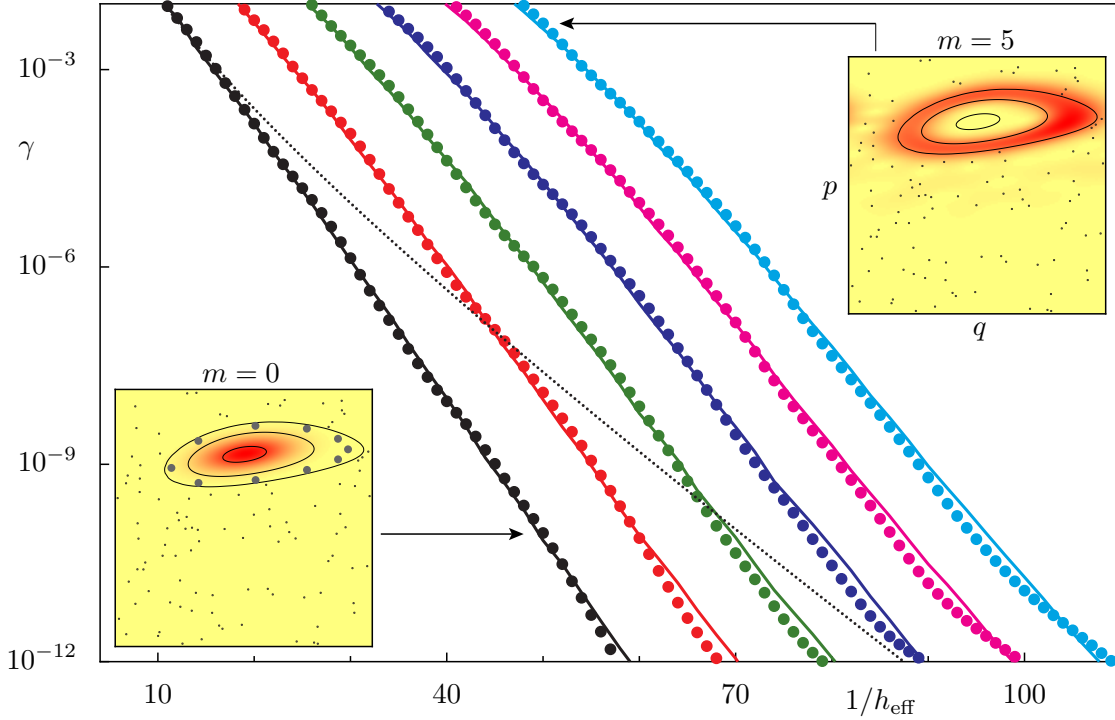


Figure 4.10: Dynamical tunneling rates from a distorted regular island to the chaotic sea for the kicked system \mathcal{F}_2 with $r_1 = 0.26$, $R = 0.4$, $Z = 0$, and $\varepsilon = 0.005$: We compare numerical results (dots) and the prediction following from Eq. (4.9) (lines) vs $1/h_{\text{eff}}$ for the quantum numbers $m \leq 5$. In addition the prediction of Eq. (4.43) [46, 47] is presented for $m = 0$ with a fitted prefactor (dotted line). The insets show Husimi representations of the regular states $m = 0$ and $m = 5$ at $1/h_{\text{eff}} = 50$ and the phase space of the system. Gray dots in the lower inset mark the position of a small 10:1 resonance.

energy E_m , and the constants c_α appear. It can be used for the further evaluation of Eq. (4.37). However, it does not allow for an analytical evaluation as in the case of the harmonic oscillator-like island, discussed previously.

Quasi-integrable systems

In Ref. [43] the authors studied the dynamical tunneling process from one regular island to the chaotic sea in a near-integrable system. This limiting case can also be modeled with the example systems \mathcal{F}_1 and we can apply our theory. Furthermore it allows to study the influence of the chaotic dynamics on the dynamical tunneling process. We show that for systems with equal regular regions properties of the chaotic dynamics can have a drastic influence on the tunneling rates. A quasi-integrable system is given by the mappings \mathcal{F}_1 with small values for the parameters r_1 and R , such as $r_1 = 0.05$ and $R = 0.1$. To apply our theoretical prediction, Eq. (4.9), we use the Lie-transformation method as described in Section 3.1.3 to obtain the fictitious integrable system. In the quasi-integrable case it is sufficient to consider the zeroth order of this perturbation expansion which has no mixed terms containing q and p

simultaneously. By neglecting linear terms in p , changing the sign, and by division with two we obtain

$$H_{\text{reg}}(q, p) = \frac{p^2}{2} + \frac{1}{2}\omega^2 q^2 - \frac{1}{6}Rq^3 \quad (4.45)$$

in which $\omega = \sqrt{r_1/2}$. The potential of the integrable approximation H_{reg} has the form of a harmonic oscillator with a cubic perturbation. The direct dynamical tunneling process is described by one-dimensional barrier tunneling through the potential $V(q) = \omega^2 q^2/2 - Rq^3/6$. Hence, the determination of tunneling rates is possible using WKB theory. By insertion of Eq. (2.14) into Eq. (4.37) we find

$$\gamma_m \approx \exp \left(-\frac{2}{\hbar_{\text{eff}}} \int_{q_m}^{q_b} \sqrt{-\frac{Rq^3}{3} + \omega^2 q^2 - 2E_m} dq \right) \quad (4.46)$$

in which q_m denote the classical turning points inside the potential well, q_b the turning points outside the potential well, and the eigenenergies E_m can be approximated by those of the harmonic oscillator for low energy eigenstates

$$E_m = \hbar_{\text{eff}}\omega \left(m + \frac{1}{2} \right). \quad (4.47)$$

A more accurate prediction of these eigenenergies is possible using time-independent perturbation theory in which $-Rq^3/6$ is the perturbation.

The considered near-integrable example systems allow to study the dependence of the tunneling process on properties of the chaotic phase-space region. If we use the mapping \mathcal{F}_1 as originally defined in Section 3.1.2 a smoothed discontinuity appears in $V'(q)$ at $q = 1/2$. For $q > 1/2$ the dynamics is completely chaotic. This can be included in our integrable approximation, Eq. (4.45), by setting the potential equal to zero for $q > 1/2$, see Fig. 4.11(b). Hence, in this situation the upper boundary of the integral appearing in Eq. (4.46) is given by $q_b = 1/2$. The results of this theoretical prediction are compared to numerical data in Fig. 4.11(a) showing excellent agreement.

If we do not apply the discontinuity in $V'(q)$ at $q = 1/2$ but extend $V'(q) = -r_1 q + Rq^2$ to the whole phase space, the integration in Eq. (4.46) has to take place in between the two turning points visualized in Fig. 4.11(d), with $q_b > 0.5$. Hence, the theoretically determined tunneling rates will decrease compared to the previously discussed situation. This can be verified with numerical data as presented in Fig. 4.11(c). Compared to Fig. 4.11(a) the slope of the exponential decay has decreased and tunneling is suppressed while the phase space is unchanged at first glance. The area and the shape of the regular island are identical in the two considered situations. However, the dynamics in the chaotic region of phase space changes. While in the case of the smoothed discontinuity the chaotic dynamics is homogeneous for

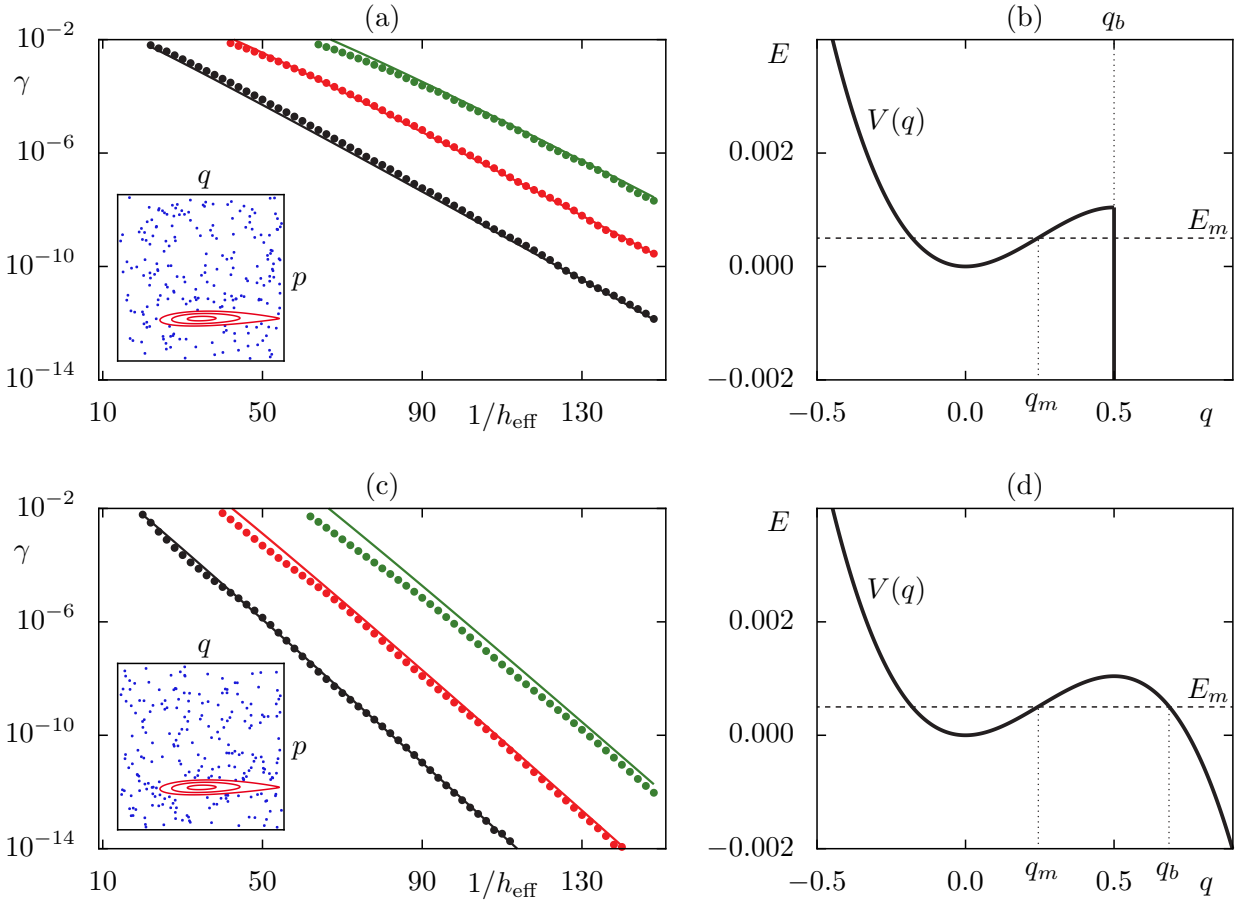


Figure 4.11: Dynamical tunneling rates from a near-integrable regular island to the chaotic sea for the kicked system \mathcal{F}_1 with $r_1 = 0.05$, $R = 0.1$, $Z = 0$, $\varepsilon = 0.005$ with a discontinuity at $q = 1/2$ (a) and without (c): We compare numerical results (dots) and the prediction following from Eq. (4.46) (lines) vs $1/h_{\text{eff}}$ for the quantum numbers $m \leq 2$. The insets show the phase space for the two cases which look almost identical. In (b) and (d) the approximate one-dimensional potentials $V(q)$ used in Eq. (4.46) are presented with the inner (outer) turning point q_m (q_b) at energy E_m .

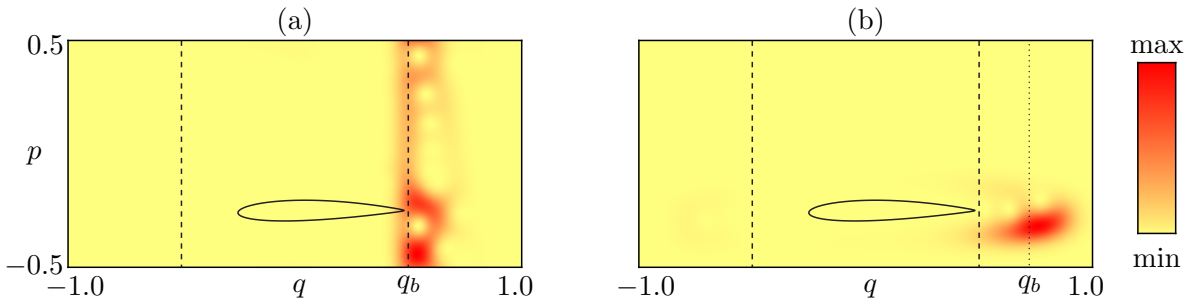


Figure 4.12: Husimi representation of the vector $(\hat{U} - \hat{U}_{\text{reg}})|\psi_{\text{reg}}^m\rangle$: In the case of a smoothed discontinuity at $q = 1/2$ (a) it is located at this position. Without this discontinuity (b) its maximal weight is located deep inside the chaotic region near the value q_b which is the outer turning point of the one-dimensional potential presented in Fig. 4.11(d).

$q > 1/2$, in the second case chaotic orbits follow the regular trajectories for a long time until they become chaotic. This effectively enlarges the area of the regular island which explains the decreasing tunneling rates, see also Fig. 4.12. Hence, in general it cannot be sufficient to consider the properties of the regular island for the determination of the direct tunneling rates. For the presented near-integrable system the varying chaotic dynamics could be described within the integrable approximation which allowed a theoretical prediction for the tunneling rates, which is an open problem for more generic systems.

Standard map

As a next step we want to apply our prediction of direct dynamical tunneling rates to the standard map. For K in between 2.5 and 3.0 it has a large generic regular island with a relatively small hierarchical region surrounded by a 4:1 resonance chain. Absorbing boundary conditions at $q = \pm 1/2$ lead to strong fluctuations of the numerically determined tunneling rates as a function of h_{eff} , presumably due to cantori. Choosing $q = \pm 1/4$, which is closer to the island, we find smoothly decaying tunneling rates (dots in Fig. 4.13). Evaluating Eq. (4.9) for $K = 2.9$ gives good agreement with these numerical data (see Fig. 4.13). Here we determine H_{reg} by first using the frequency map analysis [84] for characterizing the properties of the regular island. This information is used to find the optimal two-dimensional Fourier series of order N for H_{reg} , as described in Section 4.1.2. With increasing order N of the expansion the tunneling rates following from Eq. (4.9) diverge (see Fig. 4.2). Hence, for the predictions in Fig. 4.13 we choose $N = 4$ which is the largest order before the divergence starts to set in. Note that due to the large nonlinearity at $K > 2.5$ classical perturbation theories as e.g. the Lie transformation method are not able to reproduce the regular dynamics of the standard map around the central island. They start to diverge before a reasonable agreement is reached. Using the frequency map analysis a better result can be achieved. Nevertheless its accuracy is inferior compared to the mappings discussed previously in which the Lie transformation is applicable. Hence, the purely regular eigenstates $|\psi_{\text{reg}}^m\rangle$ show relevant deviations to the corresponding eigenstates of the mixed system inside the regular island. These deviations are compensated by the application of the projector $(\hat{1} - \hat{P}_{\text{reg}})$ in Eq. (4.9). However, this projector depends on the number of existing regular states m_{max} which grows in the semiclassical limit. If m_{max} increases by one \hat{P}_{reg} suddenly projects onto a larger region in phase space. This explains the steps seen in the theoretical predictions of Eq. (4.9) shown in Fig. 4.13.

Mapping \mathcal{F}_3 with regular stripe

Another interesting kicked system was introduced by Shudo et. al [41]. It does not show a regular island as the maps considered before but a regular stripe in phase space. Adapted to the considered phase-space unit cell it is given by Eqs. (3.41) and (3.42) with the parameters

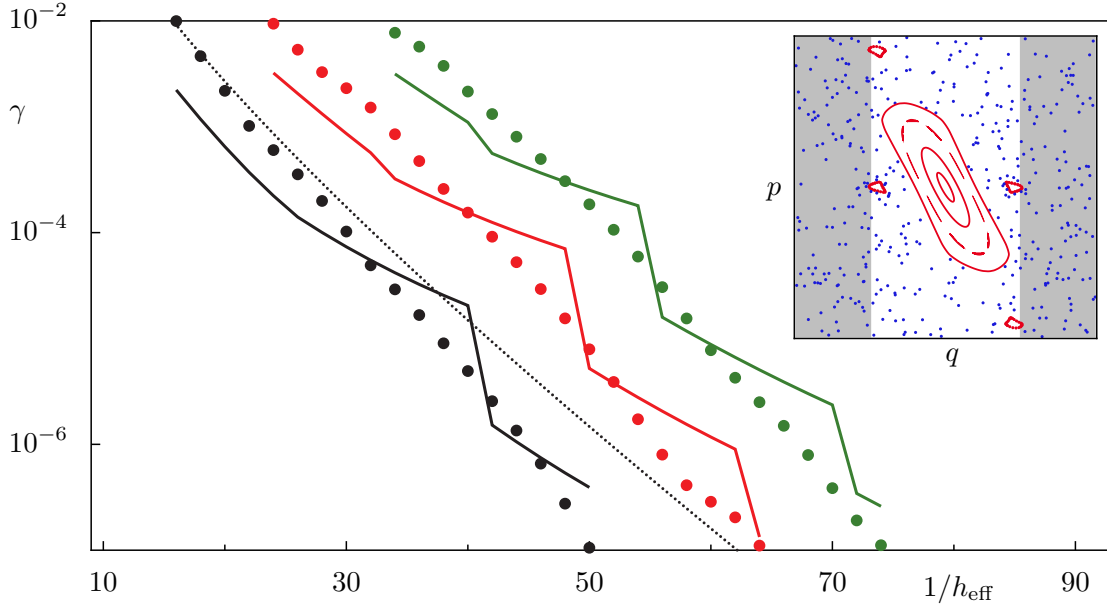


Figure 4.13: Dynamical tunneling rates for the standard map ($K = 2.9$) for $m \leq 2$: We compare the prediction of Eq. (4.9) (lines) and numerical results (dots), obtained using an absorbing boundary at $q = \pm 1/4$ (gray-shaded area of the inset). The prediction of Eq. (4.43) [46, 47] is presented for $m = 0$ with a fitted prefactor (dotted line).

a , b , d_1 , d_2 , ω , q_d , and K . The kinetic energy $T(p)$ is periodic with respect to the phase space unit cell.

The map given by Eqs. (3.41) and (3.42) is similar to the system \mathcal{F}_1 as it also destroys the integrable region by smoothly changing the map functions, here $V'(q)$ at $|q| = q_d/(8\pi)$. For $|q| < q_d/(8\pi)$ the potential term is almost linear while it tends to the standard map for $|q| > q_d/(8\pi)$. In Ref. [41] this map is used to study the evolution of a wave packet initially started in the regular region by means of complex paths. However, it can also be used to predict tunneling rates by means of Eq. (4.9). The fictitious integrable system is determined by continuing the dynamics within $|q| < q_d/(8\pi)$ to the whole phase space. The resulting integrable map is defined by the functions

$$V'(q) = -\frac{1}{2\pi} \left(\omega + \frac{d_1}{2} - \frac{d_2}{2} \right), \quad (4.48)$$

$$T'(p) = -\frac{K}{8\pi} \sin(2\pi p). \quad (4.49)$$

For sufficiently large b the dynamics of the mixed map inside the regular region is equivalent to that of the regular map. Thus Eq. (4.9) can be applied and we compare its results to numerically determined data. As for the standard map, absorbing boundary conditions at $q = \pm 1/2$ lead to strong fluctuations of the numerically determined tunneling rates as a function of h_{eff} , presumably due to dynamical localization. Choosing $q = \pm 1/4$, which is closer to the regular

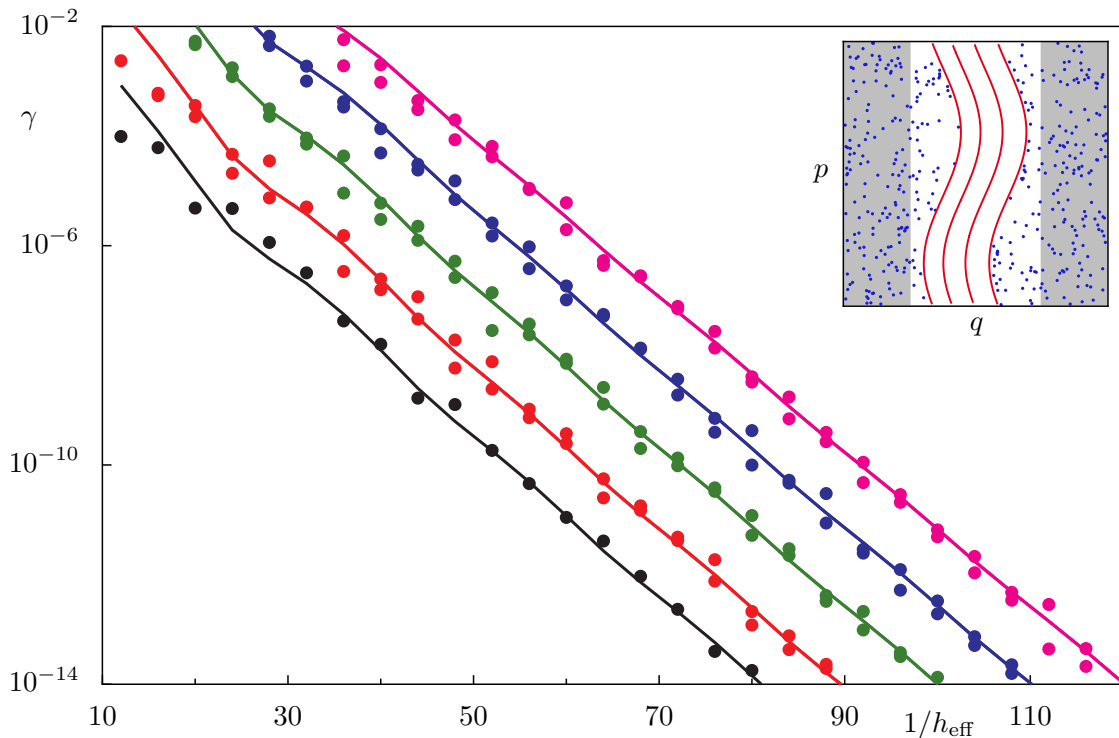


Figure 4.14: Dynamical tunneling rates from a regular stripe to the chaotic sea for the kicked system \mathcal{F}_3 with $a = 5$, $b = 100$, $d1 = -24$, $d2 = -26$, $\omega = 1$, $q_d = 5$, and $K = 3$: We compare numerical results (dots) and the prediction following from Eq. (4.9) (lines) vs $1/h_{\text{eff}}$ for the quantum numbers $|m| \leq 4$. The inset shows the phase space of the system. Absorbing boundary conditions are used in the gray region for the numerical determination of tunneling rates.

stripe, we find smoothly decaying tunneling rates. In Fig. 4.14 these results are presented, showing excellent agreement. Note that due to the symmetry of the map there always exist two regular states with comparable tunneling rates except for the central state $m = 0$. These two states are located symmetrically around the center of the regular stripe. While the theoretical prediction using Eq. (4.9) is identical for such two states the numerical results slightly differ due to the different chaotic dynamics in the vicinity of the border of the regular region (see inset in Fig. 4.14).

4.2 Unification with resonance-assisted tunneling

In the last section we studied the direct regular-to-chaotic tunneling process. It dominates in the quantum regime, $h_{\text{eff}} \lesssim A$, for which nonlinear resonance chains do not affect the tunneling process. Yet, in generic systems these classical structures will have an essential influence on the tunneling process in the semiclassical regime, $h_{\text{eff}} \ll A$. The influence of such resonances is described within the theory of resonance-assisted tunneling [53–56] which shows qualitative agree-

ment to numerical data obtained for quantum maps [55], periodically driven systems [57, 58], quantum accelerator modes [43], and for multidimensional molecular systems [59, 60]. However, especially in the experimentally relevant regime of large Planck's constant deviations of many orders of magnitude appear. Hence, neither the direct tunneling prediction nor resonance-assisted tunneling alone is able to predict dynamical tunneling rates from the quantum to the semiclassical regime.

In this section we combine the mechanism of direct tunneling with an improved resonance-assisted tunneling theory to obtain a unified prediction which is valid from the quantum to the semiclassical regime [61]. Considering two improvements to the original theory of resonance-assisted tunneling we are able to predict dynamical tunneling rates which are in excellent agreement to numerical data for a system with one or many dominating resonances. Furthermore, we present criteria which allow to determine the transition point between direct and resonance-assisted tunneling and the h_{eff} -regime in which each appearing resonance is relevant.

4.2.1 Theory of resonance-assisted tunneling

The existence of nonlinear resonances leads to an enhancement of the tunneling rates caused by quasi-degeneracies of regular states localized inside the same island [52]. These quasi-degeneracies can be qualitatively understood by considering the rotation number w_r of the resonance. If we study an $r:s$ resonance, its rotation number w_r is rational with $w_r = s/r$, i.e. during r periods of the external driving the orbit rotates s times around the central fixed point. This rational rotation number leads to quasi-degeneracies between the regular states with quantum number m and $m + lr$ ($l \in \mathbb{N}$) as the quasi-energies φ_m and φ_{m+lr} are equal modulo 2π , see Eq. (3.146). These quasi-degeneracies enable tunneling steps from the initial regular state to the chaotic sea mediated by higher excited regular states which show a faster decay towards the chaotic region. Thus, the tunneling rate of the initial regular state is enhanced. Quantitatively, a theory was derived [53–56] which describes this resonance-assisted tunneling process. In the following a modified version of its derivation will be presented which includes the unification with direct tunneling described by the theory using a fictitious integrable system, which was presented in the last section.

The influence of a nonlinear resonance onto the regular island is described by a perturbative approach. The classical Hamilton function is decomposed into an unperturbed part $H_{\text{reg}}(I)$ which is integrable and resonance-free and the perturbation $V(I, \theta, t)$ which induces the resonance

$$H(I, \theta, t) = H_{\text{reg}}(I) + \varepsilon V(I, \theta, t). \quad (4.50)$$

Here we use action-angle variables (I, θ) and ε is the perturbation strength. The unperturbed system H_{reg} describes the same fictitious integrable system which we have discussed in the last

section. If a resonance condition is fulfilled the frequency of the external driving $\omega = 2\pi$ is a rational multiple of the internal oscillation frequency $\Omega(I) = dH_{\text{reg}}/dI$, i.e.

$$r\Omega_{r:s} = s\omega, \quad (4.51)$$

where r and s are integers and $\Omega_{r:s} := \Omega(I_{r:s}) = 2\pi w_r(I_{r:s})$ is the winding number at the action $I_{r:s}$ of the $r:s$ resonance. Close to such a resonance classical perturbation theory diverges, caused by appearing small denominators in the perturbation expansion. This problem can be avoided by first using a canonical transformation to a corotating frame in which the new system rotates with the frequency of the resonance. We introduce a new angle variable $\vartheta := \theta - \Omega_{r:s}t$ which is constant under the time evolution of $H_{\text{reg}}(I)$ at $I = I_{r:s}$ and changes slowly in its vicinity. Using the new action-angle variables (I, ϑ) the Hamiltonian has the following form

$$\bar{H}(I, \vartheta, t) = H_{\text{reg}}(I) - \Omega_{r:s}I + \varepsilon\bar{V}(I, \vartheta, t) \quad (4.52)$$

where the perturbation reads

$$\bar{V}(I, \vartheta, t) = V(I, \vartheta + \Omega_{r:s}t, t). \quad (4.53)$$

As the new angle ϑ varies on time-scales which are much larger than the period of the external driving, adiabatic perturbation theory can be applied to Eq. (4.52) in order to eliminate its explicit time dependence. Therefore, we apply a canonical transformation $(I, \vartheta) \rightarrow (\bar{I}, \bar{\vartheta})$ to new action-angle variables leading to a transformation of the Hamiltonian $\bar{H} \rightarrow H_{\text{reg},r:s}$. In lowest order adiabatic perturbation theory performs a time average of \bar{V} over r driving periods. For the new effective Hamilton function one finds

$$H_{\text{reg},r:s}(\bar{I}, \bar{\vartheta}) = \tilde{H}_{\text{reg}}(\bar{I}) - \Omega_{r:s}\bar{I} + \tilde{V}(\bar{I}, \bar{\vartheta}). \quad (4.54)$$

The new action-angle variables $(\bar{I}, \bar{\vartheta})$ are introduced by a generating function G

$$I = \bar{I} + \frac{\partial G}{\partial \vartheta}(\bar{I}, \vartheta, t), \quad (4.55)$$

$$\bar{\vartheta} = \vartheta + \frac{\partial G}{\partial \bar{I}}(\bar{I}, \vartheta, t), \quad (4.56)$$

$$G(\bar{I}, \vartheta, t) = - \int_0^t \left(\varepsilon\bar{V}(\bar{I}, \vartheta, t') - \tilde{V}(\bar{I}, \vartheta) \right) dt'. \quad (4.57)$$

Using the Fourier decomposition of the perturbation

$$\tilde{V}(\bar{I}, \bar{\vartheta}) = \sum_{k=0}^{\infty} V_k(\bar{I}) \cos(kr\bar{\vartheta} + \phi_k) \quad (4.58)$$

and the second order expansion of the unperturbed system \tilde{H}_{reg} around the action $I_{r:s}$ of the resonance the time-independent effective Hamiltonian reads

$$H_{\text{reg},r:s}(I, \vartheta) = \frac{(I - I_{r:s})^2}{2M_{r:s}} + \sum_{k=1}^{\infty} V_k \cos(kr\vartheta + \phi_k). \quad (4.59)$$

The inverse derivative of the frequency ω to the action I at $I = I_{r:s}$ is denoted by $M_{r:s} := (d^2 H_{\text{reg}}/dI^2)^{-1}(I_{r:s})$, $V_k := V_k(I_{r:s})$, and we neglect the bar and tilde. In Refs. [53, 54] it was shown that the coefficients V_k decrease exponentially with k such that it is sufficient to consider V_1 and neglect the other terms. The resulting Hamiltonian describes a mathematical pendulum [53, 54, 88]

$$H_{\text{reg},r:s}(I, \vartheta) = \frac{(I - I_{r:s})^2}{2M_{r:s}} + 2V_{r:s} \cos(r\vartheta + \phi) \quad (4.60)$$

with $2V_{r:s} := V_1$ and $\phi := \phi_1$.

Using the described approximations we have managed to map the dynamics in the vicinity of a nonlinear resonance in a mixed regular-chaotic system to the dynamics of the integrable pendulum which can be evaluated more easily. If we further assume $\phi = 0$ the remaining parameters $I_{r:s}$, $M_{r:s}$, and $V_{r:s}$ can be determined directly from the classical phase space of the mixed system without introducing the action-angle variables (I, ϑ) [55, 182]. As derived in appendix B.4 the missing parameters $I_{r:s}$, $M_{r:s}$, and $V_{r:s}$ result from the area $A_{r:s}^+$ enclosed by the outer separatrix, the area $A_{r:s}^-$ enclosed by the inner separatrix of the resonance, see

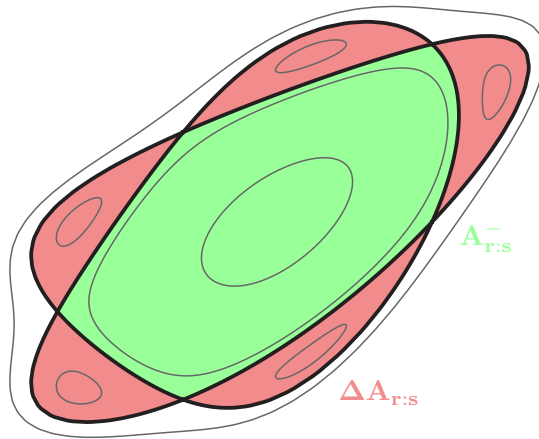


Figure 4.15: Illustration of a 5:1 resonance chain inside a regular region. The area enclosed by the inner separatrix is called $A_{r:s}^-$ (green) and the area enclosed inside the two separatrices $\Delta A_{r:s}$ (red). We have $A_{r:s}^+ = \Delta A_{r:s} + A_{r:s}^-$.

Fig. 4.15, and the trace of the linearized mapping $\mathcal{M}_{r:s}$ at resonance

$$I_{r:s} = \frac{1}{4\pi}(A_{r:s}^+ + A_{r:s}^-), \quad (4.61)$$

$$\sqrt{2M_{r:s}V_{r:s}} = \frac{1}{16}(A_{r:s}^+ - A_{r:s}^-), \quad (4.62)$$

$$\sqrt{\frac{2V_{r:s}}{M_{r:s}}} = \frac{1}{r^2} \arccos\left(\frac{\text{Tr}\mathcal{M}_{r:s}}{2}\right). \quad (4.63)$$

With this information the pendulum Hamiltonian, Eq. (4.60), is now completely known for each appearing $r:s$ resonance. In order to understand its implications on the tunneling process it has to be quantized using time-independent perturbation theory, where $\hat{H}_{\text{reg}} \approx (\hat{I} - I_{r:s})^2/2M_{r:s} + \Omega_{r:s}\hat{I}$ is the unperturbed part with $\hat{I} = -i\hbar_{\text{eff}}\frac{\partial}{\partial\vartheta}$ and $2V_{r:s} \cos(r\hat{\vartheta} + \phi)$ is the perturbation. This perturbation causes couplings between the states $|\psi_{\text{reg}}^m\rangle$ and $|\psi_{\text{reg}}^{m+r}\rangle$ from the unperturbed basis

$$\langle\psi_{\text{reg}}^{m+r}|\hat{H}_{\text{reg},r:s}|\psi_{\text{reg}}^m\rangle = V_{r:s}e^{i\phi}. \quad (4.64)$$

Applying time-independent perturbation theory we find that the eigenstates $|\psi_{\text{reg},r:s}^m\rangle$ of the full system $\hat{H}_{\text{reg},r:s}$ contain admixtures of the unperturbed states $|\psi_{\text{reg}}^{m+lr}\rangle$, $l \in \mathbb{N}$,

$$|\psi_{\text{reg},r:s}^m\rangle = |\psi_{\text{reg}}^m\rangle + A_{m,r}^{(r:s)}|\psi_{\text{reg}}^{m+r}\rangle + A_{m,r}^{(r:s)}A_{m,2r}^{(r:s)}|\psi_{\text{reg}}^{m+2r}\rangle + \dots, \quad (4.65)$$

in which the coefficients $A_{m,lr}^{(r:s)}$ are defined by

$$A_{m,lr}^{(r:s)} := \frac{V_{r:s}e^{i\phi}}{E_m - E_{m+lr} + lr\hbar_{\text{eff}}\Omega_{r:s}} \quad (4.66)$$

and E_m denote the eigenenergies of the unperturbed system \hat{H}_{reg} . Note that Eq. (4.65) is valid only if the condition $A_{m,lr}^{(r:s)} \ll 1$ is fulfilled for each l . The divergence which appears if the energy denominator in Eq. (4.66) is equal to zero does not appear in the real system, in which the two coupled states of energy E_m and E_{m+lr} will form even and odd linear combinations with equal weight on the two classical tori. The unperturbed energies are given by

$$E_m = \frac{(I_m - I_{r:s})^2}{2M_{r:s}} + \Omega_{r:s}I_m, \quad (4.67)$$

with the quantized actions

$$I_m = \hbar_{\text{eff}}\left(m + \frac{1}{2}\right). \quad (4.68)$$

The existence of a resonance in a regular island therefore provides a mechanism which couples the unperturbed state $|\psi_{\text{reg}}^m\rangle$ to higher excited states $|\psi_{\text{reg}}^{m+lr}\rangle$. These higher excited states are localized closer to the border of the regular island and have an enhanced tunneling rate to the

chaotic sea. As the eigenstate $|\psi_{\text{reg},r:s}^m\rangle$ of $\hat{H}_{\text{reg},r:s}$ contains admixtures of these higher excited states $|\psi_{\text{reg}}^{m+lr}\rangle$ its tunneling rate γ_m will be enhanced compared to the tunneling rate of the unperturbed state $|\psi_{\text{reg}}^m\rangle$ which is determined by direct tunneling only. This effect is called resonance-assisted tunneling.

As the final step we want to derive a prediction for the tunneling rates from the m th excited regular state $|\psi_{\text{reg},r:s}^m\rangle$ to the chaotic sea including resonance-assisted tunneling. In analogy to the last section, Eq. (4.8), these rates are given by

$$\gamma_m = \sum_{\text{ch}} |\langle \psi_{\text{ch}} | \hat{U} | \psi_{\text{reg},r:s}^m \rangle|^2. \quad (4.69)$$

Using the perturbative expansion for the states $|\psi_{\text{reg},r:s}^m\rangle$ obtained in Eq. (4.65) we find

$$\begin{aligned} \gamma_m &= \sum_{\text{ch}} \left| \langle \psi_{\text{ch}} | \hat{U} | \psi_{\text{reg}}^m \rangle + A_{m,r}^{(r:s)} \langle \psi_{\text{ch}} | \hat{U} | \psi_{\text{reg}}^{m+r} \rangle + \dots \right|^2, \\ &= \sum_{\text{ch}} \left\{ |\langle \psi_{\text{ch}} | \hat{U} | \psi_{\text{reg}}^m \rangle|^2 + |A_{m,r}^{(r:s)}|^2 |\langle \psi_{\text{ch}} | \hat{U} | \psi_{\text{reg}}^{m+r} \rangle|^2 \right. \\ &\quad \left. + 2\text{Re} \left(A_{m,r}^{(r:s)} \langle \psi_{\text{reg}}^m | \hat{U} | \psi_{\text{ch}} \rangle \langle \psi_{\text{ch}} | \hat{U} | \psi_{\text{reg}}^{m+r} \rangle \right) + \dots \right\}. \end{aligned} \quad (4.70)$$

$$(4.71)$$

The first term in Eq. (4.71) is given by the direct tunneling rate $\gamma_m^d = \sum_{\text{ch}} |\langle \psi_{\text{ch}} | \hat{U} | \psi_{\text{reg}}^m \rangle|^2$ of the m th unperturbed state derived in the last section while the second term includes the direct tunneling rate of the $(m+r)$ th unperturbed state γ_{m+r}^d . The mixed term in Eq. (4.71) is estimated by the following inequality

$$\left| \langle \psi_{\text{ch}} | \hat{U} | \psi_{\text{reg}}^m \rangle - A_{m,r}^{(r:s)} \langle \psi_{\text{ch}} | \hat{U} | \psi_{\text{reg}}^{m+r} \rangle \right|^2 \geq 0 \quad \Rightarrow \quad (4.72)$$

$$|\langle \psi_{\text{ch}} | \hat{U} | \psi_{\text{reg}}^m \rangle|^2 + |A_{m,r}^{(r:s)}|^2 |\langle \psi_{\text{ch}} | \hat{U} | \psi_{\text{reg}}^{m+r} \rangle|^2 \geq 2\text{Re} \left(A_{m,r}^{(r:s)} \langle \psi_{\text{reg}}^m | \hat{U} | \psi_{\text{ch}} \rangle \langle \psi_{\text{ch}} | \hat{U} | \psi_{\text{reg}}^{m+r} \rangle \right). \quad (4.73)$$

It shows that this mixed term is smaller than the sum of the two leading terms in Eq. (4.71). It is especially important if these two terms are equal. However, for most values of the effective Planck constant they will be of different orders of magnitude such that the mixed term is negligible. The same is true for all higher order mixed terms appearing in Eq. (4.71). Hence, we neglect these mixed terms and arrive at our final result for the tunneling rate of the m th regular state to the chaotic sea

$$\gamma_m = \gamma_m^d + |A_{m,r}^{(r:s)}|^2 \gamma_{m+r}^d + |A_{m,r}^{(r:s)} A_{m,2r}^{(r:s)}|^2 \gamma_{m+2r}^d + \dots \quad (4.74)$$

The first term of Eq. (4.74) describes the direct tunneling process from the m th quantized torus to the chaotic sea with the rate γ_m^d , neglecting any influence from nonlinear resonances. In the second term the matrix element $A_{m,r}^{(r:s)}$ describes one resonance-assisted tunneling step from the

m th to the $(m+r)$ th quantized torus via an $r:s$ resonance while the factor γ_{m+r}^d describes the subsequent direct tunneling into the chaotic sea. The last term accounts for two resonance-assisted and one direct tunneling step. The three terms are visualized as insets in Fig. 4.17 in the \hbar_{eff} -regime where they are most relevant. In the case when we have no contributing resonances at all, as discussed in the last section, all terms are zero except the first one and tunneling is consistently described by the direct tunneling process. Note that the divergence which appears if the energy denominator in the coefficients $A_{m,lr}^{(r:s)}$ becomes zero is unphysical. Here the maximal possible tunneling rate is given by $\gamma_m = \gamma_{m+lr}^d/2$ under the condition that the unperturbed state $|\psi_{\text{reg}}^{m+lr}\rangle$ exists inside the regular region.

Let us discuss the relation of our result to previous studies of resonance-assisted tunneling. The derived Eq. (4.74) is similar to an equation presented in Ref. [54, Eq. (7)], where instead of tunneling rates from the regular island to the chaotic sea phase splittings $\Delta\varphi$ between symmetry related regular states are used. In Appendix C.2 we show that these splittings and our tunneling rates γ are directly related quantities. In contrast to Ref. [54, Eq. (7)] which was derived for nearly integrable systems, our result, Eq. (4.74), is also applicable to generic mixed regular-chaotic systems far from integrability by introducing the direct tunneling rates γ^d .

In Ref. [55] the coupling of the initial regular state $|\psi_{\text{reg}}^m\rangle$ to the chaotic sea is described by an effective coupling matrix element

$$V_{\text{eff}} = V_{r:s} \prod_{l=1}^{l_{\text{max}}} \frac{V_{r:s}}{E_m - E_{m+lr} + \hbar_{\text{eff}}\Omega_{r:s}lr} \quad (4.75)$$

in which $l = 1, \dots, l_{\text{max}}$ and $m + l_{\text{max}}r$ denotes the maximally existing regular quantum number. The tunneling rate is obtained as

$$\gamma_m = \left(\frac{V_{\text{eff}}}{\hbar_{\text{eff}}} \right)^2. \quad (4.76)$$

Note that this equation describes the term in Eq. (4.74) which includes the maximal possible number of resonance steps at the considered value of Planck's constant. Yet, this does not have to be the dominant contribution. Furthermore, the final step to the chaotic sea is approximated by another resonant step $V_{r:s}$. This assumption leads to a prediction for the tunneling rates which depends on classical properties of the regular island only and does not include the direct tunneling rates γ^d . In the semiclassical limit, when more and more resonances contribute, the final direct tunneling step is negligible compared to the many other contributions and the prediction of Eq. (4.76) can be used. However, in the regime where only a few resonance steps occur it cannot reliably reproduce tunneling rates, as here the direct tunneling rates are relevant, see Fig. 4.17, which shows deviations of several orders of magnitude.

4.2.2 Improvements of resonance-assisted tunneling

In this section we want to consider two improvements to the original theory of resonance-assisted tunneling described above. On the one hand, the quadratic approximation of the unperturbed energies, Eq. (4.67), fails if the nonlinearity of the system is too strong, which occurs especially for resonances close to the border of the regular region. We propose a method to compute a more accurate prediction of the semiclassical energies E_m . On the other hand in the last section the coupling-matrix elements $V_{r:s}$ are assumed to be action independent. In reality they will, however, depend on the actions of the regular states which are coupled by the resonance. We calculate the lowest order correction of this action dependence $V_{r:s}(I)$.

Improved semiclassical energies \bar{E}_m

In Refs. [53,54] the unperturbed system H_{reg} is approximated quadratically for each resonance around its action $I_{r:s}$. Accordingly, the coupling between unperturbed states whose quantizing action is close to the action of the resonance $I_m \approx I_{r:s}$ is well predicted. If, however, states with quantizing actions further away from $I_{r:s}$ are involved, the quadratic approximation fails. This is especially the case for resonances located at the border of the regular island. Here, the rotation number, which is directly connected to the semiclassical energies via Eq. (3.146), changes more rapidly than in the center of the regular island, where the quadratic approximation is valid for a larger range of actions.

To account for these deviations, higher orders have to be considered in the evaluation of the semiclassical energies $E(I)$. This can be done in different ways. As a first step, we use the integrable approximation H_{reg} of the mixed system H which is obtained e.g. by the Lie-transformation or the method based on the frequency-map analysis. For this purpose, we define a straight line $u \rightarrow [p(u), q(u)]$ from the center of the regular island to its border with the chaotic sea and compute the enclosed areas $A(u) = 2\pi I(u)$ of the quasi-periodic trajectories that result from a set of initial conditions along that line. For each initial condition we know the regular energy $\bar{E}(u) = H_{\text{reg}}(p(u), q(u))$ and obtain the improved dispersion relation $\bar{E}(I)$. This procedure works best if the trajectories of the integrable approximation H_{reg} resemble the regular orbits of H with a high accuracy, which is only the case if the existing resonance chains are small compared to the size of the regular island. For large resonances the integrable approximation H_{reg} will not accurately reproduce the regular orbits of H and the prediction of the semiclassical energies $\bar{E}(I)$ will become inaccurate. In such cases a more accurate procedure consists in directly using the classical information of the kicked system H . We compute the enclosed areas $A(u)$ and rotation numbers $w_r(u)$ of the quasi-periodic trajectories that result from a set of initial conditions along the line $u \rightarrow [p(u), q(u)]$ described above. With this

information we calculate the unperturbed energies

$$\bar{E}(u) = \int_{u_0}^u du' w_r(u') \frac{dA(u')}{du'} \quad (4.77)$$

as derived in Appendix C.1 and obtain $\bar{E}(I)$ through $A(u) = I(u)/2\pi$.

The energy denominators in Eq. (4.66) are given by the improved unperturbed energies

$$\bar{E}_m - \bar{E}_{m+lr} + \hbar_{\text{eff}} \Omega_{r:s} lr. \quad (4.78)$$

This leads to an accurate prediction of the position of the resonance peaks in the tunneling rates with respect to the effective Planck constant, which occur if this energy denominator is equal to zero. A comparison between the results using the improved semiclassical energies and results for the original quadratic approximation is presented in Figs. 4.18 and 4.22.

Improved couplings $V_{r:s}$

In Refs. [53, 54] the action dependence of $V_{r:s}$ is neglected by using $V_{r:s}(I) \approx V_{r:s}(I_{r:s})$. This assumption is accurate for actions in the vicinity of the resonance $I \approx I_{r:s}$. In the semiclassical limit, when many resonances are involved in the tunneling process, the quantized tori coupled by one specific resonance will be close to its action $I_{r:s}$ and the action independent assumption of $V_{r:s}$ is valid. However, for large \hbar_{eff} corrections are necessary. Here, couplings of states with quantizing actions far away from $I_{r:s}$ occur and higher order corrections to $V_{r:s}$ have to be considered.

Following a derivation from Ref. [183] we start with a time-dependent system H which consists of an integrable part H_{reg} and a time-dependent perturbation V

$$H(q, p, t) = H_{\text{reg}}(q, p) + V(q, p, t). \quad (4.79)$$

We introduce action-angle variables (I, ϑ) with respect to the center of the regular island (q^*, p^*) such that $H_{\text{reg}}(q, p) = \bar{H}_{\text{reg}}(I)$ and use alternative variables $P = -\sqrt{2I} \sin \vartheta$, $Q = \sqrt{2I} \cos \vartheta$. The unperturbed part then reads

$$H_{\text{reg}}(q, p) = \bar{H}_{\text{reg}} \left(\frac{1}{2}(P^2 + Q^2) \right), \quad V(q, p, t) = \bar{V}(Q, P, t), \quad (4.80)$$

with

$$p(Q, P) = \sum_{k,l=0}^{\infty} p_{kl} P^k Q^l, \quad (4.81)$$

$$q(Q, P) = \sum_{k,l=0}^{\infty} q_{kl} P^k Q^l. \quad (4.82)$$

As the transformation $(q, p) \rightarrow (Q, P)$ is analytical we may write the perturbation V as a power series in the new coordinates Q and P

$$\bar{V}(Q, P, t) = \sum_{k,l=0}^{\infty} V_{kl}(t) P^k Q^l. \quad (4.83)$$

Using

$$P^k = \sqrt{2I}^k \left(\frac{i}{2} (e^{i\vartheta} - e^{-i\vartheta}) \right)^k = \sqrt{\frac{I}{2}} i^k \sum_{k'=0}^k (-1)^{k'} e^{i(k-2k')\vartheta} \binom{k}{k'}, \quad (4.84)$$

$$Q^l = \sqrt{2I}^l \left(\frac{1}{2} (e^{i\vartheta} + e^{-i\vartheta}) \right)^l = \sqrt{\frac{I}{2}} \sum_{l'=0}^l e^{i(l-2l')\vartheta} \binom{l}{l'} \quad (4.85)$$

we find the perturbation

$$\bar{V}(I, \vartheta, t) = \sum_{k,l=0}^{\infty} V_{kl}(t) \sqrt{\frac{I}{2}}^{k+l} i^k \sum_{k'=0}^k \sum_{l'=0}^l (-1)^{k'} e^{i(k+l-2k'-2l')\vartheta} \binom{k}{k'} \binom{l}{l'} \quad (4.86)$$

$$= \sum_{n=-\infty}^{\infty} \sqrt{I}^{|n|} e^{in\vartheta} \left(\sum_{k=0}^{\infty} C_{nk}(t) I^k \right) \quad (4.87)$$

as a power series in I . For the integrable approximation of the resonance dynamics in the corotating frame one obtains

$$H_{\text{reg},r:s}(I, \vartheta) = \frac{(I - I_{r:s})^2}{2M_{r:s}} + 2V_{r:s}(I) \cos(r\vartheta + \phi) \quad (4.88)$$

with

$$V_{r:s}(I) = I^{\frac{r}{2}} \sum_{k=0}^{\infty} \bar{C}_{rk} I^k \approx W_{r:s} I^{\frac{r}{2}}. \quad (4.89)$$

As the perturbation term $V_{r:s}(I)$ explicitly depends on the action we use a different quantization scheme than in the original derivation of resonance-assisted tunneling. For the quantization we introduce the ladder operators \hat{a} and \hat{a}^\dagger which are related to the action-angle variables

$$\sqrt{\hat{I}} e^{i\hat{\vartheta}} = \sqrt{\hbar_{\text{eff}}} \hat{a}^\dagger, \quad e^{-i\hat{\vartheta}} \sqrt{\hat{I}} = \sqrt{\hbar_{\text{eff}}} \hat{a}. \quad (4.90)$$

With these operators the operators of the new phase-space coordinates (\hat{Q}, \hat{P}) can be defined

$$\hat{Q} = \sqrt{\frac{\hat{I}}{2}} e^{i\hat{\vartheta}} + e^{-i\hat{\vartheta}} \sqrt{\frac{\hat{I}}{2}} = \sqrt{\frac{\hbar_{\text{eff}}}{2}} (\hat{a}^\dagger + \hat{a}), \quad \hat{P} = i\sqrt{\frac{\hat{I}}{2}} e^{i\hat{\vartheta}} - ie^{-i\hat{\vartheta}} \sqrt{\frac{\hat{I}}{2}} = i\sqrt{\frac{\hbar_{\text{eff}}}{2}} (\hat{a}^\dagger - \hat{a}) \quad (4.91)$$

and the effective pendulum Hamiltonian reads

$$H_{\text{reg},r:s} = \frac{1}{2M_{r:s}} \left[\hbar_{\text{eff}} \left(\hat{a}^\dagger \hat{a} + \frac{1}{2} \right) - I_{r:s} \right]^2 + W_{r:s} \hbar_{\text{eff}}^{\frac{r}{2}} (\hat{a}^r + \hat{a}^{\dagger r}). \quad (4.92)$$

For the matrix elements of this operator between two unperturbed states $|\psi_{\text{reg}}^m\rangle$ and $|\psi_{\text{reg}}^{m'}\rangle$ one obtains

$$\langle \psi_{\text{reg}}^m | \hat{H}_{\text{reg},r:s} | \psi_{\text{reg}}^{m'} \rangle = \epsilon_m \delta_{m,m'} + V_{m,m'} \delta_{m',m+r} + V_{m,m'} \delta_{m',m-r} \quad (4.93)$$

with

$$\epsilon_m = \frac{1}{2M_{r:s}} \left[\hbar_{\text{eff}} \left(m + \frac{1}{2} \right) - I_{r:s} \right]^2, \quad E_m = \epsilon_m + \hbar \Omega_{r:s} \left(m + \frac{1}{2} \right), \quad (4.94)$$

and the coupling-matrix elements

$$V_{m,m+r} = W_{r:s} \hbar_{\text{eff}}^{\frac{r}{2}} \sqrt{\frac{(m+r)!}{m!}}, \quad V_{m,m-r} = W_{r:s} \hbar_{\text{eff}}^{\frac{r}{2}} \sqrt{\frac{m!}{(m-r)!}}. \quad (4.95)$$

With $V_{r:s} \approx I_{r:s}^{\frac{r}{2}} W_{r:s}$ we finally obtain for the improved coupling-matrix elements

$$\bar{V}_{r:s}^{m,lr} = V_{r:s} \left(\frac{\hbar_{\text{eff}}}{I_{r:s}} \right)^{\frac{r}{2}} \sqrt{\frac{(m'+r)!}{m'!}} \quad (4.96)$$

with $m' = m + (l-1)r$. We find that the improved coupling-matrix elements depend on \hbar_{eff} and on the quantum numbers of the involved unperturbed states $|\psi_{\text{reg}}^m\rangle$ and $|\psi_{\text{reg}}^{m+lr}\rangle$. For large \hbar_{eff} the coupling-matrix elements increase while for smaller \hbar_{eff} they decrease as $\hbar_{\text{eff}}^{lr/2}$. Using the improved couplings $\bar{V}_{r:s}^{m,lr}$ in Eq. (4.66) we find that for actions near $I_{r:s}$ the result stays approximately unchanged while for quantizing tori further away, the plateau and peak values of the tunneling rates are adjusted. This leads to a more accurate prediction of tunneling rates as is shown in Figs. 4.18 and 4.22. In the semiclassical limit more and more resonances contribute to the tunneling process and the actions of the coupled regular states will be closer to the action of the relevant resonance. Hence, the improvement of the couplings $V_{r:s}$ is less important.

4.2.3 Multi-resonance effects

Up to this point we have considered the effect of one dominating resonance onto the tunneling process. In a generic system, however, infinitely many resonances exist inside the regular region which might simultaneously contribute to the tunneling process. Consequently, the m th regular state $|\psi_{\text{reg},r:s}^m\rangle$ has contributions from unperturbed states $|\psi_{\text{reg}}^n\rangle$ whose quantum number differs

from m by integer multiples a_i of the order r_i of the contributing $r_i:s_i$ resonances

$$|\psi_{\text{reg},r:s}^m\rangle = \sum_{n \leq m_{\text{max}}} \sum_{\{a_i\}} \prod_{a_i} A_{m,m'}^{(r_i:s_i)} |\psi_{\text{reg}}^n\rangle. \quad (4.97)$$

With this perturbed state $|\psi_{\text{reg},r:s}^m\rangle$ we can use Eq. (4.69) to determine a prediction for the tunneling rates γ_m in this multi-resonance situation. We arrive at a prediction similar to Eq. (4.74) in which more terms appear corresponding to the contributing $r_i:s_i$ resonances

$$\gamma_m = \gamma_m^d + \sum_{n \leq m_{\text{max}}} \left| \sum_{\{a_i\}} \prod_{a_i} A_{m,m'}^{(r_i:s_i)} \right|^2 \gamma_n^d \quad (4.98)$$

where

$$n = m + \sum_i a_i r_i, \quad (4.99)$$

i labels all relevant resonances, and $\{a_i\}$ denote the possible combinations of these resonances. As more and more resonances become important in the semiclassical limit the possible number of contributing combinations of resonances increases exponentially in Eq. (4.98). Multi-resonance couplings occur, see Fig. 4.16, in which first one or more steps are made with one resonance and afterwards further steps with other resonances. If different tunneling steps lead to the same final state $|\psi_{\text{reg}}^n\rangle$, these contributions may interfere as these terms are inside the modulus squared in Eq. (4.98). This may lead to constructive or destructive interference depending on the phases ϕ . However, these phases ϕ cannot be determined from the classical phase space in general. Only if additional symmetries exist the phases are known to be zero or π . Such an example is given by the standard map or the systems \mathcal{F}_1 with $R = 0$.

For the evaluation of Eq. (4.98) two most relevant questions occur: Which resonances contribute to the tunneling process at a given h_{eff} ? And which combinations of these resonances dominate the tunneling process? If an answer to these questions is found the number of contributing terms in Eq. (4.98) can be reduced significantly and the dominating resonance-assisted processes are found.

Let us consider the first question, namely which of the resonances contribute to the tunneling process for a certain value of the effective Planck constant h_{eff} and which do not. I.e. where is the transition between the direct tunneling regime, $h_{\text{eff}} \lesssim A$, where the considered resonance is not important, and the resonance-assisted tunneling regime, $h_{\text{eff}} \ll A$. Also the question which resonance dominates the tunneling process if more than one is relevant has to be answered.

For an $r:s$ resonance to be important it requires that the $(m+r)$ th quantized torus exists inside the regular island, i.e.

$$\frac{A}{h_{\text{eff}}} \geq m + r + \frac{1}{2} \quad (4.100)$$

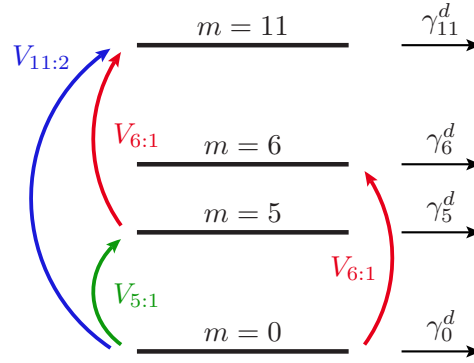


Figure 4.16: Sketch of tunneling steps in the multi resonant case: We choose a regular island with a dominating 5:1, 11:2, and 6:1 resonance chain and consider the ground state $m = 0$. For large h_{eff} the direct tunneling contribution γ_0^d is relevant. For smaller h_{eff} tunneling steps including the 5:1 (green) or the 6:1 (red) chain occur which include a final tunneling step to the chaotic sea with the direct tunneling rates γ_5^d or γ_6^d . For even smaller h_{eff} a tunneling step with the 11:2 resonance (blue) or a two-step process including the 5:1 and the 6:1 chain leads to the same final state $m = 11$ which has a direct tunneling rate γ_{11}^d .

such that a coupling between the m th and the $(m+r)$ th state is possible. Already from this simple criterion we find that resonances of high order r will be important in the semiclassical limit only, while resonances of small order r may be relevant in the quantum regime as well.

In order to determine when a resonance starts to become relevant we consider the position $h_{\text{eff}}^{\text{peak}}$ of the first peak in the tunneling rate γ_m caused by the $r:s$ resonance. It arises when Eq. (4.66) diverges for $E_m - E_{m+r} + r\hbar_{\text{eff}}\Omega_{r:s} = 0$. Using the quadratic approximation for $H_{\text{reg}}(I)$, we find

$$\frac{A_{r:s}}{h_{\text{eff}}^{\text{peak}}} = m + \frac{r}{2} + \frac{1}{2} \quad (4.101)$$

with $A_{r:s} := 2\pi I_{r:s}$. Thus, the first peak appears when the $r:s$ resonance encloses about $m+r/2$ quantized tori. It appears for the largest values of h_{eff} when its order r and the considered quantum number m is small and when its enclosed area $A_{r:s}$ is large. However, we should keep in mind that in order to see the peak in the tunneling rates, $m+r$ states have to exist inside the regular island at $h_{\text{eff}}^{\text{peak}}$. If the improved semiclassical energies \bar{E}_m are known $h_{\text{eff}}^{\text{peak}}$ results from the divergence of the improved energy denominator in Eq. (4.66).

Nevertheless, the influence of the resonance may appear much earlier than $1/h_{\text{eff}}^{\text{peak}}$. We define the transition point $1/h_{\text{eff}}^{\text{res}}$ between the direct and the resonance-assisted tunneling contribution when the first two terms in Eq. (4.74) are equal. Using $\sqrt{2M_{r:s}V_{r:s}} = \Delta A_{r:s}/16$ [55] where $\Delta A_{r:s}$ is the area enclosed between the separatrices of the $r:s$ resonance, we obtain

$$\frac{\Delta A_{r:s}}{r h_{\text{eff}}^{\text{res}}} \frac{\Delta A_{r:s}}{A_{r:s}} \sqrt{\frac{\gamma_{m+r}^d(h_{\text{eff}}^{\text{res}})}{\gamma_m^d(h_{\text{eff}}^{\text{res}})}} \frac{1}{\left(h_{\text{eff}}^{\text{res}}/h_{\text{eff}}^{\text{peak}} - 1\right)} = \frac{128}{\pi^2}. \quad (4.102)$$

This criterion explicitly involves the size $\Delta A_{r:s}$ of the $r:s$ resonance chain measured with respect to r Planck cells and to the area $A_{r:s}$ enclosed by the resonance, as well as the ratio of the direct tunneling rates from the $(m+r)$ th and the m th quantized torus. As the left-handed side of Eq. (4.102) is expected to display a monotonous increase with $1/h_{\text{eff}}^{\text{res}}$ towards the singularity at $1/h_{\text{eff}}^{\text{peak}}$, resonance chains with a large area $\Delta A_{r:s}$ will lead to a lower transition point $1/h_{\text{eff}}^{\text{res}}$ at which the crossover from direct to resonance-assisted tunneling appears. While e.g. the first peak of the 5:1 resonance in Fig. 4.18 appears at $1/h_{\text{eff}}^{\text{peak}} \approx 130$ it dominates the tunneling process already at $1/h_{\text{eff}}^{\text{res}} \approx 35$ which is even before the contributions from other resonances set in.

With the quantities $h_{\text{eff}}^{\text{peak}}$ and $h_{\text{eff}}^{\text{res}}$ the first peak in the tunneling rates and the transition point from direct to resonance-assisted tunneling can be individually calculated for each appearing $r:s$ resonance. If $h_{\text{eff}}^{\text{res}}$ is smaller than the considered value of the effective Planck constant h_{eff} the corresponding resonance can be neglected. Going from the quantum to the semiclassical regime we find that the first contributing resonances are of small order r and enclose a large area $\Delta A_{r:s}$, which is generically the case for resonance chains near the border of the regular island. For such resonances the first peak in the tunneling rates at $h_{\text{eff}}^{\text{peak}}$ might not be visible as at $h_{\text{eff}}^{\text{peak}}$ less than $m+r$ states exist inside the island. Nevertheless, these outer resonances may provide the final coupling towards the chaotic sea especially in the semiclassical limit and have to be considered. A more simple scheme for selecting relevant resonances where the tunneling rates γ^d are not required works as follows: We choose the sequence of resonances with smallest order r and determine the position $h_{\text{eff}}^{\text{peak}}$ of their first peak in the tunneling rates. If $h_{\text{eff}}^{\text{peak}} \ll h_{\text{eff}}$ the resonances are ignored otherwise taken into account. Here it may happen that too many resonances are considered which do not contribute to the tunneling process. Yet, it is a simple procedure, while the question which of many resonances dominates far inside the semiclassical regime cannot be quantitatively answered by our criteria.

Let us now consider the second question. If we know which resonances contribute to the tunneling process at a certain value of h_{eff} , which combinations of tunneling steps appearing in Eq. (4.98) are relevant? The dominating combinations of steps can be determined if the action dependence of the rotation number $w_r(I)$ is known. It can easily be determined with the frequency map analysis [84]. With its knowledge we search for degeneracies in the semiclassically predicted eigenphases of \hat{U} using

$$\varphi_m(h_{\text{eff}}) = \varphi_n(h_{\text{eff}}) \quad (4.103)$$

$$2\pi w_r(I_m) \left(m + \frac{1}{2} \right) \bmod 2\pi = 2\pi w_r(I_n) \left(n + \frac{1}{2} \right) \bmod 2\pi. \quad (4.104)$$

Under variation of h_{eff} different final states $|\psi_{\text{reg}}^n\rangle$ will be degenerate with the initial unperturbed state $|\psi_{\text{reg}}^m\rangle$. These are the final states which contribute to the tunneling process and we consider such combinations of coupling steps $\{a_i\}$ in Eq. (4.98) which lead to the final state $|\psi_{\text{reg}}^n\rangle$.

Combinations of steps leading to non-occurring final states do not have to be considered. However, different combinations of steps may lead to the same final state. To decide, which of them dominates is a non-trivial task. Semiclassically it is found that tunneling steps occur which consecutively use resonances of increasing action, $I_{r_1:s_1} \leq I_{r_2:s_2} \leq I_{r_3:s_3} \leq \dots$, from the center of the regular island to its border with the chaotic sea. If multiple combinations fulfill these criteria and lead to the same final state all of them should be considered.

4.2.4 Applications

In the last section we derived Eq. (4.98) which allows the unified prediction of dynamical tunneling rates combining the direct tunneling approach using a fictitious integrable system with resonance-assisted tunneling. We now predict dynamical tunneling rates with this Eq. (4.98) using the direct tunneling rates γ^d from Eq. (4.9) which describe the decay of the regular states by ignoring the influence of resonances. In addition we consider the improved global energies \bar{E}_m , and the action dependent couplings $\bar{V}_{r:s}$ from Eq. (4.96). The predicted tunneling rates are compared to numerical data obtained for the kicked systems \mathcal{F}_2 described in Section 3.1.2 and the standard map. Furthermore, we compare our theory with the previously existing predictions of direct and resonance-assisted tunneling individually, and visualize the effects of the two considered improvements to resonance-assisted tunneling.

The parameters r_1 , R , Z , and ε of the kicked systems \mathcal{F}_2 introduced in Section 3.1.2 can be chosen in such a way that only one large nonlinear resonance chain exists inside the regular island. We present a situation where one prominent 5:1 chain exists which dominates the tunneling process for $1/h_{\text{eff}} > 20$. Fig. 4.17 shows a comparison between the theoretical prediction of Eq. (4.98) (solid line) and numerical data (dots), obtained by opening the considered kicked system \mathcal{F}_2 at $q = \pm 1/2$. In contrast to the sole application of direct tunneling with Eq. (4.9) (dashed line) or resonance-assisted tunneling according to Eq. (4.76) (gray line) we find excellent agreement over more than 10 orders of magnitude in γ . The phase space of the system is depicted in the inset of Fig. 4.17. It shows one dominant 5:1 resonance inside the regular island. All other resonances are small and do not contribute to the tunneling rates for the shown values of h_{eff} . We find that the direct tunneling rates γ^d following from Eq. (4.9) explain the numerical data for $1/h_{\text{eff}} \lesssim 20$. For larger $1/h_{\text{eff}}$ the 5:1 resonance is important and gives rise to two characteristic peaks corresponding to the coupling of the ground state $m = 0$ to $m = 5$ and $m = 10$. Our theoretical prediction excellently reproduces the peak positions and heights.

As a next example we consider a situation where three dominant resonances exist, namely a 5:1 resonance near the center of the regular island, an 11:2, and an outer 6:1 resonance, see the inset in Fig. 4.18. Here, multi-resonance couplings occur and the tunneling rates from the torus $m = 2$ are determined with Eq. (4.98) by a summation over all relevant $r:s$ resonances. For example the peak at $1/h_{\text{eff}} \approx 84$ in the tunneling rates is caused by the coupling of the

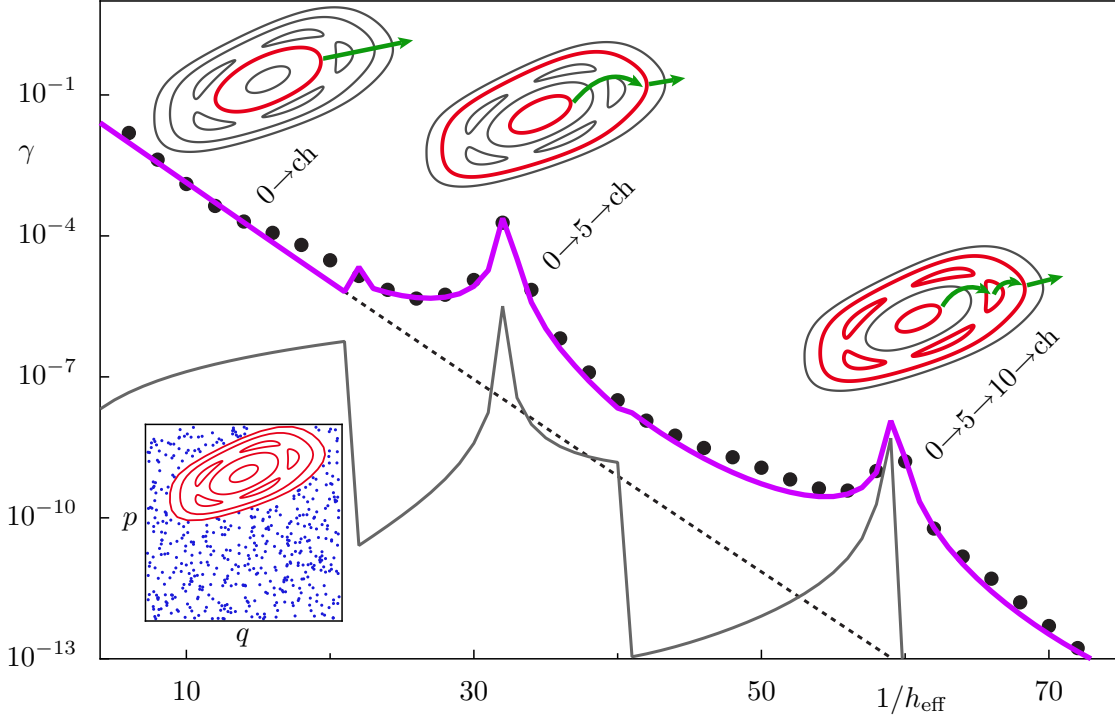


Figure 4.17: Dynamical tunneling rates γ from the innermost quantized torus ($m = 0$) of a regular island with one dominant 5:1 resonance for the system \mathcal{F}_2 with $r_1 = 0.74$, $R = 0.2$, $Z = 1$, and $\varepsilon = 0.002$. Numerical data (dots) is compared to the prediction of Eq. (4.74) (solid line) and previous results in the quantum regime due to the direct tunneling process (dashed line, Eq. (4.9), Ref. [48]) and in the semiclassical regime due to resonance-assisted tunneling (gray solid line, Eq. (4.76), Ref. [55]). The lower inset shows the phase space. The upper insets illustrate the dominant tunneling steps for three values of h_{eff} .

state $m = 2$ to the 18th excited state via the 5:1 and the 11:2 resonance. In Fig. 4.18 we compare numerical data (dots) to the prediction of Eq. (4.98) and find very good agreement. For comparison we also show the rates (dotted line) that result from using Eq. (4.98) together with Eq. (4.66) without the improved unperturbed energies \bar{E}_m and couplings $\bar{V}_{r:s}$. We still find overall agreement to the average decrease of the tunneling rates with $1/h_{\text{eff}}$. However, the reproduction of the positions and heights of the individual peaks requires to use a global approximation for the unperturbed energies and to take into account the action dependence of the coupling matrix elements.

In Fig. 4.19(a),(b) we show a comparison of numerical data (dots) to the results of Eq. (4.98) without the improved unperturbed energies \bar{E}_m and couplings $\bar{V}_{r:s}$ (dotted lines), using only the improved unperturbed energies \bar{E}_m (solid line in (b)), and only the improved couplings (solid line in (a)). The result using both improvements is presented in Fig. 4.18 (solid purple line). This allows to visualize the effect of each improvement on its own. While the improved energies account for the correct positions of the peaks in the tunneling rates with respect to $1/h_{\text{eff}}$, the improved couplings adjust the overall value of the tunneling rates but do not affect

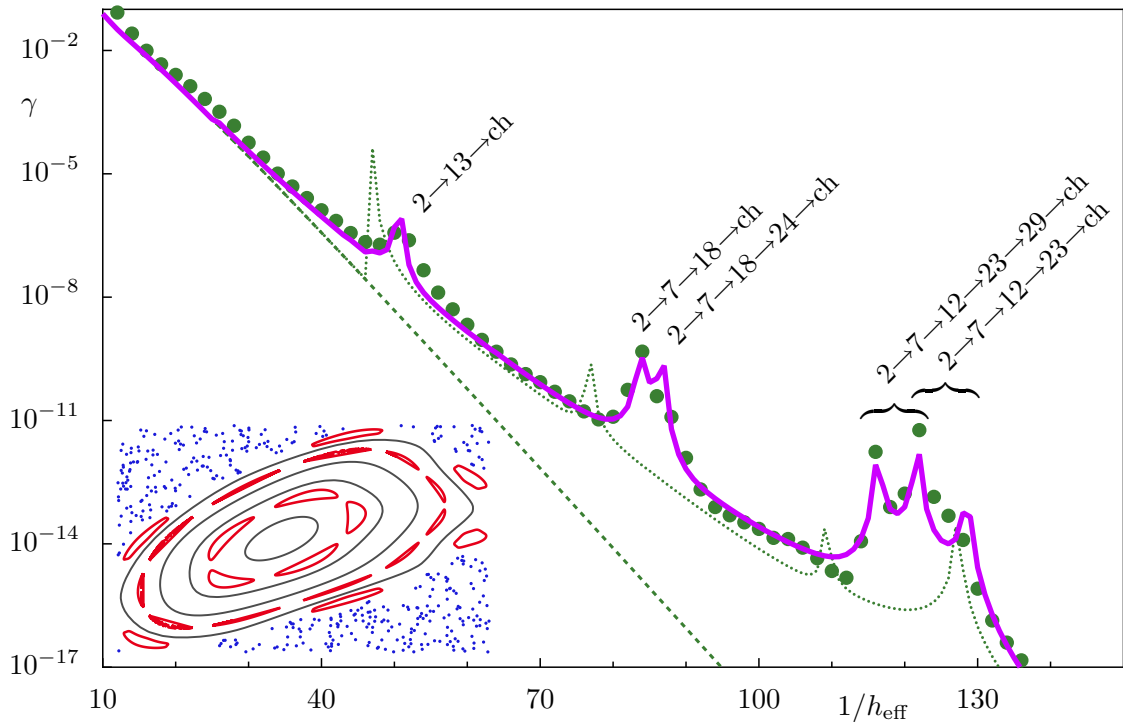


Figure 4.18: Dynamical tunneling rates γ from the quantized torus $m = 2$ of a regular island with three dominant resonances for the system \mathcal{F}_2 with $r_1 = 0.72$, $R = 0.45$, $Z = 1.2$, and $\varepsilon = 0.002$. Numerical data (dots) is compared to the prediction of Eq. (4.98) (solid line). For comparison the direct tunneling contribution (dashed line, Eq. (4.9), Ref. [48]) and the result of Eq. (4.98) without the improvements of the unperturbed energies \bar{E}_m and the couplings $\bar{V}_{r:s}$ is presented (dotted line). The inset shows the regular island of the system and the dominant 5:1, 11:2, and 6:1 resonances which cause tunneling steps as indicated by labels.

the position of the peaks. We find that a reliable prediction of tunneling rates is only achieved when using both of the improvements. In Fig. 4.19(c) the prediction of Eq. (4.98) including only the direct tunneling contribution and the first term caused by the 5:1 resonance is shown as a red line. Also the sum of the direct tunneling contribution and the first term caused by the 11:2 resonance is shown as a blue line. While the 11:2 resonance is responsible for the first peak in the tunneling rates at $1/h_{\text{eff}} \approx 50$ it does not cause the initial deviations from direct tunneling around $1/h_{\text{eff}} \approx 35$. They occur due to the 5:1 chain as presented by the red solid line. While this resonance is already important at $1/h_{\text{eff}} \approx 35$ its first peak appears far away at $1/h_{\text{eff}} \approx 130$. This shows that resonances can be relevant even before their first peak in the tunneling rates appears as discussed in Section 4.2.3. The prediction of Eqs. (4.101) and (4.102) for $1/h_{\text{eff}}^{\text{peak}}$ describing the position of the first peak and $1/h_{\text{eff}}^{\text{res}}$ describing the transition point between direct and resonance-assisted tunneling are shown in Fig. 4.19(c) by red circles for the 5:1 and green circles for the 11:2 resonance. They correctly predict that the 5:1 as well as the 11:2 resonance is relevant for $1/h_{\text{eff}} \gtrsim 40$. The 6:1 resonance is located in the chaotic region

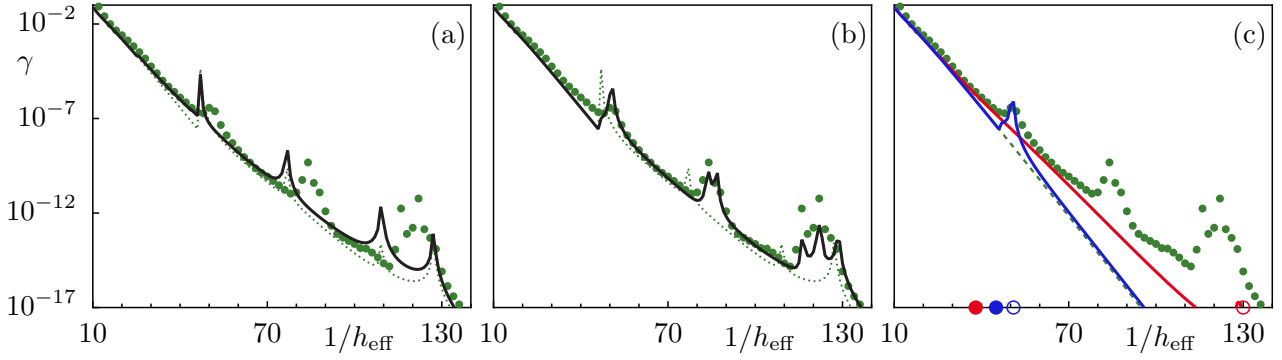


Figure 4.19: Dynamical tunneling rates as presented in Fig. 4.18 (green dots and lines): In addition (a) shows the results of Eq. (4.98) including only the improved couplings $\bar{V}_{r:s}$ (black solid line) and (b) only the improved energies \bar{E}_m (black solid line). In (c) the direct tunneling rates (dashed line) and their sum with the first resonance-assisted contribution of the 5:1 (red line) and the 11:2 resonance (blue line) is presented. We find that the first deviations from direct tunneling are caused by the 5:1 resonance while the first peak appears due to the 11:2 chain. The prediction of Eqs. (4.101) (empty circles) and (4.102) (filled circles) are presented for the 5:1 (red) and the 11:2 resonance (blue).

of phase space. Hence, Eqs. (4.101) and (4.102) are not applicable to predict its relevance. However, we find that it contributes to higher order multi-resonance steps as can be seen by the labels in Fig. 4.18.

In order to convince the reader that the presented predictions are not just exceptionally excellent results we consider a parameter variation from the case presented in Fig. 4.17 with one dominating resonance to the case shown in Fig. 4.18 with three relevant resonances. For each of the parameters r_1 , R , and Z we choose ten equidistant steps in the intervals $r_1 \in [0.74, 0.72]$, $R \in [0.2, 0.45]$, and $Z \in [1.0, 1.2]$. Following the plots in Figs. 4.20 and 4.21 from top left (a) to bottom right (j) the 5:1 resonance moves towards the center of the regular island such that its tunneling peaks are shifted towards larger $1/h_{\text{eff}}$. In (e) the 11:2 resonance enters the regular island which explains the emanating smaller peaks in the tunneling rates. This resonance also moves towards the center of the regular island and its peaks move to smaller $1/h_{\text{eff}}$ crossing the peaks of the 5:1 resonance in (i). The 6:1 chain is relevant in (i) and (j). It is responsible for the sequences of peaks located close-by at a small region in $1/h_{\text{eff}} \approx 115$. For all the systems (a)-(j) we find excellent agreement between the numerical data and our theoretical prediction.

The paradigmatic model of quantum chaos is the standard map introduced in Section 3.1.1, which for $K = 3.5$ has a large generic regular island with a dominant 6:2 resonance. Furthermore, one finds a relevant 14:5 and an 8:3 resonance. Fig. 4.22 shows the comparison between high-precision numerical data, obtained from the splitting of the eigenphases of the quantum propagator computed for different periodicity conditions [54], and the prediction of Eq. (4.98) far into the semiclassical limit. We find quantitative agreement over 30 orders of magnitude in γ . The direct tunneling process is relevant for $1/h_{\text{eff}} \lesssim 30$ beyond which several regimes

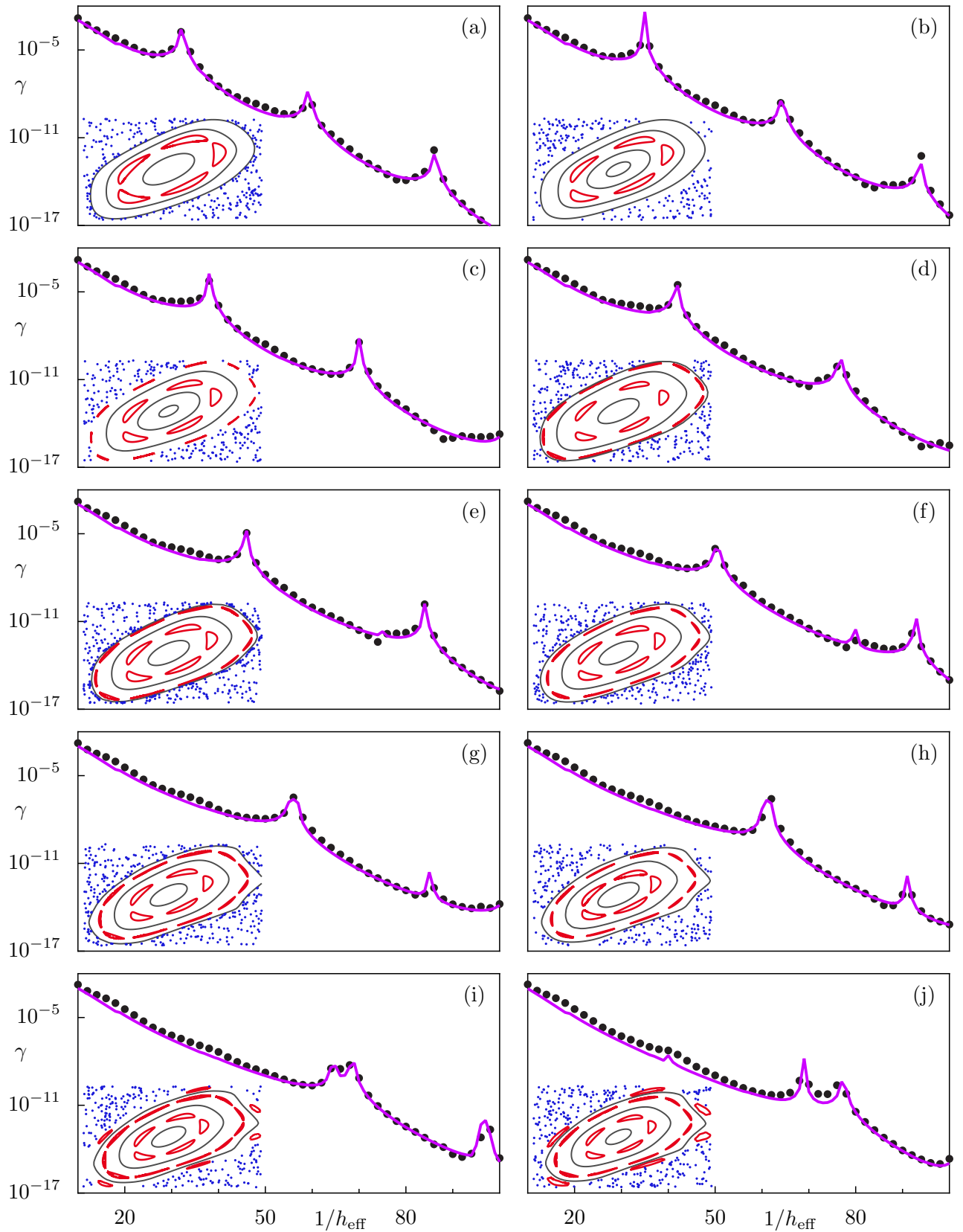


Figure 4.20: Dynamical tunneling rates γ from the quantized torus $m = 0$ of a regular island for the system \mathcal{F}_2 under parameter variation (a)-(j) from (a) $r_1 = 0.74$, $R = 0.2$, $Z = 1$ (Fig. 4.17) to (j) $r_1 = 0.72$, $R = 0.45$, $Z = 1.2$ (Fig. 4.18 for $m = 0$). Numerical data (dots) is compared to the prediction of Eq. (4.98) (solid purple line). The contributing resonances change from (a) the 5:1 chain only to (j) the 5:1, 11:2, and the 6:1 chain.

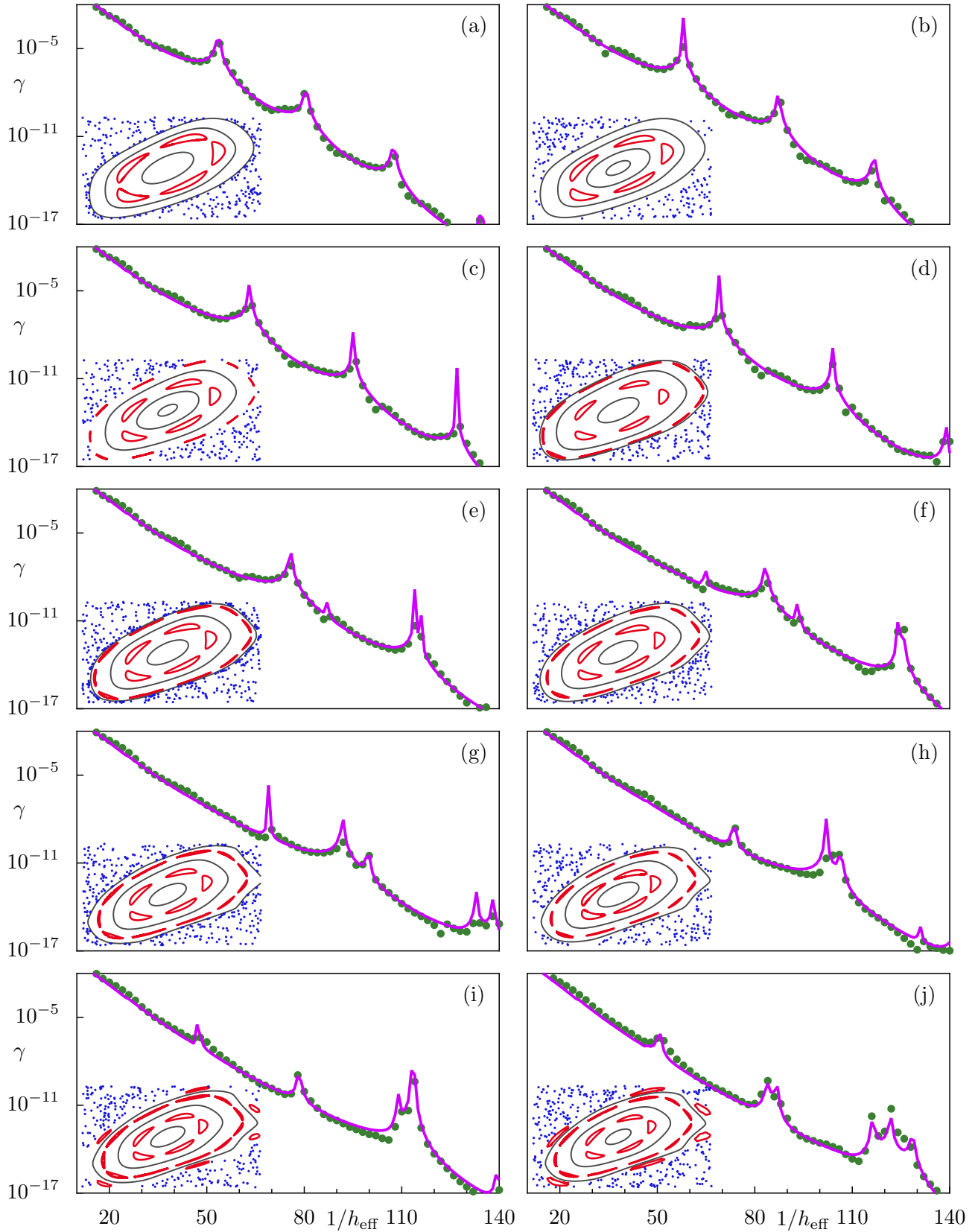


Figure 4.21: Dynamical tunneling rates γ from the quantized torus $m = 2$ of a regular island for the system \mathcal{F}_2 under parameter variation (a)-(j) from (a) $r_1 = 0.74$, $R = 0.2$, $Z = 1$ (Fig. 4.17 for $m = 2$) to (j) $r_1 = 0.72$, $R = 0.45$, $Z = 1.2$ (Fig. 4.18). Numerical data (dots) is compared to the prediction of Eq. (4.98) (solid purple line). The contributing resonances change from (a) the 5:1 chain only to (j) the 5:1, 11:2, and the 6:1 chain.

for the tunneling rates caused by different resonances are identified. We attribute the small deviations below the prediction of Eq. (4.98) to destructive interference of different tunneling sequences leading to the same final state. For this example we also consider the resonance-assisted prediction, Eq. (4.76), which does not use the direct tunneling rates. If we include the two improvements of the semiclassical energies \bar{E}_m and the couplings $\bar{V}_{r,s}$ it gives comparably good results as the full prediction of Eq. (4.98) for $1/h_{\text{eff}} \gtrsim 200$, see Fig. 4.22 (gray line). For smaller values of $1/h_{\text{eff}}$ deviations of many orders of magnitude are visible. This shows, that in the far semiclassical regime the direct tunneling rates are not necessary while in the experimentally relevant regime they cannot be neglected.

As a last example we consider the system introduced in Ref. [43] which is the standard map with an additional linear term Ωq entering the potential energy $V(q)$. For the parameters $K = 1.329$ and $2\pi\Omega = 0.5336$ one regular island appears which has a larger 6:1, 7:1, 8:1, and a smaller but relevant 19:3 chain. While the authors of Ref. [43] considered the contribution of the 6:1 and the 7:1 resonance separately, see Fig. 4.23 gray lines, we use our prediction,

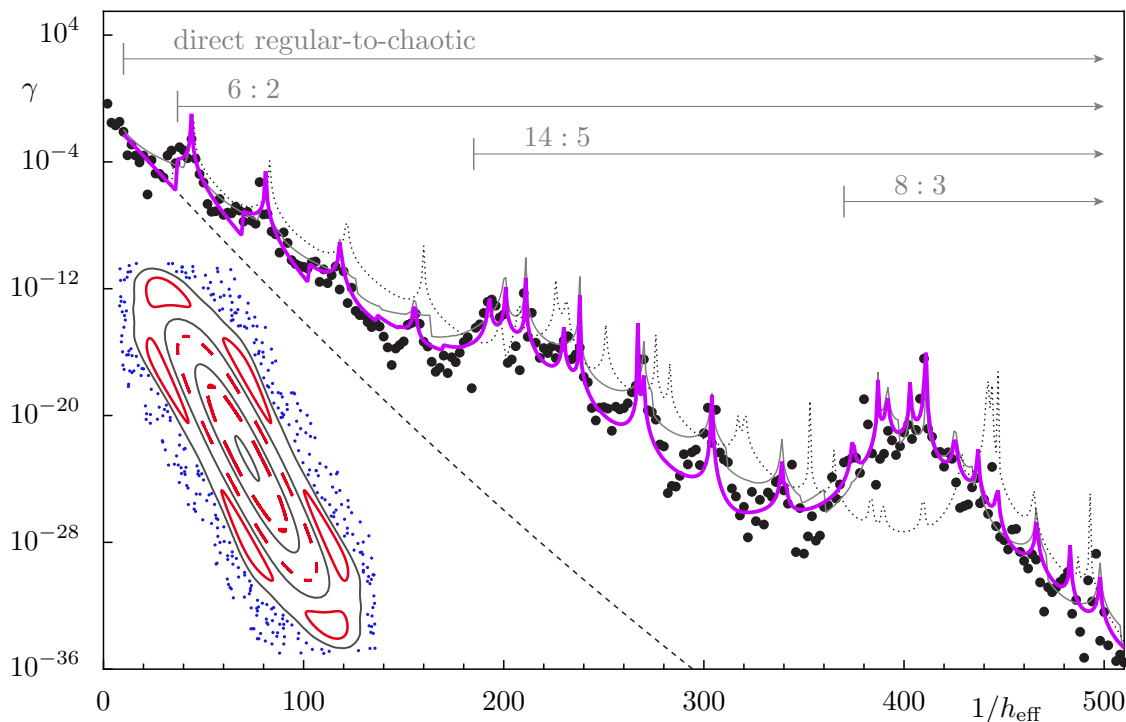


Figure 4.22: Dynamical tunneling rates γ from the innermost quantized torus $m = 0$ of the regular island for the standard map at $K = 3.5$. Numerical data (dots) is compared to the prediction of Eq. (4.98) (solid purple line). For comparison the direct tunneling contribution (dashed line, Eq. (4.9), Ref. [48]), the result of Eq. (4.98) without the improvements of the unperturbed energies \bar{E}_m and the couplings $\bar{V}_{r,s}$ (dotted line), and Eq. (4.76) without using the direct tunneling rates but including the two improvements is presented (solid gray line). The inset shows the regular island with the dominant 6:2, 14:5, and 8:3 resonances and the arrows indicate the regimes where they start to become relevant.

Eq. (4.98), which includes contributions of all four relevant resonances and find very good agreement (solid purple line). Using the direct tunneling rates we avoid artificial steps in the results which appear in the predictions of Ref. [43] (gray lines).

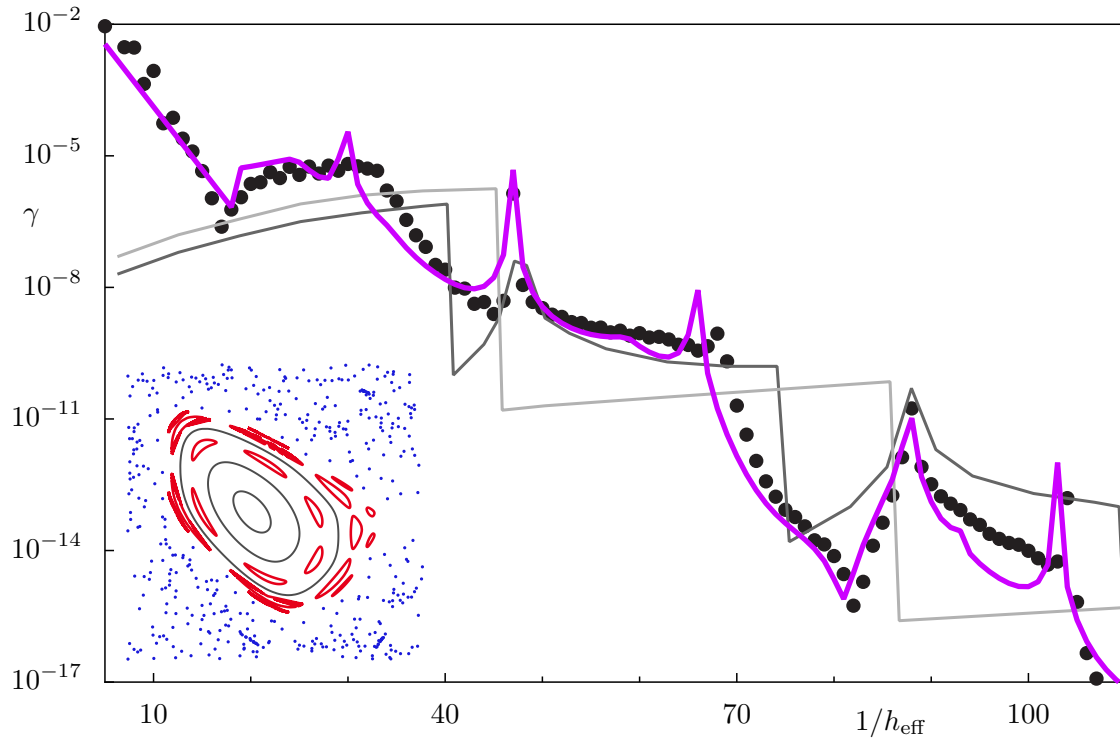


Figure 4.23: Dynamical tunneling rates γ from the innermost quantized torus ($m = 0$) of a regular island for the system considered in Ref. [43] with $K = 1.329$ and $2\pi\Omega = 0.5336$. Numerical data (dots) is compared to the prediction of Eq. (4.98) (solid purple line) and previous results due to resonance-assisted tunneling (gray lines, Ref. [43]). The dark gray line considers the 6:1 resonance while the other line includes the 7:1 chain only. The lower inset shows the phase space. For the prediction of Eq. (4.98) we consider contributions from the 6:1, 7:1, 8:1, and 19 : 3 (not shown) resonance chain.

5 Dynamical tunneling in billiard systems

In this chapter we extend our approach for the prediction of direct regular-to-chaotic dynamical tunneling rates to billiard systems with a mixed phase space. Such billiard systems can be accessed more easily in experiments and they are relevant for applications [100–103]. We study the mushroom [123] and the annular billiard [29, 30]. In both cases the phase space shows regular regions due to the whispering-gallery motion in the circular part of the system. These regions do not include nonlinear resonance chains. Hence, the direct tunneling mechanism is expected to be relevant far into the semiclassical regime $E \gg 1$. A more generic system is the cosine billiard for which we present the first numerical evidence of resonance-assisted tunneling in billiard systems. We also apply the theory using a fictitious integrable system to bouncing-ball modes and obtain tunneling rates which semiclassically decrease like a power law. Finally, we consider nanowires with one-sided disorder in a perpendicular magnetic field to reproduce the result for dynamical tunneling presented in Refs. [44, 45].

5.1 Direct regular-to-chaotic tunneling

For the derivation of a theory which predicts direct regular-to-chaotic tunneling rates for billiard systems we proceed similar to the case of quantum maps, see Section 4.1. The aim is to decompose the mixed system, which is now described by a Hamilton operator \hat{H} instead of a time evolution operator \hat{U} , into two main parts which show purely regular and purely chaotic dynamics as well as a part which includes the couplings of both phase-space regions. In order to find this decomposition we introduce a fictitious integrable system \hat{H}_{reg} in the same way as described in Section 4.1.2. It has to be chosen such that its dynamics resembles the classical motion corresponding to the mixed system \hat{H} within the regular island as closely as possible and extends this regular dynamics into the chaotic region of \hat{H} (similar as in Fig. 4.1(b) for quantum maps). The eigenstates $|\psi_{\text{reg}}\rangle$ of \hat{H}_{reg} are called purely regular as they are localized on quantizing tori in the regular region and, in contrast to the eigenstates of \hat{H} , decay into the chaotic sea. Note that there are only a few integrable billiards such as the circular, the rectangular, and the elliptical billiard. Hence, the construction of \hat{H}_{reg} is a more complicated task compared to the case of quantum maps. While a general procedure to obtain \hat{H}_{reg} for arbitrary billiards

is still under development, we can use the three integrable systems for various applications as discussed below.

With the eigenstates $|\psi_{\text{reg}}\rangle$ of \hat{H}_{reg} , $\hat{H}_{\text{reg}}|\psi_{\text{reg}}\rangle = E_{\text{reg}}|\psi_{\text{reg}}\rangle$, we define a projection operator

$$\hat{P}_{\text{reg}} = \sum_{\text{reg}} |\psi_{\text{reg}}\rangle \langle \psi_{\text{reg}}| \quad (5.1)$$

which semiclassically projects onto the regular island. Hence, only such regular states $|\psi_{\text{reg}}\rangle$ are considered which localize on quantizing tori inside the regular region of \hat{H} . As the energy spectrum of a billiard consists of infinitely many eigenvalues, the sum in Eq. (5.1) also includes infinitely many contributions. The orthogonal projector $\hat{P}_{\text{ch}} = \hat{\mathbb{1}} - \hat{P}_{\text{reg}}$ projects onto the chaotic phase-space component. For the decomposition of \hat{H} we find

$$\hat{H} = (\hat{P}_{\text{reg}} + \hat{P}_{\text{ch}})\hat{H}(\hat{P}_{\text{reg}} + \hat{P}_{\text{ch}}) = \hat{P}_{\text{reg}}\hat{H}\hat{P}_{\text{reg}} + \hat{P}_{\text{ch}}\hat{H}\hat{P}_{\text{ch}} + \hat{P}_{\text{reg}}\hat{H}\hat{P}_{\text{ch}} + \hat{P}_{\text{ch}}\hat{H}\hat{P}_{\text{reg}}. \quad (5.2)$$

Using similar transformations as presented in Section 4.1.1 with Eqs. (4.3), (4.5), and (4.6) we find for the coupling matrix elements in position representation

$$v_{\text{ch},mn} = \int_{\Omega} \psi_{\text{ch}}(\mathbf{q}) \hat{H} \psi_{\text{reg}}^{mn}(\mathbf{q}) d^2q \quad (5.3)$$

in which $\psi_{\text{reg}}^{mn}(\mathbf{q})$ and $\psi_{\text{ch}}(\mathbf{q})$ are orthogonal, in two dimensions the regular states are characterized by two quantum numbers m and n , and we choose $\hbar = 2m = 1$. The tunneling rate γ_{mn} is obtained using Fermi's golden rule

$$\gamma_{mn} = 2\pi \langle |v_{\text{ch},mn}|^2 \rangle_{\text{ch}} \rho_{\text{ch}} \approx \frac{A_{\text{ch}}}{2} \langle |v_{\text{ch},mn}|^2 \rangle_{\text{ch}} \quad (5.4)$$

where we average over coupling matrix elements $v_{\text{ch},mn}$ between one particular regular and different chaotic states of similar energy. The chaotic density of states ρ_{ch} is approximated by the leading Weyl term $\rho_{\text{ch}} \approx A_{\text{ch}}/(4\pi)$ in which A_{ch} denotes the area of the billiard times the chaotic fraction of phase space.

For the applications presented in Section 5.2 we want to use random wave descriptions as a model for the chaotic states $\psi_{\text{ch}}(\mathbf{q})$ which are not orthogonal to the regular states $\psi_{\text{reg}}^{mn}(\mathbf{q})$. For such non-orthogonal states the derivation presented in Appendix D.1 leads to modified coupling matrix elements

$$v_{\text{ch},mn} = \int_{\Omega} \psi_{\text{ch}}(\mathbf{q}) (\hat{H} - \hat{H}_{\text{reg}}) \psi_{\text{reg}}^{mn}(\mathbf{q}) d^2q. \quad (5.5)$$

Equation (5.5) can now be used in Fermi's golden rule, Eq. (5.4), and we obtain

$$\gamma_{mn} = \frac{A_{\text{ch}}}{2} \left\langle \left| \int_{\Omega} \psi_{\text{ch}}(\mathbf{q})(\hat{H} - \hat{H}_{\text{reg}})\psi_{\text{reg}}^{mn}(\mathbf{q}) d^2q \right|^2 \right\rangle_{\text{ch}} \quad (5.6)$$

which is our main result for billiard systems. It involves properties of the fictitious integrable system \hat{H}_{reg} and the difference $\hat{H} - \hat{H}_{\text{reg}}$. It predicts direct dynamical tunneling rates from any regular state to the chaotic sea. For its application we have to find a suitable integrable system \hat{H}_{reg} , its eigenstates $\psi_{\text{reg}}^{mn}(\mathbf{q})$, and a model for the purely chaotic states $\psi_{\text{ch}}(\mathbf{q})$. We choose a random wave description such that the average which appears in Eq. (5.6) becomes an ensemble average over different realizations of this random wave model. In the following we will predict direct dynamical tunneling rates using Eq. (5.6) and compare these results to numerical data for example systems with a mixed phase space.

5.2 Applications

In this section we want to apply our final expression, Eq. (5.6), to certain billiard systems in order to predict direct dynamical tunneling rates and compare the results with numerical data. For the mushroom billiard additional experimental data is considered which has been obtained by Vidmar and Robnik by means of microwave experiments in the group of Stöckmann in Marburg. Furthermore, we consider the direct regular-to-chaotic tunneling process in the annular and the cosine billiard, for which we determine the fictitious integrable system by a perturbation of the boundary. For the Sinai, the stadium, and the cosine billiard we study the coupling of bouncing-ball modes to the chaotic sea and find a power-law behavior of the tunneling rates in the semiclassical limit. For a two-dimensional nanowire with one-sided disorder in a perpendicular magnetic field we find agreement of our theoretical prediction to an existing theory. Finally, for the cosine billiard we present numerical evidence of resonance-assisted tunneling in billiard systems.

5.2.1 Mushroom billiards

We consider the desymmetrized mushroom billiard, i.e. the two-dimensional autonomous system shown in Fig. 5.1(a), characterized by the radius of the quarter circle R , the stem width a , and the stem height l . This billiard was introduced by Bunimovich [123] and is of great current interest [124, 148, 184–186] due to its phase-space structure which shows sharply separated regular and chaotic phase-space regions. There is no hierarchical regular-to-chaotic transition region and there appear no resonance chains inside the regular island. The regular trajectories show whispering-gallery motion which is not allowed to cross the small quarter circle of radius a . Each trajectory which crosses this line is chaotic, see Fig. 5.1(d). The chaotic component of

phase space was proven to be ergodic [123]. Hence, this billiard fulfills all requirements which are necessary for the application of Eq. (5.6) and the direct tunneling process dominates for all energies E . The results of this section are published in Ref. [50].

In order to apply Eq. (5.6) to the mushroom billiard we have to construct a fictitious integrable system \hat{H}_{reg} , determine its eigenstates $\psi_{\text{reg}}^{mn}(\mathbf{q})$, and find a model for the purely chaotic states $\psi_{\text{ch}}(\mathbf{q})$. In the following analysis we set $R = 1$. A natural choice for the regular system \hat{H}_{reg} is the quarter-circle billiard, see Fig. 5.1(b). According to Eq. (3.211) its eigenfunctions are analytically known

$$\psi_{\text{reg}}^{mn}(r, \varphi) = N_{mn} J_m(j_{mn} r) \sin(m\varphi), \quad (5.7)$$

in polar coordinates (r, φ) . They are characterized by the radial ($n = 1, 2, \dots$) and the az-

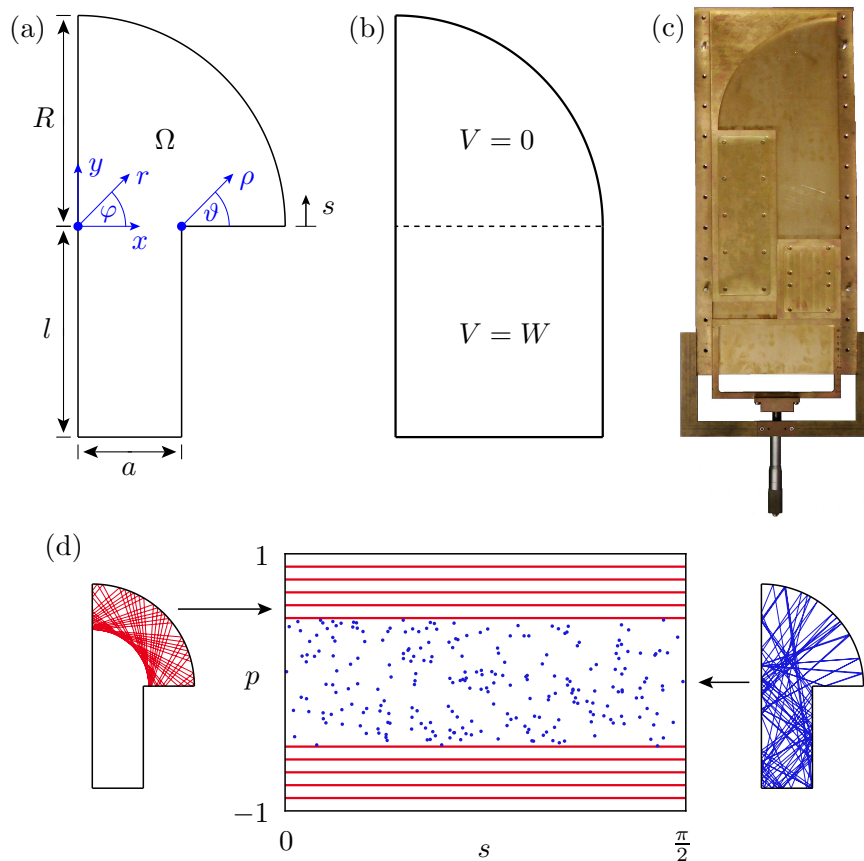


Figure 5.1: (a) Schematic picture of the mushroom billiard showing the coordinate systems used in the theoretical derivation of the direct dynamical tunneling rates. (b) Auxiliary billiard H_{reg}^W . (c) Experimental desymmetrized mushroom billiard with radius $R = 19$ cm, stem width $a = 10$ cm, and stem height $l = 0 \dots 25.7$ cm. The antenna is located 4 cm below the top and has a distance of 0.75 cm from the vertical wall. (d) Poincaré section at the quarter-circle boundary (relative tangential momentum p vs arclength s) showing regular and chaotic regions with illustrations of trajectories.

imuthal ($m = 2, 4, \dots$) quantum numbers. As we are considering the quarter-circle billiard m is allowed to take even values only. Here J_m denotes the m th Bessel function, j_{mn} the n th root of J_m , $N_{mn} = \sqrt{8/\pi}/J_{m-1}(j_{mn})$ accounts for the normalization, and $E_{mn} = j_{mn}^2$ are the eigenenergies.

Using the Hamiltonian \hat{H} of the mushroom and \hat{H}_{reg} of the quarter-circle billiard in Eq. (5.5) to determine the coupling between the regular and the chaotic states, an infinite potential difference $\hat{H} - \hat{H}_{\text{reg}} = -\infty$ occurs while $\psi_{\text{reg}}^{mn} = 0$ in the stem of the mushroom for $y < 0$ at the same time. In order to avoid this undefined product “ $-\infty \cdot 0$ ” we introduce a finite potential at $y \leq 0$, see Fig. 5.1(b),

$$\hat{H}_{\text{reg}}^W(\hat{\mathbf{q}}, \hat{\mathbf{p}}) = \hat{\mathbf{p}}^2 + V(\hat{\mathbf{q}}) \quad (5.8)$$

$$V(\hat{\mathbf{q}}) = \begin{cases} 0, & x^2 + y^2 \leq 1, x, y > 0 \\ W, & y \leq 0, 0 \leq x \leq 1 \\ \infty, & \text{otherwise} \end{cases} \quad (5.9)$$

and consider the limit $W \rightarrow \infty$ in which the quarter-circle billiard is recovered. For finite W the regular eigenfunctions $\psi_{\text{reg},W}^{mn}(\mathbf{q})$ of \hat{H}_{reg}^W decay into the region $y < 0$. To describe this decay we make the following ansatz

$$\psi_{\text{reg},W}^{mn}(x, y) = \psi_{\text{reg},W}^{mn}(x, y = 0) \exp(\lambda y). \quad (5.10)$$

Since these regular eigenfunctions and their derivatives have to be continuous at $y = 0$ we obtain

$$\lambda = \frac{\partial_y \psi_{\text{reg},W}^{mn}(x, y = 0)}{\psi_{\text{reg},W}^{mn}(x, y = 0)} \quad (5.11)$$

in which λ follows from the Schrödinger equation as

$$\lambda^2 = W - E_{mn}^W \quad (5.12)$$

and E_{mn}^W is finite. In the limit $W \rightarrow \infty$ and by extending the lower limit to $-\infty$ we find

$$\int_{-\infty}^0 dy \frac{W}{\lambda} e^{\lambda y} = \frac{W}{\lambda^2} \rightarrow 1 \quad (5.13)$$

such that

$$\frac{W}{\lambda} e^{\lambda y} \rightarrow \delta(y). \quad (5.14)$$

Evaluating Eq. (5.5) for the coupling matrix elements we obtain

$$v_{\text{ch},mn} = \lim_{W \rightarrow \infty} \int_0^a dx \int_{-l}^0 dy \psi_{\text{ch}}(x, y) (-W) \psi_{\text{reg},W}^{mn}(x, y) \quad (5.15)$$

$$= - \int_0^a dx \psi_{\text{ch}}(x, y=0) \partial_y \psi_{\text{reg}}^{mn}(x, y=0) \quad (5.16)$$

$$= -N_{mn} \int_0^a dx \psi_{\text{ch}}(x, y=0) \frac{m}{x} J_m(j_{mn}x). \quad (5.17)$$

Due to the limiting process only an integration along the line $y = 0$ remains which connects the quarter circle billiard to the stem of the mushroom. At this line deviations between H and H_{reg} emerge. Equation (5.16) contains the derivative of the regular wave function perpendicular to this line. The largest contribution of the integral in Eq. (5.17) appears at the corner of the mushroom at $x = a$. Here the regular eigenfunctions ψ_{reg}^{mn} are largest.

We can generalize this evaluation of Eq. (5.5) if H_{reg} is given by a hard-wall billiard in the following way: If the billiard region Ω_{reg} of H_{reg} fulfills $\Omega_{\text{reg}} \subset \Omega$ we define $\partial\Omega^v := \partial\Omega_{\text{reg}} \setminus \partial\Omega$, integrate in Eq. (5.16) along $\partial\Omega^v$, and use the derivative of the regular eigenfunction perpendicular to the integration path. For $\Omega \subset \Omega_{\text{reg}}$ we define $\partial\Omega^v := \partial\Omega \setminus \partial\Omega_{\text{reg}}$ and the derivative of the chaotic states perpendicular to $\partial\Omega^v$ enters in Eq. (5.16).

In order to evaluate Eq. (5.17) we have to use a random wave description to model the chaotic states $\psi_{\text{ch}}(\mathbf{q})$ which respects the Dirichlet boundary conditions in the vicinity of the corner at $x = a$. For this random wave model we use polar coordinates $\mathbf{q} = (\rho, \vartheta)$ as introduced in Fig. 5.1(a) such that the corner of angle $3\pi/2$ is located at $(0, 0)$. The Dirichlet boundary conditions at this corner are accounted for using Eqs. (3.201) and (3.202) with an angle $\theta = 3\pi/2$. The final chaotic wave function is

$$\psi_{\text{ch}}(\rho, \vartheta) = \sqrt{\frac{8}{3A_{\text{ch}}}} \sum_{s=1}^{\infty} c_s J_{\frac{2s}{3}}(k\rho) \sin\left(\frac{2s}{3}\vartheta\right) \quad (5.18)$$

in which $x - a = \rho \cos(\vartheta)$ and $y = \rho \sin(\vartheta)$. The coefficients c_s are independent Gaussian random variables with mean zero, $\langle c_s \rangle = 0$, and unit variance, $\langle c_s c_t \rangle = \delta_{st}$. Equation (5.18) fulfills the Schrödinger equation at energy $E = k^2$ and the prefactor is chosen such that $\langle |\psi_{\text{ch}}(\rho, \vartheta)|^2 \rangle = 1/A_{\text{ch}}$ holds far away from the corner. Note that we do not require these chaotic states to decay into the regular island, as Eq. (5.17) is an integral along a line of the billiard where the phase space is fully chaotic and that near the boundary, but far away from the corner, one recovers the behavior $1 - J_0(2k|x|)$ [121, 134]. Inserting this Eq. (5.18) into Eq. (5.17) at energy j_{mn}^2 and

$\vartheta = \pi$, we obtain the coupling matrix elements

$$v_{\text{ch},mn} = -N_{mn} \sqrt{\frac{8}{3A_{\text{ch}}}} \sum_{s=1}^{\infty} c_s \int_0^a J_{\frac{2s}{3}}(j_{mn}(a-x)) \sin\left(\frac{2\pi}{3}s\right) \frac{m}{x} J_m(j_{mn}x) dx \quad (5.19)$$

which give a prediction of the tunneling rates using Fermi's golden rule, Eq. (5.6),

$$\gamma_{mn} = m^2 N_{mn}^2 \sum_{s=1}^{\infty} \left[\int_0^a \frac{dx}{x} J_{\frac{2s}{3}}(j_{mn}(a-x)) J_m(j_{mn}x) \right]^2 \quad (5.20)$$

in which the prime at the summation indicates that the sum over s excludes all multiples of three. The remaining integral can be solved analytically [137, Eq. 11.3.40], leading to the final result

$$\gamma_{mn} = \frac{8}{\pi} \sum_{s=1}^{\infty} \frac{J_{m+\frac{2s}{3}}(j_{mn}a)^2}{J_{m-1}(j_{mn})^2}. \quad (5.21)$$

This gives a prediction of direct regular-to-chaotic tunneling rates of any regular state ψ_{reg}^{mn} to the chaotic sea in the mushroom billiard. The sum has its dominant contribution for $s = 1$ and evaluating Eq. (5.21) up to $s \leq 2$ gives sufficiently accurate predictions.

It is worth remarking that a very plausible estimate of the tunneling rate is given by the averaged square of the regular wave function on a circle with radius a , i.e. the boundary to the fully chaotic phase space, yielding $\gamma_{mn}^0 = N_{mn}^2 J_m(j_{mn}a)^2/2$. Surprisingly, it is just about a factor of 2 larger for the parameters we studied. In Ref. [148] a related quantity is proposed, given by the integral of the squared regular wave function over the quarter circle with radius a . This quantity, however, is too small by a factor of order 100 for the parameters under consideration.

The eigenvalues and eigenfunctions of the mushroom billiard are determined by numerically solving the Schrödinger equation. Because of its superior computational efficiency we have chosen to use the improved method of particular solutions [141, 148], see Section 3.2.2, allowing a determination of the energies E with a relative error $\approx 10^{-14}$. Analyzing the widths ΔE_i of avoided crossings between a given regular state and typically 30 chaotic states we deduce from Eq. (3.230), $\gamma \approx A_{\text{ch}} \langle |\Delta E_i|^2 \rangle_i / 8$, the tunneling rate where we use $A_{\text{ch}} = la + [\arcsin(a) + a\sqrt{1-a^2}]/2$ as derived in Appendix D.2. Note, that some pairs of regular states are very close in energy, e.g. $E_{20,1} - E_{16,2} \approx 10^{-4}$, such that their avoided crossings with a chaotic state overlap, making a numerical determination of the smaller tunneling rate unfeasible within the presented approach. Fig. 5.2 shows the tunneling rates γ_{mn} for fixed radial quantum number $n = 1, 2, 3$ and increasing azimuthal quantum number m , comparing the theoretical prediction, Eq. (5.21), with numerical results for $a = 0.5$. We find excellent agreement for tunneling rates

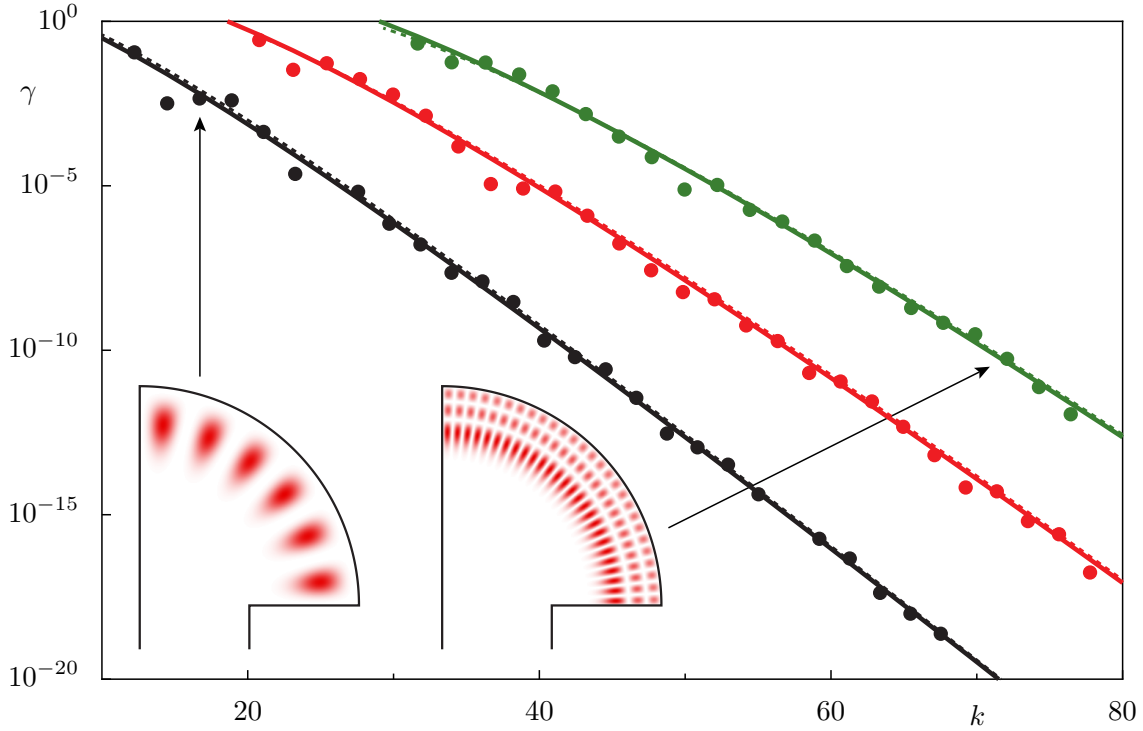


Figure 5.2: Tunneling rates of regular states with quantum numbers $n = 1$ (black), $n = 2$ (red), and $n = 3$ (green) vs k for $a = 0.5$ comparing the prediction of Eq. (5.21) (connected by solid lines) and numerical data (dots). The insets show the regular eigenfunctions $\psi_{\text{reg}}^{12,1}$ and $\psi_{\text{reg}}^{54,3}$. In addition the asymptotic prediction of Eq. (5.27) is presented (dashed lines).

γ_{mn} over 18 orders of magnitude. The small oscillations which appear in the numerical data on top of the exponential decay might be related to the two-level approximation which we use for their computation. It is not valid if two regular states are close in energy.

To further check our prediction we determined the tunneling rate of the regular state $(m, n) = (30, 1)$ under variation of the stem width a . The results presented in Fig. 5.3 show a decrease of this tunneling rate which appears faster than exponential with $1 - a$. Again we find excellent agreement to numerical data. Note that the accuracy of the numerical method used for determining eigenenergies of the mushroom is best for $a \approx 0.5$ and declines for larger or smaller a . Hence, the evaluation of avoided crossings including $\psi_{\text{reg}}^{30,1}(r, \varphi)$ for $a \leq 0.3$ is a difficult task.

Another interesting question is how the tunneling rates behave for regular states close to a classical torus described by a quarter circle in the cap of the mushroom with radius r_t . We characterize the regular states with the following criterion: The corresponding classical trajectory has the angular momentum $|L| = \sqrt{E}r_t$, which in the semiclassical limit is equal to the quantum number m . Thus, we use $m/j_{mn} \approx r_t$ (with $E = j_{mn}^2$) to find the combinations (m, n) which lead to regular states closest to the classical torus at r_t . The resulting behavior of the tunneling rates is presented in Fig. 5.4 for $r_t = 0.6$ and $r_t = 0.8$. A comparison of these predictions to numerical data shows excellent agreement.

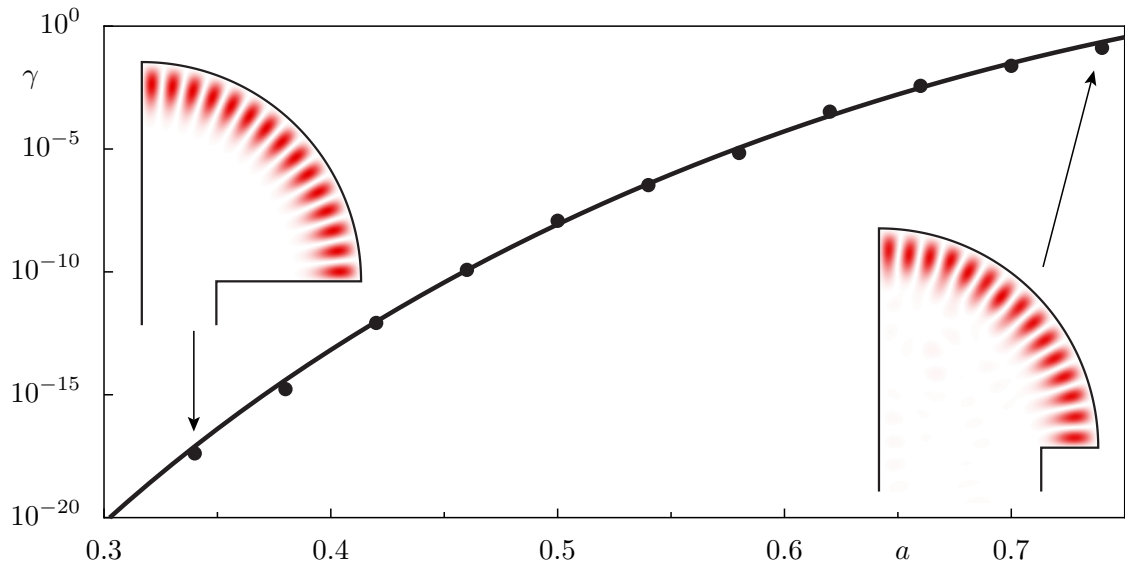


Figure 5.3: Tunneling rates of the regular state $\psi_{\text{reg}}^{30,1}$ vs the stem width a : We compare the prediction of Eq. (5.21) (connected by solid lines) and numerical data (dots). The insets show the regular eigenfunction $\psi_{\text{reg}}^{30,1}$ at $a = 0.34$ and $a = 0.74$.

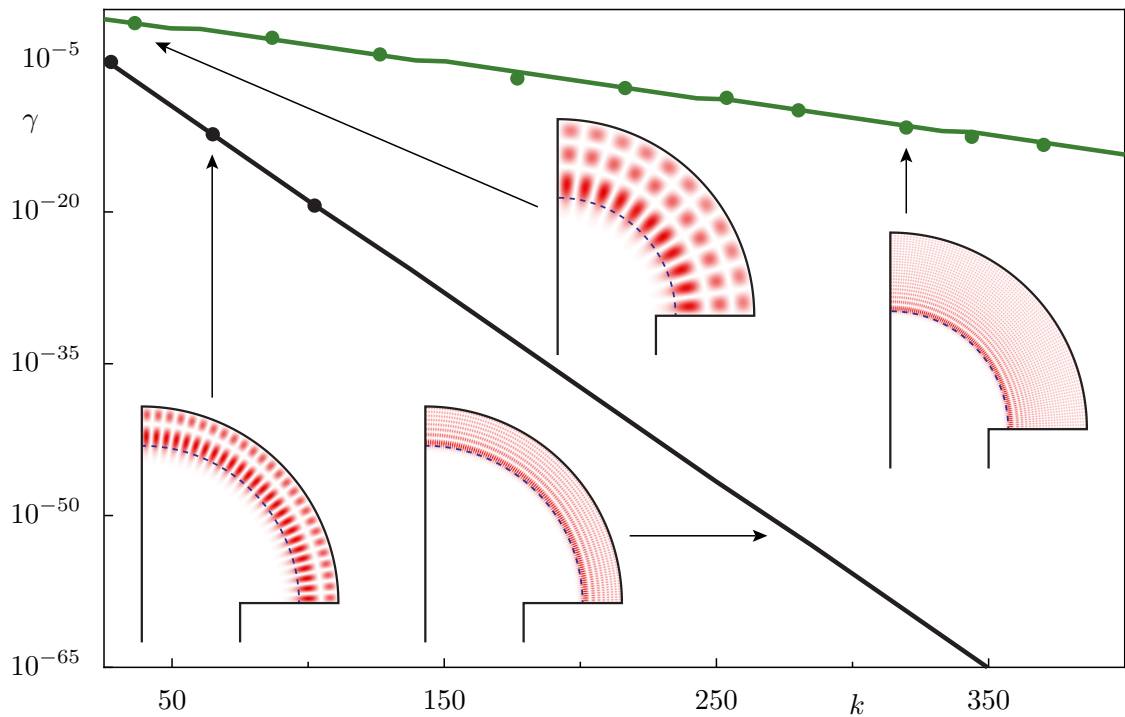


Figure 5.4: Tunneling rates of regular states localized closest to a classical torus of radius $r_t = 0.8$ (black) and $r_t = 0.6$ (green) vs k for $a = 0.5$: We compare the prediction of Eq. (5.21) (connected by solid lines) and numerical data (dots). The insets show the regular eigenfunctions $\psi_{\text{reg}}^{52,2}$, $\psi_{\text{reg}}^{228,8}$ close to $r_t = 0.8$ and $\psi_{\text{reg}}^{22,3}$, $\psi_{\text{reg}}^{192,25}$ close to $r_t = 0.6$.

For fixed azimuthal quantum number m and increasing radial quantum number n the tunneling rates increase. This behavior is presented in Fig. 5.5. Again we find excellent agreement between the predictions of Eq. (5.21) and numerical data.

Finally, we want to compare our theoretical predictions to experimental data which was obtained by Vidmar and Robnik using microwave experiments at the group of Stöckmann in Marburg. Fig. 5.1(c) shows the mushroom billiard used in the microwave experiment. Spectra have been taken as a function of the stem height l of the mushroom in the frequency regime 3.0 to 13.5 GHz, corresponding to values of kR between 11.9 and 53.8. Fig. 5.6 shows part of the obtained spectra in a small kR window. Note that $R \neq 1$ for the experiment. As the energies of the regular states in the quarter circle do not depend on the stem height, they appear as straight horizontal lines, whereas the chaotic states are shifted to lower energies with increasing stem height l , reflecting the increasing density ρ_{ch} of chaotic states.

For each of the regular states ψ_{reg}^{mn} with quantum numbers n between 1 and 5 and m between 8 and 32 all accessible splittings at avoided crossing Δk have been determined by means of a hyperbola fit (Fig. 5.6). From this we get the energy splittings $\Delta E = 2k\Delta k$ of the corresponding quantum system and by averaging over all avoided crossings, Eq. (3.230), we deduce the tunneling rate γ_{mn} of each regular state (m, n) to the chaotic sea. Apart from the results for $n = 1$ they are in very good agreement with the theoretical prediction, Eq. (5.21), see Fig. 5.7.

In the experiment the resolution of avoided crossings is limited by the line widths of the resonances due to wall absorption and antenna coupling. In the studied frequency regime the line widths were about $\Delta\nu_w = 0.01$ GHz, corresponding to $\Delta k_w R \approx 0.04$. From the

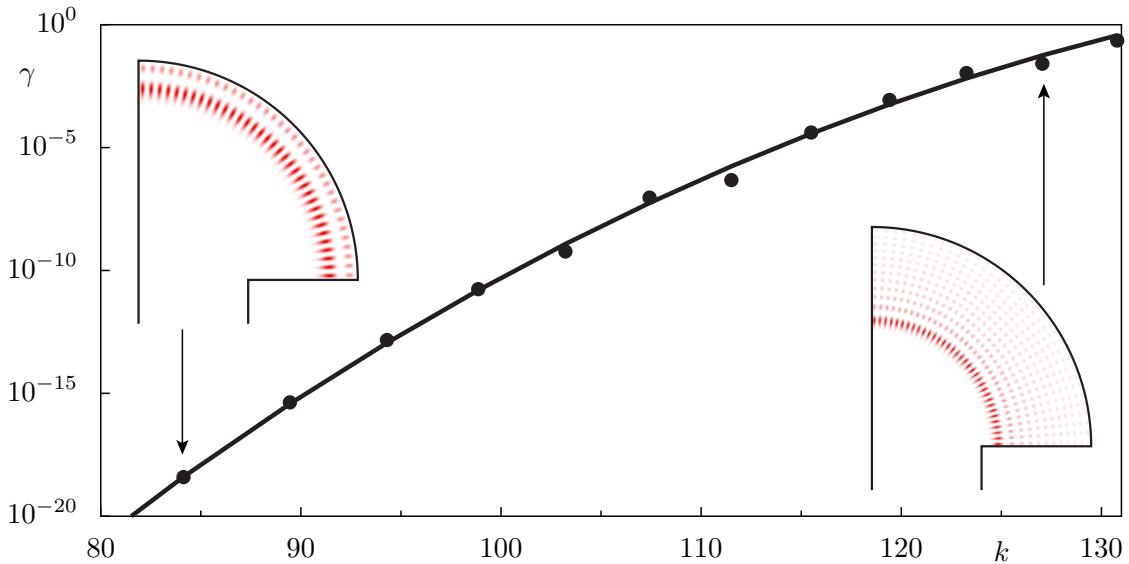


Figure 5.5: Tunneling rates of regular states with quantum number $m = 70$ vs k for $a = 0.5$ comparing the prediction of Eq. (5.21) (connected by solid lines) and numerical data (dots). The insets show the regular eigenfunctions $\psi_{\text{reg}}^{70,2}$ and $\psi_{\text{reg}}^{70,12}$.

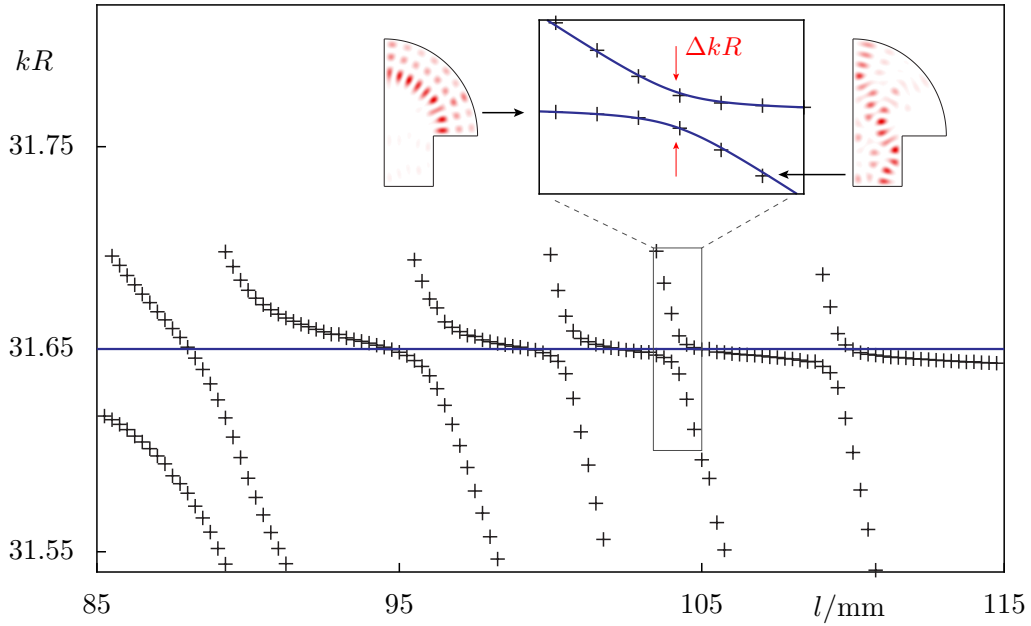


Figure 5.6: Part of the evaluated experimental resonance spectra of the mushroom microwave billiard vs stem height l . The horizontal line corresponds to the eigenfrequency of $\psi_{\text{reg}}^{18,3}$, the crosses mark the extracted resonances. The inset shows a magnification of one avoided crossing, including a hyperbola fit (solid line), and the numerically obtained regular and chaotic states involved in the crossing.

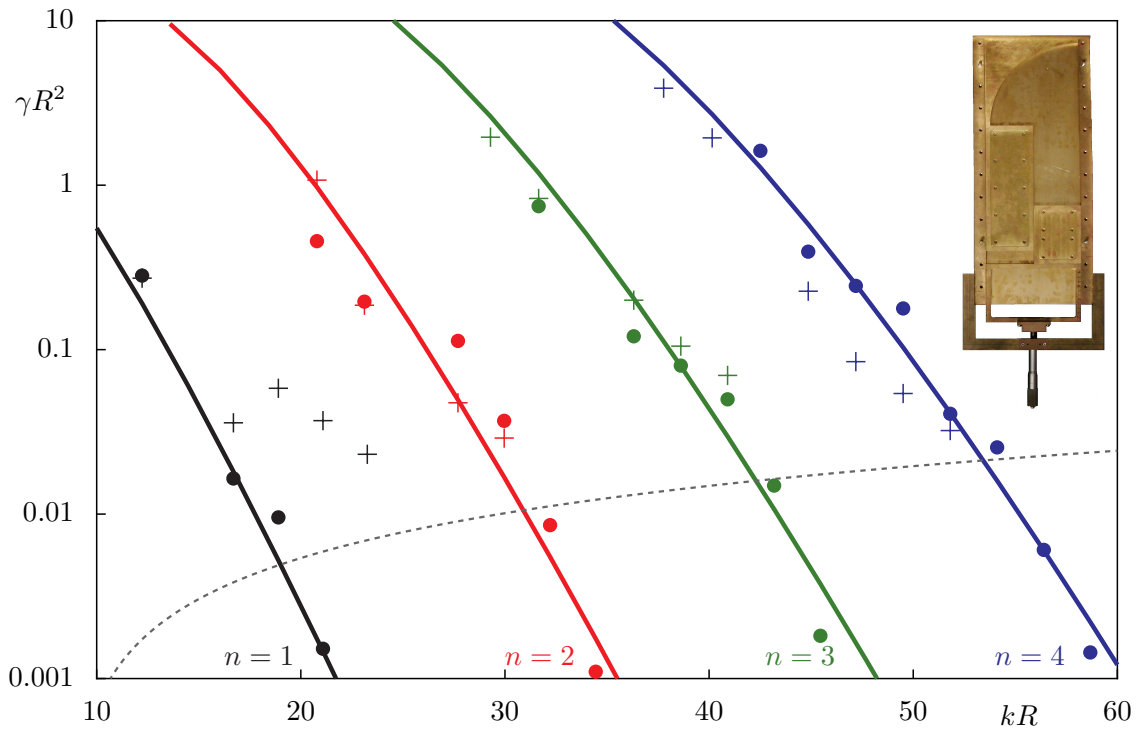


Figure 5.7: Dynamical tunneling rates from the regular region to the chaotic sea for quantum numbers $n \leq 4$ vs kR for a mushroom billiard ($a/R = 10/19$): theoretical predictions (connected by solid lines) from Eq. (5.21), experimental results (crosses), and numerical data (dots). The dashed line denotes the lower limit of the experimental resolution. The inset shows the experimental setup.

hyperbola fit of the avoided crossings all splittings ΔkR larger than $0.1\Delta k_w R$ could still be resolved, corresponding to tunneling rates γ between 0.001 and 0.024, see Fig. 5.7 (dashed line). Further experimental complications are caused by the antenna, giving rise to an additional splitting [184], which is proportional to the product of the involved wave functions $|\psi(\mathbf{q}_a)|$ at the antenna position \mathbf{q}_a . For the three rightmost data points of $n = 1$, see Fig. 5.7, $|\psi_{\text{reg}}^{m1}(\mathbf{q}_a)|$ is particularly large, which explains the deviations between experiment and theoretical prediction.

Asymptotic expansion of tunneling formula

We want to evaluate Eq. (5.21) in the semiclassical limit for large energies E in order to understand the exponential behavior which is visible in Figs. 5.2 and 5.4 with increasing wave number k . The leading term in Eq. (5.21) reads

$$\gamma_{mn} = \frac{8}{\pi} \frac{J_{m+\frac{2}{3}}(j_{mn}a)^2}{J_{m-1}(j_{mn})^2}. \quad (5.22)$$

First we consider its numerator and use Ref. [137, Eq. 9.1.63] for non-integer arguments of the Bessel function

$$J_{m+\frac{2}{3}}(j_{mn}a) \leq \left| \left(\frac{j_{mn}a}{m+\frac{2}{3}} \right)^{m+\frac{2}{3}} \frac{\exp\left(\left(m+\frac{2}{3}\right) \sqrt{1 - \left(\frac{j_{mn}a}{m+\frac{2}{3}}\right)^2} \right)}{\left(1 + \sqrt{1 - \left(\frac{j_{mn}a}{m+\frac{2}{3}}\right)^2}\right)^{m+\frac{2}{3}}} \right|. \quad (5.23)$$

For large m we could also use $m + 2/3 \approx m + 1$. Equation (5.23) provides an upper bound of $J_{m+2/3}(j_{mn}a)$. Numerically it has been confirmed, that a good approximation is given by

$$J_{m+\frac{2}{3}}(j_{mn}a) \approx \frac{1}{m^{\frac{2}{3}}} \left(a_{mn}^{\tilde{m}} \frac{\exp\left(\tilde{m}\sqrt{1-a_{mn}^2}\right)}{\left(1 + \sqrt{1-a_{mn}^2}\right)^{\tilde{m}}} \right) \quad (5.24)$$

$$= \frac{1}{m^{\frac{2}{3}}} \exp\left(\tilde{m} \left[\ln a_{mn} - \ln \left(1 + \sqrt{1-a_{mn}^2}\right) + \sqrt{1-a_{mn}^2} \right]\right), \quad (5.25)$$

where $\tilde{m} = m + 2/3$ and $a_{mn} = j_{mn}a/\tilde{m} = \sqrt{E_{mn}}a/\tilde{m}$. The denominator of Eq. (5.22) can be approximated for $n = 1$ using Ref. [137, Eq. 9.5.18]

$$J_{m-1}(j_{mn}) = J'_m(j_{mn}) \approx -1.1131 m^{-\frac{2}{3}} \approx -\frac{1}{m^{\frac{2}{3}}}. \quad (5.26)$$

For the tunneling rates we finally obtain

$$\gamma_{mn} \approx \frac{8}{\pi} \exp\left(2\tilde{m} \left[\ln a_{mn} - \ln \left(1 + \sqrt{1-a_{mn}^2}\right) + \sqrt{1-a_{mn}^2} \right]\right). \quad (5.27)$$

We find that for fixed radial quantum number n and increasing azimuthal quantum number $m \approx k_{mn}$ the tunneling rates decay exponentially with k . Fig. 5.2 shows the comparison to Eq. (5.21) assuming that Eq. (5.26) also approximately holds for $n > 1$. We find agreement within a factor of two. The prediction of Eq. (5.27) is similar to Eq. (4.39) which has been obtained for a quantum map with a harmonic oscillator-like regular island. It resembles the similarity of this system to the mushroom billiard, which both show no resonance chains in the regular island and the transition from regular to chaotic dynamics is sharp.

Mushroom billiards with elliptical hats

We extend the prediction of tunneling rates for the mushroom billiard with Eq. (5.21) to mushroom billiards with elliptic hats. Their geometry is presented in Fig. 5.8(a). The procedure to obtain a prediction of direct regular-to-chaotic tunneling rates using the approach with a fictitious integrable system works in the same way as for the mushroom billiards with a circular cap. However, we use the elliptical billiard as the integrable system H_{reg} , see Fig. 5.8(b).

For the elliptical billiard we find two types of regular dynamics: rotational motion along the boundary in analogy to the circular billiard and oscillatory motion near the symmetry line $x = 0$. In Cartesian coordinates the ellipse is described by

$$\frac{x^2}{r_a^2} + \frac{y^2}{r_b^2} = 1 \quad (5.28)$$

in which r_a and r_b denote the lengths of the two half axis. In the following we consider $r_a > r_b$. The distance of the foci from $x = 0$ is given by $f = \sqrt{r_a^2 - r_b^2}$ and we introduce hyperbolic

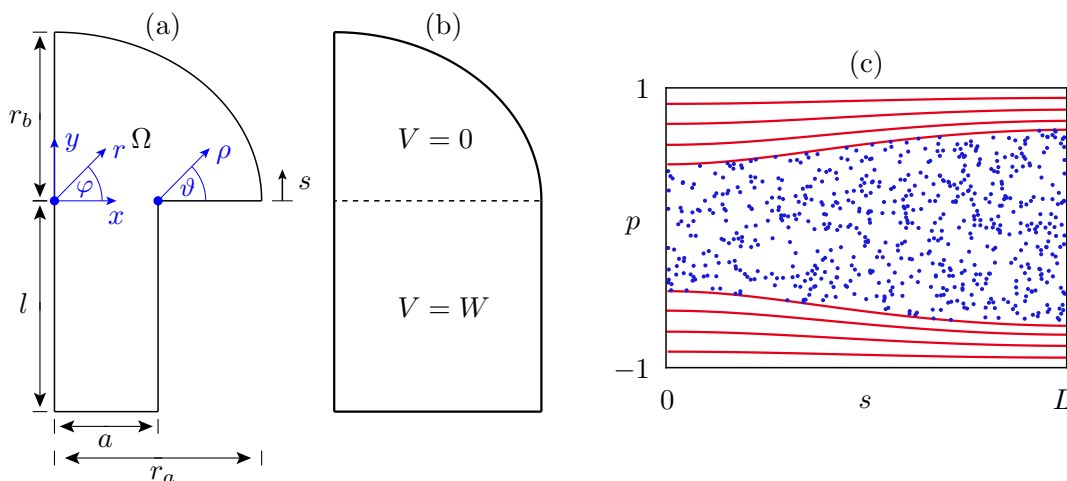


Figure 5.8: (a) Schematic picture of the mushroom billiard with elliptic cap showing the coordinate systems used in the theoretical derivation of the direct dynamical tunneling rates. (b) Auxiliary billiard H_{reg}^W . (c) Poincaré section at the elliptic boundary (relative tangential momentum p vs arclength s) showing regular and chaotic regions.

coordinates

$$x = f \cosh(\xi) \cos(\eta), \quad (5.29)$$

$$y = f \sinh(\xi) \sin(\eta). \quad (5.30)$$

In these coordinates the Schrödinger equation is separable and the eigenfunctions and eigenvalues of the elliptical billiard can be obtained as presented in Section 3.2.2. In the following we consider a desymmetrized mushroom billiard with an elliptic cap such that the regular system \hat{H}_{reg} is given by a quarter ellipse. Thus, its eigenfunctions, see Eq. (3.217), are given by

$$\psi_{\text{reg}}^{mn}(\xi, \eta) = N_{mn} M_s_m^{(1)}(\xi, q_{mn}) s e_m(\eta, q_{mn}) \quad (5.31)$$

where q_{mn} is the n th zero of the m th odd oscillatory radial Mathieu function of the first kind $M_s_m^{(1)}$ and $s e_m$ denotes the m th odd angular Mathieu function. The quantum numbers are $m = 2, 4, \dots$ as well as $n = 1, 2, \dots$, N_{mn} accounts for the normalization, and the eigenenergies result from $E_{mn} = 4q_{mn}/f^2$.

We use the same random wave model for the chaotic states as before, see Eq. (5.18), and obtain the tunneling rates

$$\gamma_{mn} = \sum_{s=1}^{\infty} \left(\int_0^a dx J_{\frac{2s}{3}}(j_{mn}(a-x)) \partial_y \psi_{\text{reg}}^{mn}(x, y=0) \right)^2. \quad (5.32)$$

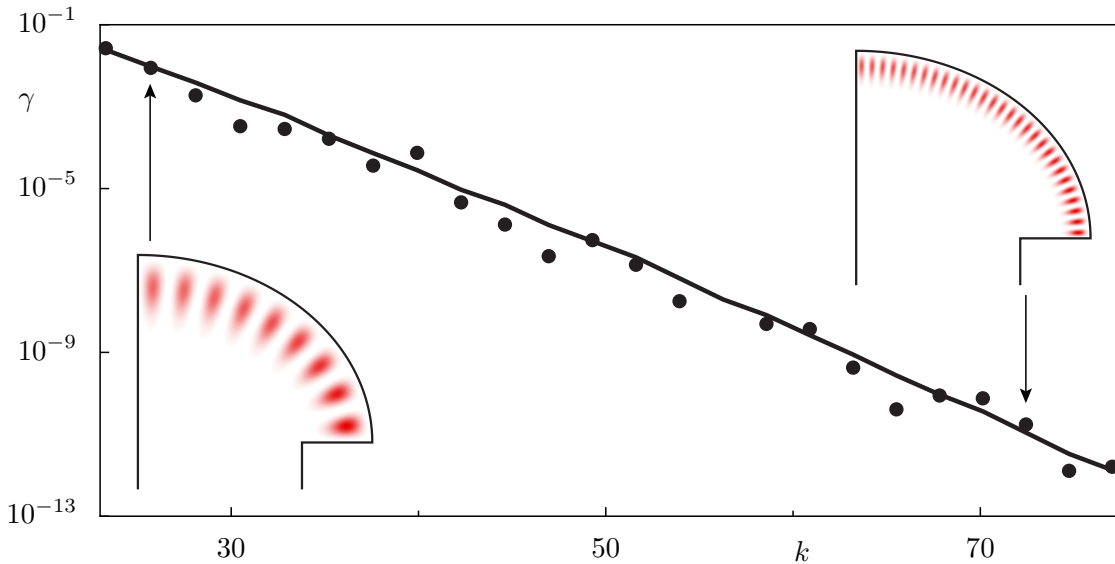


Figure 5.9: Tunneling rates from regular states with quantum numbers $n = 1$ vs k for $a = 0.7$, $r_a = 1$, and $r_b = 0.8$: We compare the prediction of Eq. (5.32) (connected by solid lines) and numerical data (dots). The insets show the regular eigenfunctions $\psi_{\text{reg}}^{18,1}$ and $\psi_{\text{reg}}^{58,1}$.

Its results are compared to numerical data which is obtained as discussed in the last section. For the parameters $r_a = 1.0$, $r_b = 0.8$, and $a = 0.7$ we find excellent agreement, see Fig. 5.9.

The theory is expected to predict reliable tunneling rates only for situations in which no oscillatory motion occurs due to the attached stem. I.e. only the regular whispering gallery motion remains. This is the case for $a > f$. Otherwise tunneling from the rotating to the oscillating part has to be additionally predicted.

5.2.2 Annular billiards

We consider the desymmetrized annular billiard characterized by the radius of the large semi-circle $R = 1$, the radius of the small semi-circle a , and the displacement of this semicircle w , see Fig. 5.10(a). In contrast to the sharply separated regular and chaotic dynamics in the mushroom billiard, the phase space of the annular billiard is more generic. Again we find regions of regular whispering-gallery motion but a more complicated chaotic sea appears in which additional regular islands and partial barriers may be located, depending on the choice of a and w . This structure leads to the existence of so-called beach states which are localized in the chaotic sea but close to the border of the regular region, influencing the dynamical tunneling process. These beach states were described by Doron and Frischat [29, 30] who also studied the dynamical tunneling process in annular billiards. In contrast to our theory their prediction of tunneling rates required fitting with a free parameter. In this section we want to apply the approach using a fictitious integrable system to find a prediction of direct dynamical tunneling rates which describe the decay of whispering-gallery modes into the chaotic sea.

To determine these direct dynamical tunneling rates in the annular billiard we proceed similar to the case of the mushroom billiard. We have to evaluate Eq. (5.5) for the coupling matrix elements $v_{ch, mn}$ and then use Fermi's golden rule, Eq. (5.6), to determine the tunneling rates. In the first step the regular system \hat{H}_{reg} and its eigenstates ψ_{reg}^{mn} have to be defined. Similar

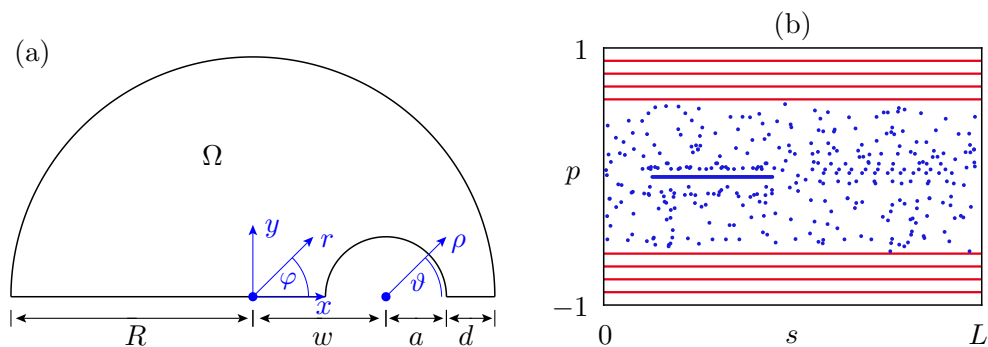


Figure 5.10: (a) Schematic picture of the desymmetrized annular billiard showing the coordinate systems used in the theoretical derivation of the direct dynamical tunneling rates. (b) Poincaré section at the semi-circle boundary (relative tangential momentum p vs arclength s) showing regular and chaotic regions for $R = 1$, $a = 0.15$, and $w = 0.45$.

to the mushroom billiard a natural choice of this regular system \hat{H}_{reg} is the semi-circle billiard which exactly reproduces the whispering-gallery motion in the annular billiard. Its eigenstates are given by

$$\psi_{\text{reg}}^{mn}(r, \varphi) = N_{mn} J_m(j_{mn}r) \sin(m\varphi) \quad (5.33)$$

in polar coordinates (r, φ) , where J_m denotes the m th Bessel function, j_{mn} is the n th root of J_m , and $N_{mn} = \sqrt{4/\pi}/J_{m-1}(j_{mn})$. The regular states are characterized by the radial quantum number $n = 1, 2, \dots$ and the azimuthal quantum number $m = 1, 2, \dots$. Hence, the tunneling rates describing the decay of the regular state $\psi_{\text{reg}}^{mn}(r, \varphi)$ will be labeled by γ_{mn} .

Evaluating Eq. (5.5) in order to determine the coupling matrix elements $v_{\text{ch},mn}$ between the regular and the chaotic states, an infinite potential difference arises within the small disc of radius a between the Hamiltonian \hat{H} of the annular and \hat{H}_{reg} of the semi-circle billiard, $\hat{H} - \hat{H}_{\text{reg}} = \infty$. At the same time for the chaotic states $\psi_{\text{ch}} = 0$ holds in that region, which leads to an undefined product “ $\infty \cdot 0$ ”. Similar to the approach presented for the mushroom billiard we circumvent this problem by considering a finite potential difference W for which at the end the limit $W \rightarrow \infty$ is performed. Since $\Omega \subset \Omega_{\text{reg}}$ we have to integrate along the semi-circle of radius a and consider the derivative of the chaotic states $\psi_{\text{ch}}(\mathbf{q})$ perpendicular to this line

$$v_{\text{ch},mn} = \int_0^\pi a \, d\vartheta \, \partial_\rho \psi_{\text{ch}}(\rho = a, \vartheta) \psi_{\text{reg}}^{mn}(\rho = a, \vartheta) \quad (5.34)$$

$$= a N_{mn} \int_0^\pi d\vartheta \, \partial_\rho \psi_{\text{ch}}(\rho = a, \vartheta) J_m(j_{mn}r) \sin(m\varphi) \quad (5.35)$$

in which we introduced the polar coordinates (ρ, ϑ) such that $x = \rho \cos(\vartheta) + w$ and $y = \rho \sin(\vartheta)$. Only the integration over ϑ from $\vartheta = 0$ to $\vartheta = \pi$ along the small semi-circle of radius a remains. Note that the regular eigenfunctions are given in polar coordinates $(r(\rho, \vartheta), \varphi(\rho, \vartheta))$, while we integrate along $\rho = a$, see Fig. 5.10(a). Along this line the regular wave function is largest near the point $(\rho, \vartheta) = (a, 0)$ for $w > 0$. Hence, we use a random wave description to model the chaotic states $\psi_{\text{ch}}(\rho, \vartheta)$ which respects the Dirichlet boundary conditions on the line $y = 0$ and on the small semi-circle of radius a .

For this random wave model we use polar coordinates (ρ, ϑ) as introduced in Fig. 5.10(a) such that the center of the small disk is located at the origin. A random wave model which accounts for the Dirichlet boundary conditions on the small disk and the line $y = 0$ is constructed by [187, §25]

$$\psi_{\text{ch}}(\rho, \vartheta) = \frac{2}{\sqrt{A_{\text{ch}}}} \sum_{s=1}^{\infty} c_s \sin(s\vartheta) \frac{J_s(k\rho)Y_s(ka) - J_s(ka)Y_s(k\rho)}{\sqrt{J_s(ka)^2 + Y_s(ka)^2}}, \quad (5.36)$$

in which the c_s are Gaussian random variables with $\langle c_s \rangle = 0$ and $\langle c_s c_t \rangle = \delta_{st}$. Furthermore, Y_s denotes the Bessel function of the second kind. The normalization constant 2 has been obtained numerically, such that $\langle |\psi_{\text{ch}}|^2 \rangle = 1/A_{\text{ch}}$ holds far away from the boundary. The chaotic states defined by Eq. (5.36) fulfill the Schrödinger equation at arbitrary energy $E = k^2$. Similar to the mushroom billiard we do not require the chaotic states to decay into the regular island, as Eq. (5.35) is an integral along a line of the billiard which is not hit by any regular whispering-gallery trajectory. Near the boundary, but away from the small circle, one recovers the behavior $\langle |\psi_{\text{ch}}|^2 \rangle = 1 - J_0(2k|\rho - a|)$ [121, 134]. Using the radial derivative of $\psi_{\text{ch}}(\rho, \vartheta)$ at $\rho = a$ we find

$$\partial_\rho \psi_{\text{ch}}(\rho = a, \vartheta) = \frac{2k}{\sqrt{A_{\text{ch}}}} \sum_{s=1}^{\infty} c_s \sin(s\vartheta) R_s(ka), \quad (5.37)$$

in which $J_{s+1}(ka)Y_s(ka) - J_s(ka)Y_{s+1}(ka) = 2/(\pi ka)$ [137, Eq. 9.1.16] and

$$R_s(ka) := \frac{2}{\pi ka \sqrt{J_s(ka)^2 + Y_s(ka)^2}}. \quad (5.38)$$

With this result we calculate the tunneling rates at energy $E = j_{mn}^2$

$$\gamma_{mn} = 2N_{mn}^2 a^2 j_{mn}^2 \sum_{s=1}^{\infty} R_s(j_{mn}a)^2 \left[\int_0^\pi d\vartheta \sin(s\vartheta) J_m(j_{mn}r(\vartheta)) \sin(m\varphi(\vartheta)) \right]^2. \quad (5.39)$$

This is our final result predicting the decay of a regular state ψ_{reg}^{mn} located in the regular whispering-gallery region to the chaotic sea. In Eq. (5.39), in contrast to the result for the mushroom billiard, Eq. (5.21), the term $s = 1$ is typically not the most important contribution. Here the corresponding s increases with energy. Note that this formula depends on the radius a of the inner semi-circle. For not too small a and fixed distance d to the large disk the tunneling rates slightly decrease with increasing a which leads to a difference of at most a factor two. In contrast to the prediction presented in Refs. [29, 30] no fitting is required.

The numerical determination of tunneling rates using avoided crossings is more difficult for the annular billiard than in the case of the mushroom billiard. In order to affect the chaotic but not the regular component of phase space we increase the radius a of the small inner circle and shift its center such that its rightmost value $a + w$ is constant. This procedure drastically affects the chaotic states while the regular whispering-gallery modes remain almost unchanged. However, under this parameter variation the phase space structure in the chaotic region changes from macroscopically chaotic to a situation in which additional regular islands and partial barriers appear.

Fig. 5.11 shows the comparison of the theoretical prediction of Eq. (5.39) to numerical data for $a + w = 0.6$, $n \leq 2$, and increasing m . We find qualitative agreement over 18 orders of magnitude. However, deviations of several orders of magnitude appear for some data points

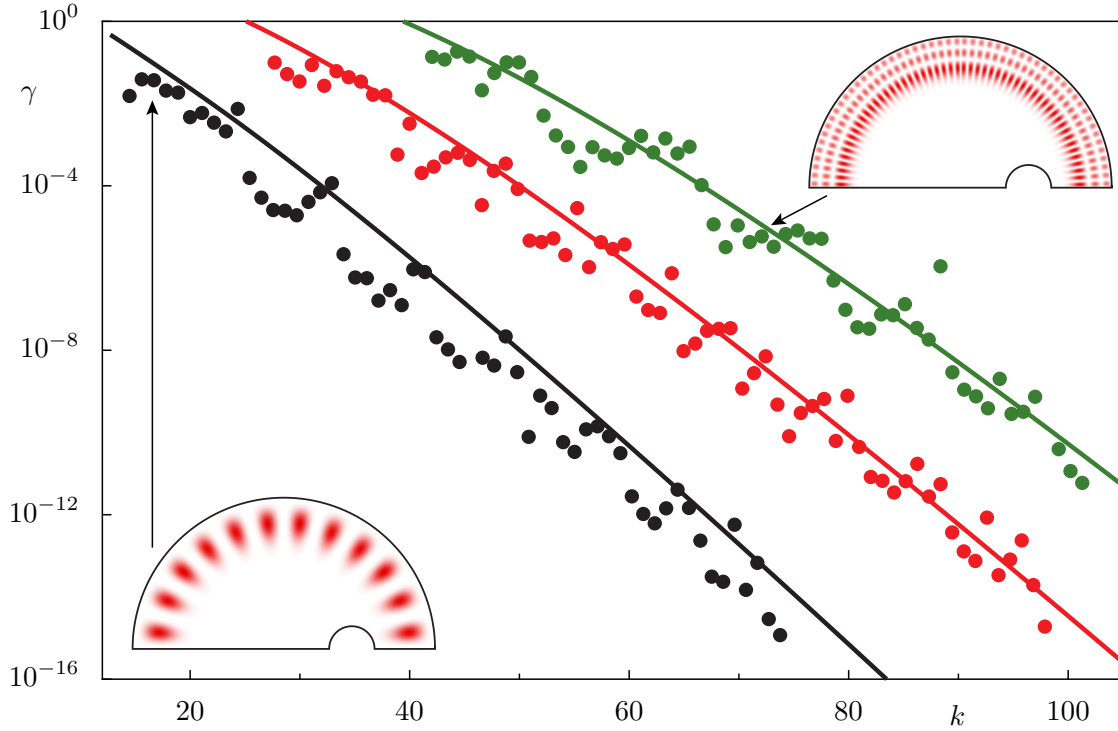


Figure 5.11: Tunneling rates from regular states with quantum numbers $n = 1$ (black), $n = 2$ (red), and $n = 3$ (green) vs k for $d = 0.4$ comparing the prediction of Eq. (5.39) (solid lines) and numerical data (dots). The insets show the regular eigenfunctions $\psi_{\text{reg}}^{12,1}$ and $\psi_{\text{reg}}^{54,3}$.

while others agree with the theoretical prediction.

The fluctuations of the tunneling rates occur most likely due to the existence of so-called beach states. These are states which exist in the chaotic region of phase space and look similar to regular states though no quantizing tori can be associated with them [29,30]. Numerically we determine the tunneling rates by evaluating avoided crossings between the whispering-gallery modes and chaotic states which change their energy under variation of the shape of the billiard, as discussed before. Beach states almost behave like regular states and their energy only slightly varies if we change the boundary of the billiard. Hence, we do not always include their contribution in the numerically determined tunneling rates. In such situations tunneling to chaotic states further away from the regular island is considered as the beach states effectively enlarge the regular region. Equation (5.39), however, predicts tunneling rates directly to the border of the regular island. It does not account for a virtually enlarged regular region due to beach states. Hence, it agrees to numerical data only if avoided crossings between beach states and the whispering-gallery modes are included. Otherwise the numerically determined tunneling rates are too small.

The influence of the beach states can be visualized by summing up the Poincaré-Husimi representations of chaotic states which cross the considered whispering-gallery mode. If beach states exist which do not cross the whispering-gallery mode, this sum will be localized far away

from the regular region while otherwise it will reach the regular-chaotic border. We find cases for which the sum of Husimi representations has pronounced contributions in the vicinity of the classical border of the regular island. For example for $m = 19, 27, 34, 41$ and $n = 1$, the numerically determined tunneling rates agree with the analytical prediction in Fig. 5.11. Here, the couplings of all relevant states are considered. For m different from these values the influence of the beach states on the tunneling process is not included numerically such that deviations from our theoretical prediction arise.

As a further test of this reasoning we determine tunneling rates varying the parameter d . For increasing d the whispering-gallery region grows such that beach states will become regular states and new beach states will appear. Hence, we expect oscillations on top of the exponentially decaying tunneling rates. This can be seen in Fig. 5.12 exemplarily for $(m, n) = (61, 1)$.

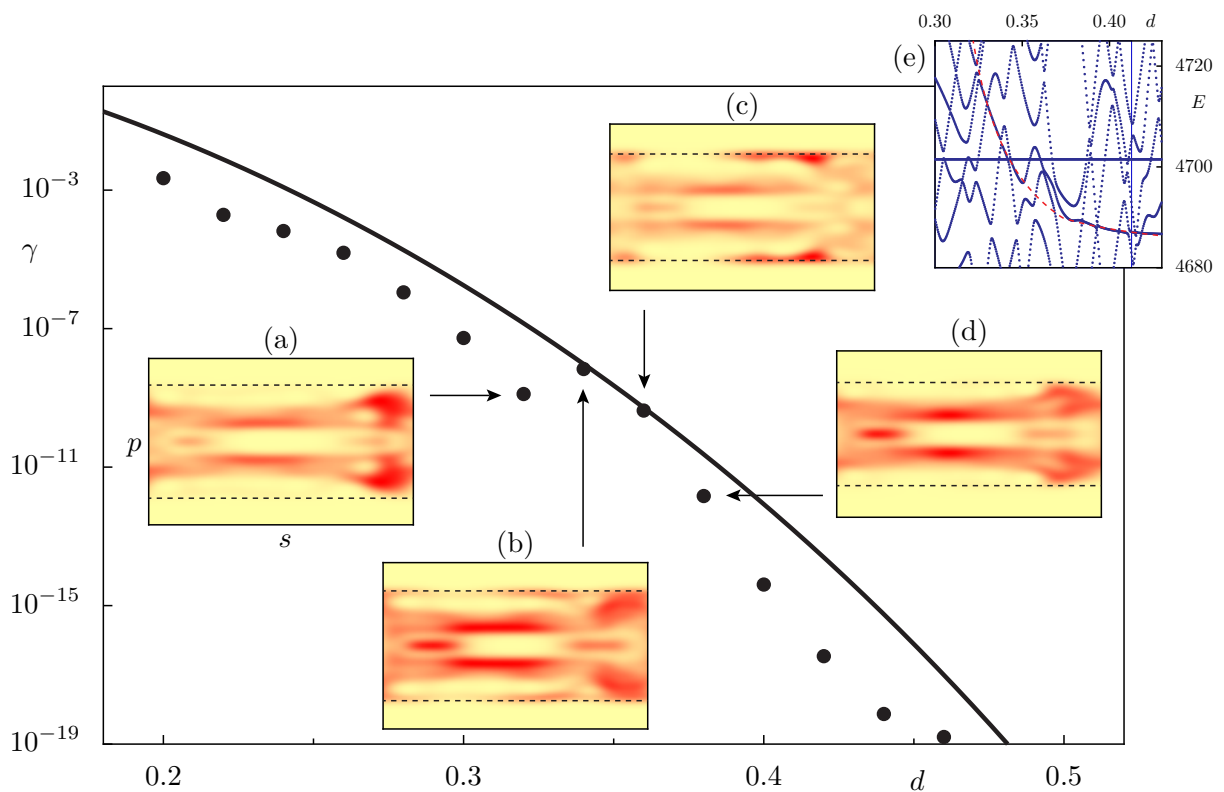


Figure 5.12: Tunneling rates from the regular state with quantum number $(m, n) = (61, 1)$ under variation of d : We compare the prediction of Eq. (5.39) (connected by solid lines) and numerical data (dots). The insets show the sum of all Poincaré Husimi representations (for the semi-circle) of chaotic states which are considered to numerically determine the tunneling rates for (a) $d = 0.32$, (b) $d = 0.34$, (c) $d = 0.36$, and (d) $d = 0.38$. For (b) and (c) we find relevant contributions in the vicinity of the border of the regular region (dashed lines). Hence, existing beach states are included and the numerical data matches our prediction. For (a) and (d) this is not the case. In (e) the spectrum is presented in the vicinity of $E_{61,1}$ (horizontal line). We find an avoided crossing with a beach state (see the red dashed line as a guide to the eye) at $d \approx 0.35$ which forms a horizontal line for $d > 0.4$.

The sum of Husimi representations of all considered chaotic states is presented in Fig. 5.12(a)-(d) under variation of d . They show contributions near the border of the regular region for $d \approx 0.35$ where a crossing of the considered regular state with a beach state occurs in the spectrum, see Fig. 5.12(e). Here, the numerically determined tunneling rates match our prediction.

This has some analogy to resonance-assisted tunneling [53–55]. If the beach state is energetically close to the considered regular one, couplings between the two states lead to an enhancement of the tunneling rate. Beach states which are energetically far away do not couple and therefore the size of the regular region is effectively enhanced, lowering the tunneling rate. In the theoretical prediction the effective enhancement of the regular region is not considered, and thus, it only matches with the numerics if the beach states are energetically close. In contrast to the theory of resonance-assisted tunneling the beach states are not localized in the regular but in the chaotic region of phase space. It remains an open task, how to include the influence of beach states into our theoretical prediction.

5.2.3 Dynamical tunneling of bouncing-ball modes

We consider the Sinai, the cosine, and the stadium billiard which all include a rectangular region in which so-called bouncing-ball motion occurs perpendicular to two parallel parts of the boundary. Classically, such trajectories have zero measure. Quantum mechanically, eigenstates of the billiards are observed which resemble the classical bouncing-ball motion located on the line $p = 0$ in the Poincaré section. Such eigenstates are called bouncing-ball modes. An interesting question concerns the coupling of such states to the rest of the chaotic region and therefore their tunneling rates γ to this domain. If there are bouncing-ball modes for which $\gamma \rightarrow 0$ in the semiclassical limit we can show their semiclassical existence. Due to the quantum ergodicity theorem [188] the bouncing-ball modes have to be a subset of all eigenstates of density zero. Hence, their number up to energy E will be described by a fractal Weyl law, $N_{\text{bb}}(E) = CE^\delta$, in which C is a constant and the exponent δ is restricted to $1/2 < \delta < 1$. In previous studies this exponent was predicted to be $\delta = 3/4$ for the stadium [189, 190] and $\delta = 9/10$ for the cosine billiard [190].

In this section we will apply our theory for direct dynamical tunneling using a fictitious integrable system to bouncing-ball modes and predict their tunneling rates to the chaotic component. The situation differs from the examples discussed before as the bouncing-ball motion is of measure zero and hence no regular island can be associated with it. Nevertheless, our theory is applicable with a slightly changed notation: The fictitious integrable system is called \hat{H}_{bb} with its eigenstates ψ_{bb} and eigenenergies E_{bb} . The desymmetrized Sinai, cosine, and stadium billiards are arranged as shown in Fig. 5.13(a)-(c) such that a rectangle of height L_0 and width B_0 appears on the left which is opened to the right.

To determine direct dynamical tunneling rates for bouncing-ball modes in these billiards, see Fig. 5.13(e) for an example, we have to evaluate Eq. (5.5) for the coupling matrix elements

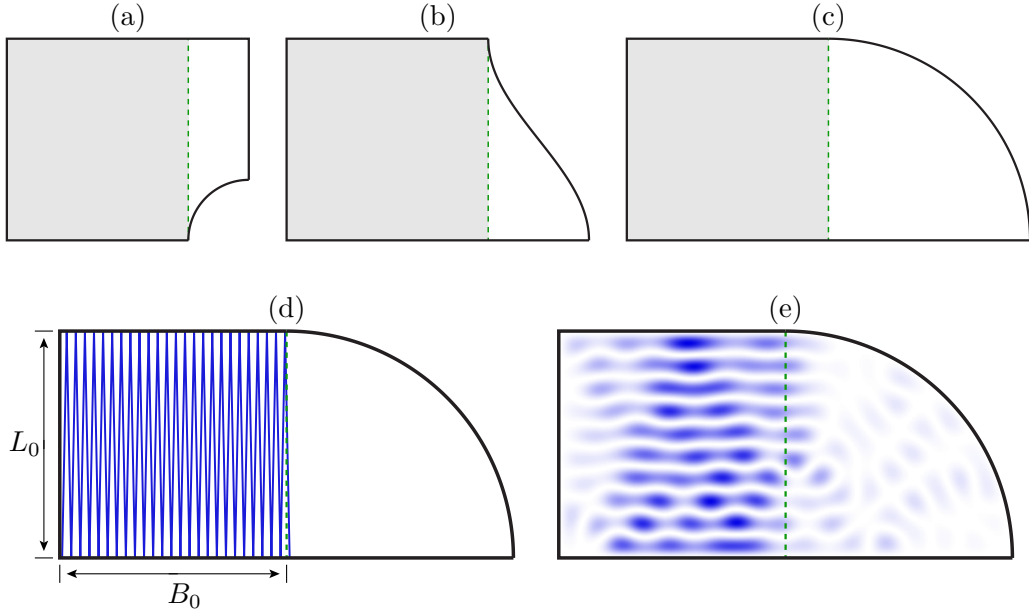


Figure 5.13: Schematic pictures of the desymmetrized (a) Sinai, (b) cosine, and (c) stadium billiard. The bouncing-ball regions are marked in gray and they are limited by green dashed lines. In (d) we show a classical trajectory near a periodic bouncing-ball orbit until it enters the circular part of the desymmetrized stadium billiard with $L_0 = 1$, $B_0 = 1$ and (e) depicts a corresponding bouncing-ball mode. For all example systems (a)-(c) the width of the rectangular bouncing-ball region is denoted by B_0 and its height by L_0 .

$v_{\text{ch},mn}$ and then use Fermi's golden rule, Eq. (5.6), to determine the tunneling rates. As the first step the fictitious integrable system \hat{H}_{bb} and its eigenstates ψ_{bb} have to be defined. The simplest choice is the rectangular billiard of width B_0 and height L_0 which exactly reproduces the bouncing-ball motion in the considered billiards. Its eigenstates are given by

$$\psi_{\text{bb}}^{mn}(x, y) = \sqrt{\frac{4}{B_0 L_0}} \sin\left(\frac{\pi n x}{B_0}\right) \sin\left(\frac{\pi m y}{L_0}\right). \quad (5.40)$$

They are characterized by the two quantum numbers $n = 1, 2, \dots$ and $m = 1, 2, \dots$ which describe the number of oscillations in x and y -direction, respectively.

As $\Omega_{\text{bb}} \subset \Omega$ we find the coupling matrix elements between the bouncing-ball modes ψ_{bb}^{mn} and the other chaotic states ψ_{ch} by integrating along $x = B_0$ and using the derivative of ψ_{bb}^{mn} in x -direction

$$v_{\text{ch},mn} = \int_0^{L_0} dy \psi_{\text{ch}}(x = B_0, y) \partial_x \psi_{\text{bb}}^{mn}(x = B_0, y) \quad (5.41)$$

$$= \sqrt{\frac{4}{B_0 L_0}} \frac{\pi n}{B_0} \int_0^{L_0} dy \psi_{\text{ch}}(x = B_0, y) \sin\left(\frac{\pi m y}{L_0}\right), \quad (5.42)$$

see the similar derivation in Section 5.2.1 for details.

We apply two different random wave models which describe the chaotic states $\psi_{\text{ch}}(\mathbf{q})$. First we use the random wave description which does not account for any boundary conditions, described by Eq. (3.194). At $x = B_0$ it reads

$$\psi_{\text{ch}}(x = B_0, y) = \sqrt{\frac{2}{NA_{\text{ch}}}} \sum_{s=1}^N c_s \cos(ky \sin \vartheta_s + kB_0 \cos \vartheta_s + \varphi_s) \quad (5.43)$$

in which the c_s are Gaussian random variables with $\langle c_s \rangle = 0$ as well as $\langle c_s c_t \rangle = \delta_{st}$ and the angles ϑ_s and φ_s are uniformly distributed in $[0, 2\pi)$. For the coupling matrix elements we find

$$v_{\text{ch},mn} = \frac{C_n}{\sqrt{NA_{\text{ch}}}} \sum_{s=1}^N c_s \int_0^{L_0} dy \cos(ky \sin \vartheta_s + \varphi_s) \sin\left(\frac{\pi my}{L_0}\right) \quad (5.44)$$

where we changed the x -coordinate such that the constant term $kB_0 \cos \vartheta_n$ in Eq. (5.43) vanishes and the prefactor is given by $C_n = \sqrt{\frac{8}{B_0 L_0} \frac{\pi n}{B_0}}$. The integral in Eq. (5.44) can be solved analytically and we obtain

$$v_{\text{ch},mn} = \frac{C_n}{\sqrt{NA_{\text{ch}}}} \sum_{s=1}^N c_s \frac{L_0 \pi m [-\cos \varphi_s + (-1)^m \cos(kL_0 \sin \vartheta_s + \varphi_s)]}{-\pi^2 m^2 + k^2 L_0^2 \sin^2 \vartheta_s}. \quad (5.45)$$

The tunneling rate is given by Fermi's golden rule, Eq. (5.6), which includes the variance of the coupling matrix elements $v_{\text{ch},mn}$. We perform an ensemble average over realizations of the random wave model by replacing the sum in Eq. (5.43) by integrals. Due to the independence of the Gaussian distributed random variables c_s one gets

$$\gamma_{mn} = \frac{1}{2} \frac{1}{4\pi^2} C_n^2 \int_0^{2\pi} d\varphi \int_0^{2\pi} d\vartheta \frac{L_0 \pi m [-\cos \varphi + (-1)^m \cos(k_{mn} L_0 \sin \vartheta + \varphi)]}{-\pi^2 m^2 + k_{mn}^2 L_0^2 \sin^2 \vartheta} \quad (5.46)$$

$$= \tilde{C}_n^2 \pi^2 m^2 \int_0^{2\pi} d\vartheta \frac{1 - (-1)^m \cos(k_{mn} L_0 \sin \vartheta)}{(-\pi^2 m^2 + k_{mn}^2 L_0^2 \sin^2 \vartheta)^2} \quad (5.47)$$

in which $\tilde{C}_n = L_0 C_n / \sqrt{4\pi}$. In Eq. (5.47) divergences appear in the integrand. Hence, we consider its numerator and denominator separately. The numerator has four roots which cancel with the roots of the denominator at $\vartheta_l = \arcsin[2\pi l / (k_{mn} L_0)]$ and $\pi - \vartheta_l$, where $l = \pm m/2$ for even m and $l = \pm(m/2 - 1/2)$ for odd m . The denominator has roots at $\vartheta_m = \arcsin[\pi m / (k_{mn} L_0)]$, $\pi - \vartheta_m$, $2\pi - \vartheta_m$, and $\pi + \vartheta_m$. They are equal to the roots of the numerator if $m = l$. For $m \gg n$ we find $\vartheta_m \rightarrow \pi/2$. We approximate

$$k_{mn}^2 = \frac{m^2 \pi^2}{L_0^2} + \frac{n^2 \pi^2}{B_0^2} \approx \frac{m^2 \pi^2}{L_0^2} \quad (5.48)$$

and therefore $k_{mn}L_0 \approx m\pi$. The tunneling rates simplify to

$$\gamma_{mn} = \frac{\tilde{C}_n^2}{\pi^2 m^2} \int_0^{2\pi} d\vartheta \frac{1 - (-1)^m \cos(\pi m \sin \vartheta)}{\cos^4 \vartheta}. \quad (5.49)$$

The integrand can be split into four equal integration intervals from 0 to $\pi/2$. At $\vartheta = \pi/2$ the denominator has a root. We expand the integrand around $\vartheta = \pi/2$

$$\frac{1 - (-1)^m \cos(\pi m \sin \vartheta)}{\cos^4 \vartheta} \approx \frac{1}{8} m^2 \pi^2 + \frac{1}{16} m^2 \pi^2 \left(\vartheta - \frac{\pi}{2} \right)^2 + \dots \quad (5.50)$$

As a first order approximation we take only the constant $m^2 \pi^2 / 8$, which can be integrated easily. Note that we approximate the complicated integrand by means of a constant function. Here we accumulate a large error compared to the previous approximations. The integration region is shortened to $[\vartheta_m, \pi/2]$ with $\vartheta_m = \arcsin(1 - 2/m)$. This root can be expanded for large m

$$\arcsin \left(1 - \frac{2}{m} \right) \approx \frac{\pi}{2} - \frac{2}{\sqrt{m}} - \frac{\sqrt{2}}{12} \left(\frac{2}{m} \right)^{\frac{3}{2}} \quad (5.51)$$

which leads to our final result for the tunneling rates for $m \gg n$

$$\gamma_{mn} = \frac{\tilde{C}_n^2}{\sqrt{m}} = \frac{2\pi L_0}{B_0^3} \frac{n^2}{\sqrt{m}}. \quad (5.52)$$

The tunneling rates show a quadratic dependence on the quantum number n and decay with \sqrt{m} . A numerical estimate of the error in Eq. (5.50) leads to an additional prefactor of $1/\sqrt{2}$

$$\gamma_{mn} = \frac{\sqrt{2}\pi L_0}{B_0^3} \frac{n^2}{\sqrt{m}}. \quad (5.53)$$

Alternatively we may use a random wave model, which accounts for the two boundary conditions at $y = 0$ and $y = L_0$. For the bouncing-ball modes we use Eq. (5.40) as before and the chaotic states are described by

$$\psi_{\text{ch}}(x, y) = 2 \sum_{s=1}^{s_{\text{max}}} c_s \sin \left(\frac{s\pi y}{L_0} \right) \sin(k_{x,s}(x - B_0) + \varphi_s), \quad (5.54)$$

where the c_s are Gaussian distributed random variables with mean zero and variance σ_s , which depends on s and still has to be determined. The wave number in x -direction is given by $k_{x,s} = \sqrt{E_{\text{bb}} - k_{y,s}^2} = \sqrt{E_{\text{bb}} - \pi^2 s^2 / L_0^2}$. For the tunneling rates we find

$$\gamma_{mn} = \frac{\pi^2 n^2 L_0 \sigma_m}{B_0^3}. \quad (5.55)$$

Only the term with $s = m$ remains due to the integration over the two sine functions. The σ_s have to be chosen in such a way that all angles α_s have the same probability. With

$$\alpha_s := \arctan\left(\frac{k_{x,s}}{k_{y,s}}\right) = \arctan\left(\sqrt{\frac{m^2 + n^2 L_0^2 / B_0^2}{s^2} - 1}\right) \quad (5.56)$$

and $s_{\max} \leq \sqrt{m^2 + n^2 L_0^2 / B_0^2}$ we find for the variances σ_s

$$\sigma_s = \frac{\alpha_{s-1} - \alpha_{s+1}}{2} \frac{2}{\pi}, \quad (5.57)$$

$$\sigma_{s=s_{\max}} = \frac{\alpha_s + \alpha_{s-1}}{2} \frac{2}{\pi}, \quad (5.58)$$

$$\sigma_{s=1} = \left(\frac{\pi}{2} - \frac{\alpha_s + \alpha_{s+1}}{2}\right) \frac{2}{\pi}. \quad (5.59)$$

For large m we assume $m = s_{\max}$ and thus

$$\sigma_m = \frac{1}{\pi}(\alpha_m + \alpha_{m-1}) = \frac{1}{\pi} \left[\arctan\left(\frac{nL_0}{mB_0}\right) + \arctan\left(\sqrt{\frac{m^2 + n^2 L_0^2 / B_0^2}{(m-1)^2} - 1}\right) \right] \quad (5.60)$$

$$\approx \frac{1}{\pi} \left(\sqrt{\frac{2}{m}} + \frac{nL_0}{mB_0} \right). \quad (5.61)$$

Finally the tunneling rate to leading order is

$$\gamma_{mn} = \frac{\sqrt{2}\pi L_0}{B_0^3} \frac{n^2}{\sqrt{m}} \quad (5.62)$$

which is the same result as given by Eq (5.53).

We determine tunneling rates numerically by evaluating the widths of avoided crossings between the bouncing-ball modes and other chaotic states. Therefore, the parameter B_0 is varied. This variation slightly affects the tunneling rates. Yet, this effect is negligible for tunneling rates of states with large energy due to the increasing density of states.

Figures 5.14, 5.15, and 5.16 show the comparison of the theoretical prediction of Eq. (5.62) to numerical data obtained for the Sinai, the cosine, and the stadium billiard for the parameters $B_0 = 1$ and $L_0 = 0.6$. For the Sinai and the cosine billiard we find agreement within a factor of two while in the case of the stadium billiard larger deviations are visible. These may originate from the choice of the fictitious integrable system which only roughly describes the bouncing-ball modes. While in the rectangular model the eigenstates are zero for $x > B_0$ they will continue to decay into this region in the mixed systems especially for the stadium billiard which shows no corner of angle $\pi/2$ at $x = B_0$. Note that the improved adiabatic model presented in Ref. [191] is not able to give a more reliable prediction.

Equation (5.62) allows a determination of the number of bouncing-ball modes $N_{\text{bb}}(E)$ which

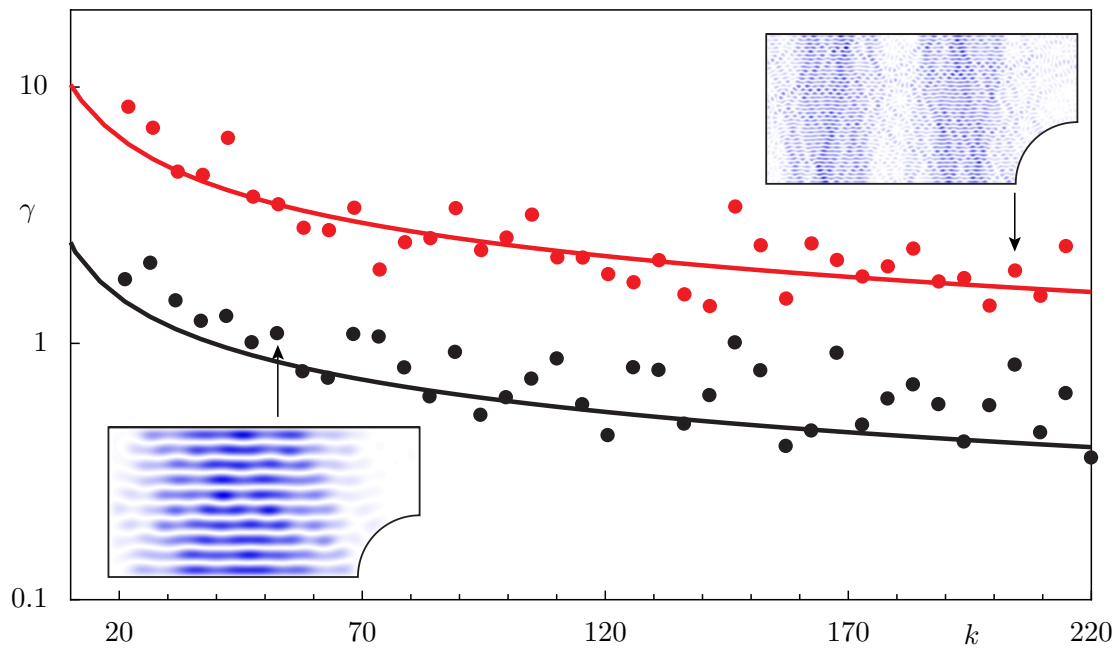


Figure 5.14: Tunneling rates from bouncing-ball modes in the Sinai billiard with quantum numbers $n = 1$ (black) and $n = 2$ (red) vs k for $B_0 = 1$ and $L_0 = 0.6$: We compare the prediction of Eq. (5.62) (connected by solid lines) and numerical data (dots). The insets show the bouncing-ball modes with quantum numbers $(m, n) = (10, 1)$ and $(m, n) = (39, 2)$.

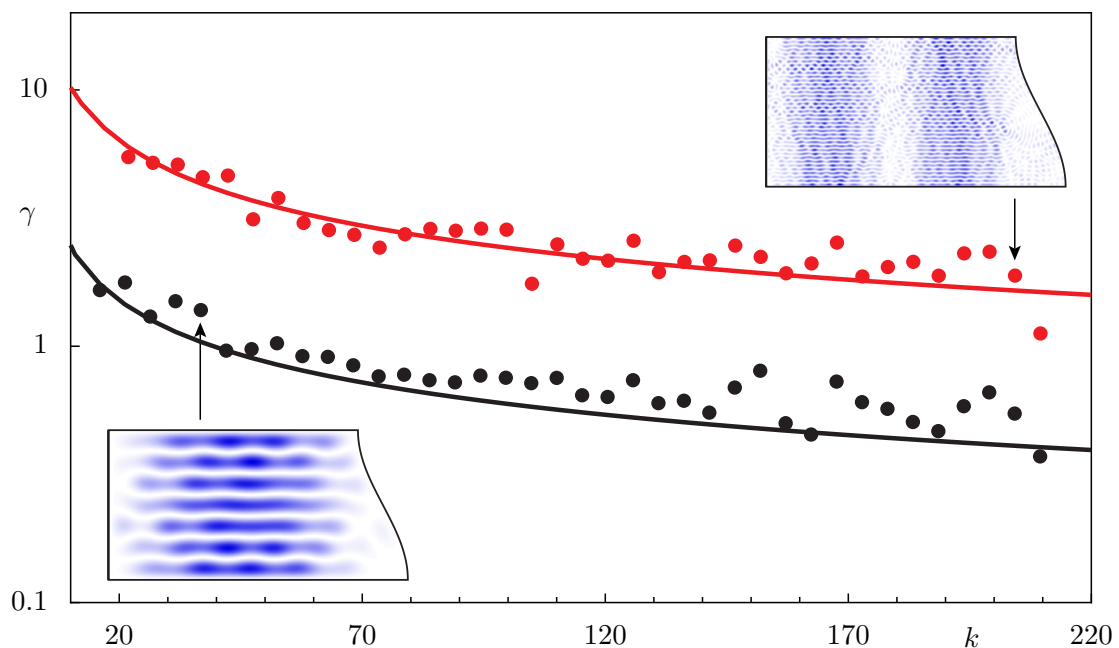


Figure 5.15: Tunneling rates from bouncing-ball modes in the cosine billiard with quantum numbers $n = 1$ (black) and $n = 2$ (red) vs k for $B_0 = 1$ and $L_0 = 0.6$: We compare the prediction of Eq. (5.62) (connected by solid lines) and numerical data (dots). The insets show the bouncing-ball modes with quantum numbers $(m, n) = (7, 1)$ and $(m, n) = (39, 2)$.

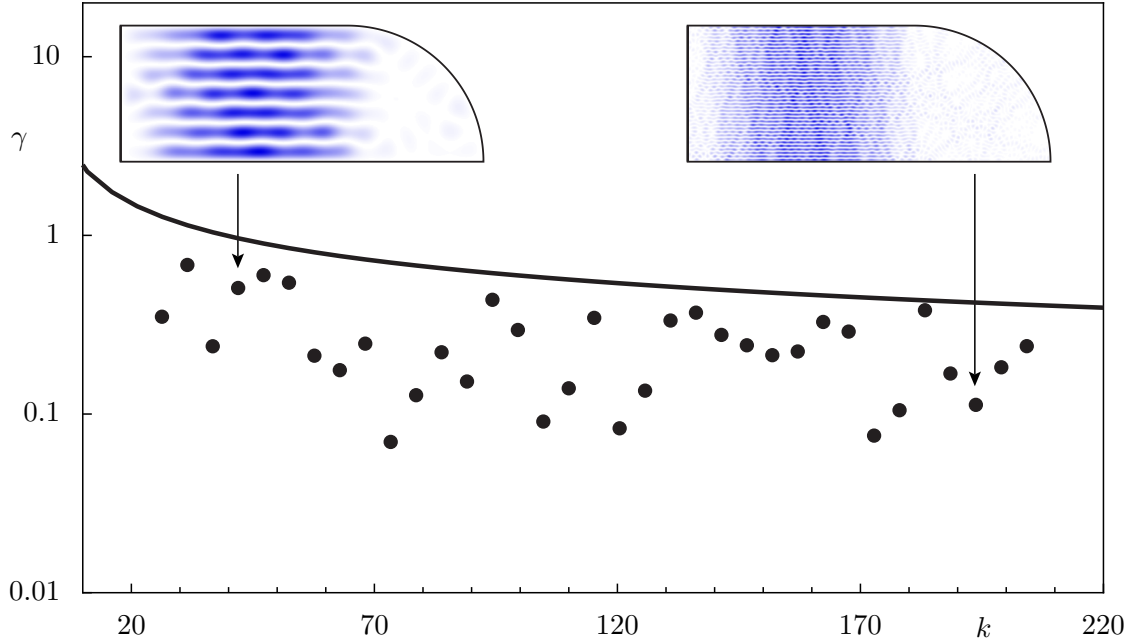


Figure 5.16: Tunneling rates from bouncing-ball modes in the stadium billiard with quantum number $n = 1$ vs k for $B_0 = 1$ and $L_0 = 0.6$: We compare the prediction of Eq. (5.62) (connected by solid lines) and numerical data (dots). The insets show the bouncing-ball modes with quantum numbers $(m, n) = (7, 1)$ and $(m, n) = (36, 1)$.

have an energy smaller than E . In particular, we want to predict the exponent δ of the fractional Weyl law $N_{\text{bb}}(E) = CE^\delta$. Thus, we include bouncing-ball modes which have a tunneling rate smaller than a given threshold, $\gamma < \gamma_{\text{cr}}$. Their number is estimated using Eq. (5.62), $E_{mn} \approx m^2\pi^2/L_0^2$, and by replacing the sum over all states by an integral

$$N_{\text{bb}}(E) \approx \frac{4}{5} \frac{L_0^{\frac{5}{4}}}{2^{\frac{1}{4}} \pi^{\frac{5}{4}}} \sqrt{\frac{B_0^3 \gamma_{\text{cr}}}{\pi L_0}} E^{\frac{5}{8}}. \quad (5.63)$$

This prediction estimates the same number of bouncing-ball modes for each of the considered billiards and an exponent $\delta = \frac{5}{8}$ for which indeed $1/2 < \delta < 1$ holds. Compared to numerics and the prediction in Ref. [190], however, it is too small. One reason for this discrepancy could be that Eq. (5.62) is valid only for $m \gg n$ and that for larger n its n -dependence might change to n^α with $\alpha < 2$. For such a generalized tunneling formula we find

$$N_{\text{bb}}(E) \approx \left(\frac{B_0^3 \gamma_{\text{cr}}}{\pi L_0} \right)^{\frac{1}{\alpha}} \frac{1}{2^{\frac{1}{2\alpha}}} \frac{1}{\frac{1}{2\alpha} + 1} \left(\frac{L_0}{\pi} \right)^{\frac{1}{2\alpha} + 1} E^{\frac{1+2\alpha}{4\alpha}}. \quad (5.64)$$

The exponent $\delta = 3/4$ for the stadium billiard is obtained by $\alpha = 1$ and $\delta = 9/10$ for the cosine billiard is found for $\alpha = 5/8$. Note that for $\alpha \rightarrow \infty$ we recover $\delta = 1/2$ as in the one-dimensional situation.

5.2.4 Two-dimensional nanowires with a magnetic field

In Refs. [44,45,192] a two-dimensional nanowire with one-sided surface disorder, see Fig. 5.17(a), was studied in the presence of a homogeneous magnetic field B perpendicular to the wire. In contrast to wires with two-sided disorder showing completely chaotic dynamics or wires with no disorder showing only regular dynamics the considered nanowire exhibits a mixed phase space, see Fig. 5.17(b). Orbits which do not hit the upper surface are regular skipping orbits while those which are reflected at the upper boundary are chaotic. Hence, dynamical tunneling between the regular and the chaotic region of phase space occurs which gives rise to exponentially increasing localization lengths ξ with increasing Fermi wave number k_F of the electrons, as found in Ref. [44]. The phase space of this system shows a sharp transition from regular to chaotic dynamics. There are no resonance chains inside the regular island and the hierarchical region does not exist. Therefore our theory which describes the direct regular-to-chaotic tunneling process is applicable. It predicts tunneling rates γ which are directly related to the localization lengths $\xi \propto 1/\gamma$ and we want to compare these results to the prediction derived in Refs. [44, 45].

The nanowire is attached to two leads of width $W = 1$ and the surface disorder is simulated by assembling the disordered boundary from L rectangular elements of width $l = W/5$ whose heights are uniformly distributed in the interval $[W - \delta/2, W + \delta/2]$ with $\delta = 2W/3$. The heights are allowed to take $M = 20$ different values including the limits of the interval. For increasing values of the Fermi wave number k_F we adjust the magnetic field B such that the cyclotron radius $r_c = \hbar k_F / (eB)$ remains constant and choose $r_c = 3W$. This leaves the classical dynamics unchanged such that the crossover from the quantum to the semiclassical regime can

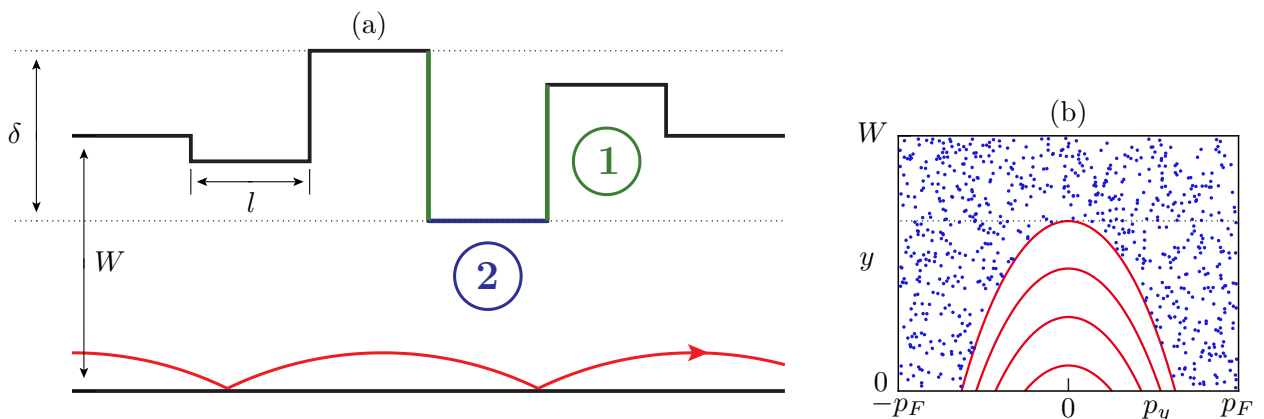


Figure 5.17: Schematic picture (a) of a magnetic wire with one-sided disorder to which leads of width W are attached. The wire is composed of rectangular elements of length l and a uniformly distributed height in $[W - \delta/2, W + \delta/2]$. For the tunneling process contributions (1) along the vertical and (2) along the horizontal parts of the upper boundary are relevant. In (b) a Poincaré section (y, p_y) at fixed x shows a large regular island (red lines) and the chaotic sea (blue dots).

be studied by $k_F \rightarrow \infty$.

In order to apply our theory for the direct dynamical tunneling rates γ using a fictitious integrable system we have to consider a closed billiard. It is obtained by closing the wire of L modules at the positions where the leads are attached. The tunneling rate is given by Fermi's golden rule, Eq. (5.6), using the coupling-matrix elements between regular and chaotic states

$$v_{\text{ch},m} = \int_{\Omega} dx dy \psi_{\text{ch}}(x, y) (\hat{H} - \hat{H}_{\text{reg}}) \psi_{\text{reg}}^m(x, y). \quad (5.65)$$

Similar to the examples discussed previously we have to find a fictitious integrable system \hat{H}_{reg} which resembles the regular part of the phase space and extends it into the chaotic sea. A reasonable choice is a billiard of length Ll with a boundary at $y = 0$ but which is open up to $y = \infty$. It shows exactly the same regular phase space as the wire with one-sided disorder and is completely integrable. Its eigenfunctions $\psi_{\text{reg}}^m(x, y)$ can be determined numerically as sketched in the Appendix D.3, where m is the quantum number in transversal direction. Using this regular system and its eigenstates in Eq. (5.65) gives

$$v_{\text{ch},m} = \int_{\mathcal{C}} ds \partial_N \psi_{\text{ch}}(x(s), y(s)) \psi_{\text{reg}}^m(x(s), y(s)). \quad (5.66)$$

In analogy to the annular billiard the derivative of the chaotic states $\partial_N \psi_{\text{ch}}(x(s), y(s))$ in normal direction along the disordered surface \mathcal{C} , which is parameterized by s , appears as the wire with one-sided disorder is completely located inside the integrable system: $\Omega_{\text{reg}} \supset \Omega$.

The upper boundary \mathcal{C} of the nanowire is composed of horizontal and vertical parts, see Fig. 5.17(a). As the regular wave functions $\psi_{\text{reg}}^m(x, y)$ decay exponentially in y -direction we have to account only for such L/M elements of \mathcal{C} which are located closest to the lower boundary at $y = W - \delta/2$. The boundary of each relevant element i is composed of one horizontal part with $x \in [il, (i+1)l]$ at $y = W - \delta/2$ and two vertical parts with $y \in [W - \delta/2, y_{\text{max}}]$ at $x = il$ and $x = (i+1)l$. Since the results are invariant under shifts of the x -coordinate we have L/M independent contributions. Furthermore, we assume that we can calculate the tunneling rates for the different contributions separately and that the final tunneling rate results from the sum of all these contributions. This assumption has been verified numerically.

Let us first consider the vertical contribution to the coupling-matrix elements $v_{\text{ch},m}$ where the x -coordinate is fixed. According to Appendix D.3 the regular states are given by

$$\psi_{\text{reg}}^m(x, y) = \frac{1}{\sqrt{lL}} e^{ik_{x,m}x} Z_m(y) \quad (5.67)$$

in which $Z_m(y)$ is numerically determined by solving the matrix equation (D.23) with $W \gg 1$. For the chaotic states $\psi_{\text{ch}}(x, y)$ we employ a random wave model with Bessel functions such

that the Dirichlet boundary condition at $x = 0$ is fulfilled

$$\psi_{\text{ch}}(r, \varphi) = \frac{2}{\sqrt{A_{\text{ch}}}} \sum_{s=1}^{\infty} c_s J_s(k_F r) \sin\left(s\varphi - \frac{\pi}{2}s\right). \quad (5.68)$$

The coefficients c_s are Gaussian random variables with mean zero and $\langle c_s c_t \rangle = \delta_{st}$. The derivative of $\psi_{\text{ch}}(x, y)$ with respect to x at $x = 0$ gives

$$\partial_x \psi_{\text{ch}}(x = 0, y) = \frac{2}{\sqrt{A_{\text{ch}}}} \sum_{s=1}^{\infty} c_s \frac{J_s(k_F y) s}{y}. \quad (5.69)$$

Hence, the contribution of the vertical part of the boundary to the coupling-matrix element is

$$v_{\text{ch},m} = \frac{2}{\sqrt{A_{\text{ch}}}} \frac{1}{\sqrt{Ll}} \sum_{s=1}^{\infty} c_s \int_0^{\infty} \frac{J_s(k_F y) s}{y} Z_m(y) dy. \quad (5.70)$$

Here we adjusted the y -coordinate such that $W - \delta/2 = 0$ and $y_{\text{max}} \rightarrow \infty$ which is valid in the semiclassical limit. By inserting Eq. (5.70) in Fermi's golden rule, Eq. (5.6), the contribution to the tunneling rate from the considered vertical boundary is found. In the whole wire $2L/M$ such contributions exist which describe the direct regular-to-chaotic tunneling contribution $\gamma_m^{(1)}$ of all relevant vertical boundaries

$$\gamma_m^{(1)} = \frac{4}{Ml} \sum_{s=1}^{\infty} s^2 \left(\int_0^{\infty} \frac{J_s(k_F y)}{y} Z_m(y) dy \right)^2. \quad (5.71)$$

We find that $\gamma_m^{(1)}$ is independent of the total number of elements L of the wire which is in agreement to the theory for the localization length derived in Refs. [44, 45].

For the horizontal contributions we consider the regular wave functions $\psi_{\text{reg}}^m(x, y)$ at $y = W - \delta/2$: $\psi_{\text{reg}}^m(x, y = W - \delta/2) =: Z_{m,0} e^{ik_x m x}$. For the chaotic wave function a random wave model respecting the Dirichlet boundary at $y = W - \delta/2$ is used and we change the y -coordinate such that $W - \delta/2 = 0$. The random wave model is given by

$$\psi_{\text{ch}}(x, y) = \frac{1}{\sqrt{A_{\text{ch}}}} \sqrt{\frac{2}{N}} \sum_{s=1}^N c_s e^{i(k_F x \cos \vartheta_s + \varphi_s)} \sin(k_F y \sin \vartheta_s) \quad (5.72)$$

where the coefficients c_s are Gaussian random variables with mean zero as well as $\langle c_s c_t \rangle = \delta_{st}$ and the angles ϑ_s and φ_s are uniformly distributed in $[0, 2\pi)$. The derivative of $\psi_{\text{ch}}(x, y)$ with respect to y at $y = 0$ reads

$$\partial_y \psi_{\text{ch}}(x, y = 0) = \frac{1}{\sqrt{A_{\text{ch}}}} \sqrt{\frac{2}{N}} k_F \sum_{s=1}^N c_s \sin \vartheta_s e^{i(k_F x \cos \vartheta_s + \varphi_s)}. \quad (5.73)$$

Hence, we obtain for the contribution of one horizontal part of the boundary to the coupling-matrix element

$$v_{\text{ch},m} = Z_{m,0} \frac{1}{\sqrt{A_{\text{ch}}}} \sqrt{\frac{2}{N}} k_F \frac{1}{\sqrt{Ll}} \sum_s c_s \sin \vartheta_s e^{i\varphi_s} \int_0^l dx e^{i(k_F \cos \vartheta_s + k_{x,m})x}. \quad (5.74)$$

Averaging over the different realizations of the random wave model results in

$$\langle |v_{\text{ch},m}|^2 \rangle_{\text{ch}} = |Z_{0,m}|^2 \frac{1}{A_{\text{ch}}} k_F^2 \frac{1}{Ll} \frac{1}{\pi} \int_0^{2\pi} d\vartheta \sin^2 \vartheta \frac{2 - 2 \cos(lk_F \cos \vartheta + lk_{x,m})}{(k_F \cos \vartheta + k_{x,m})^2}. \quad (5.75)$$

Next we use Eq. (5.75) in Fermi's golden rule, Eq. (5.6), to find the contribution to the tunneling rate from one horizontal boundary. In the whole wire there are L/M such contributions which in addition describe the direct tunneling contribution $\gamma^{(2)}$ of all relevant horizontal boundaries

$$\gamma_m^{(2)} = |Z_{0,m}|^2 \frac{1}{2\pi Ml} \int_0^{2\pi} d\vartheta \sin^2 \vartheta \frac{2 - 2 \cos \left(lk_F \left[\cos \vartheta + \frac{k_{x,m}}{k_F} \right] \right)}{\left(\cos \vartheta + \frac{k_{x,m}}{k_F} \right)^2}. \quad (5.76)$$

The total tunneling rate is given as the sum of the two contributions, Eq. (5.71) from the vertical parts of the boundary and Eq. (5.76) from the horizontal parts of the boundary,

$$\gamma_m = \gamma_m^{(1)} + \gamma_m^{(2)}. \quad (5.77)$$

We want to compare this result for the dynamical tunneling rates γ_m to the semiclassical prediction of localization lengths ξ_m for the wire with one-sided disorder. The derivation of this semiclassical theory is performed in Ref. [45] and the result is given in Appendix D.4. For the connection between tunneling rates and localization lengths we find

$$\gamma_m = \frac{v_{x,m}}{\xi_m l} = \frac{2k_{x,m}}{\xi_m l} \quad (5.78)$$

where $v_{x,m}$ is the velocity of the m th mode in x -direction, $2m_e = \hbar = 1$, and the additional factor l accounts for the scaling of Eq. (D.24) with l . The localization length ξ_m is proportional to the inverse of the tunneling rate γ_m [193]. Fig. 5.18 compares the localization lengths obtained by our approach using Eqs. (5.77) and (5.78) (solid lines) with the prediction of Eq. (D.24) (dashed lines) showing good agreement within a factor of two. Note that a comparison of the prediction, Eqs. (5.77) and (5.78), with numerical data [44] (not shown) gives a better agreement than Eq. (D.24).

Despite this good agreement we find that our result, Eqs. (5.77) and (5.78), shows an essential difference in its dependence on the length of the elements l compared to Eq. (D.24).

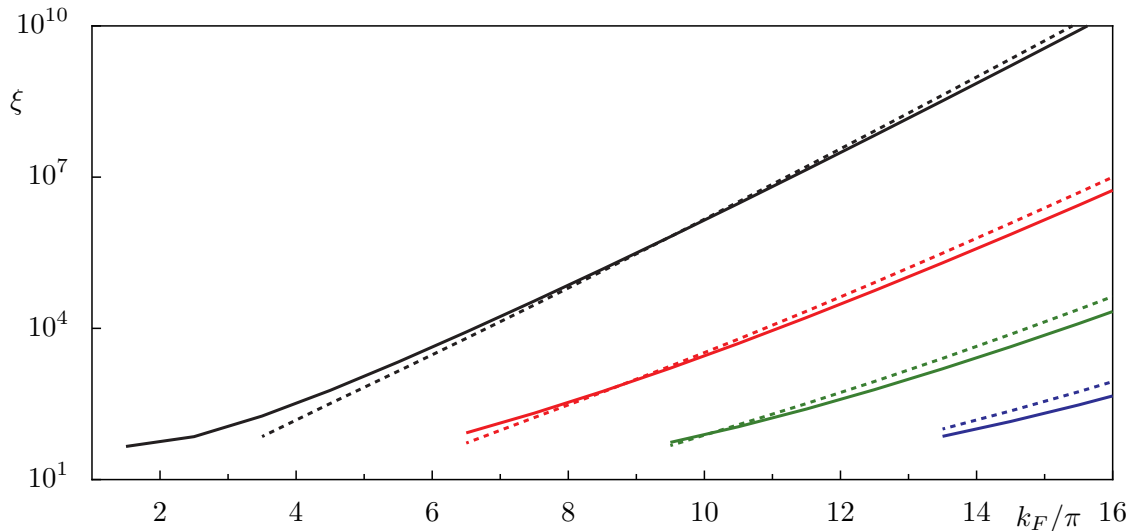


Figure 5.18: Localization lengths of transversal modes in the magnetic wire with one-sided disorder for the mode numbers $m \leq 3$ vs k_F/π for $l = 0.2$, $W = 1$, $\delta = 2/3$: We compare the prediction of Eqs. (5.77) and (5.78) (connected by solid lines) and Eq. (D.24) (connected by dashed lines).

While the localization length given by Eq. (D.24) is constant for increasing l , such that the corresponding tunneling rates decrease linearly with l , the contribution $\gamma_m^{(2)}$ in our prediction remains unchanged. The prefactor $1/l$ in Eq. (5.76) is compensated by the integral which increases linearly with l . Hence, for large l deviations between the two theories appear. They can be understood qualitatively. The approach using a fictitious integrable system assumes that tunneling into the chaotic region may occur while the electron moves inside a part of the wire of width $W - \delta/2$ and length l . However, the classical dynamics within such an element is completely regular. Couplings between regular and chaotic modes can only occur in the vicinity of the transitions between different elements of the wire in a region $\Delta x \approx 1/k_{x,m}$. This leads to a modified version of Eq. (5.74) where l in the integral is replaced by $1/k_{x,m}$ such that Eq. (5.76) decreases linearly with l . Hence we find agreement to the semiclassical prediction of the localization lengths, Eq. (D.24).

5.2.5 Cosine billiards

In this section we present the first steps in the understanding of the dynamical tunneling process for cosine billiards and discuss open issues of our theoretical approach. We consider the desymmetrized cosine billiard which is characterized by the width l and the height h of the rectangular region as well as the amplitude a of the cosine boundary, see Fig. 5.19(a). For the considered parameter values the cosine billiard shows a generic phase-space structure, see Fig. 5.19(c), with a regular island, a large transition region to the chaotic sea, and partial barriers within the chaotic component. This complicates the application of our approach as

it cannot describe the effects of the additional phase-space structures. The geometry of the billiard can be chosen such that one regular island without prominent resonances or with a large 4:1 resonance chain appears.

We apply our approach using a fictitious integrable system to find a prediction of direct dynamical tunneling rates which describe the decay of regular states into the chaotic sea. Here we face a severe difficulty: There is no integrable billiard system resembling the regular motion of the cosine billiard. An approach which constructs H_{reg} using soft-wall potentials is currently under investigation. Hence, we present a simpler method determining a hard-wall billiard system which resembles the regular motion of the cosine billiard and partially extends it into the chaotic region of H . Note that the classical dynamics of such a system H_{reg} is not necessarily regular. Yet, it has mainly regular dynamics beyond the border of the island and can therefore be used in Eq. (5.5) to predict dynamical tunneling rates with Fermi's golden rule, Eq. (5.6).

For the construction of H_{reg} we use a second order Taylor expansion of the cosine-shaped

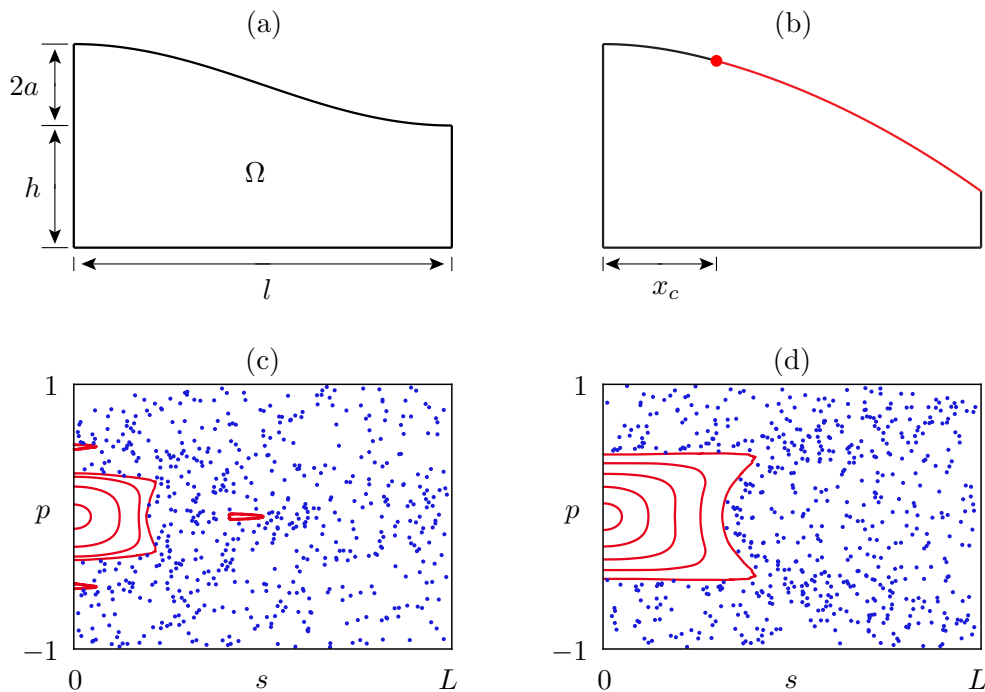


Figure 5.19: (a) Schematic picture of the desymmetrized cosine billiard which consists of a rectangular region of width l and height h . The amplitude of the cosine boundary is denoted by a . In (b) we use a second order Taylor expansion of the cosine-shaped upper boundary at $x = x_c$ for $x > x_c$. This billiard resembles the regular island of (a) and considerably extends it to the chaotic sea. In addition Poincaré sections at the horizontal lower boundary (relative tangential momentum p vs arclength s) are shown in (c) and (d) for the cosine billiard (a) and the modified billiard (b).

upper boundary at $x = x_c$ such that it reads

$$h + a + a \cos\left(\frac{\pi x}{l}\right) \quad \text{for } x \leq x_c, \quad (5.79)$$

$$c_0 + c_1(x - x_c) + c_2(x - x_c)^2 \quad \text{for } x \geq x_c, \quad (5.80)$$

in which

$$c_0 = h + a + a \cos\left(\frac{\pi x_c}{l}\right), \quad (5.81)$$

$$c_1 = -\frac{a\pi}{l} \sin\left(\frac{\pi x_c}{l}\right), \quad (5.82)$$

$$c_2 = -\frac{a\pi^2}{2l^2} \cos\left(\frac{\pi x_c}{l}\right). \quad (5.83)$$

The free parameter x_c determines the position from which on the upper boundary is modified. Classical trajectories which hit the upper boundary at $x > x_c$ will behave differently compared to the original cosine billiard. We introduce x_r as the position coordinate of the cosine boundary which a regular orbit can maximally reach. Ideally, we would like to choose $x_c > x_r$ such that the classically regular dynamics of H and H_{reg} are identical. However, the regular island of H_{reg} has to be considerably larger than that of H such that its regular eigenstates decay into the chaotic region of H . This requirement is fulfilled only for $x_c < x_r$. While the size of the regular island increases with decreasing x_c the classically regular motion of the two systems differ more and more. We choose $0.3 < x_c < 0.35$ while $x_r \approx 0.6$ for the parameter values $l = 1.3$, $h = 0.8$, and $a = 0.12$ of the cosine billiard, see Fig. 5.19(b) and (d).

To determine the tunneling rates we have to evaluate the coupling matrix elements, Eq. (5.5), given as

$$v_{\text{ch},mn} = \int_{\partial\Omega^v} \psi_{\text{ch}}(x(s), y(s)) \partial_N \psi_{\text{reg}}^{mn}(x(s), y(s)) ds, \quad (5.84)$$

in which s parameterizes the upper boundary $\partial\Omega^v$ of H_{reg} for $x > x_c$. Due to $\Omega_{\text{reg}} \subset \Omega$ the normal derivative of the regular wave function with respect to this boundary appears. We introduce the quantum numbers $m = 1, 2, \dots$ and $n = 1, 2, \dots$ which label the number of oscillations in vertical and horizontal direction, respectively.

For the chaotic states $\psi_{\text{ch}}(\mathbf{q})$ we use the random wave model of Eq. (3.194) which does not account for any boundary conditions. In Eq. (5.84) we integrate along the upper boundary of H_{reg} starting at $x = x_r$ such that we consider only parts of the boundary which are located in the chaotic component. For the direct tunneling rates we obtain

$$\gamma_{mn} = \frac{A_{\text{ch}}}{2} \left\langle \left| \int_{s(x_r)} \psi_{\text{ch}}(x(s), y(s)) \partial_N \psi_{\text{reg}}^{mn}(x(s), y(s)) ds \right|^2 \right\rangle_{\text{ch}}. \quad (5.85)$$

This equation has to be evaluated numerically as there is no analytic expression for the regular

states ψ_{reg}^{mn} . We compute the regular eigenfunction $\psi_{\text{reg}}^{mn}(\mathbf{q})$ at energy E_{reg}^{mn} of \hat{H}_{reg} and perform the ensemble average over different realizations of the random wave model in Eq. (5.85). The leading contribution of Eq. (5.85) arises at the lower boundary of integration $s(x_r)$ as the regular states decay exponentially with increasing x .

In Fig. 5.20 we compare the prediction of Eq. (5.85) with numerical data which is obtained by evaluating avoided crossings between regular and chaotic states under variation of the right vertical boundary. If we use the classically determined position of the border of the regular region, $x_r \approx 0.6$, for the lower limit of integration in Eq. (5.85) the tunneling rates are predicted too large (a), while we find better agreement e.g. for $x_r = 0.65$ (b). This might be explained by the occurrence of beach states which effectively increase the size of the regular region. Nevertheless, it remains an open task to find an improved method for the construction of a fictitious integrable system in the case of generic two-dimensional billiards.

Up to this point we have only considered the direct regular-to-chaotic tunneling process for the cosine billiard and for the other billiards discussed in the previous sections. However, the cosine billiard shows a large 4:1 resonance chain in the regular region of phase space for the parameters $l = 1$, $h = 0.36$, and $a = 0.1$, see the inset in Fig 5.21(a). Hence, we expect resonance-assisted tunneling to be relevant. We search for signatures of resonance-assisted tunneling by numerically determining the eigenenergies of the regular states with quantum number (m, n) and indeed find avoided crossings between states of quantum number n and $n + 2$. Due to the desymmetrization of the billiard the states which couple differ by 2 in n while for the full cosine billiard this difference is 4. Hence, we can identify the 4:1 resonance as the reason for the couplings of the regular states. Note that for the geometry discussed previously, which shows no 4:1 resonance, such couplings are not found. Due to these couplings

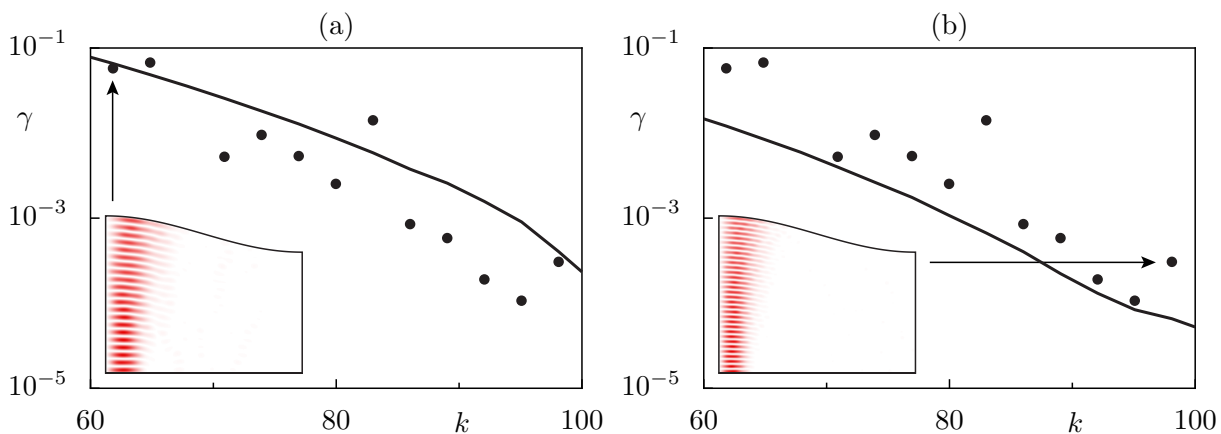


Figure 5.20: Tunneling rates from regular states in the cosine billiard with horizontal quantum number $n = 1$ vs k for $l = 1.3$, $h = 0.8$, $a = 0.12$, $x_c = 0.3$, and (a) $x_r = 0.6$ or (b) $x_r = 0.65$. We compare the prediction of Eq. (5.85) (connected by solid lines) and numerical data (dots). The insets show the regular eigenfunctions (a) $\psi_{\text{reg}}^{21,1}$ and (b) $\psi_{\text{reg}}^{32,1}$. The Poincaré section is presented in Fig. 5.19(c).

we expect resonance-assisted tunneling to dominate the tunneling process for large energies, see Section 4.2. Fig. 5.21(a) shows that peaks appear in the numerically determined tunneling rates at the positions for which the avoided crossings occur, see Fig. 5.21(b). To obtain this numerical data we attached a stem to the cosine billiard at $x > 0.5$, see the inset in Fig. 5.21(b), such that the regular dynamics remains unaffected and structures in the chaotic sea such as partial barriers are destroyed. The tunneling rates are obtained by evaluating widths of avoided crossings under variation of the length of the stem as in the case of the mushroom billiard.

Hence, we have presented numerical evidence for resonance-assisted tunneling in two-dimensional autonomous billiard systems. In the future we would like to extend the theory derived in Refs. [53–55] to these higher dimensional systems and find a prediction which explains the presented numerical data.

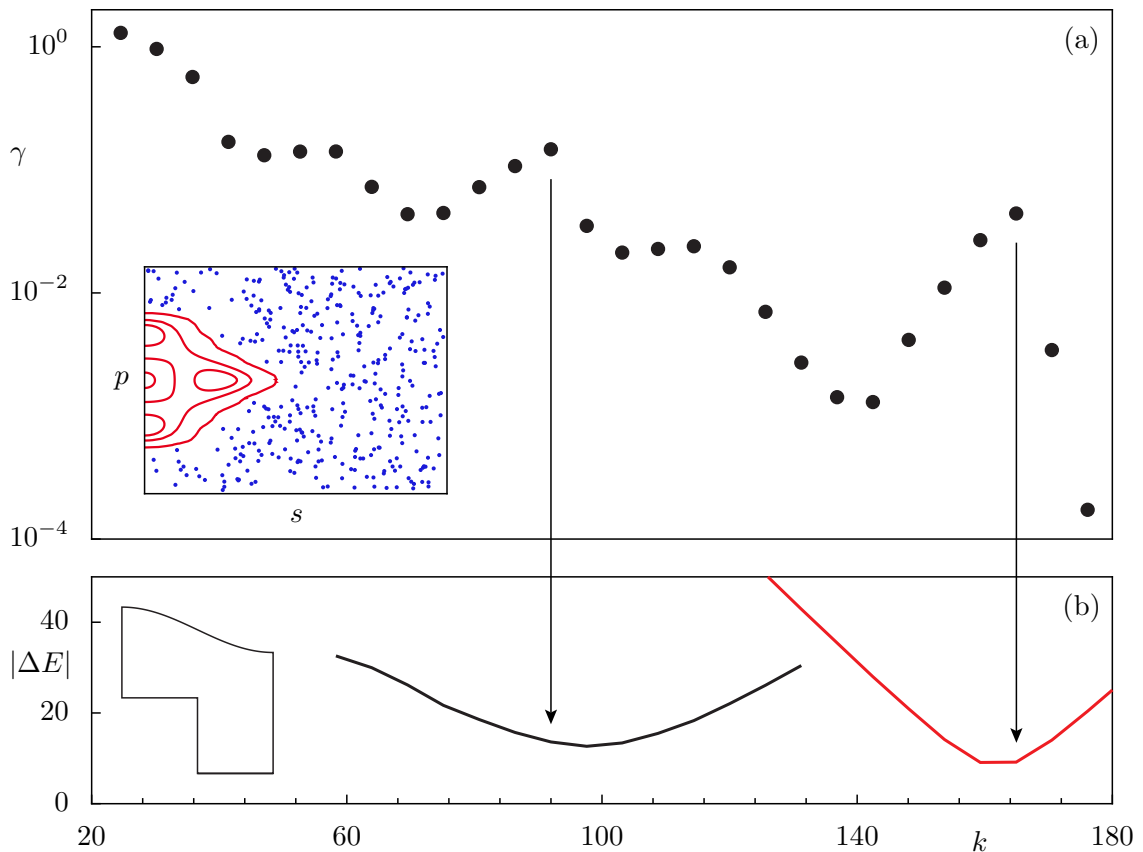


Figure 5.21: Numerically determined tunneling rates from regular states in the cosine billiard with horizontal quantum number $n = 1$ vs k for $l = 1$, $h = 0.36$, and $a = 0.1$ (a). The Poincaré section of its lower boundary shows half of a 4:1 resonance chain (inset). In (b) we present the distance $|\Delta E|$ between the energetically closest regular eigenstates of quantum number $n = 1$ and $n = 3$ (black line) and between $n = 1$ and $n = 5$ (red line). At wave numbers k where these distances have a minimum, a peak is found in the tunneling rates as appears for resonance-assisted tunneling. The inset shows the used cosine billiard to which an additional stem is attached for $x > 0.5$ such that partial barriers in the chaotic sea are destroyed.

6 Quality factors of optical microcavities

Optical microcavities in which photons can be confined in three spatial dimensions are a subject of intensive research as they are relevant for applications such as ultralow-threshold lasers [151, 152], single-photon emitters [153, 154], or correlated photon-pair emitters [155]. Especially whispering-gallery cavities such as microdisks [194–196], microspheres [197, 198], and microtoroids [199] have been investigated as they can trap photons for a long time near the boundary by total internal reflection. The corresponding whispering-gallery modes have a very high quality factor Q , which makes these cavities a candidate for the devices mentioned above. While the microdisk emits the photons isotropically, cavities with deformed surfaces may additionally lead to directed emission [158, 171, 200–209]. A particularly interesting geometry is the annular cavity [171], a microdisk with an air hole, as it allows for unidirectional emission and high quality factors simultaneously which for most applications is desirable.

In this chapter we connect the quality factors Q of optical microcavities to the concept of dynamical tunneling [23]. We provide an explicit prediction for the quality factors of whispering-gallery modes in the annular microcavity extending the approach for direct regular-to-chaotic tunneling which uses a fictitious integrable system, presented in Section 4.1.

For that purpose we first introduce the circular microcavity which serves as the fictitious integrable system. This circular cavity is an open system and its resonant states decay due to a quasi one-dimensional barrier-tunneling process. In the annular cavity this barrier tunneling competes with dynamical tunneling in which the regular modes couple to chaotic modes which have a short life-time. We compare the theoretical predictions with numerical data. The results of this chapter are published in Ref. [51].

6.1 The circular microcavity

Let us consider the circular microcavity [173] with refractive index n_Ω inside and n_0 outside the cavity of radius R . Classical trajectories started inside such a cavity are reflected at the boundary due to total internal reflection if their angle of incidence χ fulfills $\sin \chi > n_0/n_\Omega$. In the Poincaré section of the corresponding closed billiard system the escape of the particles is given by an absorbing boundary at $|p| \leq n_0/n_\Omega$.

We want to find the solutions of the wave equation (3.256) which in polar coordinates (r, φ) reads

$$-\Delta\psi(r, \varphi) = n(r)^2 k^2 \psi(r, \varphi). \quad (6.1)$$

The wave function ψ can be separated into a radial and an angular component $\psi(r, \varphi) = R(r)\phi(\varphi)$ and we obtain

$$\frac{1}{R(r)} \left(-\frac{\partial^2}{\partial r^2} - \frac{1}{r} \frac{\partial}{\partial r} \right) R(r) - \frac{1}{r^2} \left(\frac{1}{\phi(\varphi)} \frac{\partial^2}{\partial \varphi^2} \phi(\varphi) \right) = n(r)^2 k^2 = \text{const.} \quad (6.2)$$

The angular part

$$\frac{d^2}{d\varphi^2} \phi(\varphi) = -m^2 \phi(\varphi) \quad (6.3)$$

leads to $\phi(\varphi) = Ne^{im\varphi}$ where $m \in \mathbb{Z}$ and N accounts for the normalization. The radial part

$$-\left(\frac{d^2}{dr^2} + \frac{1}{r} \frac{d}{dr} \right) R(r) + V_{\text{eff}}(r)R(r) = k^2 R(r) \quad (6.4)$$

describes the motion of a particle in the effective potential

$$V_{\text{eff}}(r) = k^2(1 - n(r)^2) + \frac{m^2}{r^2} \quad (6.5)$$

in which m denotes the angular quantum number. Here an additional centrifugal potential term appears due to the conservation of angular momentum. For $n_\Omega > n_0$ this potential forms a metastable well in which resonance states are located, see Fig. 6.1. The leakage through this one-dimensional well induces their decay and leads to resonances with a finite life-time. However, as the kinetic energy term in Eq. (6.4) contains a first derivative it cannot be directly compared to the usual Schrödinger equation. In Ref. [173] it was shown that metastable states inside this potential exist for

$$\frac{m}{n_\Omega R} < \text{Re}(k) < \frac{m}{n_0 R} \quad (6.6)$$

which places the metastable level below the top of the barrier such that its decay can occur by tunneling only.

States with the lowest possible $\text{Re}(k)$ for fixed m localize closest to the boundary of the cavity at $r = R$. They are located deep inside the metastable well and hence have a long life-time. This life-time will further grow with increasing azimuthal quantum number m which enlarges the height of the tunneling barrier. As discussed in Chapter 2 for the one-dimensional case we expect exponentially decreasing tunneling rates γ_{1d} through this barrier with increasing m ,

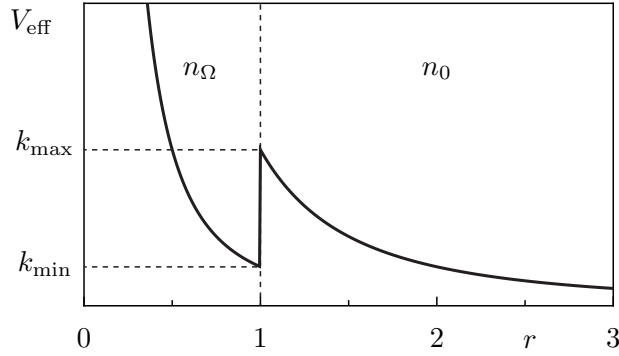


Figure 6.1: Sketch of the effective potential V_{eff} for a circular microcavity of radius one. At the boundary $r = 1$ the potential jumps due to the change of refractive index. Resonance states are located in the metastable well with wave numbers in between $k_{\text{min}} = m/n_{\Omega}$ and $k_{\text{max}} = m/n_0$ which limits the maximal radial quantum number n for each m . For $n_0 < n_{\Omega}$ and increasing n_{Ω} more and more long-lived resonances will exist.

which was indeed confirmed in Ref. [173] using a WKB approximation

$$\gamma_{1d} = \frac{1}{(n_{\Omega}/n_0)^2 - 1} e^{-(2m-1)\alpha} e^{2m \tanh(\alpha)} \quad (6.7)$$

in which

$$\alpha = \frac{1}{2} \ln \left(\frac{1 + \sqrt{1 - \text{Re}(k)^2/m^2}}{1 - \sqrt{1 - \text{Re}(k)^2/m^2}} \right). \quad (6.8)$$

Hence, for the circular microcavity the escape of resonant states γ_{1d} is completely described by one-dimensional barrier tunneling from the metastable well of the effective potential, Eq. (6.5), to the outside.

We now want to solve the radial equation (6.4). Its solutions are given as

$$R(r) = \begin{cases} A_m J_m(n_{\Omega}kr), & r < R \\ H_m^{(2)}(n_0kr) + S_m H_m^{(1)}(n_0kr), & r > R \end{cases} \quad (6.9)$$

in which the incoming wave is described by a Hankel function of the second kind $H_m^{(2)}(n_0kr)$ and the scattered wave is given by a Hankel function of the first kind $S_m H_m^{(1)}(n_0kr)$ with a certain scattering amplitude S_m . The coefficients A_m describe the amount of probability entering the cavity. If the radiation is generated within the cavity (e.g. for lasers) no incoming waves appear. The radial solutions and their derivative have to be continuous at the interface of the cavity at $r = R$

$$A_m J_m(n_{\Omega}kR) = H_m^{(2)}(n_0kR) + S_m H_m^{(1)}(n_0kR), \quad (6.10)$$

$$A_m J'_m(n_{\Omega}kR) = H_m^{(2)'}(n_0kR) + S_m H_m^{(1)'}(n_0kR) \quad (6.11)$$

which leads to

$$A_m = \frac{H_m^{(2)}(n_0 k R) + S_m H_m^{(1)}(n_0 k R)}{J_m(n_\Omega k R)}, \quad (6.12)$$

$$S_m = \frac{J'_m(n_\Omega k R) H_m^{(2)}(n_0 k R) - J_m(n_\Omega k R) H_m^{(2)'}(n_0 k R)}{J_m(n_\Omega k R) H_m^{(1)'}(n_0 k R) - J'_m(n_\Omega k R) H_m^{(1)}(n_0 k R)}. \quad (6.13)$$

At a resonance the scattering matrix has a pole such that S_m diverges. Hence, we have to find roots of the denominator of S_m for complex $k = \text{Re}(k) + i \text{Im}(k)$. We obtain the resonances k_{mn} from numerically solving

$$n_\Omega J_{m+1}(n_\Omega k_{mn} R) H_m^{(1)}(n_0 k_{mn} R) = n_0 J_m(n_\Omega k_{mn} R) H_{m+1}^{(1)}(n_0 k_{mn} R). \quad (6.14)$$

As an initial guess for the complex wave numbers k_{mn} we choose $k_{mn} \approx j_{mn}/n_\Omega - \Delta k$ which are the eigenvalues of the circular billiard in a dielectric medium of refractive index n_Ω shifted by a small positive number Δk . It accounts for the decreasing wave numbers due to the openness of the real cavity. As a resonant state we consider $\psi_{\text{reg}}^{mn}(r, \varphi) = R(r, k_{mn}) \phi_m(\varphi)$.

The imaginary part of the wave number is connected to the decay rate of the resonant states. Using

$$E = E_0 - i \frac{\gamma}{2} = n_\Omega^2 (\text{Re}(k) + i \text{Im}(k))^2 \quad (6.15)$$

$$= n_\Omega^2 (\text{Re}(k)^2 - \text{Im}(k)^2 + 2i \text{Re}(k) \text{Im}(k)) \quad (6.16)$$

and $n_0 = 1$ we find for this decay rate

$$\gamma = -4n_\Omega^2 \text{Re}(k) \text{Im}(k). \quad (6.17)$$

6.2 Direct regular-to-chaotic tunneling in the annular microcavity

A particularly suited example to study the influence of a mixed phase space onto the quality factors Q is the annular cavity. Its geometry is given by the radius R of the large disk, the radius R_2 of the small disk, and the minimal distance between the two disks d , see Fig. 6.2(a). Without loss of generality we choose $R = 1$. Under the variation of the two parameters d and R_2 the dynamics inside the cavity changes drastically from completely regular behavior when the two disks are concentric ($d = R - R_2$) to mixed regular-chaotic behavior for the general excentric case. This is clearly visible for different trajectories in the Poincaré section, see Fig. 6.2(b). The large disk has an effective refractive index n_Ω while inside the small disk and outside of the cavity the refractive index is unity, $n_0 = 1$. For the visualization of the

ray dynamics we used an annular cavity with hard wall boundary conditions at the outer disk, neglecting ray-splitting effects.

The annular cavity has been studied extensively in the context of quantum chaos [176], optomechanics [210], avoided resonance crossings, and resonant tunneling [211]. For applications it is of high interest as it allows for unidirectional light emission from high- Q modes which has been predicted in Ref. [171] and has been confirmed in recent experiments [208]. The closed system with perfectly reflecting walls, i.e. the annular billiard, is a paradigm for dynamical tunneling [29, 30, 122], see also Section 5.2.2.

The quality factor Q of a mode in an open cavity is related to the corresponding resonance with complex wave number $k = \text{Re}(k) + i \text{Im}(k)$ via

$$Q = -\frac{\text{Re}(k)}{2\text{Im}(k)}. \quad (6.18)$$

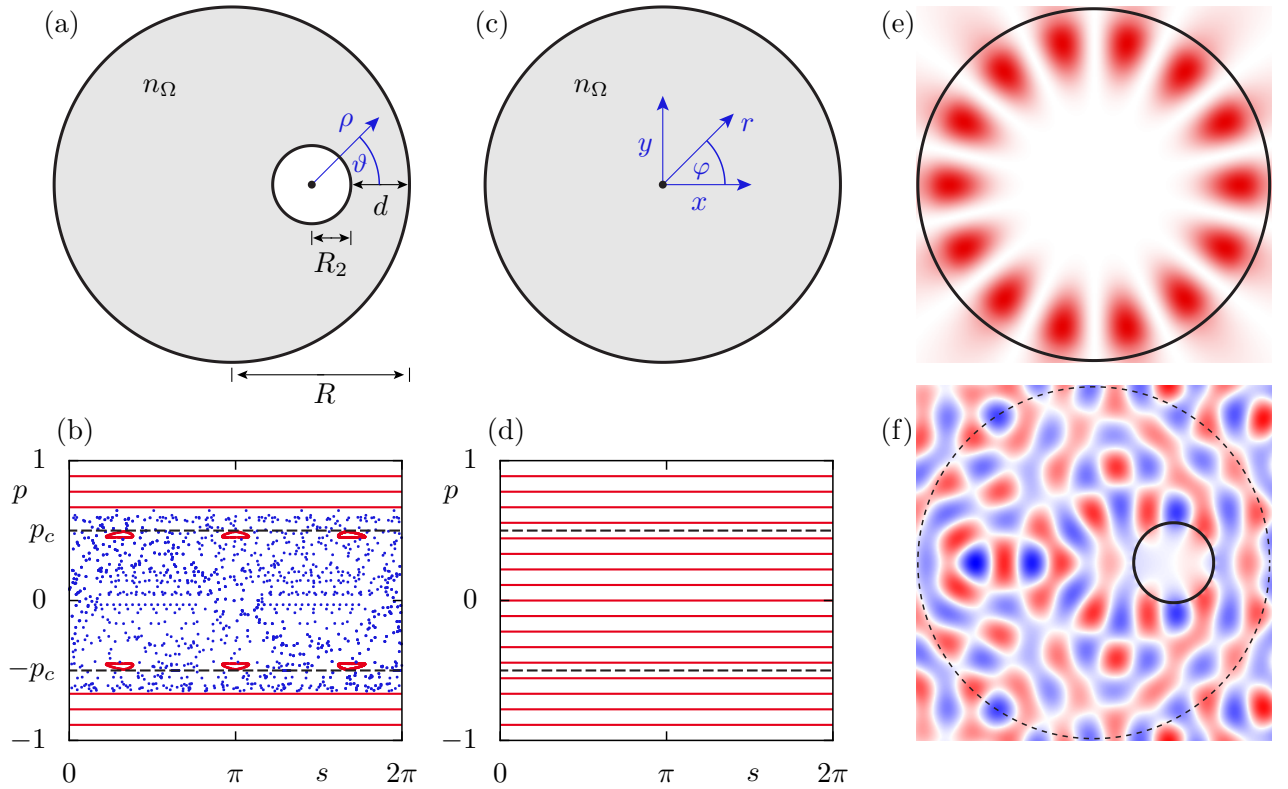


Figure 6.2: (a) Annular cavity with $R = 1$, $R_2 = 0.22$, and $d = 0.33$. (b) Corresponding Poincaré section ($s, p = \sin \chi$) for $n_\Omega = 2.0$, where s is the arclength along the boundary and χ is the angle of reflection. Between the critical lines (dashed) with $|p_c| = 1/n_\Omega$ is the leaky region, where the condition for total internal reflection is not fulfilled. In (c) we show the circular cavity, in (d) its completely regular phase space, and in (e) the resonant mode of quantum number $(m, n) = (7, 1)$. In (f) we present a wave function generated by a random wave model which respects the change of refractive index at the boundary of the small disk.

In the annular cavity the quality factor Q of a regular mode has two contributions

$$\frac{1}{Q} = \frac{1}{Q_{1d}} + \frac{1}{Q_{\text{dyn}}}. \quad (6.19)$$

Here Q_{1d} accounts for the coupling of the regular mode to the continuum which is described by a quasi one-dimensional barrier-tunneling process as in the case of the circular cavity, see Section 6.1. It can be predicted by means of a WKB approximation, Eq. (6.7), or using the numerically determined decay rates of the modes in the circular cavity. Note that for this contribution the mixed phase-space structure induced by the small disk is irrelevant. The second contribution, Q_{dyn} , is given by dynamical tunneling from the regular mode to the chaotic sea, which for $|p| < p_c$ is strongly coupled to the continuum, see Fig. 6.2(b). Here we assume that there are no further phase-space structures within the chaotic sea that affect the quality factor. A priori it is not obvious, which of these contributions will dominate.

In the following we want to derive a prediction for the direct regular-to-chaotic dynamical tunneling contribution Q_{dyn} of regular modes in optical microcavities. Therefore, we employ the approach using a fictitious integrable system which is described in Chapter 5 for hard-wall billiards. It uses Eq. (5.5) to determine the coupling-matrix elements between purely regular and chaotic modes and Fermi's golden rule, Eq. (5.6), to predict dynamical tunneling rates. The presented approach can be extended to open cavities in the following way: (i) As a fictitious integrable system H_{reg} we choose a cavity such that it resembles the regular dynamics of H . The quantum system has resonance states ψ_{reg} . (ii) As a model for the chaotic resonances ψ_{ch} a random wave model will be used, which in addition fulfills the relevant cavity boundary conditions. (iii) The tunneling rate γ determines the quality factor Q_{dyn} by

$$Q_{\text{dyn}} = \frac{2\text{Re}(k)^2 n_{\Omega}^2}{\gamma} \quad (6.20)$$

for which we used Eqs. (6.17) and (6.18).

We now want to apply this approach to the annular microcavity. To evaluate Eqs. (5.5) and (5.6) we have to find an appropriate regular system H_{reg} . For the annular cavity a natural choice is given by the circular cavity as it reproduces the regular whispering-gallery motion of the annular cavity correctly and extends it into the chaotic region of phase space, see Fig. 6.2(c) and (d). The whispering-gallery modes are labelled by the two quantum numbers m and n . Rewriting the mode equation (3.256) as an eigenvalue equation $\hat{H}\psi = k^2\psi$ the Hamiltonian of the annular cavity can be introduced as

$$\hat{H} = -\nabla^2 + [1 - n(x, y)^2]k^2 \quad (6.21)$$

where the refractive index $n(x, y)$ is n_{Ω} inside and 1 outside the cavity as well as in the disk of

radius R_2 . For the regular system \hat{H}_{reg} we choose the circular cavity

$$\hat{H}_{\text{reg}} = -\nabla^2 + [1 - n_{\text{reg}}(x, y)^2]k^2 \quad (6.22)$$

where the refractive index $n_{\text{reg}}(x, y)$ is n_Ω inside and 1 outside the circular cavity. Thus, \hat{H} and \hat{H}_{reg} differ only inside the small disk of radius R_2 with $\hat{H} - \hat{H}_{\text{reg}} = (n_\Omega^2 - 1)k^2$ and the integral in Eq. (5.5) reduces to an integral over the small disk. For the regular states inside the circular cavity we choose, as in the numerical studies, the even eigenmodes

$$\psi_{\text{reg}}^{mn}(r, \varphi) = N_{mn} J_m(n_\Omega k_{mn} r) \cos(m\varphi) \quad (6.23)$$

where k_{mn} are the complex resonant wave numbers, according to Section 6.1, and ψ_{reg}^{mn} is normalized to one with the numerically determined normalization constant N_{mn} .

To model the chaotic modes ψ_{ch} within the small disk we employ a random wave description [21], which has been extended to systems with a mixed phase space [212]. While this model accurately describes the random behavior in a medium with constant refractive index, it cannot account for the change of refractive index at the border of the small disk at $\rho = R_2$. We extend a boundary-adapted random wave model [134] to account for this boundary condition. This is essential especially for low $\text{Re}(k)$ as then all chaotic modes decay inside the small disk, which cannot be reproduced by the usual random wave model. Hence, we construct the chaotic states ψ_{ch} as a random superposition of modes of a circular cavity of radius R_2 with refractive index 1 which is surrounded by a medium with refractive index n_Ω . As follows from Eq. (6.9) these modes, at a fixed complex wave number k_{mn} and within the small disk, are

$$\psi_s(\rho, \vartheta) = A_s J_s(k_{mn}\rho) \cos(s\vartheta), \quad \rho \leq R_2. \quad (6.24)$$

The chaotic states ψ_{ch} are then constructed by a random superposition of these modes

$$\psi_{\text{ch}}(\rho, \vartheta) = \frac{1}{\sqrt{A_{\text{ch}}}} \sum_{s=1}^{\infty} c_s \psi_s(\rho, \vartheta), \quad (6.25)$$

see Fig. 6.2(f) for an example. Here the coefficients c_s are Gaussian random variables with mean zero and $\langle c_s c_t \rangle = \delta_{st}$. The random waves, constructed in such a way, fulfill the normalization condition $\langle |\psi_{\text{ch}}|^2 \rangle = 1/A_{\text{ch}}$ required for the annular cavity.

Using the fictitious regular system and the random wave model for the chaotic states we obtain the coupling matrix elements

$$v_{\text{ch}, mn} = \int_0^{R_2} \int_0^\pi \rho \, d\rho \, d\vartheta \, \psi_{\text{ch}}^*(\rho, \vartheta) (n_\Omega^2 - 1) k_{mn}^2 \psi_{\text{reg}}^{mn}(\rho, \vartheta) \quad (6.26)$$

by an integral over the small disk. In contrast to the hard-wall billiards discussed in the last

chapter where integrals along one-dimensional lines appear for the coupling matrix elements, here we integrate over a two-dimensional area. For the tunneling rate this results in

$$\gamma_{mn} = \frac{1}{2} N_{mn}^2 (n_\Omega^2 - 1)^2 |k_{mn}^2|^2 \sum_{s=1}^{\infty} |I_{s,mn}|^2 \quad (6.27)$$

where

$$I_{s,mn} = \int_0^{R_2} \int_0^\pi \rho d\rho d\vartheta \psi_s^*(\rho, \vartheta) J_m(n_\Omega k_{mn} r) \cos(m\varphi) \quad (6.28)$$

with $r = r(\rho, \vartheta)$ geometrically related to $\varphi = \varphi(\rho, \vartheta)$, see Figs. 6.2(a) and (c). With Eq. (6.20) we finally obtain the dynamical tunneling contribution to the quality factor

$$Q_{\text{dyn}}^{mn} = \frac{4n_\Omega^2}{N_{mn}^2 (n_\Omega^2 - 1)^2 |k_{mn}^2|^2 \sum_{s=1}^{\infty} |I_{s,mn}|^2} \quad (6.29)$$

of whispering-gallery modes in the annular microcavity for each quantum number m and n .

Now we compare our theoretical prediction for the quality factor, Eq. (6.19), in the annular microcavity with numerical data [179] using the boundary element method [177]. Fig. 6.3 shows the inverse quality factors at fixed quantum numbers $m = 19$ and $n = 1$ under variation of the distance d between the small and the large disk. The barrier contribution $1/Q_{1d}$, see

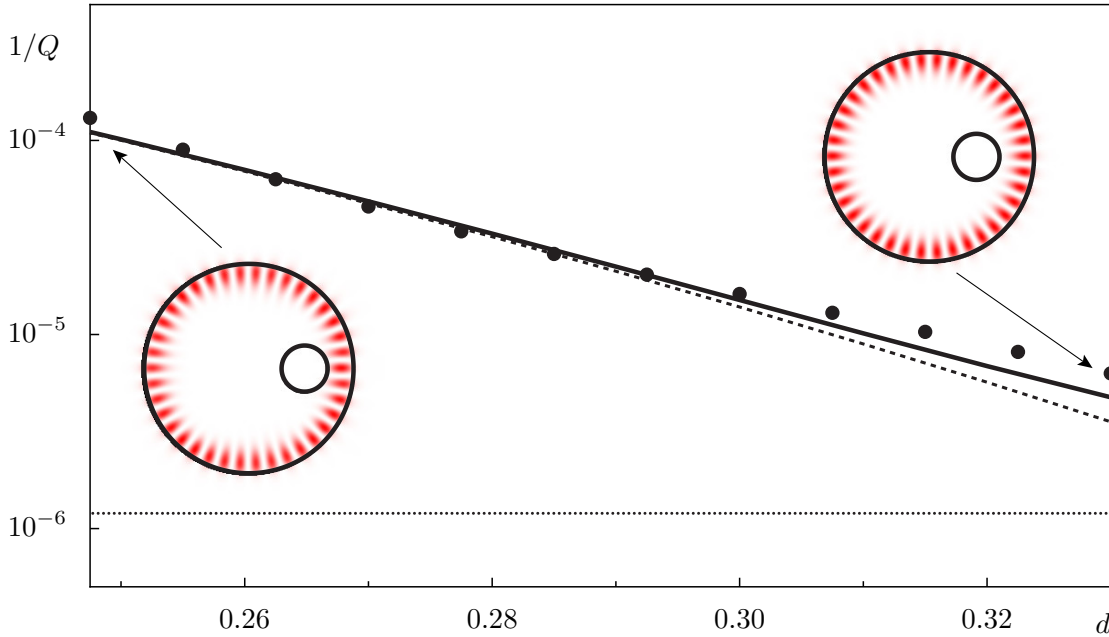


Figure 6.3: Inverse quality factors $1/Q$ for the annular microcavity with refractive index $n_\Omega = 2.0$ and $R_2 = 0.22$. Shown is the theoretical prediction (solid line), which is the sum of the barrier tunneling contribution (dotted line) and the dynamical tunneling contribution (dashed line, Eq. (6.29)), and numerical data (dots) for angular quantum number $m = 19$ and radial quantum number $n = 1$ vs the hole position d . The insets show the resonant state at $d = 0.2475$ and $d = 0.33$.

Section 6.1, is independent of the distance d . It is dominated by the dynamical tunneling contribution $1/Q_{\text{dyn}}$, Eq. (6.29), which decreases exponentially with d , as expected from the increasing regular phase-space region. We find excellent agreement of the prediction and the numerical data.

As a further test we consider the quality factors for fixed radial quantum number $n = 1$ and increasing angular quantum number $m = 7, \dots, 21$, comparing the theoretical prediction with numerical results, see Fig. 6.4. For small $\text{Re}(k)$ we find that barrier tunneling from the whispering-gallery modes to the continuum is relevant while for large $\text{Re}(k)$ the dynamical-tunneling contribution dominates. Again our prediction shows excellent agreement with the numerical data. Moreover, we point out that our theory allows to determine quality factors for large $\text{Re}(k)$, where numerical methods fail. The boundary element method cannot compute the quality factors of quantum numbers $n = 1$ and $m > 21$ reliably as the exponentially increasing quality factor requires an extremely fine spatial discretization.

In the derivation of the dynamical tunneling contribution $1/Q_{\text{dyn}}$ to the quality factor we assumed that there are no further structures in the chaotic part of phase space such as small regular islands or partial barriers. If this assumption is not fulfilled the tunneling rates γ_{mn} as

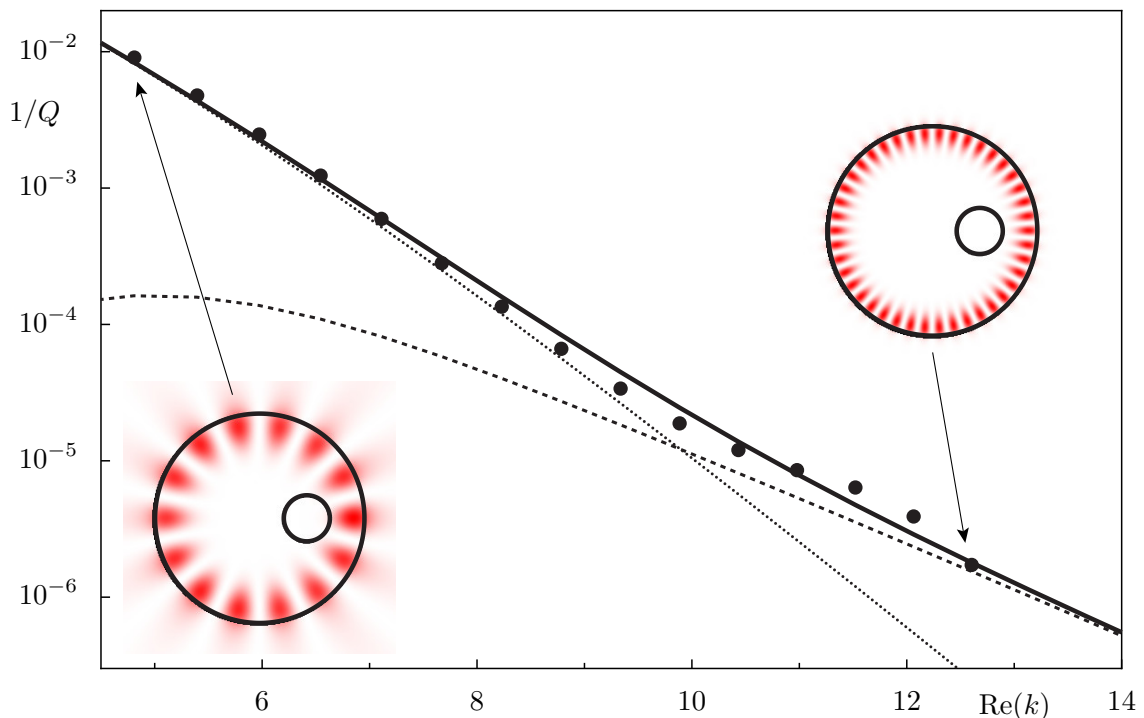


Figure 6.4: Inverse quality factors $1/Q$ for the annular microcavity with $n_{\Omega} = 2.0$. Shown is the theoretical prediction (solid line) which is the sum of the barrier tunneling contribution (dotted line) and the dynamical tunneling contribution (dashed line, Eq. (6.29)), and numerical data (dots) for $m = 7, \dots, 21$ and $n = 1$ at $d = 0.33$ and $R_2 = 0.22$. The insets exemplarily show the resonant states of angular quantum number $m = 7$ (left) and $m = 21$ (right).

well as the quality factors are modified. This can be demonstrated when choosing $d = 0.33$, $R_2 = 0.22$, and increasing n_Ω from 2.0 to 2.3. At $n_\Omega = 2.0$ no additional structures are visible in the chaotic part of phase space above the critical line (see Fig. 6.2(b)). At $n_\Omega = 2.3$ the critical line p_c is shifted to smaller values and a period-three island chain is now located above p_c , see the inset in Fig. 6.5. These structures presumably cause the oscillations of the numerically determined quality factors around the theoretical prediction which are visible in Fig. 6.5.

To support the conjecture, that the island chain is responsible for the oscillations, Figs. 6.6(a) and (b) display the incident Husimi functions [213], representing the wave analogue of the Poincaré section (see also [136]), of the mode $m = 14$ (near the minimum of the oscillation) and $m = 18$ (near the maximum). In the former case the island chain is clearly a barrier for the mode. The mode cannot penetrate the leaky region so easily which increases its quality factor. In the latter case the island chain seems to have no strong influence on the mode. While the average behavior of the quality factors is still well predicted by Eq. (6.29), these oscillations cannot be explained by our theory. The interesting task to predict tunneling rates through more complicated phase space structures in the chaotic sea remains as a future challenge.

In summary, we have presented a theory for the intrinsic optical losses of annular microcavities. Our theory gives an analytical expression for the quality factor which is in very good agreement with the full numerical simulations of Maxwell's equations.

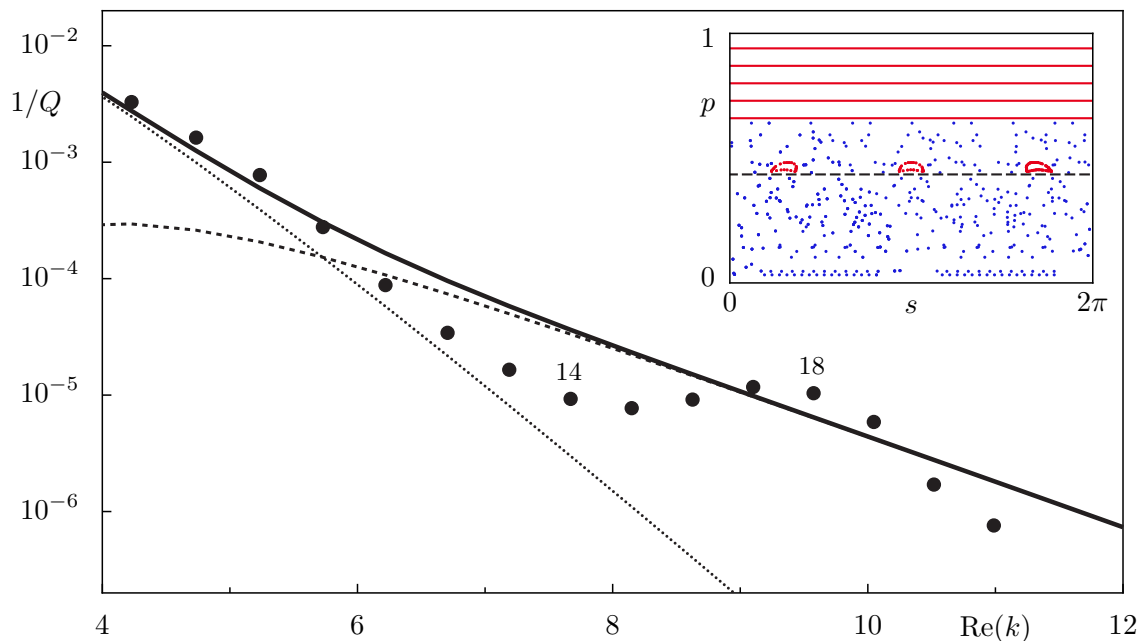


Figure 6.5: Inverse quality factor $1/Q$ for the annular microcavity. Shown is the theoretical prediction (solid line) which is the sum of the barrier tunneling contribution (dotted line) and the dynamical tunneling contribution (dashed line), and numerical data (dots) for $m = 7, \dots, 21$, $n = 1$ at $d = 0.33$, $R_2 = 0.22$, and $n_\Omega = 2.3$. The inset shows part of the Poincaré section of the classical phase space, where the critical line $p = p_c$ is marked (dashed line).

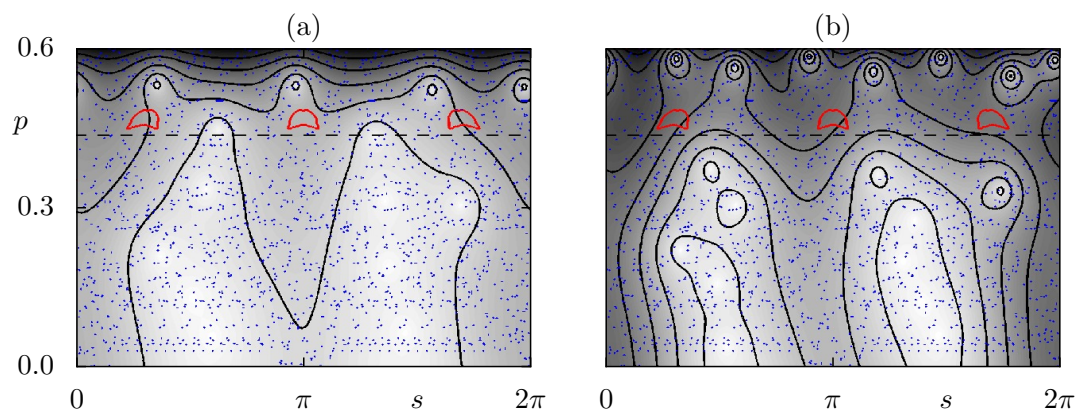


Figure 6.6: Husimi functions [179] (gray scale and contour lines) of the modes with angular quantum number (a) $m = 14$ and (b) $m = 18$ superimposed onto part of the Poincaré section of the classical phase space, where the critical line $p = p_c$ is marked (dashed line). The radial quantum number is $n = 1$ and the refractive index is $n_\Omega = 2.3$ as in Fig. 6.5.

7 Summary and outlook

In this thesis we have studied the dynamical tunneling process in systems with a mixed phase space. Depending on the value of the effective Planck constant h_{eff} different mechanisms dominate this tunneling process: When the effective Planck constant is smaller but comparable to the area of the regular region, $h_{\text{eff}} \lesssim A$, the *direct regular-to-chaotic tunneling* mechanism [42,43,46] is relevant. In the semiclassical regime, $h_{\text{eff}} \ll A$, nonlinear resonances lead to enhanced tunneling rates. They form typical peak and plateau structures and are qualitatively described by the theory of *resonance-assisted tunneling* [53–55]. Both of the regimes were studied in this thesis. We derived a quantitative theory which predicts dynamical tunneling rates from the quantum to the semiclassical regime. It includes the intermediate regime in which resonances start to become important. This is of particular relevance for the experimental search of signatures of resonance-assisted tunneling. These results are expected to have an impact on various fields in physics in which dynamical tunneling plays a role, such as atomic and molecular physics, optical microcavities, cold atoms in engineered optical potentials, and electronic mesoscopic physics.

In the quantum regime, $h_{\text{eff}} \lesssim A$, fine-scale structures of the phase space such as nonlinear resonances are not resolved by quantum mechanics and the regular-to-chaotic tunneling mechanism is relevant. To describe this tunneling process we introduced the fictitious integrable system H_{reg} . It allows to decompose the mixed system H into one part which accounts for the uncoupled regular and chaotic dynamics and another part which accounts for their coupling. This leads to a formula

$$\gamma_m^d = \|\hat{P}_{\text{ch}}(\hat{H} - \hat{H}_{\text{reg}})|\psi_{\text{reg}}^m\rangle\|^2 \quad (7.1)$$

which predicts the direct tunneling rate γ_m^d of the m th regular state $|\psi_{\text{reg}}^m\rangle$ to the chaotic sea [48,49]. For quantum maps we replace \hat{H} and \hat{H}_{reg} by \hat{U} and \hat{U}_{reg} . In Eq. (7.1) the fictitious integrable system \hat{H}_{reg} enters. It has to be chosen such that its dynamics resembles the regular dynamics of the original mixed system \hat{H} as closely as possible and extends it into the chaotic sea. The determination of this system is the most delicate problem in the application of this approach. While for quantum maps the Lie transformation, normal-form analysis, or methods based on the frequency map analysis can be used, a general procedure which computes \hat{H}_{reg} for billiards or optical microcavities is still missing. The tunneling rates predicted by Eq. (7.1) are determined mainly by properties of the regular component while chaotic properties only enter

via the projector \hat{P}_{ch} onto the chaotic sea. Hence, it assumes a structureless chaotic sea and does not include effects caused by partial barriers inside the chaotic region.

In Chapter 4 dynamical tunneling rates have been determined numerically and compared to the results of Eq. (7.1) for different examples of quantum maps. We found excellent agreement over several orders of magnitude in γ . For a harmonic oscillator-like island embedded in a chaotic sea it was even possible to derive a semiclassical expression for the tunneling rates which depends on the area of the regular region and the effective Planck constant only [48, 49, 94]. Furthermore, in Chapter 5 we applied Eq. (7.1) to billiard systems where we used random wave models to describe the chaotic states. For the mushroom billiard our prediction is in excellent agreement with numerical and experimental data [50]. However, deviations occur for the annular billiard which can be explained by the appearance of so-called beach states which effectively enlarge the size of the regular island. For the cosine billiard we presented a first numerical method for the determination of \hat{H}_{reg} and studied the coupling of bouncing-ball modes to the chaotic sea. Finally, we confirmed our prediction of direct dynamical tunneling rates using the annular microcavity in Chapter 6 [51].

In the semiclassical regime, $h_{\text{eff}} \ll A$, fine-scale structures of phase space can be resolved by quantum mechanics. Especially nonlinear resonances have an important impact on the dynamical tunneling process which is qualitatively described by the theory of resonance-assisted tunneling [53–55]. Hence, Eq. (7.1), which considers only the direct tunneling mechanism, is not applicable to generic systems with a mixed phase space in the semiclassical regime. In Section 4.2 we derived a unified framework that combines the direct regular-to-chaotic and the resonance-assisted tunneling mechanism and obtained

$$\gamma_m = \gamma_m^d + |A_{m,r}^{(r:s)}|^2 \gamma_{m+r}^d + |A_{m,r}^{(r:s)} A_{m,2r}^{(r:s)}|^2 \gamma_{m+2r}^d + \dots \quad (7.2)$$

Beyond the direct tunneling contribution γ_m^d there are additional contributions: They consist of resonance-assisted tunneling steps within the regular island and, in contrast to previous studies [43, 55], a final direct tunneling step to the chaotic sea. Using two important improvements for the amplitudes $A_{m,kr}^{(r:s)}$ excellent quantitative agreement with numerically determined tunneling rates is found on the level of individual resonance peaks. This also highlights the validity of the underlying direct and resonance-assisted mechanisms [61]. We therefore expect that these mechanisms leave characteristic traces in semiclassical approaches based on complex classical trajectories [38, 39], and allow for predicting dynamical tunneling rates also in more complicated, multidimensional quantum systems. A first numerical evidence of resonance-assisted tunneling in billiard systems was presented for the cosine billiard in Section 5.2.5.

In the future our theory allows for further applications: It can be applied to study the level-spacing statistics of systems with a mixed phase space. Deviations from Berry-Robnik statistics [214] can be quantitatively explained [215] using our prediction of dynamical tunneling rates. Furthermore, we want to understand the influence of partial barriers in the chaotic part

of phase space on the tunneling process. In the quantum regime these partial barriers act like complete barriers, while semiclassically they do not limit quantum dynamics. This transition and the behavior in the quantum regime, where tunneling through the barrier occurs, is of particular interest.

Another question is how to determine the fictitious integrable system \hat{H}_{reg} for generic billiards, which resembles the classically regular motion of \hat{H} and extends it into the chaotic sea. In general it will not be in the class of billiard systems. This will allow for the prediction of tunneling rates and is essential for the extension of the theory of resonance-assisted tunneling to two-dimensional billiard systems. A further open task is to apply our approach using a fictitious integrable system to determine tunneling rates in higher dimensional systems. Here it is of particular interest how the classical Arnold diffusion competes with quantum tunneling.

Finally, it is aspired to obtain a complete semiclassical treatment of Eqs. (7.1) and (7.2) also for systems with a generic regular island. Ultimately, the theory should predict tunneling rates and their dependence on the effective Planck constant \hbar_{eff} directly from classical properties of the regular island, such as its size, shape, or winding number and properties of the chaotic sea, such as unstable fixed points, partial barriers, and transport properties. The most promising approach seems to be the complex-path formalism which has been successfully applied to study the tunneling tails of a time-evolved wave packet in mixed regular-chaotic systems [38–40]. Using the stationary-phase approximation a semiclassical expression for \hat{U} can be obtained similarly to the Van Vleck-Gutzwiller propagator. In addition to the real paths appearing in this propagator, complex paths are used to describe the decay into the classically forbidden domain. Using these semiclassical expressions in Eq. (7.1) might give further insight into the dynamical tunneling process.

These questions show, that the topic of dynamical tunneling offers many interesting challenges for the future.

A Dimensionless variables

Throughout this thesis we perform calculations in dimensionless variables which are given as multiples of typical quantities of the considered system. In this appendix we will introduce such dimensionless variables for a one-dimensional time-independent system with a potential energy $V(q)$. In position representation the Schrödinger equation is given by

$$\left(-\frac{\hbar^2}{2m} \frac{d^2}{dq^2} + V(q)\right) \psi(q) = E\psi(q). \quad (\text{A.1})$$

We use q_0 as the typical length and V_0 as the typical energy such that we obtain for the new dimensionless length and energy variables: $\tilde{q} := q/q_0$, $\tilde{E} := E/V_0$, and $\tilde{V}(\tilde{q}) := V(\tilde{q})/V_0$. The precise choice of q_0 and V_0 depends on the considered system. With these new dimensionless quantities the Schrödinger equation reads

$$\left(-\frac{\hbar^2}{2mV_0q_0^2} \frac{d^2}{d\tilde{q}^2} + \tilde{V}(\tilde{q})\right) \tilde{\psi}(\tilde{q}) = \tilde{E}\tilde{\psi}(\tilde{q}). \quad (\text{A.2})$$

By introducing the effective Planck constant $\hbar_{\text{eff}} := \hbar/\sqrt{mV_0q_0^2}$ we obtain a completely dimensionless Schrödinger equation

$$\left(-\frac{\hbar_{\text{eff}}^2}{2} \frac{d^2}{d\tilde{q}^2} + \tilde{V}(\tilde{q})\right) \tilde{\psi}(\tilde{q}) = \tilde{E}\tilde{\psi}(\tilde{q}). \quad (\text{A.3})$$

Let us consider the harmonic oscillator potential $V(q) = m\omega^2q^2/2$ as an example. We introduce the typical time t_0 as $t_0 := \sqrt{q_0^2m/V_0}$ such that $\tilde{\omega} := \omega t_0$ and $\tilde{V}(\tilde{q}) = \tilde{\omega}^2\tilde{q}^2/2$ is the potential energy. For the dimensionless eigenenergies of the harmonic oscillator we find

$$\tilde{E}_n = \hbar_{\text{eff}}\tilde{\omega} \left(n + \frac{1}{2}\right). \quad (\text{A.4})$$

The time-dependent Schrödinger equation using $\tilde{t} = t/t_0$ reads

$$i\frac{\hbar}{V_0} \sqrt{\frac{V_0}{q_0^2m}} \frac{\partial}{\partial \tilde{t}} \tilde{\psi}(\tilde{q}, \tilde{t}) = i\hbar_{\text{eff}} \frac{\partial}{\partial \tilde{t}} \tilde{\psi}(\tilde{q}, \tilde{t}) = \hat{H} \tilde{\psi}(\tilde{q}, \tilde{t}). \quad (\text{A.5})$$

For normalized wave functions it holds

$$1 = \int_{-\infty}^{\infty} dq |\psi(q, t)|^2 = \int_{-\infty}^{\infty} d\tilde{q} \left| \tilde{\psi}(\tilde{q}, \tilde{t}) \right|^2 \quad \Rightarrow \quad \tilde{\psi}(\tilde{q}, \tilde{t}) := \sqrt{q_0} \psi(q, t). \quad (\text{A.6})$$

The typical momentum $p_0 := \sqrt{mV_0}$ is expressed using the previous definitions. With its help we obtain the classical Hamilton function in dimensionless form

$$\tilde{H}(\tilde{q}, \tilde{p}) = \frac{\tilde{p}^2}{2} + \tilde{V}(\tilde{q}). \quad (\text{A.7})$$

Throughout the thesis we will use only the new variables and we neglect the tilde in their notation. The effective Planck constant $\hbar_{\text{eff}} = 2\pi\hbar_{\text{eff}}$ goes to zero in the semiclassical limit as the typical lengths q_0 and energy scales V_0 increase. For billiard systems and optical microcavities we use a different set of dimensionless variables. For such systems we set $\hbar = 1$, $2m = 1$, and choose a typical length q_0 such that the semiclassical limit is reached for $E \rightarrow \infty$.

B Classical kicked systems

B.1 Smoothing of designed discontinuous mappings

In Section 3.1.2 we explained how classical kicked systems can be designed such that their phase space shows a simpler structure than the phase space of commonly used systems such as the standard map. By discontinuously glueing together piecewise defined functions the derivatives of the kinetic energy $t'(p)$ and potential energy $v'(q)$ were obtained. With this designing procedure we can control the size of the regular island, its shape, the existence of nonlinear resonances, as well as the existence of partial barriers in the chaotic sea, and the size of the hierarchical region. However, for quantum mechanics continuous systems are preferred. A continuous mapping is obtained by the convolution of the discontinuous functions $t'(p)$ and $v'(q)$ with a Gaussian of width ε

$$T'(p) = \int_{p_1}^{p_2} G_\varepsilon(p-x)t'(x) dx, \quad V'(q) = \int_{q_1}^{q_2} G_\varepsilon(q-x)v'(x) dx \quad (\text{B.1})$$

where the Gaussian is given by

$$G_\varepsilon(x) = \frac{1}{\sqrt{2\pi\varepsilon^2}} e^{-\frac{x^2}{2\varepsilon^2}} \quad (\text{B.2})$$

and q_1, q_2 as well as p_1, p_2 are the borders of phase space in position and momentum direction.

The functions $t'(p)$ and $v'(q)$ are piecewise defined and given as a power series

$$f(x) = \sum_{n=0}^{\infty} a_n f_n(x) = \sum_{n=0}^{\infty} a_n x^n \quad (\text{B.3})$$

where the function $f(x)$ represents $t'(p)$ or $v'(q)$. As the convolution is a linear operation we can individually apply it to each term $f_n(x)$ in the power series and then sum up the results. This will be demonstrated for the first four terms which are required for the maps \mathcal{F}_1 and \mathcal{F}_2 . With the abbreviations

$$\text{erf}_1 := \text{erf}\left(\frac{y-y_1}{\sqrt{2\varepsilon}}\right), \quad \text{erf}_2 := \text{erf}\left(\frac{y-y_2}{\sqrt{2\varepsilon}}\right), \quad (\text{B.4})$$

$$\text{exp}_1 := \sqrt{\frac{2}{\pi}} \exp\left(-\frac{(y-y_1)^2}{2\varepsilon^2}\right), \quad \text{exp}_2 := \sqrt{\frac{2}{\pi}} \exp\left(-\frac{(y-y_2)^2}{2\varepsilon^2}\right), \quad (\text{B.5})$$

where erf denotes the error function, we find for the smoothed functions

$$f_{G,0}(y) := \int_{y_1}^{y_2} G_\varepsilon(y-x)x^0 dx = \frac{1}{2} [\text{erf}_1 - \text{erf}_2] \quad (\text{B.6})$$

and similarly

$$f_{G,1}(y) = \frac{1}{2} [\varepsilon \exp_1 - \varepsilon \exp_2 + y(\text{erf}_1 - \text{erf}_2)], \quad (\text{B.7})$$

$$f_{G,2}(y) = \frac{1}{2} [\varepsilon(y_1 + y) \exp_1 - \varepsilon(y_2 + y) \exp_2 + (y^2 + \varepsilon^2)(\text{erf}_1 - \text{erf}_2)], \quad (\text{B.8})$$

$$f_{G,3}(y) = \frac{1}{2} [(yy_1 + y_1^2 + 2\varepsilon^2 + y^2)\varepsilon \exp_1 - (yy_2 + y_2^2 + 2\varepsilon^2 + y^2)\varepsilon \exp_2 + y(y^2 + 3\varepsilon^2)(\text{erf}_1 - \text{erf}_2)]. \quad (\text{B.9})$$

Here y_1 and y_2 enclose the region on which each piecewise function is defined. The continuous version of Eq. (B.3) now reads

$$f_G(y) = \sum_{n=0}^{\infty} a_n f_{G,n}(y). \quad (\text{B.10})$$

It can be differentiated to arbitrary order in y .

For quantum mechanics we need to find the smoothed versions of the kinetic energy $t(p)$ and the potential $v(q)$. As they are also given by a power series they are found by integration of the functions $f_{G,n}(y)$ with respect to y

$$F_{G,0}(y) := \int f_{G,0}(y) dy = \frac{1}{2} [\varepsilon(\exp_1 - \exp_2) + (y - y_1)\text{erf}_1 - (y - y_2)\text{erf}_2] \quad (\text{B.11})$$

and similarly

$$F_{G,1}(y) = \frac{1}{4} [\varepsilon(y + y_1) \exp_1 - \varepsilon(y + y_2) \exp_2 + (y^2 + \varepsilon^2 - y_1^2)\text{erf}_1 - (y^2 + \varepsilon^2 - y_2^2)\text{erf}_2], \quad (\text{B.12})$$

$$F_{G,2}(y) = \frac{1}{6} [\varepsilon(y^2 + y_1^2 + yy_1 + 2\varepsilon^2) \exp_1 - \varepsilon(y^2 + y_2^2 + yy_2 + 2\varepsilon^2) \exp_2 + (y^3 + \varepsilon^2 - y_1^3 + 3\varepsilon^2 y)\text{erf}_1 - (y^3 + \varepsilon^2 - y_2^3 + 3\varepsilon^2 y)\text{erf}_2], \quad (\text{B.13})$$

$$F_{G,3}(y) = \frac{1}{8} [\varepsilon((3y_1 + 5y)\varepsilon^2 + (y_1 + y)(y^2 + y_1^2)) \exp_1 - \varepsilon((3y_2 + 5y)\varepsilon^2 + (y_2 + y)(y^2 + y_2^2)) \exp_2 + (3\varepsilon^4 + 6\varepsilon^2 y^2 - y_1^4 + y^4)\text{erf}_1 - (3\varepsilon^4 + 6\varepsilon^2 y^2 - y_2^4 + y^4)\text{erf}_2]. \quad (\text{B.14})$$

For the evaluation of the linearized dynamics the functions $t''(p)$ and $v''(q)$ have to be

smoothed as well. They result from the differentiation of $f_{G,n}(y)$ with respect to y

$$df_{G,0}(y) := \frac{df_{G,0}(y)}{dy} = \frac{1}{2\varepsilon} [\exp_1 - \exp_2] \quad (\text{B.15})$$

and similarly

$$df_{G,1}(y) = \frac{1}{2\varepsilon} [y_1 \exp_1 - y_2 \exp_2 + \varepsilon \text{erf}_1 - \varepsilon \text{erf}_2], \quad (\text{B.16})$$

$$df_{G,2}(y) = \frac{1}{2\varepsilon} [(y_1^2 + 2\varepsilon^2) \exp_1 - (y_2^2 + 2\varepsilon^2) \exp_2 + (2y\varepsilon)(\text{erf}_1 - \text{erf}_2)], \quad (\text{B.17})$$

$$df_{G,3}(y) = \frac{1}{2\varepsilon} [(3(y_1 + y)\varepsilon^2 + y_1^3) \exp_1 - (3(y_2 + y)\varepsilon^2 + y_2^3) \exp_2 + 3\varepsilon(y^2 + \varepsilon^2)(\text{erf}_1 - \text{erf}_2)]. \quad (\text{B.18})$$

Application to example system \mathcal{F}_1

For demonstration we want to show how the mapping \mathcal{F}_1 after the convolution with a Gaussian is obtained and determine the potential and kinetic energy. The discontinuous functions $t'(p)$ and $v'(q)$ are given by

$$t'(p) = -2(p - k) - \frac{1}{2} \quad \text{for } p \in \left[-\frac{1}{2} + k, \frac{1}{2} + k\right), \quad (\text{B.19})$$

$$v'(q) = \begin{cases} -r_1 q + Rq^2 + Zq^3 & , \quad q \in \left[-\frac{1}{2}, \frac{1}{2}\right) \\ r_2(q - k) & , \quad q \in \left[-\frac{1}{2} + k, \frac{1}{2} + k\right) , \quad k \neq 0 \end{cases} \quad (\text{B.20})$$

where k labels the phase-space unit cells in q and p -direction. By equating coefficients we find for the kinetic term $t'(p)$: $a_0 = -1/2$, $a_1 = -2$, $a_2 = a_3 = 0$, $p_1 = -1/2$, and $p_2 = 1/2$. Using these relations the smoothed function $T'(p)$ is found to be

$$T'(p) = \sum_k \left[-\frac{1}{2} f_{G,0}(p - k) - 2f_{G,1}(p - k) \right]. \quad (\text{B.21})$$

For the kinetic energy one obtains

$$T(p) = \sum_k \left[-\frac{1}{2} F_{G,0}(p - k) - 2F_{G,1}(p - k) \right] + \text{const.} \quad (\text{B.22})$$

and for its second derivative we find

$$T''(p) = \sum_k \left[-\frac{1}{2} df_{G,0}(p - k) - 2df_{G,1}(p - k) \right]. \quad (\text{B.23})$$

By equating coefficients we obtain for the potential term $v'(q)$ in the central cell $k = 0$: $a_0 = 0$, $a_1 = -r_1$, $a_2 = R$, $a_3 = Z$, $q_1 = -1/2$, and $q_2 = 1/2$. For the other cells the coefficients a_n are:

$a_0 = a_2 = a_3 = 0$ and $a_1 = r_2$. Using these relations the smoothed function $V'(q)$ is found

$$V'(q) = -r_1 f_{G,1}(q) + R f_{G,2}(q) + Z f_{G,3}(q) + \sum_{k \neq 0} [r_2 f_{G,1}(q - k)]. \quad (\text{B.24})$$

For the potential energy we obtain

$$V(q) = -r_1 F_{G,1}(q) + R F_{G,2}(q) + Z F_{G,3}(q) + \sum_{k \neq 0} [r_2 F_{G,1}(q - k)] + \text{const.} \quad (\text{B.25})$$

and for its second derivative we find

$$V''(q) = -r_1 df_{G,1}(q) + R df_{G,2}(q) + Z df_{G,3}(q) + \sum_{k \neq 0} [r_2 df_{G,1}(q - k)]. \quad (\text{B.26})$$

In this form the kicked system \mathcal{F}_1 is evaluated classically as well as quantum mechanically in this thesis. By choosing small values of ε the dynamics of the discontinuous system is mainly reproduced, see Section 3.1.2 for further discussions. In the same way as presented here, the mapping \mathcal{F}_2 introduced in Section 3.1.2 is smoothed to obtain its continuous version.

B.2 An example of the Lie transformation

We want to present how the first two orders of the Lie transformation are calculated for a one-dimensional kicked system $H(q, p, t)$ as it is the method most commonly used throughout this thesis to determine the fictitious integrable system H_{reg} . A similar example is presented in Ref. [54].

First we eliminate the explicit time-dependence of the kicked system by introducing new variables $\theta := 2\pi t/\varepsilon$ and $I := -\varepsilon H(q, p, t)/(2\pi)$. With $H_0(I) := I$ and $H_1(q, p, \theta) := H(q, p, \theta)/2\pi$ a new time-independent two-dimensional Hamilton function is defined as

$$H(q, p, \theta, I) := H_0(I) + \varepsilon H_1(q, p, \theta). \quad (\text{B.27})$$

Hence, time-independent perturbation theory can be applied to this two-dimensional system. Now we want to find the generating function w which canonically transforms the Hamilton function H to the new phase space variables \bar{q} , \bar{p} , $\bar{\theta}$, and \bar{I} . The power series expansion of Eq. (B.27) is used in the recursion relation (3.60). Through the trivial dependence of $H(q, p, \theta, I)$ on the action-angle variables (I, θ) many terms in the Deprit perturbation series, Eq. (3.60), vanish. It remains

$$2\pi \frac{\partial w_n}{\partial \theta} = n \bar{H}_{n-1} - \sum_{m=1}^{n-1} L_{n-m} \bar{H}_m - T_{n-1}^{-1} H. \quad (\text{B.28})$$

This expression is integrated with respect to θ

$$w_n(q, p, \theta) = -\frac{1}{2\pi} \int_0^\theta \left(\sum_{m=1}^{n-1} L_{n-m} \bar{H}_m + T_{n-1}^{-1} H \right) d\theta' + \frac{n}{2\pi} \int_0^\theta \bar{H}_{n-1} d\theta'. \quad (\text{B.29})$$

The $(n-1)$ th coefficient of the new Hamilton function \bar{H} is determined by an average over θ

$$\bar{H}_{n-1}(q, p) = \frac{1}{n} \left\langle \sum_{m=1}^{n-1} L_{n-m} \bar{H}_{m-1} + T_{n-1}^{-1} H \right\rangle (q, p). \quad (\text{B.30})$$

For the generating function one obtains

$$w_n = -\frac{1}{2\pi} \int_0^\theta \left\{ \sum_{m=1}^{n-1} L_{n-m} \bar{H}_{m-1} + T_{n-1}^{-1} H \right\} d\theta' \quad (\text{B.31})$$

where we used the following abbreviations

$$\langle a \rangle (q, p) := \frac{1}{2\pi} \int_0^{2\pi} a(q, p, \theta) d\theta, \quad (\text{B.32})$$

$$\{a\} (q, p, \theta) := a(q, p, \theta) - \langle a \rangle (q, p). \quad (\text{B.33})$$

The perturbation expansion shall now be determined for a periodically driven system

$$H(q, p, \theta) = H_0(q, p) + K(\theta)V(q). \quad (\text{B.34})$$

We define

$$K_1(\theta) := \frac{1}{2\pi} \int_0^\theta \{K\}(\theta') d\theta', \quad K_2(\theta) := \frac{1}{2\pi} \int_0^\theta \{K_1\}(\theta') d\theta'. \quad (\text{B.35})$$

The zeroth order of the new Hamilton function reads

$$\bar{H}_0(\bar{q}, \bar{p}) = \langle H \rangle (\bar{q}, \bar{p}) = H_0(\bar{q}, \bar{p}) + \langle K \rangle V(\bar{q}). \quad (\text{B.36})$$

In first order we find for the generating function

$$w_1(q, p, \theta) = -\frac{1}{2\pi} \int_0^\theta \{H\}(q, p, \theta') d\theta' = -K_1(\theta)V(q) \quad (\text{B.37})$$

with $T_1^{-1} = L_1$ and for the new Hamilton function

$$\bar{H}_1 = \frac{1}{2} \langle L_1 \bar{H}_0 + T_1^{-1} H \rangle = -\frac{\partial V}{\partial \bar{q}} \frac{\partial H_0}{\partial \bar{p}} \langle K_1 \rangle. \quad (\text{B.38})$$

In second order perturbation theory we obtain

$$w_2(q, p, \theta) = -\frac{1}{2\pi} \int_0^\theta \{L_1 \bar{H}_0 + T_1^{-1} H\} d\theta' = 2 \frac{\partial V}{\partial q} \frac{\partial H_0}{\partial p} K_2(\theta), \quad (\text{B.39})$$

$$L_2 = 2K_2(\theta) \left(\frac{\partial^2 V}{\partial q^2} \frac{\partial H_0}{\partial p} \frac{\partial}{\partial p} + \frac{\partial V}{\partial q} \frac{\partial^2 H_0}{\partial q \partial p} \frac{\partial}{\partial p} - \frac{\partial V}{\partial q} \frac{\partial^2 H_0}{\partial p^2} \frac{\partial}{\partial q} \right), \quad (\text{B.40})$$

$$T_2^{-1} = \frac{1}{2} L_2 + \frac{1}{2} L_1^2 \quad (\text{B.41})$$

and finally for the new Hamilton function

$$\bar{H}_2 = \frac{1}{3} \langle L_2 \bar{H}_0 + L_1 \bar{H}_1 + T_2^{-1} H \rangle \quad (\text{B.42})$$

$$\begin{aligned} &= \frac{1}{3} \left(\langle K_1 \rangle^2 + \frac{1}{2} \langle K_1^2 \rangle - 2 \langle K \rangle \langle K_2 \rangle - \langle K K_2 \rangle \right) \left(\frac{\partial V}{\partial \bar{q}} \right)^2 \frac{\partial^2 H_0}{\partial \bar{p}^2} \\ &+ \langle K_2 \rangle \left(\frac{\partial^2 V}{\partial \bar{q}^2} \left(\frac{\partial H_0}{\partial \bar{p}} \right)^2 + \frac{\partial V}{\partial \bar{q}} \left(\frac{\partial^2 H_0}{\partial \bar{q} \partial \bar{p}} \frac{\partial H_0}{\partial \bar{p}} - \frac{\partial^2 H_0}{\partial \bar{p}^2} \frac{\partial H_0}{\partial \bar{q}} \right) \right). \end{aligned} \quad (\text{B.43})$$

This iterative procedure can be continued and the new Hamilton function is found as a power series expansion in the perturbation parameter ϵ which is here equal to the period of the driving $\epsilon = 1$

$$\bar{H}(\bar{q}, \bar{p}) = H_0(\bar{q}, \bar{p}) + \langle K \rangle V(\bar{q}) + \sum_{n=1}^N \epsilon^n \bar{H}_n(\bar{q}, \bar{p}). \quad (\text{B.44})$$

The result of Eq. (B.44) can now be evaluated up to second order for the specific example of the kicked system \mathcal{F}_1 introduced in Section 3.1.2 with the Hamilton function

$$H(q, p, t) = -\left(p^2 + \frac{p}{2}\right) + \sum_{n \in \mathbb{Z}} \delta(n - t) \left(\frac{q^2}{2} \left[-r_1 + \frac{2Rq}{3} \right] \right) \quad (\text{B.45})$$

and $Z = 0$ for simplicity. The functions H_0 , K , and V can be determined by comparison of Eq. (B.34) with Eq. (B.45) using $\theta = 2\pi t$. We find $K(\theta) = \sum_{n \in \mathbb{Z}} \delta(\theta/2\pi - n)$, $H_0(p) = -p^2 - p/2$, and $V(q) = -r_1 q^2/2 + Rq^3/3$. For the functions $K_1(\theta)$ and $K_2(\theta)$ one obtains

$$K_1(\theta) = 1 - \frac{\theta}{2\pi}, \quad (\text{B.46})$$

$$K_2(\theta) = \frac{\theta}{4\pi} - \frac{\theta^2}{8\pi^2}. \quad (\text{B.47})$$

After calculating the first two orders of the perturbation expansion for the new Hamilton function \bar{H} using the Lie transformation we find

$$\begin{aligned} \bar{H}(\bar{q}, \bar{p}) = & -\bar{p}^2 - \frac{1}{2}\bar{p} - \frac{1}{2}r_1\bar{q}^2 + \frac{1}{3}R\bar{q}^3 \\ & + \frac{\epsilon}{2} \left(-2\bar{q}r_1\bar{p} - \frac{1}{2}\bar{q}r_1 + 2\bar{q}^2R\bar{p} + \frac{1}{2}\bar{q}^2R \right) \\ & + \frac{\epsilon^2}{12} \left(-2r_1^2\bar{q}^2 - 2R^2\bar{q}^4 - \frac{1}{4}r_1 + 4R\bar{q}^3r_1 \right. \\ & \left. - 4r_1\bar{p}^2 - 2r_1\bar{p} + 8R\bar{q}\bar{p}^2 + 4R\bar{q}\bar{p} + \frac{1}{2}R\bar{q} \right). \end{aligned} \quad (\text{B.48})$$

The relation of the new phase-space variables to the old ones is given by the operator T , $(q, p) = T^{-1}(\bar{q}, \bar{p})$. Using the power series expansion of T^{-1} up to second order we find

$$q = \bar{q} + (-r_1\bar{q} + R\bar{q}^2) t(\epsilon - t), \quad (\text{B.49})$$

$$p = \bar{p} - (\epsilon - t) (-r_1\bar{q} + R\bar{q}^2) + \frac{1}{2}(r_1 - 2R\bar{q}) \left(2p - \frac{1}{2} \right) t(\epsilon - t). \quad (\text{B.50})$$

If we consider the kicked system shortly after or before the kick only the times $t \in \mathbb{Z}$ are relevant and $\epsilon = 1$. Hence, the old and the new phase-space variables are equal and Eq. (B.48) can be directly evaluated without any change of coordinates. This behavior remains when going to higher orders of the perturbation expansion and is a great advantage of this method as the computationally extensive change of coordinates is not required.

From Eq. (B.48) it is found that the linearized dynamics of the kicked system in the vicinity of the fixed point (q^*, p^*) in the center of the regular island is not correctly reproduced. However, this linearized dynamics is analytically known and described by the Hamilton function

$$H_{\text{lin}}(q, p) = aq^2 + bqp + cp^2 \quad (\text{B.51})$$

with the parameters

$$a = \frac{\omega}{2}\sigma' \left(\cos^2(\theta) + \frac{\sin^2(\theta)}{\sigma'^2} \right), \quad (\text{B.52})$$

$$b = \omega\sigma' \cos(\theta) \sin(\theta) \left(1 - \frac{1}{\sigma'^2} \right), \quad (\text{B.53})$$

$$c = \frac{\omega}{2}\sigma' \left(\sin^2(\theta) + \frac{\cos^2(\theta)}{\sigma'^2} \right). \quad (\text{B.54})$$

Hence, all terms which contribute to the linearized dynamics can be eliminated from Eq. (B.48). These are the terms which do not contain the parameter R . They can be replaced by Eq. (B.51). The parameters σ' , θ , and $\omega = 2\pi w_r$ result from Eqs. (3.20), (3.19), and (3.21). Note that this

procedure of eliminating terms in the perturbational result is not applicable for any kicked system. It is a uniqueness of the considered system that for $R = 0$ the regular island displays the linearized dynamics only. Nevertheless, it has proven to be useful in order to increase the accuracy of the perturbational result in this case.

B.3 An example of the normal-form analysis

In this appendix we present how the non-resonant normal-form analysis can be applied to a simple symplectic mapping, see also Ref. [90]. The main issue is finding the solution of the following functional equation

$$\mathcal{F} \circ \Phi = \Phi \circ \mathcal{U}, \quad (\text{B.55})$$

where \mathcal{F} is the given symplectic mapping, \mathcal{U} is this mapping in normal form, and Φ transforms the new complex phase-space coordinates (ξ, ξ^*) to the old ones (z, z^*) .

For an explicit application we consider the Hénon map [216] for simplicity. Using the complex variables z and z^* it is given as

$$z' = \mathcal{F}(z, z^*) = e^{i\omega} z + \sum_{n \geq 2} \sum_{k=0}^n f_{k, n-k} z^k z^{*n-k} = e^{i\omega} \left(z - \frac{i}{4} (z + z^*)^2 \right). \quad (\text{B.56})$$

The remaining coefficients of the mapping \mathcal{F} are $f_{2,0} = f_{0,2} = -ie^{i\omega}/4$ and $f_{1,1} = 2f_{2,0}$. For the map in normal form \mathcal{U} we find

$$\xi' = \mathcal{U}(\xi, \xi^*) = e^{i\omega} \xi + \sum_{n \geq 2} \sum_{k=0}^n u_{k, n-k} \xi^k \xi^{*n-k} = e^{i\Omega(\xi, \xi^*)} \xi \quad (\text{B.57})$$

and the transformation Φ from the new to the old phase-space variables is

$$z = \Phi(\xi, \xi^*) = \xi + \sum_{n \geq 2} \sum_{k=0}^n \phi_{k, n-k} \xi^k \xi^{*n-k} = \xi + \sum_{n \geq 2} [\Phi]_n. \quad (\text{B.58})$$

By inserting Eqs. (B.56), (B.57), and (B.58) into the functional equation (B.55) this functional equation can be iteratively solved in arbitrary order to determine the mapping \mathcal{U} in normal form [89]. The first non-trivial order is the second one, as the first order describes the analytically known linearized dynamics around the central fixed point which is given by the rotation $e^{i\omega}$ with the winding number $\omega = 2\pi w_r$. For the second order we first consider the

left-hand side of Eq. (B.55) and find

$$[\mathcal{F} \circ \Phi]_2(\xi, \xi^*) = [e^{i\omega} \Phi(\xi, \xi^*) + [\mathcal{F}]_2(\Phi, \Phi^*)]_2 \quad (\text{B.59})$$

$$= e^{i\omega} [\Phi]_2(\xi, \xi^*) + [\mathcal{F}]_2(\xi, \xi^*) \quad (\text{B.60})$$

$$= e^{i\omega} (\phi_{2,0}\xi^2 + \phi_{1,1}\xi\xi^* + \phi_{0,2}\xi^{*2}) + f_{2,0}\xi^2 + f_{1,1}\xi\xi^* + f_{0,2}\xi^{*2}. \quad (\text{B.61})$$

Similarly, for the right-hand side we obtain

$$[\Phi \circ \mathcal{U}]_2(\xi, \xi^*) = [\mathcal{U}(\xi, \xi^*) + [\Phi]_2(\mathcal{U}, \mathcal{U}^*)]_2 \quad (\text{B.62})$$

$$= u_{2,0}\xi^2 + u_{1,1}\xi\xi^* + u_{0,2}\xi^{*2} + e^{2i\omega}\phi_{2,0}\xi^2 + \phi_{1,1}\xi\xi^* + e^{-2i\omega}\phi_{0,2}\xi^{*2}. \quad (\text{B.63})$$

The coefficients of \mathcal{U} can be determined by expanding the equation $\mathcal{U}(\xi, \xi^*) = e^{i\Omega(\xi\xi^*)}\xi$ up to second order. As Ω does only depend on the products $\xi\xi^*$ many coefficients are zero

$$\mathcal{U}(\xi, \xi^*) = e^{i\Omega(\xi\xi^*)}\xi \quad (\text{B.64})$$

$$= e^{i\omega}\xi + ie^{i\omega}\Omega_2\xi^2\xi^* + O(|\xi|^5). \quad (\text{B.65})$$

We find that $u_{2,0} = u_{1,1} = u_{0,2} = u_{3,0} = u_{1,2} = u_{0,3} = 0$ and $u_{2,1} = ie^{i\omega}\Omega_2$. By equating Eqs. (B.62) and (B.64), using the coefficients $f_{i,j}$ and the following relation

$$(e^{ik\omega} - 1)^{-1} = -\frac{1}{2} - \frac{i}{2} \cot\left(\frac{k\omega}{2}\right) \quad (\text{B.66})$$

the transformation Φ is found in second order

$$\phi_{0,2} = \frac{1}{8} \left(\cot\left(\frac{3\omega}{2}\right) + i \right), \quad (\text{B.67})$$

$$\phi_{1,1} = \frac{1}{4} \left(\cot\left(\frac{\omega}{2}\right) + i \right), \quad (\text{B.68})$$

$$\phi_{2,0} = \frac{1}{8} \left(-\cot\left(\frac{\omega}{2}\right) + i \right). \quad (\text{B.69})$$

The third order of the normal-form analysis leads to a contribution of the mapping \mathcal{U} in normal form. Again we consider the right-hand and left-hand side of Eq. (B.55)

$$[\mathcal{F} \circ \Phi]_3(\xi, \xi^*) = e^{i\omega} [\Phi]_3(\xi, \xi^*) + [[\mathcal{F}]_2(\Phi, \Phi^*)]_3 \quad (\text{B.70})$$

$$= -\frac{i}{2}e^{i\omega} (\xi^3 (\phi_{2,0} + \phi_{0,2}^*) + \xi^2\xi^* (\phi_{1,1} + \phi_{1,1}^* + \phi_{2,0} + \phi_{0,2}^*) + \xi\xi^{*2} (\phi_{0,2} + \phi_{2,0}^* + \phi_{1,1} + \phi_{1,1}^*) + \xi^{*3} (\phi_{0,2} + \phi_{2,0}^*)), \quad (\text{B.71})$$

$$[\Phi \circ \mathcal{U}]_3(\xi, \xi^*) = [\mathcal{U}(\xi, \xi^*) + [\Phi]_2(\mathcal{U}, \mathcal{U}^*) + [\Phi]_3(\mathcal{U}, \mathcal{U}^*)]_3 \quad (\text{B.72})$$

$$= e^{3i\omega}\phi_{3,0}\xi^3 + e^{i\omega}\phi_{2,1}\xi^2\xi^* + e^{-i\omega}\phi_{1,2}\xi\xi^{*2} + e^{-3i\omega}\phi_{0,3}\xi^{*3} + u_{2,1}\xi^2\xi^*. \quad (\text{B.73})$$

With these last two equations the coefficients of the transformation Φ are found in third order as well as the first non-zero coefficient of the mapping in normal form

$$\phi_{0,3} = \frac{i}{16} \frac{1}{e^{-4i\omega} - 1} \left[\cot\left(\frac{\omega}{2}\right) - \cot\left(\frac{3\omega}{2}\right) \right], \quad (\text{B.74})$$

$$\phi_{1,2} = -\frac{i}{16} \frac{1}{e^{-2i\omega} - 1} \left[3 \cot\left(\frac{\omega}{2}\right) + \cot\left(\frac{3\omega}{2}\right) \right], \quad (\text{B.75})$$

$$\phi_{3,0} = \frac{i}{16} \frac{1}{e^{2i\omega} - 1} \left[\cot\left(\frac{\omega}{2}\right) - \cot\left(\frac{3\omega}{2}\right) \right], \quad (\text{B.76})$$

$$\Omega_2 = -ie^{-i\omega} u_{2,1} = -\frac{1}{16} \left[3 \cot\left(\frac{\omega}{2}\right) + \cot\left(\frac{3\omega}{2}\right) \right]. \quad (\text{B.77})$$

In addition we have to find the coefficient $\phi_{2,1}$. It is partially determined by requiring that the mapping \mathcal{F} is symplectic. The symplectic condition reads

$$\frac{\partial\Phi}{\partial\xi} \frac{\partial\Phi^*}{\partial\xi^*} - \frac{\partial\Phi^*}{\partial\xi} \frac{\partial\Phi}{\partial\xi^*} = 1. \quad (\text{B.78})$$

Using the power series of Φ in third order we find

$$\text{Re}(\phi_{2,1}) = |\phi_{0,2}|^2 - |\phi_{2,0}|^2. \quad (\text{B.79})$$

Hence, the imaginary part remains undetermined and can be set equal to zero. As our result we find the mapping \mathcal{U} in normal form in third order

$$\sum_{n \leq 3} [\mathcal{U}]_n = e^{i\omega\xi} - \frac{ie^{i\omega}}{16} \left[3 \cot\left(\frac{\omega}{2}\right) + \cot\left(\frac{3\omega}{2}\right) \right] \xi^2 \xi^* \quad (\text{B.80})$$

as well as the interpolating time-independent Hamilton function following from Eq. (3.78)

$$\bar{H}_{\text{reg}}(\xi, \xi^*) = i\omega\xi\xi^* - \frac{i}{32} \left[3 \cot\left(\frac{\omega}{2}\right) + \cot\left(\frac{3\omega}{2}\right) \right] (\xi\xi^*)^2 + O((\xi\xi^*)^3). \quad (\text{B.81})$$

Using $\xi = \Phi^{-1}(z, z^*)$ in Eq. (B.81) the integrable one-dimensional Hamilton function \bar{H}_{reg} is transformed back to the original phase-space variables (z, z^*) such that it interpolates the dynamics of the original mapping \mathcal{F} . This procedure can be performed to arbitrary order in ξ and can be applied to other mappings. For the mapping introduced in Section 3.1.2 the resulting terms would be far more complicated such that using symbolically calculating programs such as MAPLE is reasonable.

B.4 Calculation of the pendulum parameters $V_{r:s}$, $I_{r:s}$, $M_{r:s}$

The Hamilton function of the pendulum, Eq. (4.60), approximates the dynamics of a mixed system in the vicinity of an $r:s$ resonance chain. It can be easily quantized. Using quantum mechanical perturbation theory the effects of the resonances on dynamical tunneling rates can be predicted within the theory of resonance-assisted tunneling, see Section 4.2. Therefore, it is necessary to obtain the parameters $I_{r:s}$, $M_{r:s}$, and $V_{r:s}$ appearing in the Hamilton function of the pendulum. In Refs. [43, 56] these parameters are determined via Eqs. (4.61), (4.62), and (4.63) from the areas enclosed inside and outside of the separatrix $A_{r:s}^+$ and $A_{r:s}^-$ as well as the trace of the linearized mapping at resonance, see Fig. B.1. Here we want to derive these equations.

We consider the Hamilton function of the pendulum in the corotating frame

$$H(I, \vartheta) = \frac{1}{2M_{r:s}}(I - I_{r:s})^2 + 2V_{r:s} \cos(r\vartheta). \quad (\text{B.82})$$

It describes r regions of bounded motion which are separated from the unbounded motion by a separatrix. On this separatrix the potential $V(\vartheta) = 2V_{r:s} \cos(r\vartheta)$ has maxima. For these maxima we find

$$\frac{dV}{d\vartheta} = -2V_{r:s}r \sin(r\vartheta) = 0, \quad \frac{d^2V}{d\vartheta^2} < 0 \quad (\text{B.83})$$

which leads to $\vartheta = 2k\pi/r$, $k \in \mathbb{Z}$, for the angle variable ϑ . For these values $I = I_{r:s}$ and the energy of the dynamics on the separatrix is given by

$$E_s = 2V_{r:s} \cos(2k\pi) = 2V_{r:s}. \quad (\text{B.84})$$

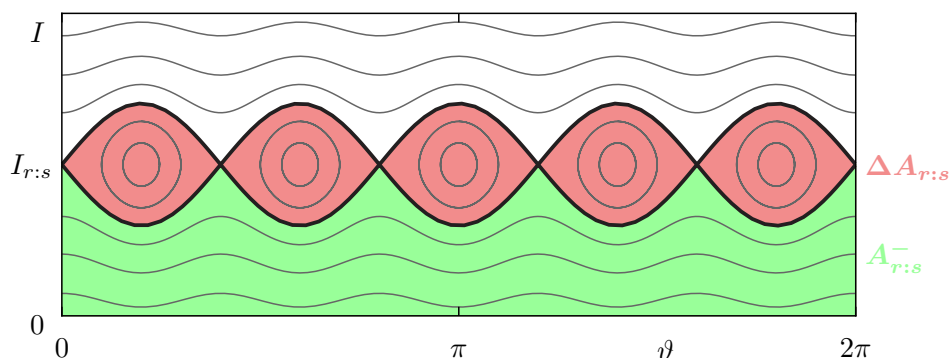


Figure B.1: Phase space of the Hamilton function, Eq. (B.82), of the pendulum. We show the area enclosed by the inner separatrix $A_{r:s}^-$ (green) and the area of the 5:1 resonance chain $\Delta A_{r:s}$ (red) with $A_{r:s}^+ = A_{r:s}^- + \Delta A_{r:s}$. The action of the resonance is denoted by $I_{r:s}$.

Now we insert Eq. (B.84) into Eq. (B.82) and find

$$2V_{r:s} = \frac{1}{2M_{r:s}}(I - I_{r:s})^2 + 2V_{r:s} \cos(r\vartheta), \quad (\text{B.85})$$

such that for the action on the separatrix it follows

$$I_{\pm}(\vartheta) = I_{r:s} \pm 2\sqrt{M_{r:s}V_{r:s}[1 - \cos(r\vartheta)]}. \quad (\text{B.86})$$

The areas $A_{r:s}^+$ and $A_{r:s}^-$ enclosed by the outer and inner separatrix are invariant under canonical transformations. Hence, they are identical in the original phase-space variables and in the action-angle variables (I, ϑ) . They are calculated as

$$A_{r:s}^+ + A_{r:s}^- = \int_0^{2\pi} \left(I_{r:s} + 2\sqrt{M_{r:s}V_{r:s}[1 - \cos(r\vartheta)]} \right) d\vartheta + \quad (\text{B.87})$$

$$\int_0^{2\pi} \left(I_{r:s} - 2\sqrt{M_{r:s}V_{r:s}[1 - \cos(r\vartheta)]} \right) d\vartheta \quad (\text{B.88})$$

$$= 4\pi I_{r:s}, \quad (\text{B.89})$$

$$A_{r:s}^+ - A_{r:s}^- = \int_0^{2\pi} 4\sqrt{M_{r:s}V_{r:s}[1 - \cos(r\vartheta)]} d\vartheta \quad (\text{B.90})$$

$$= 16\sqrt{2M_{r:s}V_{r:s}}. \quad (\text{B.91})$$

Hence, we have derived Eqs. (4.61) and (4.62) presented in Section 4.2.

The derivation of Eq. (4.63) is more involved. First we consider the Hamilton equations of motion for the system of Eq. (B.82) using $I - I_{r:s} \rightarrow I$

$$\dot{\vartheta} = \frac{\partial H}{\partial I} = \frac{I}{M_{r:s}}, \quad (\text{B.92})$$

$$\dot{I} = -\frac{\partial H}{\partial \vartheta} = 2V_{r:s}r \sin(r\vartheta). \quad (\text{B.93})$$

Equations (B.92) and (B.93) can be linearized in the vicinity of the resonance around $\vartheta = (2k + 1)\pi/r$ and combined to an ordinary differential equation of second order

$$\ddot{\vartheta} + \omega_0^2 \vartheta = 0, \quad (\text{B.94})$$

with $\omega_0 = r\sqrt{2V_{r:s}/M_{r:s}}$. This differential equation (B.94) is of harmonic-oscillator type. With the initial conditions $\vartheta(0) = \vartheta_0$ and $I(0) = I_0$ we find for the solution of the differential

equation (B.94)

$$\vartheta(t) = \vartheta_0 \cos(\omega_0 t) + \frac{I_0}{M_{r:s}\omega_0} \sin(\omega_0 t), \quad (\text{B.95})$$

$$I(t) = -M_{r:s}\omega_0\vartheta_0 \sin(\omega_0 t) + I_0 \cos(\omega_0 t). \quad (\text{B.96})$$

The monodromy matrix $\mathcal{M}_{r:s}$ in resonance is determined by the linearized mapping iterated r times. Using

$$\begin{pmatrix} \vartheta(r) \\ I(r) \end{pmatrix} = \mathcal{M}_{r:s} \begin{pmatrix} \vartheta(0) \\ I(0) \end{pmatrix} \quad (\text{B.97})$$

it is obtained

$$\mathcal{M}_{r:s} = \begin{pmatrix} \cos(\omega_0 r) & \frac{1}{M_{r:s}\omega_0} \sin(\omega_0 r) \\ -M_{r:s}\omega_0 \sin(\omega_0 r) & \cos(\omega_0 r) \end{pmatrix}. \quad (\text{B.98})$$

For the trace of the linearized map we find

$$\text{Tr}(\mathcal{M}_{r:s}) = 2 \cos(\omega_0 r) = 2 \cos \left(r^2 \sqrt{\frac{2V_{r:s}}{M_{r:s}}} \right). \quad (\text{B.99})$$

After further manipulations we derive Eq. (4.63) as

$$\sqrt{\frac{2V_{r:s}}{M_{r:s}}} = \frac{1}{r^2} \arccos \left(\frac{\text{Tr}(\mathcal{M}_{r:s})}{2} \right). \quad (\text{B.100})$$

C Quantum maps

C.1 Semiclassical energies of kicked systems

As a kicked system is time-dependent the energy is not a conserved quantity. However, we may construct a regular system H_{reg} which approximates the regular dynamics of the mixed system H , as discussed in Section 3.1.3, where the energy is conserved and fixed for each trajectory. This energy shall be approximated by a procedure using the classical dynamics of the mixed system. The following derivation assumes a map whose regular orbits have just two turning points q_t and $q'_t(q_t)$ which are located at positions where $dp/dq = \pm\infty$. At these points the two real branches of the momentum $p_{\pm}(q, q_t)$ meet which is shown in Fig. C.1.

We want to find the energy $E(q_T)$ associated with a specific classical orbit in dependence of its turning point q_T . For that purpose we consider the enclosed area $A(q_t)$ of the orbits

$$A(q_t) = \int_{q'_t(q_t)}^{q_t} (p_+(q, q_t) - p_-(q, q_t)) dq. \quad (\text{C.1})$$

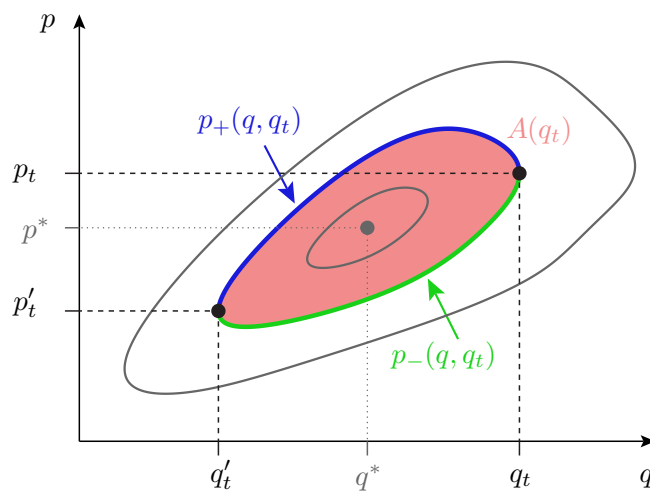


Figure C.1: Phase space of a regular island: We show the two turning points (q'_t, p'_t) and (q_t, p_t) of the torus given by the two momentum branches $p_{\pm}(q, q_t)$ (blue and green line). The area enclosed by these branches is denoted by $A(q_t)$.

It is differentiated with respect to the upper limit q_t of the integration

$$\begin{aligned} \frac{dA(q_t)}{dq_t} &= p_+(q_t, q_t) - p_+(q'_t, q_t) \frac{dq'_t(q_t)}{dq_t} + \int_{q'_t}^{q_t} \frac{\partial p_+(q, q_t)}{\partial q_t} dq \\ &\quad - p_-(q_t, q_t) + p_-(q'_t, q_t) \frac{dq'_t(q_t)}{dq_t} - \int_{q'_t}^{q_t} \frac{\partial p_-(q, q_t)}{\partial q_t} dq. \end{aligned} \quad (\text{C.2})$$

As the two branches of the momentum p_{\pm} are identical at the turning points, it just remains

$$\frac{dA(q_t)}{dq_t} = \int_{q'_t}^{q_t} \left(\frac{\partial p_+(q, q_t)}{\partial q_t} - \frac{\partial p_-(q, q_t)}{\partial q_t} \right) dq. \quad (\text{C.3})$$

The energy E is described by a one-dimensional time-independent Hamilton function $E = H(q, p(q, q_t))$ as discussed in Section 3.1.3. If we consider the derivative of the energy with respect to the turning point q_t , using Hamilton's equations of motion, we obtain

$$\frac{dE}{dq_t} = \frac{\partial H}{\partial p_{\pm}(q, q_t)} \frac{\partial p_{\pm}(q, q_t)}{\partial q_t} \quad (\text{C.4})$$

$$= v_{\pm}(q, q_t) \frac{\partial p_{\pm}(q, q_t)}{\partial q_t} \quad (\text{C.5})$$

where v_{\pm} is the velocity of rotation. Using Eq. (C.5) in Eq. (C.3) we find

$$\frac{dA(q_t)}{dq_t} = \int_{q'_t}^{q_t} \frac{dE}{dq_t} \left(\frac{1}{v_+(q, q_t)} - \frac{1}{v_-(q, q_t)} \right) dq \quad (\text{C.6})$$

$$= \frac{dE}{dq_t} (T_+(q_t) + T_-(q_t)) = \frac{dE}{dq_t} T(q_t). \quad (\text{C.7})$$

By integrating Eq. (C.7) from q^* to q_T where q^* is the position of the stable fixed point in the center of the regular island it follows

$$E(q_T) = E(q^*) + \int_{q^*}^{q_T} \frac{dA(q_t)}{dq_t} \frac{1}{T(q_t)} dq_t \quad (\text{C.8})$$

$$= \int_{q^*}^{q_T} \frac{dA(q_t)}{dq_t} w_r(q_t) dq_t. \quad (\text{C.9})$$

In Eq. (C.9) we assumed that the energy in the central fixed point is zero, $E(q^*) = 0$. The energy E of a regular orbit with turning point q_T can finally be determined with Eq. (C.9). For that purpose one requires the enclosed areas A and the rotation number w_r as a function

of q_t . The semiclassical prediction of the energy thus solely depends on quantities which are directly accessible from the mixed system. Note that the determination of the area enclosed by an orbit is not possible inside a resonance chain. Such orbits should not be taken into account. Eq. (C.9) is used to find a fictitious integrable system H_{reg} as explained in Section 3.1.3.

C.2 Phase splittings and tunneling rates

In Refs. [53, 54, 56] the splitting of regular eigenphases is computed and compared to a theoretical prediction in order to understand the dynamical tunneling process. These splittings are obtained by changing the periodicity conditions of the quantum map and determining the difference $\Delta\varphi = 2\pi\Delta E/h_{\text{eff}}$ of the eigenphases, where ΔE is the corresponding energy splitting. In contrast, we use the tunneling rate γ describing the decay of a wave packet from the regular region to the chaotic sea. We want to show that both quantities, $\Delta\varphi$ and γ , are related.

Using quantum mechanical perturbation theory the energy splitting ΔE is determined by

$$\Delta E \approx \frac{|v|^2}{|E_c - E_r|}, \quad (\text{C.10})$$

resulting from a 3×3 matrix model [24] which describes the coupling of two regular states with energy E_r via a chaotic state of energy E_c with a coupling matrix element v

$$\hat{H} = \begin{pmatrix} E_r & v & 0 \\ v & E_c & v \\ 0 & v & E_r \end{pmatrix} \quad (\text{C.11})$$

if $|v|^2 \ll |E_r - E_c|$ holds. For the phase splitting $\Delta\varphi$ we obtain with Eq. (C.10)

$$\Delta\varphi = \frac{2\pi}{h_{\text{eff}}} \frac{|v|^2}{|E_c - E_r|} \approx \frac{1}{\hbar_{\text{eff}}} |v|^2 \rho(E_c) \approx \frac{\gamma}{2\pi}. \quad (\text{C.12})$$

We find that the splitting $\Delta\varphi$ between the eigenphases of a regular state with different periodicity conditions is related to the tunneling rate γ from the corresponding quasimode to the chaotic sea with a prefactor of $1/(2\pi)$. Here we used that the energy denominator $|E_c - E_r|$ is approximately the inverse of the local density of states $\rho(E_c)$ and Fermi's golden rule for the connection to γ in the last step. This result agrees with numerical calculations where phase splittings $\Delta\varphi$ showed agreement with our numerically determined tunneling rates.

C.3 Tunneling rates and coupling matrix elements

In Chapter 4 we used Eq. (4.8) which connects the tunneling rate of a purely regular state $|\psi_{\text{reg}}^m\rangle$ to the coupling matrix elements $v_{\text{ch},m} = \langle\psi_{\text{ch}}|\hat{U}|\psi_{\text{reg}}^m\rangle$ between this regular and different purely chaotic states. We want to derive this equation.

The considered purely regular state $|\psi_{\text{reg}}^m\rangle$ decays exponentially in time with the tunneling rate γ_m at most up to the Heisenberg time $\tau_H = h_{\text{eff}}/\Delta$ where Δ is the mean level spacing. Therefore

$$|\langle\psi_{\text{reg}}^m|\hat{U}^t|\psi_{\text{reg}}^m\rangle|^2 = e^{-\gamma_m t} \quad (\text{C.13})$$

holds for $t < \tau_H$. For closed systems the norm of $|\psi_{\text{reg}}^m\rangle$ after the application of \hat{U} is unity

$$1 = \langle\psi_{\text{reg}}^m|\hat{U}^\dagger\hat{U}|\psi_{\text{reg}}^m\rangle. \quad (\text{C.14})$$

Now we insert the completeness relation in the basis of the orthogonal purely regular and chaotic states

$$\hat{\mathbb{1}} = \sum_{n=0}^{n_{\text{max}}} |\psi_{\text{reg}}^n\rangle\langle\psi_{\text{reg}}^n| + \sum_{\text{ch}} |\psi_{\text{ch}}\rangle\langle\psi_{\text{ch}}| \quad (\text{C.15})$$

and obtain

$$1 = \sum_{n=0}^{n_{\text{max}}} \langle\psi_{\text{reg}}^m|\hat{U}^\dagger|\psi_{\text{reg}}^n\rangle\langle\psi_{\text{reg}}^n|\hat{U}|\psi_{\text{reg}}^m\rangle + \sum_{\text{ch}} \langle\psi_{\text{reg}}^m|\hat{U}^\dagger|\psi_{\text{ch}}\rangle\langle\psi_{\text{ch}}|\hat{U}|\psi_{\text{reg}}^m\rangle. \quad (\text{C.16})$$

If the direct regular-to-chaotic tunneling process dominates resonance-assisted tunneling is not relevant such that we neglect coupling matrix elements between different regular states, $\langle\psi_{\text{reg}}^n|\hat{U}|\psi_{\text{reg}}^m\rangle \approx 0$, for $m \neq n$. The remaining coupling matrix element of equal quantum number $m = n$ is given by Eq. (C.13) which yields

$$1 = e^{-\gamma_m} + \sum_{\text{ch}} |\langle\psi_{\text{ch}}|\hat{U}|\psi_{\text{reg}}^m\rangle|^2. \quad (\text{C.17})$$

For $\gamma_m \ll 1$ we finally obtain

$$\gamma_m = \sum_{\text{ch}} |\langle\psi_{\text{ch}}|\hat{U}|\psi_{\text{reg}}^m\rangle|^2 \quad (\text{C.18})$$

which is the relation used in Chapter 4, Eq. (4.8). Note that this equation can also be derived from Fermi's golden rule adapted to quantum maps.

D Billiard systems

D.1 Coupling matrix elements of non-orthogonal states

For the applications presented in Section 5.2 random wave descriptions are used as a model for the purely chaotic states $\psi_{\text{ch}}(\mathbf{q})$ which are not orthogonal to the purely regular states $\psi_{\text{reg}}^{mn}(\mathbf{q})$. In such a case, in which

$$\chi := \int_{\Omega} \psi_{\text{ch}}(\mathbf{q}) \psi_{\text{reg}}^{mn}(\mathbf{q}) \, d^2q \neq 0, \quad (\text{D.1})$$

we may use our approach for the direct tunneling rates with a small modification. In order to apply Fermi's golden rule, Eq. (5.4), we introduce orthonormal states $\tilde{\psi}_{\text{reg}}^{mn}(\mathbf{q}) := \psi_{\text{reg}}^{mn}(\mathbf{q})$ and $\tilde{\psi}_{\text{ch}}(\mathbf{q}) := (\psi_{\text{ch}}(\mathbf{q}) - \chi \psi_{\text{reg}}^{mn}(\mathbf{q})) / \sqrt{1 - |\chi|^2}$, leading to

$$\int_{\Omega} \tilde{\psi}_{\text{ch}}(\mathbf{q}) \tilde{\psi}_{\text{reg}}^{mn}(\mathbf{q}) \, d^2q = 0. \quad (\text{D.2})$$

For small $|\chi|^2$ we find for the coupling matrix elements up to first order

$$v_{\text{ch},mn} = \int_{\Omega} \tilde{\psi}_{\text{ch}}(\mathbf{q}) \hat{H} \tilde{\psi}_{\text{reg}}^{mn}(\mathbf{q}) \, d^2q \quad (\text{D.3})$$

$$= \frac{1}{\sqrt{1 - |\chi|^2}} \int_{\Omega} [\psi_{\text{ch}}(\mathbf{q}) - \chi \psi_{\text{reg}}^{mn}(\mathbf{q})] \hat{H} \psi_{\text{reg}}^{mn}(\mathbf{q}) \, d^2q \quad (\text{D.4})$$

$$\approx \int_{\Omega} \psi_{\text{ch}}(\mathbf{q}) \hat{H} \psi_{\text{reg}}^{mn}(\mathbf{q}) \, d^2q - E_{\text{reg}}^{mn} \int_{\Omega} \psi_{\text{ch}}(\mathbf{q}) \psi_{\text{reg}}^{mn}(\mathbf{q}) \, d^2q \quad (\text{D.5})$$

$$= \int_{\Omega} \psi_{\text{ch}}(\mathbf{q}) (\hat{H} - \hat{H}_{\text{reg}}) \psi_{\text{reg}}^{mn}(\mathbf{q}) \, d^2q. \quad (\text{D.6})$$

In Eq. (D.5) we used the approximations $1/\sqrt{1 - |\chi|^2} \approx 1$ and

$$\int_{\Omega} \psi_{\text{reg}}^{mn}(\mathbf{q}) \hat{H} \psi_{\text{reg}}^{mn}(\mathbf{q}) \, d^2q \approx E_{\text{reg}}^{mn}. \quad (\text{D.7})$$

In contrast to Eq. (5.5), $\hat{H} - \hat{H}_{\text{reg}}$ enters in the coupling matrix elements, Eq. (D.6).

D.2 Derivation of A_{ch} for the mushroom billiard

We want to show how the area A_{ch} , which is the area of the billiard times the fraction of the chaotic phase-space volume, is determined exemplarily for the mushroom billiard. The phase space of the mushroom billiard, see Section 5.2.1, is given for a fixed energy by $\{(r, \varphi, \vartheta) : (r, \varphi) \in \Omega, \vartheta \in [0, 2\pi)\}$, in which (r, φ) are polar coordinates in position space and ϑ denotes an angle which determines the direction of momentum. Hence, A_{ch} is given by the chaotic phase-space volume divided by 2π .

All trajectories which enter the stem of the mushroom or cross the line $r = a$ in the cap are chaotic. Additionally the region $r > a$ contains regular and chaotic dynamics. We denote its contribution to A_{ch} by I and obtain for the mushroom billiard

$$A_{\text{ch}} = 2la + \frac{\pi}{2}a^2 + I. \quad (\text{D.8})$$

The probability $P(r)$ of finding a chaotic trajectory in the cap for $r > a$ is dependent on the radial coordinate r only

$$P(r) = \frac{2}{\pi} \arcsin\left(\frac{a}{r}\right), \quad (\text{D.9})$$

as can be seen with the help of Fig. D.1. For each position inside the area $r > a$ the chaotic trajectories can be identified as they cross the line $r = a$. In Fig. D.1 an example is shown where they are located inside the red cone. Hence, we perform an integration over the momentum coordinate ϑ of the phase space yielding $4\vartheta'$ in which ϑ' is given by trigonometric relations as $\vartheta' = \arcsin\left(\frac{a}{r}\right)$. With its multiplication by 4 and division by 2π we obtain Eq. (D.9).

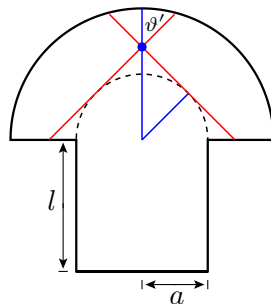


Figure D.1: Sketch of the mushroom billiard: All classical trajectories which enter the stem or the small circle of radius a (dashed line) are chaotic. Trajectories which cross a point in the cap of the mushroom (blue dot) are chaotic when they evolve inside the red cone of angle $2\vartheta'$. Otherwise they are regular.

Now we integrate over the region $r > a$ in the cap of the mushroom and find

$$I = \int_0^\pi \int_a^R r \, dr \, d\varphi P(r) \quad (\text{D.10})$$

$$= R^2 \arcsin\left(\frac{a}{R}\right) + a\sqrt{R^2 - a^2} - \frac{1}{2}\pi a^2. \quad (\text{D.11})$$

Inserting this expression into Eq. (D.8) we finally obtain

$$A_{\text{ch}} = 2la + \left[R^2 \arcsin\left(\frac{a}{R}\right) + a\sqrt{R^2 - a^2} \right] \quad (\text{D.12})$$

as the the area of the mushroom billiard times the fraction of the chaotic phase-space volume. For the desymmetrized mushroom used in Section 5.2.1 this result has to be divided by two.

D.3 Eigenmodes of a wire in a magnetic field

We consider a two-dimensional wire which is infinitely stretched in x -direction and has a width W in y -direction. Perpendicular to this two-dimensional plane we apply a magnetic field B . Our aim is to derive the effective quantum dynamics for an electron in this system [217]. In three dimensions the Hamiltonian is given as

$$\left(-\frac{\hbar^2}{2m_e} \frac{\partial^2}{\partial z^2} + \frac{1}{2m_e} \left(\frac{\hbar}{i} \nabla + q\mathbf{A} \right)^2 + V_{\text{eff}}(z) + V(x, y) \right) \psi(x, y, z) = E\psi(x, y, z). \quad (\text{D.13})$$

Here $\mathbf{A} = -By\mathbf{e}_x$ is the vector potential, $V_{\text{eff}}(z)$ denotes the confinement potential in z -direction, $V(x, y)$ describes the confinement by the wire, and m_e is the mass of the electron. For the two-dimensional electron gas after separating out the z -component in the wave function we find

$$\left(-\frac{\hbar^2}{2m_e} \frac{\partial^2}{\partial y^2} + \frac{1}{2m_e} \left(\frac{\hbar}{i} \frac{\partial}{\partial x} - qBy \right)^2 + V(x, y) \right) \psi(x, y) = E\psi(x, y). \quad (\text{D.14})$$

The following commutators hold if $V(x, y) = V(y)$: $[\hat{p}_x, \hat{H}] = [\hat{p}_z, \hat{H}] = [\hat{p}_x, \hat{p}_z] = 0$ such that the wave function can be further separated: $\psi(x, y) = X(x)Z(y)$. As the potential $V(y)$ does not act in x -direction the x -dependence of the eigenfunctions will be given by plane waves. With $\hat{p}_x\psi(x, y) = \hbar k_x\psi(x, y)$ we find $X(x) = 1/\sqrt{k_x} e^{ik_x x}$ and the Hamiltonian reads

$$\left(\frac{1}{2m_e} \hat{p}_y^2 + \frac{q^2 B^2}{2m_e} \left(y - \frac{\hbar k_x}{qB} \right)^2 + V(y) \right) Z(y) = EZ(y). \quad (\text{D.15})$$

With $\omega_c = qB/m_e$ and $y_0 = \hbar k_x/qB$ we find

$$\left(\frac{1}{2m_e} \hat{p}_y^2 + \frac{m_e \omega_c^2}{2} (y - y_0)^2 + V(y) \right) Z(y) = EZ(y) \quad (\text{D.16})$$

which is the eigenequation for a harmonic oscillator with an additional potential $V(y)$. For a free particle with $V(y) = 0$ the solutions $Z(y)$ are the eigenfunctions of the harmonic oscillator

$$Z_m(y) = \frac{1}{\sqrt{2^m m! \sqrt{\pi} l_m}} e^{-\frac{(y-y_0)^2}{2l_m^2}} H_m \left(\frac{y-y_0}{l_m} \right) \quad (\text{D.17})$$

with the magnetic length $l_m = \sqrt{\hbar/qB}$, the m th Hermite polynomial H_m , and $E_m = \hbar\omega_c(m + 1/2)$.

Now we consider a wire of width W such that $V(y)$ is zero in $y \in (0, W)$ and infinity outside. We decompose $Z(y)$ into a Fourier series

$$Z(y) = \sum_n a_n \sin \left(\frac{n\pi y}{W} \right) \quad (\text{D.18})$$

with the expansion coefficients a_n , $n = 1, \dots, n_{\max}$, where numerically n_{\max} is chosen such that the coefficients a_n have decayed sufficiently. Inserting this expression into the Schrödinger equation (D.16), integration with $\int_0^W dy \sin(k\pi y/W) 2/W$, and using the substitutions $z = y\pi/W$, $z_0 = y_0\pi/W$ results in

$$\frac{\hbar^2}{2m_e} \left(\frac{k\pi}{W} \right)^2 a_k + \sum_n F_{nk} a_n = E a_k \quad (\text{D.19})$$

where

$$F_{nk} = \frac{m_e \omega_c^2 W^2}{2\pi^3} \int_0^\pi dz (z - z_0)^2 (\cos(n-k)z - \cos(n+k)z) \quad (\text{D.20})$$

which can be solved analytically. One obtains

$$F_{nk}^{n \neq k} = \frac{m_e \omega_c^2 W^2}{\pi^2} \left[\left(1 - \frac{y_0}{W} \right) \left(\frac{\cos \pi(n-k)}{(n-k)^2} - \frac{\cos \pi(n+k)}{(n+k)^2} \right) + \frac{y_0}{W} \frac{4nk}{(n^2 - k^2)^2} \right], \quad (\text{D.21})$$

$$F_{nk}^{n=k} = \frac{m_e \omega_c^2 W^2}{\pi^2} \left[\frac{\pi^2 \left(\left(1 - \frac{y_0}{W} \right)^3 + \frac{y_0^3}{W^3} \right)}{6} - \frac{1}{4k^2} \right]. \quad (\text{D.22})$$

By diagonalizing the system

$$\left(\frac{\hbar^2}{2m_e} \left(\frac{k\pi}{W} \right)^2 \delta_{kn} + F_{kn} \right) a_n = E a_k \quad (\text{D.23})$$

we find the expansion coefficients $\{a_k\}_m$ of the modes $Z_m(y)$ in y -direction at one specific value of y_0 . For electrons with the Fermi energy E_F we have to find $y_{0,m}$ for each transversal mode labelled with m , by numerically searching for the root $E(y_{0,m}) = E_F$. This gives the quantized modes $Z_m(y)$ in y -direction. It implies that the wave number in x -direction is also dependent on the mode number, $k_{x,m} = y_{0,m}qB/\hbar$. For small m the modes are concentrated around $y = 0$. Thus, $y_{0,m}$ will be close to $-r_c$ such that $k_{x,m} \approx k_F$. Note that $y_{0,m}$ which is the center of the classical cyclotron orbit is negative for small m such that the particle is reflected at the lower boundary $y = 0$. In the limit $W \rightarrow \infty$ we find a wire with just one boundary at $y = 0$.

D.4 Semiclassical description of localization lengths in wires with one-sided disorder

In Ref. [45] a semiclassical derivation of the mode localization lengths ξ_m for a two-dimensional wire with one-sided surface disorder in a perpendicular magnetic field is performed. These results will be reported in this section. For large k_F or small $h_{\text{eff}} = \pi/(k_F W)$ the localization lengths in units of the width l of the elements of the wire are found to be

$$\xi_m = \left(a_m h_{\text{eff}}^{-\frac{2}{3}} - b_m \right) \exp \left(\frac{c_0}{h_{\text{eff}}} \left[1 - d_m h_{\text{eff}}^{\frac{2}{3}} \right]^{\frac{3}{2}} \right) \quad (\text{D.24})$$

in the case of a constant cyclotron radius $r_c = \hbar k_F / (eB)$ with the dimensionless parameters

$$a_m = 2^{\frac{1}{3}} \pi^{\frac{5}{3}} M \mu_m \frac{\Delta}{\zeta^{\frac{1}{3}}} \left(\frac{2 + \Delta/\zeta}{1 + \Delta/\zeta} \right), \quad (\text{D.25})$$

$$b_m = -\pi z_m M \mu_m \left(1 + \frac{\zeta^2}{(\Delta + \zeta)^2} \right), \quad (\text{D.26})$$

$$c_0 = \frac{4\sqrt{2}\pi}{3} \frac{\Delta^{\frac{3}{2}}}{\zeta^{\frac{1}{2}}} \left(1 + \frac{3}{20} \frac{\Delta}{\zeta} \right), \quad (\text{D.27})$$

$$d_m = -\frac{z_m}{2^{\frac{1}{3}} \pi^{\frac{2}{3}}} \frac{\xi^{\frac{1}{3}}}{\Delta}, \quad (\text{D.28})$$

where $\Delta = 1 - \delta/(2W)$, $\zeta = r_c/W$, z_m is the m th root of the Airy function, and

$$\mu_m = \int_{z_m}^{\infty} \text{Ai}^2(z) dz. \quad (\text{D.29})$$

Bibliography

- [1] J. Elster and H. Geitel: *Versuche an Becquerelstrahlen*, Ann. Phys. **66** (1898) 735–740.
- [2] E. Rutherford: *A radioactive substance emitted from Thorium compounds*, Phil. Mag. **49** (1900) 1–15.
- [3] G. Gamow: *Quantum theory of the atomic nucleus*, Z. f. Phys. **51** (1928) 204 [9 pages].
- [4] G. Gamow: *The quantum theory of nuclear disintegration*, Nature **122** (1928) 805–806.
- [5] G. Gamow: *Constitution of Atomic Nuclei and Radioactivity*, Clarendon Press, Oxford, (1931).
- [6] L. Esaki: *Long journey into tunneling*, Rev. Mod. Phys. **46** (1974) 237–244.
- [7] I. Giaever: *Electron tunneling and superconductivity*, Rev. Mod. Phys. **46** (1974) 245–250.
- [8] B. D. Josephson: *The discovery of tunneling supercurrent*, Science **184** (1974) 527–530.
- [9] L. J. Lauhon and W. Ho: *Direct observation of the quantum tunneling of single hydrogen atoms with a scanning tunneling microscope*, Phys. Rev. Lett. **85** (2000) 4566–4569.
- [10] A. Yazdani: *Watching an atom tunnel*, Nature **409** (2001) 471–472.
- [11] W. K. Hensinger, H. Häffner, A. Browaeys, N. R. Heckenberg, K. Helmerson, C. McKenzie, G. J. Milburn, W. D. Phillips, S. L. Rolston, H. Rubinsztein-Dunlop and B. Uppcroft: *Dynamical tunnelling of ultracold atoms*, Nature **412** (2001) 52–55.
- [12] D. A. Steck, W. H. Oskay and M. G. Raizen: *Observation of chaos-assisted tunneling between islands of stability*, Science **293** (2001) 274–278.
- [13] M. Greiner, O. Mandel, T. Esslinger, T. W. Hänsch and I. Bloch: *Quantum phase transition from a superfluid to a Mott insulator in a gas of ultracold atoms*, Nature **415** (2002) 39–44.
- [14] A. Zenesini, H. Lignier, D. Ciampini, O. Morsch and E. Arimondo: *Coherent Control of Dressed Matter Waves*, Phys. Rev. Lett. **102** (2009) 100403 [4 pages].

- [15] L. D. Landau and E. M. Lifschitz: *Lehrbuch der theoretischen Physik, Band 3: Quantenmechanik*, Akademie Verlag, Berlin, (1979).
- [16] M. Wilkinson: *Tunnelling between tori in phase space*, Physica D **21** (1986) 341–354.
- [17] M. Wilkinson and J. H. Hannay: *Multidimensional tunnelling between excited states*, Physica D **27** (1987) 201–212.
- [18] E. Gildener and A. Patrascioiu: *Pseudoparticle contributions to the energy spectrum of a one-dimensional system*, Phys. Rev. D **16** (1977) 423–430.
- [19] A. Mouchet: *Importance of the Wick rotation on tunnelling*, J. Phys. A **40** (2007) F663–F669.
- [20] I. C. Percival: *Regular and irregular spectra*, J. Phys. B **6** (1973) L229–L232.
- [21] M. V. Berry: *Regular and irregular semiclassical wavefunctions*, J. Phys. A **10** (1977) 2083–2091.
- [22] A. Voros: in *Stochastic Behavior in Classical and Quantum Hamiltonian Systems*, Springer Verlag, Berlin, (1979).
- [23] M. J. Davis and E. J. Heller: *Quantum dynamical tunneling in bound states*, J. Chem. Phys. **75** (1981) 246–254.
- [24] S. Tomsovic and D. Ullmo: *Chaos-assisted tunneling*, Phys. Rev. E **50** (1994) 145–162.
- [25] M. V. Berry and M. Tabor: *Level clustering in the regular spectrum*, Proc. R. Soc. Lond. A **356** (1977) 375–394.
- [26] O. Bohigas, M.-J. Giannoni and C. Schmit: *Characterization of chaotic quantum spectra and universality of level fluctuation laws*, Phys. Rev. Lett. **52** (1984) 1–4.
- [27] W. A. Lin and L. E. Ballentine: *Quantum tunneling and chaos in a driven anharmonic oscillator*, Phys. Rev. Lett. **65** (1990) 2927–2930.
- [28] O. Bohigas, S. Tomsovic and D. Ullmo: *Manifestations of classical phase space structures in quantum mechanics*, Phys. Rep. **223** (1993) 43–133.
- [29] E. Doron and S. D. Frischat: *Semiclassical Description of Tunneling in Mixed Systems: The Case of the Annular Billiard*, Phys. Rev. Lett. **75** (1995) 3661–3664.
- [30] S. D. Frischat and E. Doron: *Dynamical tunneling in mixed systems*, Phys. Rev. E **57** (1998) 1421–1443.

- [31] V. A. Podolskiy and E. E. Narimanov: *Chaos-assisted tunneling in dielectric microcavities*, Opt. Lett. **30** (2005) 474–476.
- [32] C. Dembowski, H.-D. Gräf, A. Heine, R. Hofferbert, H. Rehfeld and A. Richter: *First Experimental Evidence for Chaos-Assisted Tunneling in a Microwave Annular Billiard*, Phys. Rev. Lett. **84** (2000) 867–870.
- [33] R. Hofferbert, H. Alt, C. Dembowski, H.-D. Gräf, H. L. Harney, A. Heine, H. Rehfeld and A. Richter: *Experimental investigations of chaos-assisted tunneling in a microwave annular billiard*, Phys. Rev. E **71** (2005) 046201 [21 pages].
- [34] S. Tomsovic: *Chaos-assisted tunneling in the absence of reflexion symmetry*, J. Phys. A **31** (1998) 9469–9481.
- [35] F. Grossmann, T. Dittrich, P. Jung and P. Hänggi: *Coherent destruction of tunneling*, Phys. Rev. Lett. **67** (1991) 516–519.
- [36] V. Averbukh, S. Osovski and N. Moiseyev: *Controlled Tunneling of Cold Atoms: From Full Suppression to Strong Enhancement*, Phys. Rev. Lett. **89** (2002) 253201 [4 pages].
- [37] J. Zakrzewski, D. Delande and A. Buchleitner: *Ionization via chaos assisted tunneling*, Phys. Rev. E **57** (1998) 1458–1474.
- [38] A. Shudo and K. S. Ikeda: *Complex Classical Trajectories and Chaotic Tunneling*, Phys. Rev. Lett. **74** (1995) 682–685.
- [39] A. Shudo and K. S. Ikeda: *Chaotic tunneling: A remarkable manifestation of complex classical dynamics in non-integrable quantum phenomena*, Physica D **115** (1998) 234–292.
- [40] T. Onishi, A. Shudo, K. S. Ikeda and K. Takahashi: *Tunneling mechanism due to chaos in a complex phase space*, Phys. Rev. E **64** (2001) 025201 [4 pages].
- [41] A. Ishikawa, A. Tanaka and A. Shudo: *Quantum suppression of chaotic tunneling*, J. Phys. A. **40** (2007) F397–F405.
- [42] J. D. Hanson, E. Ott and T. M. Antonsen: *Influence of finite wavelength on the quantum kicked rotator in the semiclassical regime*, Phys. Rev. A **29** (1984) 819–825.
- [43] M. Sheinman, S. Fishman, I. Guarneri and L. Rebuzzini: *Decay of quantum accelerator modes*, Phys. Rev. A **73** (2006) 052110 [12 pages].
- [44] J. Feist, A. Bäcker, R. Ketzmerick, S. Rotter, B. Huckestein and J. Burgdörfer: *Nanowires with surface disorder: Giant localization lengths and quantum-to-classical crossover*, Phys. Rev. Lett. **97** (2006) 116804 [4 pages].

- [45] J. Feist, A. Bäcker, R. Ketzmerick, J. Burgdörfer and S. Rotter: *Nanowires with surface disorder: Giant localization length and dynamical tunneling in the presence of directed chaos*, Phys. Rev. B **80** (2009) 245322 [14 pages].
- [46] V. A. Podolskiy and E. E. Narimanov: *Semiclassical Description of Chaos-Assisted Tunneling*, Phys. Rev. Lett. **91** (2003) 263601 [4 pages].
- [47] M. Sheinman: *Decay of Quantum Accelerator Modes*, Master Thesis, Technion, Haifa, Israel (2005).
- [48] A. Bäcker, R. Ketzmerick, S. Löck and L. Schilling: *Regular-to-chaotic tunneling rates using a fictitious integrable system*, Phys. Rev. Lett. **100** (2008) 104101 [4 pages].
- [49] A. Bäcker, R. Ketzmerick and S. Löck: in preparation (2009).
- [50] A. Bäcker, R. Ketzmerick, S. Löck, M. Robnik, G. Vidmar, R. Höhmann, U. Kuhl and H.-J. Stöckmann: *Dynamical tunneling in mushroom billiards*, Phys. Rev. Lett. **100** (2008) 174103 [4 pages].
- [51] A. Bäcker, R. Ketzmerick, S. Löck, J. Wiersig and M. Hentschel: *Quality factors and dynamical tunneling in annular microcavities*, Phys. Rev. A **79** (2009) 063804 [6 pages].
- [52] L. Bonci, A. Farusi, P. Grigolini and R. Roncaglia: *Tunneling rate fluctuations induced by nonlinear resonances: A quantitative treatment based on semiclassical arguments*, Phys. Rev. E **58** (1998) 5689–5692.
- [53] O. Brodier, P. Schlagheck and D. Ullmo: *Resonance-assisted tunneling in near-integrable systems*, Phys. Rev. Lett. **87** (2001) 064101 [4 pages].
- [54] O. Brodier, P. Schlagheck and D. Ullmo: *Resonance-Assisted Tunneling*, Ann. of Phys. **300** (2002) 88–136.
- [55] C. Eltschka and P. Schlagheck: *Resonance- and Chaos-Assisted Tunneling in Mixed Regular-Chaotic Systems*, Phys. Rev. Lett. **94** (2005) 014101 [4 pages].
- [56] P. Schlagheck, C. Eltschka and D. Ullmo: *Resonance- and Chaos-Assisted Tunneling*, in *Progress in Ultrafast Intense Laser Science I*, edited by K. Yamanouchi, S. L. Chin, P. Agostini and G. Ferrante, Springer, Berlin, (2006).
- [57] A. Mouchet, C. Eltschka and P. Schlagheck: *Influence of classical resonances on chaotic tunneling*, Phys. Rev. E **74** (2006) 026211 [11 pages].
- [58] S. Wimberger, P. Schlagheck, C. Eltschka and A. Buchleitner: *Resonance-Assisted Decay of Nondispersive Wave Packets*, Phys. Rev. Lett. **97** (2006) 043001 [4 pages].

- [59] S. Keshavamurthy: *On dynamical tunneling and classical resonances*, J. Chem. Phys. **122** (2005) 114109 [12 pages].
- [60] S. Keshavamurthy: *Resonance-assisted tunneling in three degrees of freedom without discrete symmetry*, Phys. Rev. E **72** (2005) 045203 [4 pages].
- [61] S. Löck, A. Bäcker, R. Ketzmerick and P. Schlagheck: *Regular-to-Chaotic Tunneling Rates: From the Quantum to the Semiclassical Regime*, arXiv:0906.4893v2 [nlin.CD] (2009).
- [62] M. V. Berry and K. E. Mount: *Semiclassical approximations in wave mechanics*, Rep. Proc. Phys. **35** (1972) 315–397.
- [63] S. C. Miller and R. H. Good: *A WKB-Type Approximation to the Schrödinger Equation*, Phys. Rev. **91** (1953) 174–179.
- [64] R. B. Dingle: *The method of comparison equations in the solution of linear second-order differential equations (generalized W.K.B. method)*, Appl. Sc. Res. **B5** (1956) 345–367.
- [65] H. Jeffreys: *On certain approximate solutions of linear differential equations of the second order*, Proc. Lond. Math. Soc. **23** (1923) 428–436.
- [66] H. A. Kramers: *Wellenmechanik und halbzahlige Quantisierung*, Z. Physik **39** (1926) 828–840.
- [67] W. Nolting: *Quantenmechanik – Methoden und Anwendungen*, Springer-Verlag, Berlin, (2004).
- [68] E. Merzbacher: *Quantum mechanics*, Wiley, New York, (1998).
- [69] G. von Neumann and E. P. Wigner: *Über das Verhalten von Eigenwerten bei adiabatischen Prozessen*, Physik. Zeitschr. **30** (1929) 467–470.
- [70] S. C. Creagh: *Tunneling in two dimensions*, in *Tunneling in Complex Systems*, World Scientific, Singapore, (1998).
- [71] M. Tabor: *Chaos and integrability in nonlinear Dynamics. An Introduction.*, Wiley, New York, (1989).
- [72] I. P. Cornfeld, S. V. Fomin and Y. G. Sinai: *Ergodic Theory*, no. 245 in Grundlehren der mathematischen Wissenschaften, Springer-Verlag, Berlin, (1982).
- [73] M. Nakahara: *Geometry, Topology and Physics*, Graduate Student Series in Physics. Institute of Physics Publishing, Bristol, (1990).

- [74] G. Haag: *Quantisierte chaotische Abbildungen*, Diplomarbeit, Universität Ulm, (1999).
- [75] B. V. Chirikov: *A universal instability of many-dimensional oscillator systems*, Physics Reports **52** (1979) 263–379.
- [76] M. V. Berry: *Regular and irregular motion*, Am. Inst. Phys. Conf. Proc. **46** (1978) 16–120.
- [77] D. K. Arrowsmith and C. M. Place: *An introduction to dynamical systems*, Cambridge University Press, Cambridge, (1990).
- [78] R. S. MacKay, J. D. Meiss and I. C. Percival: *Transport in Hamiltonian systems*, Physica D **13** (1984) 55–81.
- [79] J. M. Greene: *Two-dimensional measure-preserving mappings*, J. Math. Phys. **20** (1968) 760–768.
- [80] H. Schanz, T. Dittrich and R. Ketzmerick: *Directed Chaotic Transport in Hamiltonian Ratchets*, Phys. Rev. E **71** (2005) 026228 [20 pages].
- [81] G. Casati, B. V. Chirikov and D. L. Shepelyansky: *Quantum Limitations for Chaotic Excitation of the Hydrogen Atom in a Monochromatic Field*, Phys. Rev. Lett. **53** (1984) 2525–2528.
- [82] D. L. Shepelyansky: *Localization of quasienergy eigenfunctions in action space*, Phys. Rev. Lett. **56** (1986) 677–680.
- [83] H. Schanz, M.-F. Otto, R. Ketzmerick and T. Dittrich: *Classical and Quantum Hamiltonian Ratchets*, Phys. Rev. Lett. **87** (2001) 070601 [4 pages].
- [84] J. Laskar, C. Froeschlé and A. Celletti: *The means of chaos by the numerical analysis of the fundamental frequencies. Application to the standard mapping*, Physica D **56** (1992) 253–269.
- [85] J. Laskar: *Frequency analysis for multi-dimensional systems. Global dynamics and diffusion*, Physica D **67** (1993) 257–281.
- [86] A. Bäcker, R. Ketzmerick and A. G. Monastra: *Flooding of Chaotic Eigenstates into Regular Phase Space Islands*, Phys. Rev. Lett. **94** (2005) 054102 [4 pages].
- [87] A. Bäcker, R. Ketzmerick and A. G. Monastra: *Universality in the flooding of regular islands by chaotic states*, Phys. Rev. E **75** (2007) 066204 [11 pages].
- [88] A. J. Lichtenberg and M. A. Liebermann: *Regular and Stochastic Motion*, Springer, New York, (1983).

- [89] A. Bazzani, M. Giovannozzi, G. Servizi, E. Todesco and G. Turchetti: *Resonant normal forms, interpolating Hamiltonians and stability of area preserving maps*, Physica D **64** (1993) 66–97.
- [90] A. Bazzani, E. Todesco, G. Turchetti and G. Servizi: *A normal form approach to the theory of nonlinear betatron motion*, CERN Yellow Reports **94-02** (1994) [232 pages].
- [91] P. Crehan: *The proper quantum analogue of the Birkhoff-Gustavson method of normal forms*, J. Phys. A **23** (1990) 5815–5828.
- [92] R. Schubert, H. Waalkens and S. Wiggins: *Efficient Computation of Transition State Resonances and Reaction Rates from a Quantum Normal Form*, Phys. Rev. Lett. **96** (2006) 218302 [4 pages].
- [93] H.-J. Stöckmann: *Quantum Chaos. An introduction*, University Press, Cambridge, (1999).
- [94] L. Schilling: *Direct dynamical tunneling in a mixed phase space*, Ph.D. thesis, TU-Dresden, Germany, (2006).
- [95] F. Bloch: *Über die Quantenmechanik der Elektronen in Kristallgittern*, Z. f. Phys. **52** (1928) 555–600.
- [96] S.-J. Chang and K.-J. Shi: *Evolution and exact eigenstates of a resonant quantum system*, Phys. Rev. A **34** (1986) 7–22.
- [97] J. P. Keating, F. Mezzadri and J. M. Robbins: *Quantum boundary conditions for torus maps*, Nonlinearity **12** (1999) 579–591.
- [98] M. V. Berry, N. L. Balzas, M. Tabor and A. Voros: *Quantum Maps*, Ann. of Phys. **122** (1979) 26–63.
- [99] V. F. Lazutkin: *KAM theory and semiclassical approximations to eigenfunctions*, Springer-Verlag, Berlin, (1993).
- [100] H.-J. Stöckmann and J. Stein: *“Quantum” chaos in billiards studied by microwave absorption*, Phys. Rev. Lett. **64** (1990) 2215–2218.
- [101] S. Sridhar: *Experimental observation of scarred eigenfunctions of chaotic microwave cavities*, Phys. Rev. Lett. **67** (1991) 785–788.
- [102] H. Linke, T. E. Humphrey, P. E. Lindelof, A. Löfgren, R. Newbury, P. Omling, A. O. Sushkov, R. P. Taylor and H. Xu: *Quantum ratchets and quantum heat pumps*, Appl. Phys. A **75** (2002) 237–246.

- [103] A. Löfgren, C. A. Marlow, I. Shorubalko, R. P. Taylor, P. Omling, L. Samuelson and H. Linke: *Symmetry of two-terminal, non-linear electric conduction*, Phys. Rev. Lett. **92** (2004) 046803 [4 pages].
- [104] A. Bäcker: *Classical and Quantum Chaos in Billiards*, Ph.D. thesis, Universität Ulm, Germany, (1998).
- [105] G. D. Birkhoff: *Dynamical Systems*, no. 9 in Colloquium publications, American Mathematical Society, Providence, Rhode Island, revised edn., (1966), originally published (1927).
- [106] Y. G. Sinai: *Dynamical systems with elastic reflections*, Russ. Math. Surveys **25** (1970) 137–189.
- [107] G. Gallavotti: *Lectures on the billiard*, Lect. Notes in Phys. **38** (1975) 236–295.
- [108] A. Katok and J.–M. Strelcyn (with the collaboration of F. Ledrappier and F. Przytycki): *Invariant Manifolds, Entropy and Billiards; Smooth Maps with Singularities*, Lect. Notes in Math. **1222** (1986).
- [109] V. V. Kozlov and D. V. Treshchëv: *Billiards. A genetic Introduction to the Dynamics of Systems with Impacts*, vol. 89 of *Translations of Mathematical Monographs*, American Mathematical Society, Providence, Rhode Island, (1991).
- [110] P. H. Richter, A. Wittek, M. P. Kharlamov and A. P. Kharlamov: *Action integrals for ellipsoidal billiards*, Z. Naturforsch. **50a** (1995) 693–710.
- [111] H. Waalkens, J. Wiersig and H. R. Dullin: *Elliptic Quantum Billiard*, Ann. Phys. **260** (1997) 50–90.
- [112] L. A. Bunimovich: *On ergodic properties of certain billiards*, Funct. Anal. Appl. **8** (1974) 254–255.
- [113] L. A. Bunimovich: *On the ergodic properties of nowhere dispersing billiards*, Commun. Math. Phys. **65** (1979) 295–312.
- [114] M. Robnik: *Classical dynamics of a family of billiards with analytic boundaries*, J. Phys. A **16** (1983) 3971–3986.
- [115] Ya. G. Sinai: *On the foundations of the ergodic hypothesis for a dynamical system of statistical mechanics*, Sov. Math. Dokl. **4** (1963) 1818–1822.
- [116] G. Gallavotti and D. S. Ornstein: *Billiards and Bernoulli schemes*, Commun. Math. Phys. **38** (1974) 83–101.

- [117] N. I. Chernov and C. Haskell: *Nonuniformly hyperbolic K-systems are Bernoulli*, *Ergod. Th. & Dynam. Sys.* **16** (1996) 19–44.
- [118] M. Wojtkowski: *Principles for the design of billiards with nonvanishing Lyapunov exponents*, *Commun. Math. Phys.* **105** (1986) 391–414.
- [119] D. Szász: *On the K-property of some planar hyperbolic billiards*, *Commun. Math. Phys.* **145** (1992) 595–604.
- [120] R. Markarian: *New ergodic billiards: exact results*, *Nonlinearity* **6** (1993) 819–841.
- [121] A. Bäcker, R. Schubert and P. Stifter: *Rate of quantum ergodicity in Euclidean billiards*, *Phys. Rev. E* **57** (1998) 5425–5447.
- [122] O. Bohigas, D. Boosé, R. E. de Carvallho and V. Marvulle: *Quantum tunneling and chaotic dynamics*, *Nucl. Phys. A* **560** (1993) 197–210.
- [123] L. A. Bunimovich: *Mushrooms and other billiards with divided phase space*, *Chaos* **11** (2001) 802–808.
- [124] E. G. Altmann, A. E. Motter and H. Kantz: *Stickiness in mushroom billiards*, *Chaos* **15** (2005) 033105 [7 pages].
- [125] H.-D. Gräf, H. L. Harney, H. Lengers, C. H. Lewenkopf, C. Rangacharyulu, A. Richter, P. Schardt and H. A. Weidenmüller: *Distribution of eigenmodes in a superconducting stadium billiard with chaotic dynamics*, *Phys. Rev. Lett.* **69** (1992) 1296–1299.
- [126] J. Stein and H.-J. Stöckmann: *Experimental determination of billiard wave functions*, *Phys. Rev. Lett.* **68** (1992) 2867–2870.
- [127] H. Alt, A. Bäcker, C. Dembowski, H.-D. Gräf, R. Hofferbert, H. Rehfeld and A. Richter: *Mode fluctuation distribution for spectra of superconducting microwave billiards*, *Phys. Rev. E* **58** (1998) 1737–1742.
- [128] M. C. Gutzwiller: *Chaos in classical and quantum mechanics*, Springer-Verlag, New York, (1990).
- [129] V. I. Arnold: *Modes and quasimodes*, *Funct. Anal. Appl.* **6** (1972) 94–101.
- [130] V. F. Lazutkin: *Asymptotics of the eigenvalues of the Laplacian and quasimodes. A series of quasimodes corresponding to a system of caustics close to the boundary*, *Math. USSR Izv.* **7** (1973) 439–466.
- [131] M. Shapiro and G. Goelman: *Onset of chaos in an isolated energy eigenstate*, *Phys. Rev. Lett.* **53** (1984) 1714–1717.

- [132] B. Li and M. Robnik: *Statistical properties of high-lying chaotic eigenstates*, J. Phys. A **27** (1994) 5509–5523.
- [133] S. W. McDonald and A. N. Kaufmann: *Wave chaos in the stadium: Statistical properties of short-wave solutions of the Helmholtz equation*, Phys. Rev. A **37** (1988) 3067–3086.
- [134] M. V. Berry: *Statistics of nodal lines and points in chaotic quantum billiards: perimeter corrections, fluctuations, curvature*, J. Phys. A **35** (2002) 3025–3038.
- [135] R. S. Lehman: *Developments at an analytic corner of solutions of elliptic partial differential equations*, J. Math. Mech. **8** (1959) 727–760.
- [136] A. Bäcker, S. Fürstberger and R. Schubert: *Poincaré Husimi representation of eigenstates in quantum billiards*, Phys. Rev. E **70** (2004) 036204 [10 pages].
- [137] M. Abramowitz and I. A. Stegun: *Handbook of mathematical functions*, Dover Publications, Inc., New York, (1970).
- [138] A. J. Burton and G. F. Miller: *The application of integral equation methods to the numerical solution of some exterior boundary-value problems*, Proc. R. Soc. Lond. A **323** (1971) 201–210.
- [139] R. E. Kleinman and G. F. Roach: *Boundary integral equations for the three dimensional Helmholtz equation*, SIAM Rev. **16** (1974) 214–236.
- [140] K. Hornberger and U. Smilansky: *The boundary integral method for magnetic billiards*, J. Phys. A **33** (2000) 2829–2855.
- [141] T. Betcke and L. N. Trefethen: *Reviving the Method of Particular Solutions*, SIAM Rev. **47** (2005) 469–491.
- [142] E. Vergini and M. Saraceno: *Calculation by scaling of highly excited states of billiards*, Phys. Rev. E **52** (1995) 2204–2207.
- [143] E. J. Heller: *Wave packet dynamics and quantum chaology*, in *Chaos and Quantum Physics*, edited by M-J. Giannoni, A. Voros, and J. Zinn-Justin, Les Houches 89, Session LII, (1991).
- [144] E. Doron and U. Smilansky: *Chaotic Spectroscopy*, Phys. Rev. Lett. **68** (1992) 1255–1258.
- [145] B. Dietz and U. Smilansky: *A scattering approach to the quantization of billiards – The inside-outside duality*, Chaos **3** (1993) 581–589.
- [146] H. Schanz and U. Smilansky: *Quantization of Sinai’s billiard – a scattering approach*, Chaos, Solitons & Fractals **5** (1995) 1289–1309.

- [147] L. Fox, P. Henrici and C. B. Moler: *Approximations and bounds for eigenvalues of elliptic operators*, SIAM J. Numer. Anal. **4** (1967) 89–102.
- [148] A. H. Barnett and T. Betcke: *Quantum mushroom billiards*, Chaos **17** (2007) 043125 [13 pages].
- [149] T. Betcke: *The generalized singular value decomposition and the method of particular solutions*, SIAM J. Sci. Comput. **30** (2008) 1278–1295.
- [150] F.-M. Dittes: *The decay of quantum systems with a small number of open channels*, Habilitationsschrift, Dresden, (1998).
- [151] H.-G. Park, S.-H. Kim, S.-H. Kwon, Y.-G. Ju, J.-K. Yang, J.-H. Baek, S.-B. Kim and Y.-H. Lee: *Electrically Driven Single-Cell Photonic Crystal Laser*, Science **305** (2004) 1444–1447.
- [152] S. M. Ulrich, C. Gies, S. Ates, J. Wiersig, S. Reitzenstein, C. Hofmann, A. Löffler, A. Forchel, F. Jahnke and P. Michler: *Photon Statistics of Semiconductor Microcavity Lasers*, Phys. Rev. Lett. **98** (2007) 043906 [4 pages].
- [153] J. Kim, O. Benson, H. Kan and Y. Yamamoto: *A single-photon turnstile device*, Nature **397** (1999) 500–503.
- [154] P. Michler, A. Imamoglu, M. D. Mason, P. J. Carson, G. F. Strouse and S. K. Buratto: *Quantum correlation among photons from a single quantum dot at room temperature*, Nature **406** (2000) 968–970.
- [155] M. Benyoucef, S. M. Ulrich, P. Michler, J. Wiersig, F. Jahnke and A. Forchel: *Correlated photon pairs from single (In,Ga)As/GaAs quantum dots in pillar microcavities*, J. Appl. Phys. **97** (2005) 023101 [4 pages].
- [156] R. E. Slusher: *Optical Processes in Microcavities*, Semicond. Sci. Technol **9** (1994) 2025–2039.
- [157] D. Stone: *Wave-Chaotic Optical Resonators and Lasers*, Physica Scripta **T90** (2001) 248–262.
- [158] J. U. Nöcker and A. D. Stone: *Ray and wave chaos in asymmetric resonant optical cavities*, Nature **385** (1997) 45–47.
- [159] S.-B. Lee, J.-H. Lee, J.-S. Chang, H.-J. Moon, S. W. Kim and K. An: *Observation of Scarred Modes in Asymmetrically Deformed Microcylinder Lasers*, Phys. Rev. Lett. **88** (2002) 033903 [4 pages].

- [160] S.-B. Lee, J. Yang, S. Moon, J.-H. Lee, K. An, J.-B. Shim, H.-W. Lee and S. W. Kim: *Universal output directionality of single modes in a deformed microcavity*, Phys. Rev. A **75** (2007) 011802(R) [4 pages].
- [161] S. Shinohara and T. Harayama: *Signature of ray chaos in quasibound wave functions for a stadium-shaped dielectric cavity*, Phys. Rev. E **75** (2007) 036216 [4 pages].
- [162] M. Lebental, J. S. Lauret, J. Zyss, C. Schmit and E. Bogomolny: *Directional emission of stadium-shaped microlasers*, Phys. Rev. A **75** (2007) 033806 [5 pages].
- [163] F. Goos and H. Hänchen: *Ein neuer und fundamentaler Versuch zur Totalreflexion*, Ann. Phys. (Leipzig) **1** (1947) 333–346.
- [164] H. Schomerus and M. Hentschel: *Correcting Ray Optics at Curved Dielectric Microresonator Interfaces: Phase-Space Unification of Fresnel Filtering and the Goos-Hänchen Shift*, Phys. Rev. Lett. **96** (2006) 243903 [4 pages].
- [165] D. Müller, D. Tharanga, A. A. Stahlhofen and G. Nimtz: *Nonspecular shifts of microwaves in partial reflection*, Europhys. Lett. **73** (2006) 526–532.
- [166] H. E. Tureci and A. D. Stone: *Deviation from Snell's law for beams transmitted near the critical angle: application to microcavity lasers*, Opt. Lett. **27** (2002) 7–9.
- [167] N. B. Rex, H. E. Tureci, H. G. L. Schwefel, R. K. Chang and A. D. Stone: *Fresnel Filtering in Lasing Emission from Scarred Modes of Wave-Chaotic Optical Resonators*, Phys. Rev. Lett. **88** (2002) 094102 [4 pages].
- [168] J. Unterhinninghofen, J. Wiersig and M. Hentschel: *Goos-Hänchen shift and localization of optical modes in deformed microcavities*, Phys. Rev. E **78** (2008) 016201 [8 pages].
- [169] E. G. Altmann, G. D. Magno and M. Hentschel: *Non-Hamiltonian dynamics in optical microcavities resulting from wave-inspired corrections to geometric optics*, Europhys. Lett. **84** (2008) 10008 [6 pages].
- [170] J. Wiersig and J. Main: *Fractal Weyl law for chaotic microcavities: Fresnel's laws imply multifractal scattering*, Phys. Rev. E **77** (2008) 036205 [8 pages].
- [171] J. Wiersig and M. Hentschel: *Unidirectional light emission from high-Q modes in optical microcavities*, Phys. Rev. A **73** (2006) 031802(R) [4 pages].
- [172] J. D. Jackson: *Klassische Elektrodynamik*, Walter de Gruyter, Berlin, (1983).
- [173] J. U. Nöckel: *Resonances in Nonintegrable Open Systems*, Ph.D. thesis, Yale University, (1997).

- [174] R. H. Landau: *Quantum Mechanics*, vol. 2, Wiley, New York, 2nd edn., (1996).
- [175] P. L. Kapur and R. Peierls: *The Dispersion Formula for Nuclear Reactions*, Proc. R. Soc. Lond. A **166** (1938) 277–295.
- [176] M. Hentschel and K. Richter: *Quantum chaos in optical systems: The annular billiard*, Phys. Rev. E **66** (2002) 056207 [13 pages].
- [177] J. Wiersig: *Boundary element method for resonances in dielectric microcavities*, J. Opt. A: Pure Appl. Opt. **5** (2003) 53–60.
- [178] P. A. Knipp and T. L. Reinecke: *Boundary-element method for the calculation of electronic states in semiconductor nanostructures*, Phys. Rev. B **54** (1996) 1880–1891.
- [179] J. Wiersig: private communication, (2009).
- [180] R. Scharf: *Quantum maps, adiabatic invariance and the semiclassical limit*, J. Phys. A **21** (1988) 4133–4147.
- [181] S. C. Creagh: *Tunnelling in multidimensional systems*, J. Phys. A. **27** (1994) 4969–4993.
- [182] S. Tomsovic, M. Grinberg and D. Ullmo: *Semiclassical Trace Formulas of Near-Integrable Systems: Resonances*, Phys. Rev. Lett. **75** (1995) 4346–4349.
- [183] P. Schlagheck and S. Keshavamurthy: private communication, (2009).
- [184] G. Vidmar, H.-J. Stöckmann, M. Robnik, U. Kuhl, R. Höhmann and S. Grossmann: *Beyond the Berry&Robnik regime: a random matrix study of tunneling effects*, J. Phys. A **40** (2007) 13883–13905.
- [185] H. Tanaka and A. Shudo: *Recurrence time distribution in mushroom billiards with parabolic hat*, Phys. Rev. E **74** (2006) 036211 [5 pages].
- [186] B. Dietz, T. Friedrich, M. Miski-Oglu, A. Richter and F. Schäfer: *Spectral properties of Bunimovich mushroom billiards*, Phys. Rev. E **75** (2007) 035203 [4 pages].
- [187] A. Sommerfeld: *Vorlesungen über theoretische Physik, Band 6: Partielle Differentialgleichungen der Physik*, Verlag Harri Deutsch, Thun, (1978).
- [188] S. Zelditch and M. Zworski: *Ergodicity of eigenfunctions for ergodic billiards*, Comm. Math. Phys. **175** (1996) 673–682.
- [189] G. Tanner: *How chaotic is the stadium billiard? A semiclassical analysis*, J. Phys. A **30** (1997) 2863–2888.

- [190] A. Bäcker, R. Schubert and P. Stifter: *On the number of bouncing ball modes in billiards*, J. Phys. A **30** (1997) 6783–6795.
- [191] Y. Y. Bai, G. Hose, K. Stefański and H. S. Taylor: *Born-Oppenheimer adiabatic mechanism for regularity of states in the quantum stadium billiard*, Phys. Rev. A **31** (1985) 2821–2826.
- [192] A. García-Martín, M. Governale and P. Wölfle: *Magnetic-field effects on the transport properties of one-sided rough wires*, Phys. Rev. B **66** (2002) 233307 [4 pages].
- [193] L. Hufnagel, R. Ketzmerick, M.-F. Otto and H. Schanz: *Eigenstates Ignoring Regular and Chaotic Phase-Space Structures*, Phys. Rev. Lett. **89** (2002) 154101 [4 pages].
- [194] S. L. McCall, A. F. J. Levi, R. E. Slusher, S. J. Pearton and R. A. Logan: *Whispering-gallery mode microdisk lasers*, Appl. Phys. Lett. **60** (1992) 289–291.
- [195] C. P. Michael, K. Srinivasan, T. J. Johnson, O. Painter, K. H. Lee, K. Hennessy, H. Kim and E. Hu: *Wavelength- and material-dependent absorption in GaAs and AlGaAs microcavities*, Appl. Phys. Lett. **90** (2007) 051108 [3 pages].
- [196] T. J. Kippenberg, J. Kalkman, A. Polman and K. J. Vahala: *Demonstration of an erbium-doped microdisk laser on a silicon chip*, Phys. Rev. A **74** (2006) 051802(R) [4 pages].
- [197] L. Collot, V. Lefèvre-Seguin, M. Brune, J. M. Raimond and S. Haroche: *Very High-Q Whispering-Gallery Mode Resonances Observed on Fused Silica Microspheres*, Europhys. Lett. **23** (1993) 327–334.
- [198] S. Götzinger, L. d. S. Menezes, A. Mazzei, S. Kühn, V. Sandoghdar and O. Benson: *Controlled photon transfer between two individual nanoemitters via shared high-Q modes of a microsphere resonator*, Nano Lett. **6** (2006) 1151–1154.
- [199] D. K. Armani, T. J. Kippenberg, S. M. Spillane and K. J. Vahala: *Ultra-high-Q toroid microcavity on a chip*, Nature **421** (2003) 925–928.
- [200] A. F. J. Levi, R. E. Slusher, S. L. McCall, J. L. Glass, S. J. Pearton and R. A. Logan: *Directional light coupling from microdisk lasers*, Appl. Phys. Lett. **62** (1993) 561–563.
- [201] C. Gmachl, F. Capasso, E. E. Narimanov, J. U. Nöckel, A. D. Stone, J. Faist, D. L. Sivco and A. Y. Cho: *High-Power Directional Emission from Microlasers with Chaotic Resonators*, Science **280** (1998) 1556–1564.
- [202] M. S. Kurdoglyan, S.-Y. Lee, S. Rim and C.-M. Kim: *Unidirectional lasing from a microcavity with a rounded isosceles triangle shape*, Opt. Lett. **29** (2004) 2758–2760.

- [203] M. Hentschel and T.-Y. Kwon: *Designing and understanding directional emission from spiral microlasers*, Opt. Lett. **34** (2009) 163–165.
- [204] M. Kneissl, M. Teepe, N. Miyashita, N. M. Johnson, G. D. Chern and R. K. Chang: *Current-injection spiral-shaped microcavity disk laser diodes with unidirectional emission*, Appl. Phys. Lett. **84** (2004) 2485–2487.
- [205] T. Tanaka, M. Hentschel, T. Fukushima and T. Harayama: *Classical Phase Space Revealed by Coherent Light*, Phys. Rev. Lett. **98** (2007) 033902 [4 pages].
- [206] J. Wiersig and M. Hentschel: *Combining Directional Light Output and Ultralow Loss in Deformed Microdisks*, Phys. Rev. Lett. **100** (2008) 033901 [4 pages].
- [207] Q. H. Song, H. Cao, B. Y. Liu, S. T. Ho, W. Fang and G. S. Solomon: *Chaotic Microcavity Laser with Low Threshold and Unidirectional Output*, arXiv0810.3923 (2008).
- [208] F. Wilde: *Unidirectional photoluminescence emission of pierced microdisks*, Ph.D. thesis, University of Hamburg, Germany, (2008).
- [209] C. Yan, Q. Wang, L. Diehl, M. Hentschel, J. Wiersig, N. Yu, C. Pflüg, M. A. Belkin, M. Yamanishi, H. Kan and F. Capasso: *Deformed microcavity quantum cascade lasers with directional emission*, to be submitted (2009).
- [210] H. Schomerus, J. Wiersig and M. Hentschel: *Optomechanical probes of resonances in amplifying microresonators*, Phys. Rev. A **70** (2004) 012703 [8 pages].
- [211] G. Hackenbroich and J. U. Nöckel: *Dynamical tunneling in optical cavities*, Europhys. Lett. **39** (1997) 371–376.
- [212] A. Bäcker and R. Schubert: *Amplitude distribution of eigenfunctions in mixed systems*, J. Phys. A **35** (2002) 527–538.
- [213] M. Hentschel, H. Schomerus and R. Schubert: *Husimi functions at dielectric interfaces: Inside-outside duality for optical systems and beyond*, Europhys. Lett. **62** (2003) 636–642.
- [214] M. V. Berry and M. Robnik: *Semiclassical level spacings when regular and chaotic orbits coexist*, J. Phys. A **17** (1984) 2413–2421.
- [215] A. Bäcker, R. Ketzmerick, S. Löck and N. Mertig: in preparation (2009).
- [216] M. Hénon: *Numerical Study of Quadratic Area-Preserving Mappings*, Quar. Appl. Math. **27** (1969) 291–312.
- [217] L. E. Ballentine: *Quantum Mechanics: A Modern Development*, World Scientific, Singapore, (1999).

Acknowledgments

It is a pleasure to thank Prof. Dr. Roland Ketzmerick for this interesting research project, valuable discussions, and his continuous support. I am particularly grateful to my supervisor Dr. Arnd Bäcker for his support, many interesting discussions, and his continuous encouragement.

I thank Prof. J. Wiersig, Prof. P. Schlagheck, Dr. M. Hentschel, Prof. H.-J. Stöckmann, Dr. U. Kuhl, Dr. R. Höhmann, and N. Mertig for enjoyable and successful collaborations and for helpful discussions and comments during several stages of this work. It is also a pleasure to thank Normann Mertig, Matthias Michler, and Martin Richter for proof-reading this thesis.

Furthermore, I thank all members of the computational physics group and our secretary G. Schädlich for the pleasant working atmosphere. This research was supported by the Deutsche Forschungsgemeinschaft DFG under contract KE 537/3-3 and the Forschergruppe 760.

Especially I would like to thank my parents for their support during the past years and Stephanie Schindhelm for her caring motivation while writing this thesis.

The plots in this thesis were generated with the software `PyXGraph` which simplifies the usage of `PyX` (<http://pyx.sourceforge.net/>). The programs for numerical computations were written in Python (<http://www.python.org>) using NumPy and SciPy (<http://www.scipy.org>).

Erklärung

Hiermit versichere ich, dass ich die vorliegende Arbeit ohne unzulässige Hilfe Dritter und ohne Benutzung anderer als der angegebenen Hilfsmittel angefertigt habe; die aus fremden Quellen direkt oder indirekt übernommenen Gedanken sind als solche kenntlich gemacht. Die Arbeit wurde bisher weder im Inland noch im Ausland in gleicher oder ähnlicher Form einer anderen Prüfungsbehörde vorgelegt.

Die Dissertation wurde in der Zeit Januar 2007 bis Dezember 2009 unter der Betreuung von Herrn Prof. Dr. Roland Ketzmerick am Institut für Theoretische Physik der Technischen Universität Dresden angefertigt. Es haben keine früheren erfolglosen Promotionsverfahren stattgefunden. Ich erkenne die Promotionsordnung der Fakultät Mathematik und Naturwissenschaften an der Technischen Universität Dresden vom 20. März 2000 an.

Dresden, den 16.12.2009

Steffen Lök